ISSN 1811-1165 (Print)
ISSN 2413-2179 (Online)

EURASIAN PHYSICAL TECHNICAL JOURNAL

VOLUME 22, NO. 1(51), 2025

phtj.buketov.edu.kz

EURASIAN PHYSICAL TECHNICAL JOURNAL

p - ISSN 1811-1165
e - ISSN 2413-2179

Volume 22, No. 1(51), 2025

1st issue – June, 2004

Journal Founder:

**NLC "KARAGANDY UNIVERSITY
OF THE NAME OF ACADEMICIAN
E.A. BUKETOV**

https://phtj.buketov.edu.kz

www.facebook.com/groups/1103109540750967

Registration Certificate No.4382-Zh,
November 7, 2003.

Re-registration Certificate No.KZ50VPY00027647,
October 6, 2020 issued by Information Committee of
the Ministry of Information and Public Development
of the Republic of Kazakhstan

Contact information:

Editorial board of EAPhTJ
(Build. 2, room 216)
Karaganda Buketov University
Universitetskaya Str.28, Karaganda,
Kazakhstan, 100024
Subscription index: 75240

Tel: +7(7212) 77-04-03
Fax: +7(7212) 35-63-98
E-mail: ephtj@mail.ru,
ephtj2021@gmail.com

Signed to print 18.03.2025
Format 60x84 1/8. Offset paper.
Volume 17.75 p.sh. Circulation 300 copies.
Order No. 34.

Printed in the Publishing House of
Karagandy University of the name
of academician E.A. Buketov

Tel. +7 (7212) 35-63-16. E-mail:
izd_karu@buketov.edu.kz

Chief EDITOR

Sakipova S.E., Karaganda Buketov University, Karaganda, Kazakhstan

EDITORIAL BOARD

Aringazin A.K., L.N. Gumilyov Eurasian National University, Astana, Kazakhstan

Dzhumanov S., Institute of Nuclear Physics, Uzbekistan Academy of Sciences, Tashkent, Uzbekistan

Ibrayev N.Kh., Institute of Molecular Nanophotonics, Karaganda Buketov University, Karaganda, Kazakhstan

Jakovics A., Institute of Numerical Modelling, University of Latvia, Riga, Latvia

Kucherenko M.G., Director of the Laser and Information Biophysics Centre, Orenburg State University, Orenburg, Russia

Kuritnyk I.P., Department of Electronics and Automation, High school in Oswiecim, Poland

Kushpil S., Heavy Ion Group, Nuclear Physics Institute of the Czech Academy of Science, Řež near Prague, Czech Republic

Miau J.J., Department of Aeronautics and Astronautics, National Cheng Kung University, Tainan, Taiwan

Miroshnichenko A.S., Department of Physics and Astronomy, University of North Carolina at Greensboro, North Carolina, USA

Saulebekov A.O., Kazakhstan Branch of Lomonosov Moscow State University, Astana, Kazakhstan

Senyut V.T., Joint Institute of Mechanical Engineering of National Academy of Sciences of Belarus, Minsk, Belarus

Shrager E.R., National Research Tomsk State University, Tomsk, Russia

Stoev M., South-West University «Neofit Rilski», Blagoevgrad, Bulgaria

Suprun T., Institute of Engineering Thermophysics of NASU, Kyiv, Ukraine

Trubitsyn A.A., Ryazan State Radio Engineering University, Ryazan, Russia

Zeinidenov A.K., Karaganda Buketov University, Karaganda, Kazakhstan

Zhanabaev Z.Zh., Al-Farabi Kazakh National State University, Almaty, Kazakhstan

TECHNICAL EDITOR

Kambarova Zh.T., Karaganda Buketov University, Karaganda, Kazakhstan

© Karaganda Buketov University, 2025

Eurasian Physical Technical Journal, 2025, Vol. 22, No. 1(51)

CONTENTS

Dear authors and readers!
Dear colleagues!

In the preface, we traditionally inform the authors and readers about the most important achievements of the Eurasian Physical Technical Journal at the moment.

Thanks to our authors and the qualified work of the editorial board members, the journal continues to be indexed in the Scopus database in all four scientific areas with a max percentile 27% on the Engineering direction. These indicators were achieved thanks to the objective and highly qualified examination of materials by our reviewers, which guarantees the quality of published in the Eurasian Physical Technical Journal articles. According to the Scimago Journal & Country Rank (SJR) website, as of March 2025, the journal's Hirsch index is 7, the journal is in the Q3 quartile in the Engineering area.

An analysis of the website's statistical indicators shows that the period of consideration of articles from the moment of receiving materials on the site until the official publication date in 2024 was from 3 to 6 months (an average of 127 days). There are quite a lot of people wishing to be published, and despite the fact that almost 60% of articles are rejected, a queue is created for authors. But at the same time, the number of citations of articles published in the journal does not increase sufficiently. Therefore, it is very encouraging that on March 5, 2025, the CiteScore Tracker indicator reached a value of 1.2 for the first time, the value of which directly depends on the number of citations of articles published in the Eurasian Physical Technical Journal.

This first issue of 2025 contains 14 articles, 5 of which are co-authored by highly rated authors with high Hirsch index. Let's move on to a description of the contents of this issue.

The Materials Science section presents new original results on the study of material properties under various external influences. In particular, readers will be interested in the results of the assessment of the «destruction processes of the strength and thermal parameters of two-phase lithium-containing ceramics subjected to high-dose irradiation with protons, the effect of which simulates the processes of hydrogen swelling». The Kazakh authors found that «in the case of two-phase ceramics, an increase in the stability of maintaining strength properties is observed under long-term temperature changes».

Astana researchers have analyzed the «processes of elastic scattering of a nuclear system from the point of view of the microscopic theory of energy near the Coulomb barrier». The results obtained «allow us to more accurately determine nuclear properties and improve the saturation characteristics of the nuclear environment». In an article by Almaty scientific centers researchers, «the effect of different concentrations of polyethylene terephthalate filler on the strength, rupture, and relative elongation at rupture of polyimide films under uniaxial tension" was studied. It was determined that for all types of samples, the initial mechanical load causes a sharp increase in relative elongation, which «is explained by the rotation of globules and the alignment of matrix macromolecules into elongated chains along the direction of the load». Buketov University employees together with a Tomsk scientist, used in their research» a method of two-sided two-stage anodization to obtain films of anodic aluminum oxide with periodic and regularly located pores». As a result, absorption and reflection spectra of a porous film of anodized aluminum were obtained, where «the maximum value of the refractive index is observed in the short-wave and long-wave regions of the spectrum».

The Energy section contains articles on environmental aspects of energy, both for power plants using alternative energy sources and for improving the efficiency of power units and assessing potential safety threats. The work by authors from Tashkent takes into account the specific features of the arid climate of Uzbekistan. The «efficiency of photothermal devices of various capacities with a new type of cooling system» that does not require constant use of water was studied. As a result of joint research by authors from Tomsk and Astana, the «dependence of the efficiency of a single-loop power unit with a helium reactor and a hydrogen module on the degree of regeneration" was determined. It was shown that «a gas-cooled reactor with a turbine and compressor allows the use of a thermodynamic cycle» with high efficiency. Research by authors from Indonesia shows that «biogas as a dual-fuel fuel can improve engine performance while reducing harmful emissions, making it a sustainable energy alternative».

The article by the authors from the Kurchatov Research Center presents the development of a «portable coaxial HPGe detector in combination with FRAM software for determining uranium enrichment under shielding and without it». The results of gamma spectrometric measurements of fuel rod samples with low uranium content showed that this method provides a reliable and rapid enrichment assessment with low error».

The Engineering section articles examine practically important technical developments and solutions to current problems in the automation of modern technologies, control and monitoring systems. In the article, authors from Russia and Egypt developed a «thermoelectric method for monitoring the value of contact connection transition resistance» to detect faulty contact connections in an electrical network» ... with resistance exceeding the values specified in regulatory documents. Authors from Temirtau studied the composition and properties of road marking coatings that have «high weather resistance, in particular, resistance to temperature changes, moisture resistance, and good anti-corrosion properties». The developed road marking coatings are clearly visible at any time of day and night, and can be used "to protect exposed steel structures».

The Karaganda Saginov Technical University scientists' article is devoted to the analysis of the study of changes in «some physical and structural properties of melts under certain parameters of ultrasonic treatment" causing acoustic cavitation of liquid metal. Ultrasonic treatment is "an effective method of dynamic impact on liquid and crystallizing metal». The possibility of implementing various mechanisms of structural changes in the same melt in different temperature ranges is shown. In the last article of this section, the authors also studied the properties of ceramics based on beryllium oxide (BeO), also formed using ultrasound. Such ceramics showed more intense sintering, less shrinkage and a lower sintering temperature compared to ceramics obtained without ultrasound. It is shown that the rheological properties of the thermoplastic slip change with ultrasonic activation, which improves the properties of castings.

The Physics and Astronomy section presents the results of a study of the physical characteristics of macroscopic processes in the galaxy to microscopic processes of photoluminescence as a result of electron recombination. The first article in this section examines the variability processes of active galactic nuclei, which play a key role in understanding the physical processes in their central regions. The authors conducted an "analysis of the photometric and spectral variability of two Seyfert galaxies, MRK 6 and MRK 1040, based on archival and modern observations». This made it possible to estimate the "velocity dispersions and the corresponding velocities along the line of sight, which may indicate the outflow of matter from the central regions of galaxies. In the second article, the "photoluminescence spectra of indium antimonide at a certain concentration consisting of two lines, the maxima of which shift toward higher energies with increasing concentration are investigated. The authors found that the short-wavelength emission line of doped n-type indium antimonide crystals is due to the recombination of electrons located at the Fermi level with holes at the top of the valence band.

We hope the presented articles will be of interest to scientists, teachers, doctoral and master's students. We will be glad to see you among our readers and authors of the next issues, in which it is planned to publish articles by leading scientists on the most relevant and priority areas of modern physics and technology.

We also invite authors and readers to visit our Facebook (https://www.facebook.com/groups/1103109540750967/members), where announcements and news about the Eurasian Physical Technical Journal are posted, and write your opinions and wishes.

With respect and best wishes for health and well-being to our authors and readers,

Editor-in-Chief, Professor Sakipova S.E.
March, 2025

EURASIAN PHYSICAL TECHNICAL JOURNAL
2025, Volume 22, No. 1 (51)
https://doi.org/10.31489/2025N1/5-18

Received: 13/12/2024 Revised: 21/02/2025 Accepted: 18/03/2025

Research Article

UDC 53.043

STUDY OF THE EFFECT OF THE COMPONENT RATIO VARIATION IN TWO-PHASE CERAMICS ON THE RESISTANCE TO HIGH-DOSE PROTON IRRADIATION SIMULATING THE EFFECTS OF HYDROGEN SWELLING

Kozlovskiy A.L.[1,2*], Kenzhina I.E.[1,2,3,4], Tolenova A.[1], Askerbekov S.[1,2]

[1] Satbayev University, Almaty, Kazakhstan
[2] The Institute of Nuclear Physics, Almaty, Kazakhstan
[3] Institute of Experimental and Theoretical Physics, Al-Farabi Kazakh National University, Almaty, Kazakhstan
[4] Kazakh-British Technical University, Almaty, Kazakhstan
*Corresponding author: kozlovskiy.a@inp.kz

Abstract. *The paper presents the evaluation results of the destruction processes of the strength and thermal parameters two-phase lithium-containing ceramics subjected to high-dose irradiation with protons, the impact of which simulates the processes of hydrogen swelling. Interest in this research topic is primarily due to the possibilities of determining the influence of variation in the ratio of two components of lithium meta zirconate and lithium orthosilicate on maintaining stability and resistance to radiation damage, and diffusion processes associated with post-radiation isothermal annealing of samples, typical for simulation of desorption processes. During the conducted studies of the effect of the component ratio variation in two-phase ceramics on resistance to radiation-induced softening processes and reduction in crack resistance, it was determined that, unlike single-component ceramics, the combination of two phases in the composition leads not only to an elevation in the initial strength parameters, but also to a softening resistance growth due to the presence of interphase boundaries. In the case of testing the studied ceramics to thermal impact processes (thermal resistance tests), it was found that in the case of two-phase ceramics, a rise in the stability of maintaining strength properties to long-term temperature changes is observed.*

Keywords: hydrogen swelling; breeders; two-phase ceramics; high-dose irradiation; lithium meta zirconate; lithium orthosilicate.

1. Introduction

The use of alternative energy sources, including nuclear and thermonuclear energy, is the most promising way to solve global problems associated with the increase in global demand for energy consumption, as well as reducing the negative impact on the environment associated with the depletion of fossil resources, as well as the need to reduce the amount of harmful emissions that lead to the threat of global warming [1]. In the case of using nuclear energy to solve these problems, great emphasis is placed on the development of concepts for the use of new types of nuclear reactors, which consist of increasing the power and service life by changing the concept of nuclear fuel, as well as the use of materials capable of withstanding high temperatures [2]. When considering thermonuclear energy as an alternative energy source, much attention is paid to the use of the D-T fuel cycle, which includes the use of deuterium and tritium as the basis of thermonuclear fuel, the use of which allows for the production of large amounts of energy, as well as the almost complete absence of nuclear waste.

The concept of obtaining tritium to maintain the fuel D-T cycle in thermonuclear reactors is to produce tritium in a blanket containing lithium, the use of which is due to the possibility of obtaining tritium as a result of nuclear reactions of lithium with neutrons, the fission products of which are tritium and helium [3]. At the same time, for stable maintenance of the D-T cycle in a thermonuclear reactor, it is necessary that the tritium production coefficient in the blanket be greater than 1, which imposes a definition of the condition for ceramic materials of lithium-containing ceramics, the key one of which is a high lithium content in the composition. One of the most suitable types of ceramics containing a large amount of tritium are lithium orthosilicate ceramics (Li_4SiO_4), which, due to their structure, contain much more lithium than other types of ceramics, such as lithium titanate (Li_2TiO_3), lithium aluminate ($LiAlO_2$) or lithium metazirconate (Li_2ZrO_3). Also, an important role in the selection of blanket materials is played by their thermophysical properties, which determine the mechanisms for transforming the energy of incident fast neutrons into thermal energy, thereby reducing the risk of overheating effects, as well as reducing energy costs for plasma containment using electromagnetic forces [4-6]. It is important to highlight that the ceramic materials of the blanket, in addition to the above properties, must have sufficiently high indicators of resistance to destruction during the radiation damage accumulation, which is caused by both the impact of neutrons and fission products of nuclear reactions in the form of helium and hydrogen, the accumulation of which occurs in the near-surface layers of the blanket, due to the high mobility of these elements, alongside an increase in their diffusion at high temperatures, the maintenance of which is required by operating conditions, as well as the need to initialize the desorption processes of the formed tritium in the ceramics.

In view of this, in recent years, much attention has been paid to developments in the field of creating ceramic materials used as tritium breeders for blankets of thermonuclear reactors, the use of which will solve the problem of producing tritium, which is necessary to maintain thermonuclear reactions [7,8]. At the same time, the most intensive research in this area is aimed at finding optimal compositions of lithium-containing ceramics with high rates of chemical inertness and stability to mechanical impacts, high density of lithium in the composition, radiation resistance and resistance to the radiation damage accumulation caused by neutron irradiation, as well as the influence of nuclear reaction products in the form of helium and hydrogen. The most promising types of lithium-containing ceramics are considered to be two-phase ceramics with different phase contents [8], core-shell structures [9,10] or composite ceramics, which are substitution or interstitial solid solutions [11]. Among these types of lithium-containing ceramics, the most promising are two-phase ceramics obtained by various synthesis methods, such as sol-gel or hydrothermal methods [12], rolling methods [13], mechanochemical solid-phase synthesis combined with thermal annealing of samples [14,15]. Interest in them is due to the possibility of combining the properties of various components of lithium-containing ceramics, as well as the formation of interphase or dispersion strengthening effects arising due to size effects [16], as well as variations in the ratio of phases in the composition [17]. At the same time, despite a fairly large number of existing works in this area, interest in such studies does not subside, and the annual number of scientific publications on the topic of research related to the development of technology for obtaining lithium-containing ceramics, as well as the study of the processes of their interaction with ionizing radiation, including neutron, proton and alpha particles, only increases, which indicates the high significance of such studies due to the need to solve the problem of tritium production.

The main idea of this study is to determine the influence of variation in the ratio of lithium meta zirconate and orthosilicate components on the resistance to radiation damage associated with hydrogenation processes in the near-surface layer.

At the same time, the effect of the component ratio variation on resistance to hydrogenation processes was assessed by measuring the trends of hardness reduction, crack resistance and cracking under mechanical action, as well as the degradation kinetics of ceramics subjected to hydrogenation and subsequent thermal action, simulating thermal aging processes. In this case, long-term high-temperature heating initiates the processes of implanted hydrogen diffusion, which leads to its agglomeration in voids, thereby increasing the deformation distortion of the crystalline structure, which has a negative effect on the strength properties of ceramics. Also, the presented results of experimental work related to determining the influence of irradiation temperature on the degree of change in strength parameters caused by thermal expansion of the crystalline structure and more pronounced diffusion made it possible to establish the influence of variation in the ratio of components in two-phase ceramics on resistance to degradation.

The novelty of this study lies in determining the prospects for using two-component lithium-containing ceramics as blanket materials for tritium breeding, with the main emphasis in the study being placed on assessing the influence of hydrogenation processes on changes in the strength characteristics of ceramics.

2. Material and methods of research

Five types of ceramics were selected as objects for conducting studies related to determining the effect of varying the ratio of lithium orthosilicate and lithium metazirconate components on the resistance to hydrogen swelling and destruction of the surface layer under high-dose irradiation. Two of them are single-phase ceramics based on lithium metazirconate (Li_2ZrO_3) and lithium orthosilicate (Li_4SiO_4), as well as three types of two-phase ceramics obtained by varying the ratio of $xLi_2ZrO_3 – (1-x)Li_4SiO_4$ components at x equal to 0.75, 0.5 and 0.25 M. Moreover, in the work [18], published earlier by our research group, a detailed analysis and characterization of the strength and thermal physical parameters of these types of ceramics in the initial state with variations in the ratio of powder components was carried out, according to which it was determined that the most optimal compositions with the highest indicators of hardness, resistance to cracking under single compression, and crack resistance are two-phase ceramics with an equal ratio of components in the composition. At the same time, test trials of the radiation resistance of these ceramics to the accumulation of structural damage associated with high-temperature irradiation with He^{2+} ions showed that two-phase ceramics are more resistant to radiation damage caused by the accumulation of implanted helium in the surface layers, while single-phase ceramics have fairly low stability indicators of strength and thermal physical parameters to radiation damage [18]. Table 1 reveals the parameters of the strength and thermal characteristics of the studied ceramics obtained in [18], which were used as reference data for a comparative analysis of changes associated with the accumulation of radiation damage with variations in irradiation fluence. According to the data presented, an alteration in the ratio of components $(1-x)Li_2ZrO_3 – xLi_4SiO_4$ in the composition of ceramics leads to a change in the strength parameters, up to an equal ratio of components. At the same time, the dominance of Li_4SiO_4 in the composition of ceramics at concentrations above 0.5 M leads to a decrease in the strength parameters relative to the maximum values obtained for ceramics with an equal ratio of components in the composition. It is important to note that in the case of single-component ceramics, the strength indicators for Li_2ZrO_3 ceramics are higher than for Li_4SiO_4, which in turn indicates a higher resistance to external influences of lithium metazirconate in comparison with lithium orthosilicate, which was also confirmed by irradiating samples with He^{2+} ions [18]. According to the studies cited, the highest resistance to external influences under single compression and three-point bending are found in ceramics with an equal ratio of components in the composition, for which the increase in resistance is about 10 %. Such alterations in this case can be explained both by the effect of the presence of interphase boundaries and by dispersion strengthening, the presence of which is due to changes in the size of grains and the density of their packing, as shown in Figure 1. The morphological characteristics of the studied ceramics were measured using the scanning electron microscopy method, performed using a Phenom™ ProX microscope (Thermo Fisher Scientific, Eindhoven, Netherlands).

Table 1. Parameters of hardness, resistance to single compression, crack resistance, thermal conductivity coefficient

Paramater	**(1-x) $Li_2ZrO_3 – xLi_4SiO_4$ ceramics**				
	0	**0.25**	**0.5**	**0.75**	**1**
Hardness, HV	752±7	761±6	795±8	775±6	685±7
Crush load, N	44.5±1.4	48.7±1.8	51.6±1.7	47.2±1.3	34.5±1.6
Crack resistance, MPa×$m^{1/2}$	1.65±0.14	1.71±0.09	1.94±0.11	1.82±0.12	1.67±0.13
Thermal conductivity, W/(m×K)	1.75±0.13	1.81±0.11	1.97±0.08	1.94±0.14	1.73±0.12

The influence of variation in the ratio of components in two-phase ceramics on resistance to hydrogen embrittlement and related processes of degradation of strength and thermal parameters was determined by simulation of the processes of implanted hydrogen accumulation due to irradiation with protons with an energy of 1 MeV and various irradiation fluences from 10^{15} to 10^{18} cm^{-2}. These fluences, according to the presented method of converting fluence into the value of atomic displacements (dpa) [19, 20], which is a universal parameter used to compare the values of radiation damage caused by different types of ionizing radiation, correspond to the range of 0.04 – 40 dpa, which, when converted to neutron flux, is about 10^{18} – 10^{22} neutron/cm^2 (for neutrons with an energy of more than 0.1 MeV).

The study of the mechanisms responsible for the reduction of the strength parameters (hardness, resistance to cracking, crack resistance) was carried out using standard methods for determining hardness by the indentation method, single compression of samples to determine resistance to crack formation, and determination of resistance to three-point bending to determine the value of crack resistance. Methods for assessing changes in strength characteristics used for lithium-containing ceramics are presented in [5].

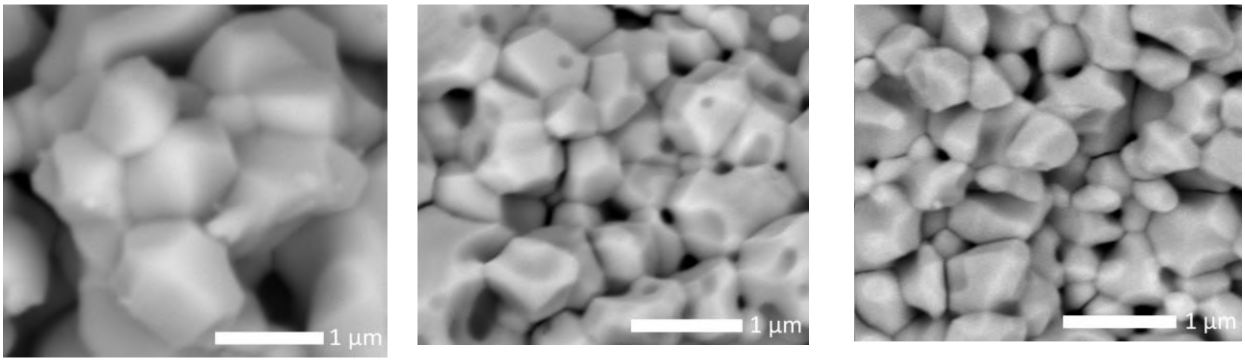

Li_2ZrO_3 0.75 Li_2ZrO_3 – 0.25 Li_4SiO_4 0.5 Li_2ZrO_3 – 0.5 Li_4SiO_4

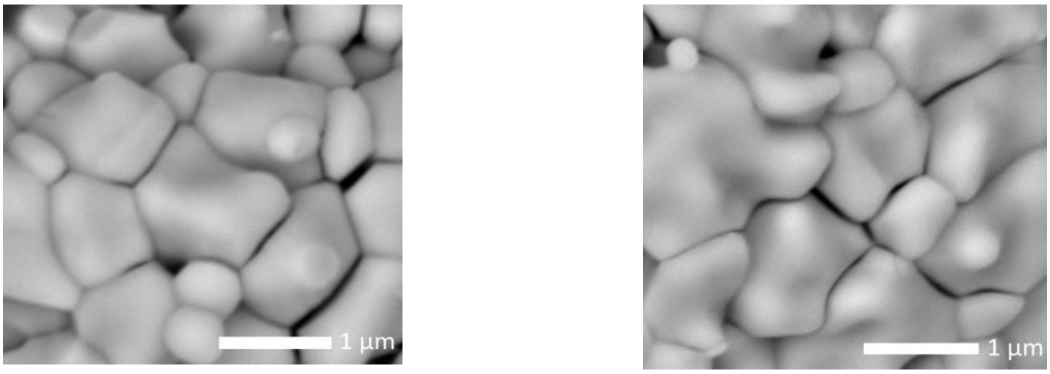

0.25 Li_2ZrO_3 – 0.75 Li_4SiO_4 Li_4SiO_4

Fig. 1. Assessment results of the morphological features of the studied ceramics contingent upon the ratio of components in the composition, reflecting the influence of their variation on dimensional factors, as well as the possibility of forming the effect of dispersion hardening

In this case, the change in the ratio of components in the composition of two-phase ceramics leads to the formation of a structure containing both rhomboid grains of Li_2ZrO_3 and spherical grains characteristic of Li_4SiO_4, which have larger sizes. The observed strengthening effects in this case are due to the influence of the presence of interphase boundaries, which arise due to differences in grain sizes, as well as the formation of a structure of the type of larger grains of Li_4SiO_4, surrounded by a finely dispersed fraction of Li_2ZrO_3.

The thermal conductivity coefficient was measured by determining changes in the stationary heat flow using a universal thermal conductivity meter KIT-800 (KB Teplofon, Moscow, Russia).

The influence of the accumulated dose of proton irradiation on resistance to high-temperature effects (non-thermal resistance tests) was determined by rapidly heating the samples to a temperature of 1000 °C (heating rate 50 °C/min), holding for 1 hour at this temperature and abrupt cooling by removing the samples from the muffle furnace into the air. As a result of these manipulations with the samples, the effect of sharp temperature changes typical of emergency situations arising in critical situations during the operation of ceramic samples during abnormal situations is simulated. The number of tests was about 10 consecutive cycles, which made it possible to evaluate the degradation resistance of samples in the initial state and irradiated with fluences of 10^{16} and 10^{18} proton/cm^2. The results of these experiments made it possible to establish not only the kinetics of sample destruction under conditions characteristic of extreme situations during operation, but also to establish the effect of variation in the component ratio on the resistance of ceramics to thermal effects. All experimental work was carried out in several parallels in order to determine measurement errors and standard deviation, as well as the convergence of results. The experiments carried out allowed us to exclude factors that could have a negative impact on the project results, as well as to exclude inaccuracies in the data presented.

3. Results and discussion

The key parameters for using lithium-containing ceramics for tritium multiplication, in addition to the efficiency of multiplication and subsequent desorption of tritium, are their resistance to degradation of strength properties, the change of which can make significant adjustments to the service life. In this case, deterioration of resistance to external influences due to the accumulation of structural damage and defective inclusions, which in most cases are agglomerations of point defects and oxygen vacancies in the damaged layer, can lead to deterioration of tritium desorption processes, as well as their destruction due to loss of stability to external mechanical effects associated with compression of samples during thermal expansion. Also, an important role in determining the potential of application is played by the thermophysical parameters of the studied ceramics, the deterioration of which is caused, as a rule, by the processes of accumulation of disordered areas, creating additional barriers for phonon heat exchange mechanisms. In some cases, one of the factors that allows increasing the resistance of ceramics to external influences, as well as radiation damage, is the creation of interphase boundaries, due to the variation of the phase ratio, as well as the effect of dispersion strengthening, which occurs when the grain sizes decrease, and, as a consequence, the dislocation density increases. The combination of these factors allows not only to increase the mechanical properties of ceramics, as shown in Table 1, but also to increase resistance to external influences associated with the accumulation of structural damage resulting from the accumulation of the damage dose during irradiation.

Figure 2 demonstrates the assessment results of the change in the strength characteristics (hardness, resistance to cracking and crack resistance) of the studied ceramics depending on the irradiation fluence (recalculated for the value of atomic displacements). The general form of the presented dependencies reflects the degradation of the strength properties of the studied ceramics, as well as the influence of the variation in the ratio of components in the composition of two-phase ceramics on resistance to softening associated with the accumulation of structural damage. It should be noted that the measurements were carried out on a series of samples, which made it possible to establish the measurement error, as well as the values of the standard deviation, the values of which indicate the repeatability of the changes observed during irradiation, which also confirms the fact of the stability of the technological process for manufacturing ceramics according to the proposed production method.

As can be seen from the presented dependences of the change in strength properties on the magnitude of atomic displacements, the observed trends of changes indicate a difference in the trends of degradation of strength properties caused by the effect of accumulation of structural damage caused by proton irradiation and, as a consequence, a change in the magnitude of atomic displacements in the damaged layer. At irradiation fluences corresponding to the value of atomic displacements up to 1 dpa, the changes in the strength parameters are minimal and are within the permissible measurement errors, which indicates a high resistance of ceramics to softening at low irradiation doses (less than 1 dpa corresponds to a fluence range from 10^{15} to 5×10^{16} proton/cm^2). In this case, small changes in the strength parameters are due to the cumulative effect of structural distortions that appear during high-dose irradiation. While at low fluences, the resulting point and vacancy defects are able to relax, which leads to the formation of isolated structurally distorted areas in the damaged layer, the dimensions (in particular, the diameter and length), as shown in [21,22], directly depend on the type of interacting particles, as well as their energy. In the case of protons used for these experiments, due to their nature, the damaged areas have a large extended shape (more than 20 μm in size) and a diameter of less than 1 nm, which leads to their isolation from each other even in the case of sufficiently high irradiation fluences.

At the same time, according to a number of studies [23], the main structural defects in lithium-containing ceramics are E-centers associated with the formation of oxygen vacancies, while at high irradiation fluences (in atomic displacement values above 1-5 dpa), the accumulation of radiolysis products, i.e. complex defects associated with physicochemical processes, begins in the structure. In this regard, small changes in strength parameters at irradiation fluences below 5×10^{16} proton/cm^2 may be due to the effects of small structural changes caused by the formation of vacancy defects, the accumulation of which, together with the products of physicochemical radiolysis processes, leads to the formation of complex defects, the presence of which has a more significant negative effect on the change in strength parameters, expressed in a change in the trends of hardness reduction, the value of maximum pressure under single compression and crack resistance determined in three-point bending tests. In this case, it can be noted that the critical irradiation fluences, upon reaching which a change in the trends of changes in strength parameters is observed, is a value of about 10^{17} proton/cm^2. It is also important to reflect the fact that changes in the ratio of components in the composition of ceramics lead to a change in the trends of degradation of strength properties, which in turn indicates a positive dynamic of the effect of variation in the phase composition of ceramics on strengthening and an increase in resistance to radiation-induced destruction processes in comparison with single-phase ceramics.

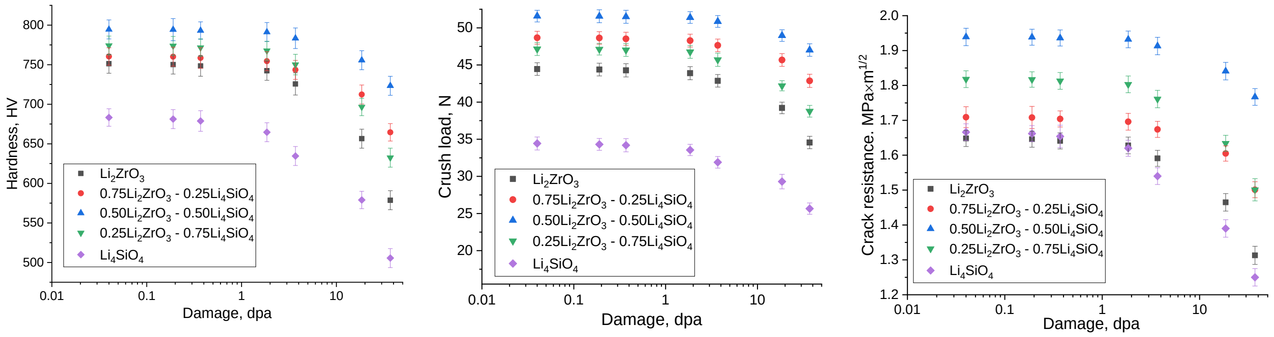

a) b) c)

Fig. 2. Assessment results of changes in the strength parameters of (1-x)Li_2ZrO_3 – xLi_4SiO_4 ceramics subjected to proton irradiation: a) results of changes in the hardness of ceramics depending on the value of atomic displacements; b) results of the maximum pressure that ceramics can withstand during a single compression depending on the value of atomic displacements; c) results of changes in the crack resistance value determined by the three-point bending method depending on the value of atomic displacements

It is noteworthy that the critical irradiation fluence of the order of 10^{17} proton/cm^2, at which a nearly exponential nature of the decrease in the trends of strength parameters is observed, is in good agreement with a number of works related to the study of the processes of swelling of the near-surface layer of ceramics subjected to helium irradiation [24,25]. The similarity of the observed changes in this case can be explained by the fact that in both cases, at high irradiation fluences, agglomeration of implanted helium and hydrogen occurs in pores and voids due to diffusion processes and weak solubility of these types of ions, which in turn leads to the formation of gas-filled bubbles in the near-surface damaged layer, the deformation expansion of which leads to the destruction of the near-surface layer. In this case, as was shown in the work [26], the evolution of the processes of accumulation of products of nuclear reactions in the form of tritium, helium, hydrogen and their isotopes is accompanied by filling of voids in lithium-containing ceramics, with subsequent release of gas from these voids, which can be accompanied by deformation opening of these voids, as well as partial embrittlement of the surface layer. In this case, it can be concluded that the main observed changes in the reduction of strength parameters, as in the case of helium accumulation in the surface layer, are associated with the processes of deformation embrittlement caused by the effects of diffusion and agglomeration of hydrogen in voids with a subsequent increase in the deformation of the crystalline structure. It should also be noted that the observed differences in the trends of reduction in strength properties are primarily associated with a change in the ratio of components in the composition of ceramics, from which it follows that the formation of two-phase ceramics, especially in which the Li_4SiO_4 content is 0.25 and 0.5 M, leads to an elevation in resistance to softening caused by high-dose irradiation. In this case, the observed effect of growth in resistance to softening caused by the accumulation of structural distortions, and in the case of high doses of irradiation of the products of physical and chemical processes of radiolysis, is due to the presence of interphase boundaries, as well as dispersion hardening associated with changes in grain sizes (and, as a consequence, dislocation density). The observed effect of dislocation hardening associated with an increase in the resistance of ceramics to radiation damage caused by high-dose irradiation is in good agreement with the results of works [27, 28].

Figure 3 illustrates the dependences of the change in the softening factors of the parameters under study, caused by the influence of the destruction of the crystal structure, as well as the accumulation of structural damage caused by proton irradiation. The data presented in Figures 3a-c were obtained by comparative analysis of the values of the strength parameters of the irradiated samples with the values obtained for the samples in the initial state. In this case, the values of the softening factors are given in percentage terms, reflecting the dependence of the degradation of strength properties with the accumulation of structural damage in the samples under study. The general form of the observed changes in the softening factors indicates a two-factor effect of both the irradiation fluence (in this case, the magnitude of atomic displacements caused by irradiation) and the ratio of components on the stability of two-phase ceramics. In the case of a change in the irradiation fluence, and as a consequence, the magnitude of atomic displacements in the damaged layer, an exponential growth of the softening factors is observed, indicating a negative effect of accumulated structural damage on the strength parameters, which are most pronounced when the magnitude of atomic displacements exceeds 5 dpa. When this threshold value of atomic displacements is reached, in the case of single-phase (Li_2ZrO_3 and Li_4SiO_4) ceramics, a sharp increase in changes in the softening factors is observed. At the same time, comparing the observed changes, it can be concluded that the degradation of strength properties has a similar order of magnitude (the differences are less than 1 %), from which it follows that the accumulation of deformation distortions affects both the degree of resistance to external influences and a decrease in crack resistance, due to the formation of defective inclusions that create additional deformation stresses in the structure of the damaged layer. It should be noted that in the case of two-phase ceramics, the use of an equal ratio of Li_2ZrO_3 and Li_4SiO_4 components in the composition results in more than twofold increase in the resistance of strength parameters to degradation, according to the dependences presented in Figures 2 and 3. Such changes associated with the increase in the resistance of two-phase ceramics to the softening effect under high-dose irradiation can be explained by the presence of interphase boundaries, the change in the concentration of which, together with dispersion hardening (caused by size effects) leads to the creation of additional obstacles in the form of dislocations at grain boundaries, restraining diffusion processes. The observed effects of increasing resistance to high-dose irradiation, causing an increase in resistance to external influences due to the presence of interphase boundaries, are in good agreement with the results of [29,30]. It should also be noted that an increase in the concentration of the Li_4SiO_4 component to more than 0.5 M in the composition results in the hardening efficiency reduction, as in the case of lower concentrations of Li_4SiO_4 (less than 0.5 M), from which it follows that the optimal ratio of the components is 0.5 M Li_4SiO_4 and 0.5 M Li_2ZrO_3. According to the presented data for this type of ceramics, the maximum decrease in the strength parameters at an irradiation fluence of 10^{18} protons/cm^2 is no more than 10% of the initial value, while for single-phase ceramics the degree of softening at the maximum fluence is more than 20 %. At the same time, the general analysis of strength parameters indicates that the key role in determining the strength characteristics is played by the content of the Li_2ZrO_3 phase, a change in the concentration of which causes deterioration in strength properties due to lower strength indicators of Li_4SiO_4.

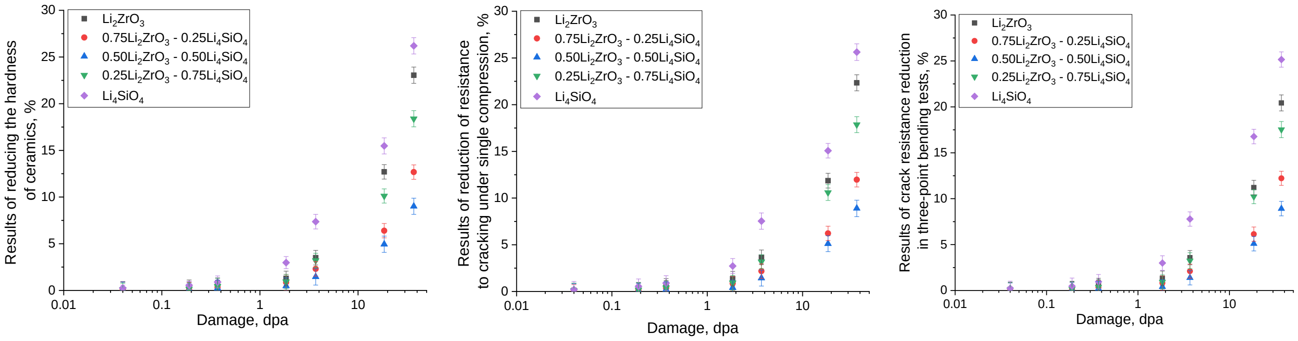

a) b) c)

Fig. 3. Results of alterations in the softening factors of the main strength parameters: a) results of changes in the hardness value of ceramics, characterizing the softening of the near-surface layer; b) results of changes in the value of resistance of ceramics to single compression of ceramic samples; c) results of changes in the value of crack resistance of ceramics during three-point bending tests.

It should be noted that Li_4SiO_4 has a higher percentage of tritium yield among all lithium-containing ceramics under consideration [31,32], which makes it possible to conclude that the use of an equal ratio of components in two-phase ceramics makes it possible to establish a balance between the tritium production efficiency, as well as resistance to destructive changes in strength parameters as a result of high-dose irradiation. Figure 4 reveals the assessment results of changes in the thermal conductivity coefficient of the studied ceramics depending on the value of atomic displacements, obtained for different types of ceramics, in the case of variation in the ratio of components. The general form of the observed changes in the thermal conductivity coefficient contingent upon the value of atomic displacements has a similar trend, which is the case of the observed changes in the strength parameters, however, the nature of the changes, especially with high-dose irradiation, has a smaller order of magnitude (approximately, the changes in the thermal conductivity coefficient are two times lower than the changes in the strength parameters, see the comparison of the results presented in Figures 3a-c and 4b).

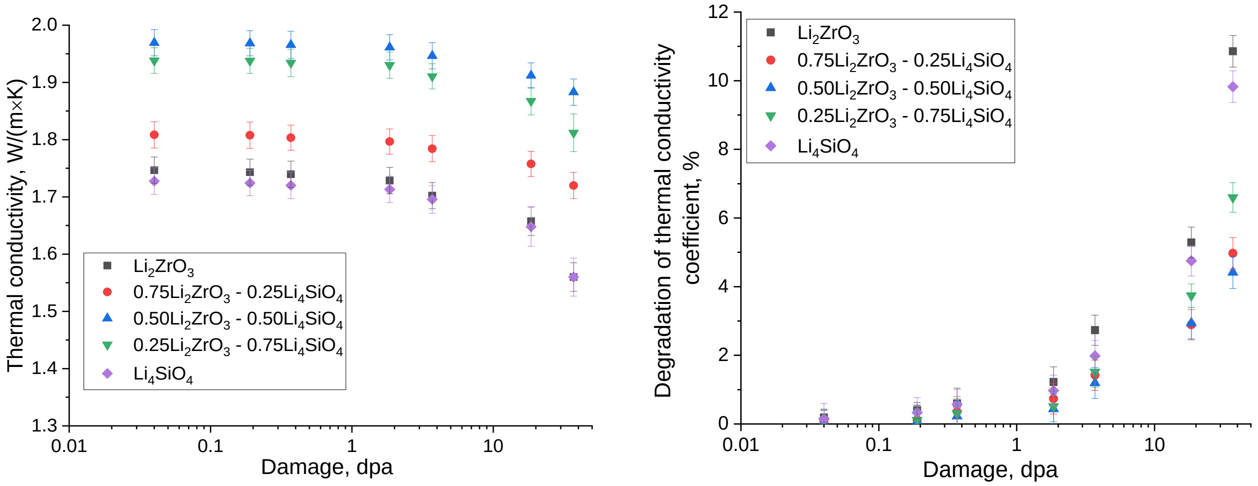

a) b)

Fig. 4. a) Results of changes in the thermal conductivity coefficient of the studied ceramics depending on the value of atomic displacements; b) Evaluation of changes in thermal conductivity reflecting thermal conductivity degradation associated with disordering.

Moreover, as in the case of strength parameters, a change in the ratio of components in the composition of two-phase ceramics leads to an elevation in resistance to degradation of the thermal conductivity coefficient. Analysis of the observed changes in the thermal conductivity coefficient in comparison with the value of atomic displacements indicates that the most significant changes are observed when the value of atomic displacements exceeds 1 dpa, which corresponds to the effect of the emergence of complex defects in the structure of the products of physicochemical radiolysis processes. From which it follows that the formation of disordered regions and the accumulation of complex defects greatly affect the decrease in the rate of heat transfer due to phonon mechanisms, while an increase in the concentration of point and vacancy defects at low irradiation fluences does not seriously affect the change in thermophysical parameters. It should also be noted that the highest resistance to a decrease in thermal physical parameters is exhibited by 0.5 M Li_4SiO_4 - 0.5 M Li_2ZrO_3 ceramics, for which the decrease in the thermal conductivity coefficient at maximum irradiation fluence is less than 4 %, while for single-phase ceramics the degradation of the thermal conductivity coefficient is more than 10 % compared to the initial value. Such a difference in degradation values, as in the case of a change in strength parameters, is due to the effects of increasing radiation resistance due to the presence of two phases in the composition, which in turn restrain the processes of radiation embrittlement and softening due to the presence of a large number of grain boundaries that restrain the diffusion of structural defects, thereby preventing them from agglomerating into larger clusters or filling voids. Accordingly, interphase boundaries and increased dislocation density caused by fine grain sizes positively influence not only the strengthening mechanisms, but also the stability of thermophysical properties under degrading conditions.

Figure 5 illustrates the results of changes in the strength parameters of the studied ceramics contingent upon the number of heat resistance test cycles, which reflect the resistance of the samples to temperature changes, as well as the effect of the accumulated radiation dose (in units of atomic displacements) on the stability to softening caused by thermal effects. The data are presented for three series of samples in the initial (non-irradiated) state, as well as those irradiated with fluences of 10^{16} and 10^{18} proton/cm^2. The choice of these samples as objects of study for assessment of their resistance to thermal effects (sudden temperature changes) was based on the need to determine the influence of the value of structural damage at which the onset of a decrease in strength parameters is observed (at a fluence of 10^{16} proton/cm^2) and in the case when the degradation of strength properties is maximum in a given experiment (at a fluence of 10^{18} proton/cm^2).

The general appearance of the observed changes in hardness values (the graphs show the values of hardness changes after thermal testing with the initial values) indicates a destructive nature associated with thermal exposure, initiating the formation of metastable states in the composition of the samples, associated both with oxidation processes due to thermal exposure and with diffusion processes of implanted hydrogen and oxygen vacancies, the presence of which is due to the destructive effect of irradiation (in the case of irradiated samples), and in the case of initial samples, thermal expansion of the crystal lattice, initiating processes of migration of defects and vacancies in the structure.

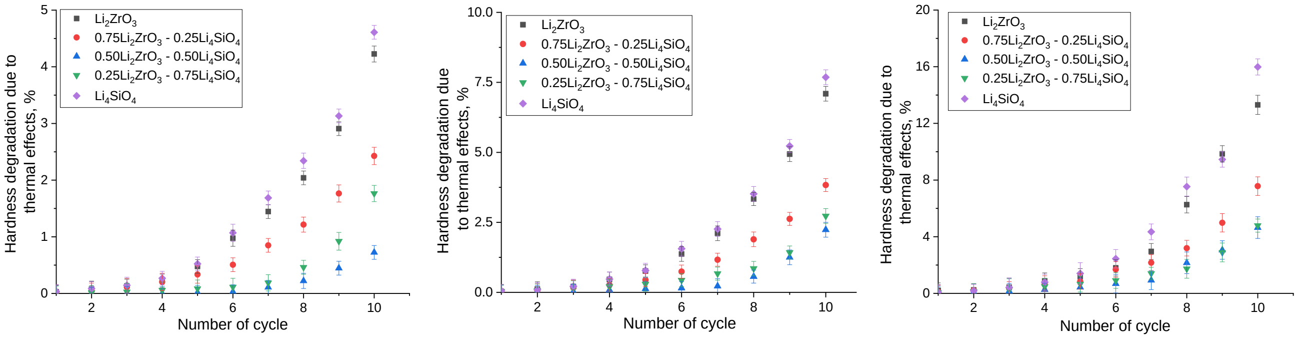

a) b) c)

Fig. 5. Test results of ceramics for heat resistance of the studied ceramics, reflecting the change in the hardness of the samples depending on the number of test cycles: a) test results of ceramics in the initial state; b) test results of ceramics irradiated with a fluence of 10^{16} ion/cm^2; c) test results of ceramics irradiated with a fluence of 10^{18} ion/cm^2

At the same time, the general analysis of the observed changes indicates that the thermal effect affects both the initial samples (non-irradiated) for which the maximum reduction after 20 cycles is about 4 – 5 % in the case of single-component ceramics, and 0.5 – 2 % in the case of two-phase ceramics, and the irradiated samples. Moreover, a change in the concentration of defects in the structure (in the case of a change in the irradiation fluence) results in more pronounced changes, indicating an intensification of the destruction processes due to temperature differences during thermal exposure. It should be noted that for two-phase ceramics, especially for samples with an equal ratio of components, the value of hardness changes after 10 test cycles is more than 3.5 – 4 times lower than for single-component ceramics, which indicates high resistance of these ceramics to external influences, including thermal expansion and oxidation, which causes a significant decrease in the rate of destruction. At the same time, in contrast to single-component ceramics, for which an intensive decrease in hardness is observed after 5 – 6 cycles, for two-component ceramics the most significant changes are observed after 7 – 8 cycles, which indicates not only higher resistance to external influences, but also a slowdown in degradation processes with long-term temperature changes.

One of the key factors influencing the assessment of the applicability of two-phase lithium-containing ceramics for tritium multiplication is their resistance not only to radiation damage, but also to temperature effects during irradiation. To test the studied ceramics for the resistance of strength characteristics to irradiation at various temperatures, the range of which was selected relative to the proposed operating regulations, the studied samples were irradiated with a fluence of 10^{18} proton/cm^2. In this case, irradiation was carried out at various temperatures, the range of which was from 300 to 1000 K. The results of the comparative analysis of the trends in the reduction of strength parameters depending on the irradiation temperature are presented in Figure 6 in the form of dependencies of the change in hardness parameters, the value of the maximum pressure under single compression and crack resistance of the studied samples depending on the irradiation temperature.

The general form of the presented dependencies indicates a negative effect of increasing the irradiation temperature on the stability of strength parameters in comparison with the initial values of strength indicators. At the same time, the downward trend is observed for all the studied types of ceramics, however, the dynamics of the decrease depending on the irradiation temperature at the same irradiation fluence for the studied single-phase ceramics in comparison with two-phase ones is more pronounced. Similar changes, as in the case of the presented dependences of the degradation of strength and thermal parameters under irradiation with fluence variation, indicate a positive effect of the influence of the presence of interphase boundaries and dispersion hardening caused by a change in grain size on the degradation resistance growth of ceramics exposed to irradiation.

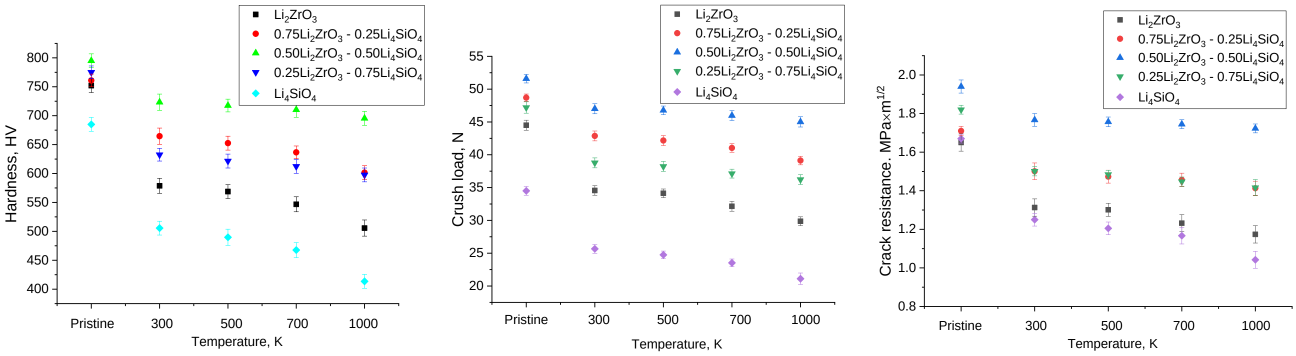

a) b) c)

Fig. 6. Results of changes in the values of hardness (a), the value of the maximum pressure under single compression (b), crack resistance (c) of the studied ceramics subjected to proton irradiation with a fluence of 10^{18} proton/cm^2, with variations in the irradiation temperature (the graphs also show the values of the strength parameters in the initial state for the purpose of a visual comparison of changes with variations in the irradiation temperature)

Figure 7 illustrates the results of a comparative analysis of changes in softening factors (changes in hardness, resistance to cracking under single compression, and crack resistance) depending on the irradiation temperature for all the samples under study. The data are presented to identify the influence of temperature exposure on the degree of softening, as well as to determine the most stable ceramics to high-temperature irradiation. The analysis of strength parameter variations across different types of ceramics indicates that two-phase ceramics, especially those with an equal component ratio, demonstrate greater resistance to strength degradation compared to single-phase ceramics.

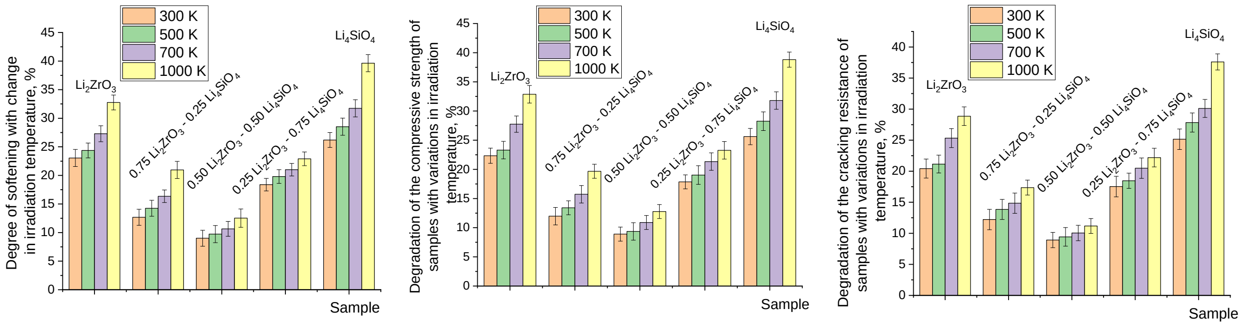

a) b) c)

Fig. 7. Results of changes in the softening factors of the main strength parameters of the samples depending on the irradiation temperature: a) results of changes in the hardness of ceramics, characterizing the softening of the surface layer; b) results of changes in the resistance of ceramics to single compression of ceramic samples; c) results of changes in the crack resistance of ceramics during three-point bending tests

As can be seen from the presented data on changes in the strength parameters of the studied ceramics, an increase in the irradiation temperature at one value of the accumulated fluence leads to an increase in the degradation of the strength parameters, with the most significant changes observed at high irradiation temperatures of about 700 – 1000 K. Such observed effects are caused by several factors, the combination of which leads to an acceleration of the degradation of the near-surface damaged layer, thereby reducing the strength indicators. Firstly, when the irradiation temperature varies, effects arise related to the temperature impact both on the crystal structure of the target and on the defects formed as a result of the interaction of incident particles with the electron and nuclear subsystems of the target. In this case, the thermal impact on the crystal structure of the target leads to the occurrence of effects related to the thermal expansion of the crystal structure (a rise in the volumetric and linear coefficients of thermal expansion), changes in the amplitude of thermal vibrations of atoms, which together results in greater mobility of atoms in the crystal structure of the ceramics.

The result of such changes may be effects associated with the migration of point and vacancy defects caused by thermal exposure, as well as lower resistance to external effects, which, during collisions of incident particles, due to the transfer of kinetic energy and its subsequent transformation into thermal energy, may lead to the formation of a greater number of defects than in the case of irradiation at room temperature. These results are confirmed by a direct dependence of the change in the values of degradation of strength parameters with an increase in the irradiation temperature, in the case of the same fluence values. In this case, the observed changes have an identical trend for all the studied types of ceramics with variations in the irradiation temperature with a difference only in the order of magnitude of the degree of degradation.

An elevation in the concentration of defective inclusions in the composition of the damaged layer initiates the growth of metastable highly deformed areas, which in turn leads to a decrease in resistance to mechanical impacts and a more pronounced decrease in crack resistance. Secondly, changing the irradiation temperature helps to accelerate the migration of implanted hydrogen, which, together with the formed oxygen vacancies, can lead to more intensive diffusion processes deep into the damaged layer, thereby increasing the thickness of the damaged layer, which has lower strength parameters, which also helps to accelerate the destruction processes and reduce strength properties.

It should also be noted that at high temperatures the process of agglomeration of small gas-filled cavities into larger ones is initiated due to migration and diffusion processes, which leads to an increase in the volume of these cavities due to their unification [33,34], and as a consequence, the initiation of processes of deformation distortion of the surface layer due to the creation of tensile deformation stresses caused by the pressure of gas-filled cavities on the crystalline structure of ceramics. It should be noted that for two-phase ceramics, the presence of interphase boundaries leads to the inhibition of these processes, which is clearly demonstrated in less pronounced changes in strength parameters, the difference of which, in comparison with single-component samples, is more than a two-fold growth in resistance to destruction at high irradiation temperatures. In the case of single-component ceramics, an increase in the irradiation temperature above 700 K results in more than 1.5-fold increase in the degree of destructive reduction in strength parameters in comparison with similar changes observed during irradiation of samples at room temperature (300 K), which indicates a negative impact of temperature exposure on the resistance of ceramics to radiation damage, and also imposes restrictions on the possibilities of using these ceramics in the case of high-temperature radiation exposure with high doses of damage.

4. Conclusion

Analyzing the obtained results of the dependences of the change in the strength and thermal physical parameters of the studied (1-x)Li_2ZrO_3 – xLi_4SiO_4 ceramics depending on the fluence of proton irradiation, the use of which is due to the processes of modeling the effects of hydrogenation, alongside the accumulation of products of the physicochemical processes of radiolysis that occur during high-dose irradiation, the following conclusions can be made.

The use of proton irradiation for modeling hydrogenation processes in the case of lithium-containing ceramics allows us to estimate the kinetics of changes in strength and thermal parameters depending on the dose of accumulated structural damage, which have different character of changes caused by variations in irradiation fluence. At low irradiation fluences, structural changes are caused by the formation of point defects and oxygen vacancies, to which, according to the presented data, the studied ceramics have fairly good resistance indicators, especially two-phase ceramics. At fluences above 10^{17} proton/cm^2, at which the initialization of physical and chemical processes of radiolysis occurs, an exponential decrease in strength parameters is observed, which is most pronounced for single-component ceramics.

According to the data presented, it was established that the formation of two-phase ceramics leads to a rise in radiation damage accumulation resistance during high-dose irradiation with protons, the accumulation of which results in acceleration of destructive embrittlement and softening processes (reduction of strength parameters). In the case of two-phase ceramics in which the Li_2ZrO_3 content is 0.75 and 0.5 M, the growth in resistance to destructive embrittlement and softening processes is more than two times compared to single-component ceramics. The results of heat resistance tests revealed that in the case of two-phase ceramics, an elevation in the number of test cycles has a lesser destructive effect on the reduction in hardness, the change of which is caused by oxidation processes that occur as a result of sudden temperature changes, as well as emerging metastable states, most pronounced for samples irradiated with fluences of 10^{18} proton/cm^2.

Analysis of the irradiation temperature effect of the studied samples of (1-x)Li_2ZrO_3 – xLi_4SiO_4 ceramics revealed that the presence of two phases in the samples results in suppression of the softening effects caused by the combination of thermal expansion of the crystal structure, as well as accelerated migration of defects in the samples. The increase in resistance in this case is due to higher resistance values of lithium metazirconate to thermal expansion, which, together with the presence of interphase boundaries, creates additional obstacles to softening of the samples due to the suppression of migration processes at the grain boundaries.

Conflict of interest statement.
The authors declare that they have no conflict of interest in relation to this research, whether financial, personal, authorship or otherwise, that could affect the research and its results presented in this paper.

CRediT author statement
Kozlovskiy A.L., Kenzhina I.E., Askerbekov S.: Conceptualization, Data Curation, Writing Original Draft; Methodology, Investigation; **Tolenova A.**: Writing Review & Editing, Supervision.
The final manuscript was read and approved by all authors.

Funding
This research was funded by the Science Committee of the Ministry of Education and Science of the Republic of Kazakhstan (No. AP19679905)

References

1 Mathew M. D. (2022) Nuclear energy: A pathway towards mitigation of global warming. *Progress in Nuclear Energy*, *143*, 104080. https://doi.org/10.1016/j.pnucene.2021.104080

2 Bekmuldin M.K., Skakov K., Baklanov V.V., Gradoboyev A.V., Akaev A.S. (2021) Heat-resistant composite coating with a fluidized bed of the under-reactor melts trap of a light-water nuclear reactor. *Eurasian Physical Technical Journal*, *18*(3 (37)), 65-70. https://doi.org/10.31489/2021No3/65-70

3 Meschini S., Ferry S. E., Delaporte-Mathurin R., Whyte D. G. (2023) Modeling and analysis of the tritium fuel cycle for ARC-and STEP-class DT fusion power plants. *Nuclear Fusion*, *63*(12), 126005. https://doi.org/10.1088/1741-4326/acf3fc

4 Geng R., Hu J., Zhai Y., Yan J., Wang K., Zhang W., Wang K. (2024) Preparation of Li4SiO4 pebbles with high strength and inhibited lithium volatilization via lithium alginate. *Journal of Nuclear Materials*, *592*, 154973. https://doi.org/10.1016/j.jnucmat.2024.154973

5 Kenzhina I.E., Kozlovskiy A.L., Chikhray Y., Kulsartov T., Zaurbekova Z., Begentayev M., Askerbekov S. (2023) Study of Gas Swelling Processes under Irradiation with Protons and He2+ Ions in Li4SiO4–Li2TiO3 Ceramics. *Crystals*, *13*(10), 1526. https://doi.org/10.3390/cryst13101526

6 Kulsartov T., Zaurbekova Z., Knitter R., Kenzhina I., Chikhray Y., Shaimerdenov A., Zholdybayev T. (2024) Comparative analysis of gas release from biphasic lithium ceramics pebble beds of various pebbles sizes and content under neutron irradiation conditions. *Nuclear Materials and Energy*, *38*, 101583. https://doi.org/10.1016/j.nme.2024.101583

7 Wang Q., Zhou Q., Xiong Q., Zhou J., Li S., Hirata S., Oya Y. (2022) Preparation of Li2TiO3-Li4SiO4-Pb tritium breeding ceramic and its mechanical properties. *Ceramics International*, *48*(18), 26742-26749. https://doi.org/10.1016/j.ceramint.2022.05.369

8 Chen X., Gong Y., Kang K., Wang Y., Li J., Li Z., Zhang G. (2023) Enhancing properties of Li2TiO3/Li4SiO4 tritium breeding ceramics by chitosan addition. *Nuclear Materials and Energy*, *37*, 101515. https://doi.org/10.1016/j.nme.2023.101515

9 Chen R., Ipponsugi A., Oyama R., Qi J., Wang H., Huang Z., Katayama K. (2023) Long-term thermal stability of Li4TiO4–Li2TiO3 core–shell breeding pebbles under continuous heating in H2/Ar atmosphere. *International Journal of Applied Ceramic Technology*, *20*(4), 2576-2585. https://doi.org/10.1111/ijac.14392

10 Ipponsugi A., Katayama K., Hoshino T. (2023) Tritium release behavior from neutron-irradiated Li_2+ xTiO_3+ y with 20wt% Li_2ZrO_3 pebbles under different atmospheres. *Fusion Engineering and Design*, *194*, 113825. https://doi.org/10.1016/j.fusengdes.2023.113825

11 Yan J., He N., Chen X., Xiao C., Zhao L.J., Gao T. (2021) Design, synthesis and characterization of advanced tritium breeder: Li4Si1-xTixO4 ceramics. *Ceramics International*, *47*(10), 14178-14182. https://doi.org/10.1016/j.ceramint.2021.02.004

12 Liu W., Di J., Zhang W., Xue L., Yan Y. (2019) Influence of titanium sources on the microstructures and properties of Li2TiO3 ceramics prepared by hydrothermal method. *Fusion Engineering and Design*, *138*, 364-371. https://doi.org/10.1016/j.fusengdes.2018.12.033

13 Guo H., Wang H., Chen R., Gong Y., Yang M., Ye D., Lu T. (2021) Characterization of Li-rich Li2TiO3 ceramic pebbles prepared by rolling method sintered in air and vacuum. *Journal of Nuclear Materials*, *546*, 152786. https://doi.org/10.1016/j.jnucmat.2021.152786

14 Guo H., Wang H., Chen R., Huang Z., Gong Y., Zeng Y., Lu T. (2019) Low-cost fabrication of Li2TiO3 tritium breeding ceramic pebbles via low-temperature solid-state precursor method. *Ceramics International*, *45*(14), 17114-17119. https://doi.org/10.1016/j.ceramint.2019.05.263

15 Park Y. H., Min K.M., Cho S., Ahn M.Y., Lee Y.M. (2017) Li2TiO3 powder synthesis by solid-state reaction and pebble fabrication for tritium breeding material. *Fusion Engineering and Design*, *124*, 730 -734. https://doi.org/10.1016/j.fusengdes.2017.05.015

16 Wang H., Qi J., Guo H., Chen R., Yang M., Gong Y., Lu T. (2021) Influence of helium ion radiation on the nano-grained Li2TiO3 ceramic for tritium breeding. *Ceramics International*, *47*(20), 28357-28366. https://doi.org/10.1016/j.ceramint.2021.06.253

17 Kolb M.H.H., Mukai K., Knitte, R., Hoshino T. (2017) Li4SiO4 based breeder ceramics with Li2TiO3, LiAlO2 and LiXLaYTiO3 additions, part I: Fabrication. *Fusion Engineering and Design*, *115*, 39-48. https://doi.org/10.1016/j.fusengdes.2016.12.033

18 Shlimas D. I., Borgekov D.B., Kadyrzhanov K.K., Kozlovskiy A.L., Zdorovets M.V. (2024) Study of the Surface-Layer Softening Effects in xLi2ZrO3–(1− x) Li4SiO4 Ceramics under Irradiation with He2+ Ions. *Ceramics*, *7*(2), 547-561. https://doi.org/10.3390/ceramics7020036

19 Egeland G.W., Valdez J.A., Malo, S.A., McClellan K.J., Sickafus K.E., Bond G.M. (2013) Heavy-ion irradiation defect accumulation in ZrN characterized by TEM, GIXRD, nanoindentation, and helium desorption. *Journal of nuclear materials*, *435*(1-3), 77-87. https://doi.org/10.1016/j.jnucmat.2012.12.025

20 Shlimas D., Borgekov D.B., Tynyshbayeva K.M., Giniyatova S.G., Moldabayeva G.Z., Kozlovskiy A.L. (2024) Effect of ion-induced dislocation hardening on diffusion and gas swelling mechanisms in carbide ceramics. *Eurasian Journal of Physics and Functional Materials*, *8*(4), 1-147. https://doi.org/10.69912/2616-8537.1233

21 Rymzhanov R.A., Medvedev N., O'Connell J.H., Skuratov V.A., van Vuuren A. J., Gorbunov S.A., Volkov A. E. (2020) Insights into different stages of formation of swift heavy ion tracks. *Nuclear Instruments and Methods in Physics Research Section B: Beam Interactions with Materials and Atoms*, *473*, 27-42. https://doi.org/10.1016/j.nimb.2020.04.005

22 Kadyrzhanov K.K., Tinishbaeva K., Uglov V.V. (2020) Investigation of the effect of exposure to heavy Xe22+ ions on the mechanical properties of carbide ceramics. *Eurasian Physical Technical Journal*, *17*(1 (33)), 46-53. https://doi.org/10.31489/2020No1/46-53

23 Moritani K., Tanaka S., Moriyama H. (2000) Production behavior of irradiation defects in lithium silicates and silica under ion beam irradiation. *Journal of nuclear materials*, *281*(2-3), 106-111. https://doi.org/10.1016/S0022-3115(00)00364-0

24 Tynyshbayeva K. M., Kozlovskiy A. L., Rakhimov R. V., Uglov V. V., Zdorovets M. V. (2023) Study of The Gas-Swelling Mechanisms in Silicon Carbide Ceramics under High-Temperature Irradiation with Helium Ions. *Materials*, *16*(17), 5750. https://doi.org/10.3390/ma16175750

25 Ryskulov A.E., Ivanov I.A., Kozlovskiy A.L., Konuhova M. (2024) The effect of residual mechanical stresses and vacancy defects on the diffusion expansion of the damaged layer during irradiation of BeO ceramics. *Optical Materials: X*, *24*, 100375. https://doi.org/10.1016/j.omx.2024.100375

26 Kenzhina I., Kulsartov T., Knitter R., Chikhray, Y., Kenzhin Y., Zaurbekova Z., Nesterov E. (2022) Analysis of the reactor experiments results on the study of gas evolution from two-phase Li2TiO3-Li4SiO4 lithium ceramics. *Nuclear Materials and Energy*, *30*, 101132. https://doi.org/10.1016/j.nme.2022.101132

27 Estrin Y., Tóth L.S., Molinari A., Bréchet Y. (1998) A dislocation-based model for all hardening stages in large strain deformation. *Acta materialia*, *46*(15), 5509-5522. https://doi.org/10.1016/S1359-6454(98)00196-7

28 Xie Q., Li Z., Ma H., Liu S., Liu X., Liu J., Sidor J. J. (2023) Correlation between dislocation hardening and the geometrically-necessary-dislocation densities in a hexagonal-close-packed Zr-2wt% Ti alloy. *Materials Science and Engineering: A*, *868*, 144768. https://doi.org/10.1016/j.msea.2023.144768

29 Yin Z., Huang C., Zou B., Liu H., Zhu H., Wang J. (2013) Study of the mechanical properties, strengthening and toughening mechanisms of Al2O3/TiC micro-nano-composite ceramic tool material. *Materials Science and Engineering: A*, *577*, 9-15. https://doi.org/10.1016/j.msea.2013.04.033

30 Syed K., Motley N. B., Bowman W.J. (2022) Heterointerface and grain boundary energies, and their influence on microstructure in multiphase ceramics. *Acta Materialia*, *227*, 117685. https://doi.org/10.1016/j.actamat.2022.117685

31 Gong Y., Yu X., Yang M., Wei J., Shi Y., Huang Z., Huang W. (2015) A facile approach to fabricate Li4SiO4 ceramic pebbles as tritium breeding materials. *Materials Letters*, *159*, 245 - 248. https://doi.org/10.1016/j.matlet.2015.06.108

32 Rao G. J., Mazumder R., Dixit D., Ghoroi C., Bhattacharyya S., Chaudhuri P. (2019) Fabrication and characterization of Li4SiO4 pebbles by extrusion spheroidization technique: Effects of three different binders. *Ceramics International*, *45*(3), 4022-4034. https://doi.org/10.1016/j.ceramint.2018.11.081

33 Snead L. L., Katoh Y., Connery S. (2007) Swelling of SiC at intermediate and high irradiation temperatures. *Journal of Nuclear Materials*, *367*, 677-684. https://doi.org/10.1016/j.jnucmat.2007.03.097

34 Snead L.L., Burchell T.D., Katoh Y. (2008) Swelling of nuclear graphite and high-quality carbon fiber composite under very high irradiation temperature. *Journal of Nuclear Materials*, *381*(1-2), 55-61. https://doi.org/10.1016/j.jnucmat.2008.07.033

AUTHORS' INFORMATION

Kozlovskiy, Artem Leonidovich – PhD (Phys.), Associate Professor, Head of the Laboratory of Solid-State Physics, Astana branch of the Institute of Nuclear Physics; Ministry of Energy of the Republic of Kazakhstan, Astana; Scopus Author ID: 55632118900; https://orcid.org/0000-0001-8832-7443; kozlovskiy.a@inp.kz

Kenzhina, Inesh – PhD, Leading Researcher, Satbayev University, Almaty, Kazakhstan; Scopus Author ID: 57191291007; https://orcid.org/0000-0002-9397-5848; kenzhina@physics.kz

Tolenova, Aktolkyn – PhD student, Researcher, Satbayev University, Almaty, Kazakhstan; Scopus Author ID: 57221646205; https://orcid.org/0000-0002-7353-1932; aktolkyntolen@gmail.com

Askerbekov, **Saulet K.** – PhD, Leading Researcher, Satbayev University, Almaty, Kazakhstan; Scopus Author ID: 57191892035; https://orcid.org/0000-0001-7204-4887; askerbekov@physics.kz

EURASIAN PHYSICAL TECHNICAL JOURNAL

2025, Volume 22, No.1 (51)

https://doi.org/10.31489/2025N1/19-27

Received: 09/08/2024 Revised: 23/12/2024 Accepted: 18/03/2025 Published online: 31/03/2025

Research Article

UDC 539.171.016

ANALYSIS OF THE EFFECT OF THE B3Y-FETAL POTENTIAL ON ENERGY NEAR THE COULOMB BARRIER FOR THE ^{9}Be+^{12}C SYSTEM

Soldatkhan D., Baratova A.A.*

L.N. Gumilyov Eurasian National University, Astana, Kazakhstan
*Corresponding author: aa.baratova@yandex.kz

Abstract. *The experimental data of the elastic scattering process of the $^{9}Be+^{12}C$ nuclear system were analyzed from the point of view of microscopic theory in energy near the Coulomb barrier. The new Botswana 3-Yukawa -Fetal potential, created in a variational approach with lower-order constraints on two body matrices, was first used for the $^{9}Be+^{12}C$ system as a real part of the optical potential. In the double folding model, density-dependent parameters were introduced into the nucleon density distribution formula, and they were applied to the Botswana 3-Yukawa - Fetal and Michigan 3-Yukawa - Paris potentials based on effective nucleon-nucleon interactions. As a result, modified real microfolding potentials were created. The results of a semi-microscopic analysis calculated on the basis of new microfolding potentials were presented. The uniqueness of the research lies in the calculation of density-dependent parameters based on the incompressibility coefficient, which characterizes the saturation properties of the nuclear medium. The equations of state of the elastic scattering process were formulated at the saturation density (ρ_0=0.17 fm^{-3}), determined from the density dependence of the nuclear binding energy. The analysis results allow for a more accurate determination of nuclear properties and enhance the saturation properties of the nuclear medium. The efficiency of the new real potential was determined from a microscopic perspective, and the optimal parameters of the optical potential were found.*

Keywords: microscopic analysis, elastic scattering, double folding model, B3Y-Fetal.

1. Introduction

Accurate determination of the depth of the potential of the interaction of a ^{9}Be ion accelerated at low energy with light nuclei, the calculation of the contribution of the cluster transition mechanism is important in nuclear astrophysics. The study of the interaction of radioactive ^{9}Be ion radiation with light nuclei in nuclear power plants is an urgent problem in the energy sector. In a reactor, the neutron source controlling the chain reaction is beryllium mixed with an alpha emitter. Alpha particles formed as a result of decay lead to the release of neutrons from beryllium when it turns into a ^{12}C - core.

It is known from Rutherford's experience that the study of experimental data on elastic scattering at energies close to the Coulomb barrier is the main way to obtain information about the structure of the nucleus. Analysis of compound particle scattering in low-energy nuclei is an important source of information about the properties of the inter-nuclear potential [1]. The formation of the experimental cross-section in the process of elastic scattering was explained in the optical model by the fact that the real part of the optical potential (OP) depends on potential scattering, and the imaginary part as absorption depends on the mechanisms of cluster transition. In recent years, microscopically, the description of a real part of an op in the context of a form of local density based on effective nucleon-nucleon (NN) forces has given correct results [2-5]. The Michigan 3-Yukawa (M3Y) potential of effective NN interactions can be improved based on the density-dependent form of nucleon distribution proposed by Dao T. Khoa [6-8]. The traditional M3Y-Reid, M3Y-Paris potentials defined in the tensor correlation calculation of Yukawa matrix elements have been in use for many years [7-9]. Recently, a new B3Y-Fetal potential was developed, calculated on the basis of a low-order limited variation approach [10]. This was a new step in the position of microscopic theory. Botswana 3-Yukawa (B3Y)-Fetal potential Ochala I., Fiase J.O. scientists have successfully used in symmitric $^{16}O+^{12}C$, $^{12}C+^{12}C$ systems and found that M3Y interaction is very similar in many channels [11-12]. In double folding model (DFM), a real part of the OP is created and density-dependent parameters are entered. In the overlapping region of the nucleons of the colliding nuclei, the central part of the effective NN interaction accumulates, which makes it possible to characterize the properties of the nucleus. The equations of state created in this central region depend on the density of the nucleus, the saturation property of the medium.

We conducted a comparative study in order to increase the saturation property of the medium by applying the potentials B3Y-Fetal, M3Y-Paris to the $^{9}Be+^{12}C$ system. From this, the results of a semi-microscopic analysis of experimental data of elastic scattering at energies of E_{lab}=13 MeV, E_{lab}=17.3 MeV, E_{lab}=20 MeV near the Coulomb barrier were presented. Modified folding potentials in the form of CDM3Y2-Paris and CDB3Y2-Fetal were tested. The results of the analysis are used in nuclear astrophysics in describing the initial nucleosynthesis and hydrostatic combustion of stars and as a way to know exactly the rate of nuclear reactions, to construct the nuclear state equations of a complex compound.

2. Calculation of the K - incompressibility factor depending on the saturation property of the nucleus

To increase the saturation property of nuclear matter, the equilibrium condition of the density-dependent specific bond energy is sufficient. To satisfy this saturation condition, calculated density – dependent parameters that depend on K - incompressibility must be introduced into the effective M3Y interaction. In particular, it is necessary to construct equations of state at value ρ_0=0,17 фм$^{-3}$ of the saturation density of nuclear matter.

Specific binding energy of density-dependent infinite nuclear matter [13]:

$$\frac{\varepsilon_0}{A}(\rho) = \frac{3\hbar^2 k_F^2}{10m} + F(\rho)\frac{\rho}{2}(J_D + \int[\hat{j}_1(k_F r)]^2 v^{EX}(r)d^3r) \tag{1}$$

where m - is the nucleon mass, J_D - volume integral, $\hat{j}_1(x)$ - Bessel spherical function, ρ - nucleon density, k_F - Fermi pulse.

From the equilibrium saturation condition of the binding energy of the nucleus [13]:

$$\frac{d\varepsilon}{d\rho} = \frac{\hbar^2 k_F^2}{5mp} + \frac{J_D C}{2}(1 - \frac{5}{3}\beta(\varepsilon)\rho^{\frac{2}{3}}) = 0 \tag{2}$$

From equation (2), the formula for bond energy, which depends on the density parameters, is written as follows:

$$\varepsilon = \frac{3\hbar^2 k_F^2}{10m} + \frac{\rho J_D}{2}C(1 - \beta(\varepsilon)\rho^{\frac{2}{3}}) \tag{3}$$

Density-dependent parameters and saturation density [13]:

$$C = -\frac{2\hbar^2 k_F^2}{5mJ_D\rho(1-\frac{5}{3}\beta(\varepsilon)\rho^{\frac{2}{3}})} \tag{4}$$

$$\beta(\varepsilon) = \frac{(3-3p)}{(9-5p)} \cdot \frac{1}{\rho^{5/3}} \tag{5}$$

$$\rho_0 = -\frac{10m\varepsilon}{\hbar^2(1.5\pi^2\rho)^{2/3}} \tag{6}$$

The nuclear incompressibility factor is calculated by the following equation [13]:

$$K_\propto = -\left[\frac{3\hbar^2 k_F^3}{5m} + 5J_D C\beta(\varepsilon)\rho^{5/3}\right]_{\rho=\rho_0} \tag{7}$$

The following figure shows a curve of dependence of the specific binding energy of the nucleus on the density of nucleons. The saturation density point corresponds to the value ρ_0=0,17 fm^{-3}.

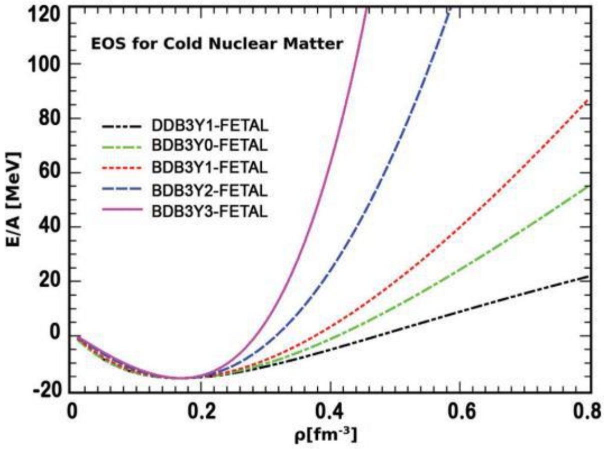

Fig.1. Saturation point of the density dependence of the binding energy of the nucleus [14]

3. Interaction on effective NN forces M3Y-Paris and B3Y-Fetal potentials

The interaction of M3Y is the sum of the $U^D(\vec{R})$ - direct and $U^{EX}(\vec{R})$ - exchange potentials by effective NN forces.

$$U(\vec{R}) = U^D(\vec{R}) + U^{EX}(\vec{R}) \tag{8}$$

Direct potential [15, 16]:

$$U^D(\vec{R}) = \iint \rho^{(1)}(\vec{r}_1)\upsilon_D(\vec{s})\rho^{(2)}(\vec{r}_2)d\vec{r}_1 d\vec{r}_2 \tag{9}$$

where $\upsilon_D(\vec{s})$ - direct component of effective interaction, $\rho^{(1)}(\vec{r}_1)$, $\rho^{(2)}(\vec{r}_2)$ - nucleon density of colliding nuclei, s - effective NN interaction distance. $s = r_2 - r_1 + R$

Exchange potential [16, 17]:

$$U^{EX}(\vec{R}) = \iint \rho^{(1)}(\vec{r}_1, \vec{r}_1 + \vec{s})\upsilon_{EX}(\vec{s})\,\rho^{(2)}(\vec{r}_2, \vec{r}_2 - \vec{s})\,exp[\,i\vec{k}(\vec{R})\vec{s}/\eta]d\vec{r}_1 d\vec{r}_2 \tag{10}$$

where $\upsilon_{\text{EX}}(\vec{s})$ - effective NN interaction exchange component, $\rho^{(1)}(\vec{r}_1, \vec{r}_1)$, $\rho^{(2)}(\vec{r}_2, \vec{r}_2 - \vec{s})$ - density matrix of colliding nuclei.

For the calculation of potentials, it is important to clearly take into account the transition effects of NN - interaction [13]:

$$\upsilon_{D(EX)} = 1/16\,(3\upsilon_{TE}^c + 3\upsilon_{SE}^c \pm 9\upsilon_{TO}^c \pm \upsilon_{SO}^c) \tag{11}$$

where $(\upsilon_{TE}^c, \upsilon_{SE}^c)$, $(\upsilon_{TO}^c, \upsilon_{SO}^c)$ - triplet and singlet components of central forces.

Direct and exchange components based on the G-мatrix element of the M3Y-Paris potential [18]:

$$v_D(s) = 11061{,}6\frac{exp(-4s)}{4s} - 2537{,}5\frac{exp(-2{,}5s)}{2{,}5s} \tag{12}$$

$$v_D(s) = -1524{,}0\frac{exp(-4s)}{4s} - 518{,}8\frac{exp(-2{,}5s)}{2{,}5s} - 7{,}8474\frac{exp(-0{,}7072s)}{0{,}7072s} \tag{13}$$

B3Y-Fetal radial form of the isoscalar portion of interaction [10]:

$$v_D(s) = 10472{,}13\frac{exp(-4s)}{4s} - 2203{,}11\frac{exp(-2{,}5s)}{2{,}5s} \tag{14}$$

$$v_{\mathrm{EX}}(s) = 499{,}63\frac{exp(-4s)}{4s} - 1347{,}77\frac{exp(-2{,}5s)}{2{,}5s} - 7{,}8474\frac{exp(-0{,}7072s)}{0{,}7072s} \tag{15}$$

4. The theoretical basis of semi-microscopic analysis

When analyzing experimental data of elastic scattering within the framework of an optical model (OM), the Woods-Saxon form of potential was used.

$$U(r) = V_o\left[1 + exp\left(\frac{r-R_V}{a_V}\right)\right] - iW_o\left[1 + exp\left(\frac{r-R_W}{a_W}\right)\right] + V_C(r) \tag{16}$$

where V_o, W_V, a_V, a_W, R_V, R_W are real, imaginery potentials, diffusion, radius, $V_C(r)$ is the Coulomb potential.

In a semi-microscopic analysis, the optical potential of the interacting nuclei is calculated by the following formula [7]:

$$U(r) = N_r[v_D(s) + v_{\mathrm{EX}}(s)] - iW_0 f(r, r_W, a_W) + V_C(r) \tag{17}$$

where $v_D(s)$, $v_{\mathrm{EX}}(s)$ – direct and exchange components of interaction potential, N_r – renormalization factor. W_0, r_W, a_W – imaginary potential, radius, diffusion, $V_C(r)$ – Coulomb potential.

The direct and exchange components of the real potential are calculated on the basis of DFM, resulting in the folding potential.

$$v_D(s) + v_{\mathrm{EX}}(s) = V_F(r) \tag{18}$$

For the imaginary part of the optical potential, we use the woods-Saxon form factor in volumetric form.

$$U(r) = N_r V_F(r) - iW_o\left[1 + exp\left(\frac{r-r_W}{a_W}\right)\right] + V_c(r) \tag{19}$$

$V_C(r)$ - Coulomb potential [16],

$$V_C(R) = \begin{cases} \frac{Z_1Z_2e^2}{2R_C}\left(3 - \frac{R^2}{R_C}\right) & \text{For} \quad R \le R_C \\ \frac{Z_1Z_2e^2}{R} & \text{For} \quad R \ge R_C \end{cases} \tag{20}$$

M3Y-Paris and B3Y-Fetal potentials are density and energy dependent.

$$v_{D(\mathrm{EX})}(E,\rho,s) = F(E,\rho)g(E)v_{D(EX)}(s), \tag{21}$$

A formfactor proposed based on the density-dependent parameters [19]

$$F(\rho) = C[1 + \alpha\, exp(-\beta\rho) - \gamma\rho^{n}] \tag{22}$$

the energy-dependent factor $g(E)$ is expressed as [7]:

$$g(E) = 1 - 0.003(E/A) \tag{23}$$

The nuclear matter density distribution was calculated in the harmonic-oscillator model [20, 2]:

$$\rho(r) = \rho_0(1 + \alpha(r/a)^2)\, exp(-(r/a)^2) \tag{24}$$

where ρ_0=0,17 fm^{-3}, α (alfa) and *a* are charge density distribution parameters. For the ^{9}Be core, α=1.77 fm, *a*=0.631 fm, and for the ^{12}C core, α =1.687 fm, *a*=1.067 fm [20].

Table 1. Density-dependent parameters [8, 14].

Density dependence	C	a	β (fm^3)	γ (fm^3)	K (MeV)
CDM3Y2-Paris CDB3Y2-Fetal	0.3346	3.0357	3.0685	1.0	204
CDB3Y3-Fetal	0.2985	3.4528	2.6388	1.5	217

5. Discussion of results

At energies of E_{lab}=13.0 MeV, E_{lab}=17.3 MeV, E_{lab}=20.0 MeV near the Coulomb barrier for the ^{9}Be+^{12}C system, the density-dependent CDM3Y2-Paris, CDB3Y2-Fetal and CDB3Y3-Fetal folding potentials were built on the basis of the DFM model. From the picture, the depth of the CDB3Y2-Fetal and CDB3Y3-Fetal potentials was more sensitive than that of the CDM3Y2-Paris version. Theoretical calculations of semi-microscopic analysis were performed on the basis of the FRESCO code [21]. The following figure shows the results of a semi-microscopic analysis of experimental sections of elastic scattering for the ^{9}Be+^{12}C system.

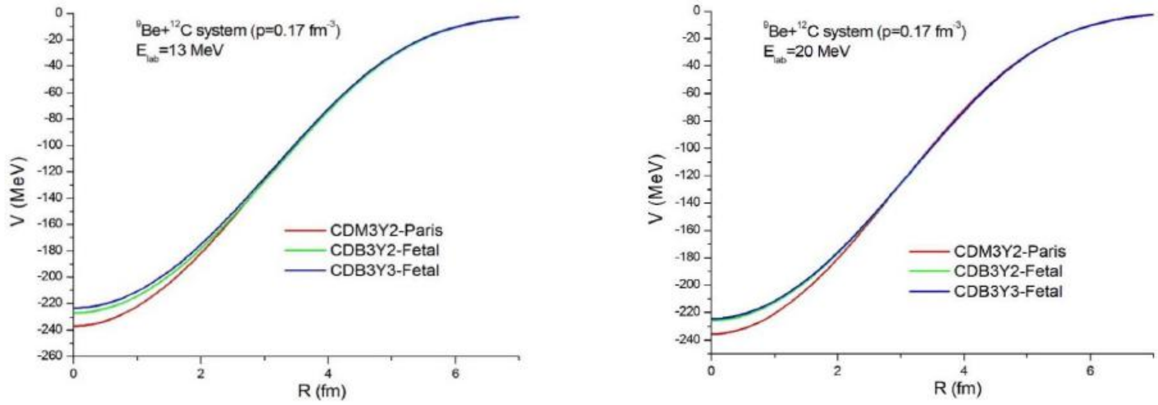

a) b)

Fig.2. The depth of the generated real DF potentials for the ^{9}Be+^{12}C system at:
a) E_{lab} = 13.0 MeV and b) E_{lab} = 20.0 MeV energies

Theoretical cross-sections at an energy of E_{Lab}=13 MeV described the experimental cross-section in the range of up to 90^0, as can be seen from the images. This is because at low energies close to the Coulomb barrier, the scattering process prevails over the absorption process. Therefore, the share of the imaginary potential is small. And to characterize the increase in the Section at large angles after 90^0, it is necessary to take into account the proportion of the cluster transition. The following figures show the dependence of the normalized scattering cross-section ($d\sigma/d\sigma_{Ruth}$) on the scattering angle (θ_{cm}) in the center-of-mass system for the ^{9}Be+^{12}C nuclear system at incident energies of E_{Lab}=13.0 MeV, E_{Lab}=17.3 MeV, and E_{Lab}=20.0 MeV.

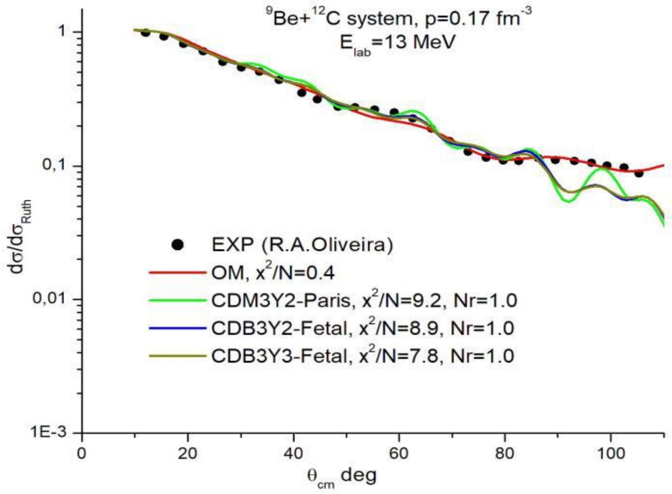

Fig.3. The result of the analysis at energy E$_{Lab}$=13 MeV

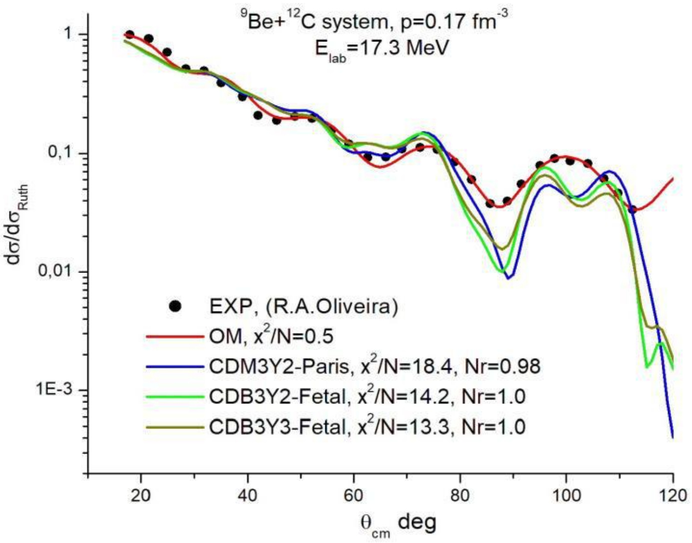

Fig.4. The result of the analysis at energy E$_{Lab}$=17.3 MeV

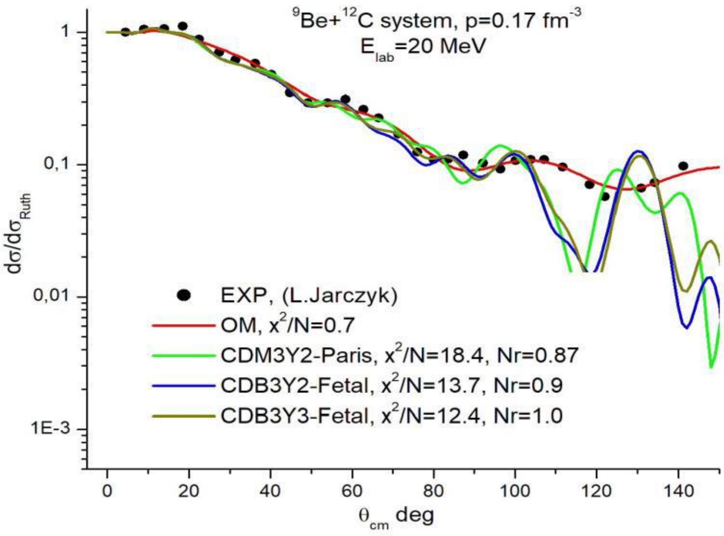

Fig.5. The result of the analysis at energy E$_{Lab}$=20 MeV

The optical model (OM) potential parameters presented in Table 2 were calculated using equation (16), while the semi-microscopic model (DFOM) parameters were calculated using equation (17). The calculations were performed based on the FRESCO code.

Table 2. The values of the optimal parameters of the elastic scattering Section at energies E_{Lab}=13.0 MeV, E_{Lab}=17.3 MeV, E_{Lab}=20.0 MeV for the $^{9}Be+^{12}C$ system are shown in the following table.

E, MeV	Model	WS parameters and types of DF potential			N_r	Parameters of the imaginary potential WS			$\sigma_{R,}$ mb	χ^2/N
		$V_{0,}$ MeV	$r_{V,}$ fm	$a_{V,}$ fm		$Wo,$ MeV	$r_{W,}$ fm	$a_{W,}$ fm		
13.0	OM	65.8	1.69	0.12	-	5.36	1.74	1.19	2211	0.4
	DFOM	CDM3Y2-Paris			1.0	5.36	1.88	0.9	2037	9.25
	DFOM	CDB3Y2- Fetal			1.0	5.36	1.88	0.9	2134	8.9
	DFOM	CDB3Y3- Fetal			1.0	5.36	1.88	0.9	2129	7.8
17.3	OM	28.5	1.28	0.62	-	5.6	1.49	0.19	1088	0,5
	DFOM	CDM3Y2-Pari			0.98	5.5	1.45	0.9	1508	18.4
	DFOM	CDB3Y2- Fetal			1.0	5.5	1.45	0.9	1492	14.2
	DFOM	CDB3Y3- Fetal			1.0	5.5	1.45	0.9	1501	13.3
20.0	OM	154.7	1.06	0.17	-	10.6	0.78	1.48	1352	0.7
	DF	CDM3Y2-Paris			0.87	6.59	1.44	0.63	1151	19.8
	DF	CDB3Y2-Fetal			0.9	6.59	1.44	0.63	1163	19.8
	DF	CDB3Y2-Fetal			1.0	6.59	1.44	0.63	1158	19.8

The Nr - factor of semi-microscopic analysis was determined close to 1.0. From this you can see the good result of the new CDB3Y2-Fetal, CDB3Y3-Fetal folding potentials, which is created as a real potential. As a relative error of experimental and theoretical sections, the values of the χ2/N – parameter did not exceed 20 percent. Weak values of *Wo* - imaginary potential 1 indicate the opacity of the optical potential to be determined for system $^{9}Be+^{12}C$. The fact that the values of the $Wo, r_{W,} a_W$ – Woods-Saxon parameters are unchanged in different models again proves the truthfulness of the real potential. The dependence of the σ_R - cross section on the beam energy is preserved in all models (OM, DFOM). The CDB3Y2-FetaL CDB3Y3-Fetal folding potentials created at an energy close to the Coulomb barrier were investigated relative to the CDM3Y2-Paris variant.

6. Conclusion

For the $^{9}Be+^{12}C$ system, a new B3Y-Fetal potential based on variational calculations was used for the first time in a semi-microscopic analysis. Studying the effectiveness of the new B3Y-Fetal potential was important from the point of view of applying the theoretical breakthrough. At the energy close to the Coulomb barrier, the real part of the optical potential shows dominance in the mechanism of elastic scattering cross-section formation. The CDM3Y2-Paris, CDB3Y2-Fetal and CDB3Y3-Fetal folding potentials were established, elastic scattering sections and optimal parameters were determined. Were able to describe the experimental data on the basis of K - incompressibility dependent parameters calculated for the actual density of ρ_0=0.17 fm^{-3} - in accordance with the saturation condition of nuclear matter. So we were able to increase the saturation property of the nuclear medium.

The result of the work makes it possible to determine the interaction characteristics of heavy ions up to a very small inter-core distance. The results obtained are used in nuclear astrophysics for model calculations of nuclear reactions.

Conflict of interest statement
The authors declare that they have no conflict of interest in relation to this research, whether financial, personal, authorship or otherwise, that could affect the research and its results presented in this paper.

CRedit author statement.
Soldatkhan, D. - performed theoretical calculations and analysis; **Baratova, A.A. -** supervised the work carried out in the research. The final manuscript was read and approved by all authors.

Acknowledgments
We thank the participants who made this research possible.

References

1 Soldatkhan D., Amangeldi N., Baltabekov A., Yergaliuly G. (2022) Investigation of the energy dependence of the interaction potentials of the $^{16}O+^{12}C$ nuclear system with a semi-microscopic method. *Eurasian Physical Technical Journal*, 19, 3(41), 39 – 44. https://doi.org/10.31489/2022No3/39-44

2 Masadeh S.B., Abdallah D.A., Jaghoub M.I. (2023) Analysis of nucleon-nucleus scattering data using a density-dependent semi-microscopic optical model with channel coupling. *Physical Review C*, *107*(2) 024616. https://doi.org/10.1103/PhysRevC.107.024616

3 Morzabayev A., Amangeldi N., Awad A. Ibraheem, Soldatkhan D., Yergaliuly G., Mauyey B., Anuar A. O., Hamada. Sh. (2023) Dynamics of ^{7}Li Breakup and its Influence on Elastic Scattering: A Study of $^{7}Li+^{144}Sm$ System. *Chinese Physics C*, 4, 31 - 40. https://doi.org/10.1055/s12138-135-01108-0

4 Soldatkhan D., Amangeldi N., Makhanov K.M., Smagulov Zh.K. (2023) Application of the new B3Y-Fetal potential in the semi-microscopic analysis of the scattering of accelerated ^{6}li - lithium and ^{16}O - oxygen nuclei from the ^{12}C - carbon nucleus. *Eurasian Physical Technical Journal*, 25, 4(46), 22 - 30. https://doi.org/10.31489/2023No4/17-22

5 Mauyey B., Amangeldi N., Raiymbekov Y., Soldatkhan D., Al-Jahwashi E., Awad A. Ibraheem, Al-Ghamdi A.H., Hamada Sh. (2024) Deuteron breakup effects on the $d+^{12}C$, ^{15}N, ^{16}O, ^{24}Mg, ^{32}S, ^{58}Ni, and ^{70}Ge elastic scattering angular distributions. *Chinese Journal of Physics*, *90*, 155-165. https://doi.org/10.1016/j.cjph.2024.05.003

6 Amangeldi N., Burtebayev N., Soldatkhan D., Maulen Nassurlla, Mauyey B., Yergaliuly G., Marzhan Nassurlla, Awad A. Ibraheem, Hamada, Sh. (2024) Recent Measurement and Theoretical Analysis for the Elastic Scattering of the 15N+11B System. *Brazilian Journal of Physics*, *54*(5), 169. https://doi.org/10.1007/s13538-024-01547-2

7 Khoa D.T., Phuc N. H., Loan D. T., Loc B.M. (2016) Nuclear mean field and double-folding model of the nucleus-nucleus optical potential. *Physical Review C*, *94*(3), 034612. https://doi.org/10.1103/PhysRevC.94.034612

8 Khoa D.T., Satchler G.R., Von Oertzen W. (1997) Nuclear incompressibility and density dependent NN interactions in the folding model for nucleus-nucleus potentials. *Physical Review C*, 56(2), 954. https://doi.org/10.1103/PhysRevC.56.954

9 Amangeldi N., Burtebayev N., Artemov S.V., Maulen Nassurlla, Mauyey B., Yergaliuly G., Marzhan Nassurlla, Ergashev F.Kh., Soldatkhan D., Shaudirbayeva D.S., Awad A., Ibraheem, Hamada Sh. (2024) Efficiency of the new B3Y-fetal potential in the analysis of the elastic and inelastic angular distributions for the 10B+12C system. *Pramana*, *98*(3), 106. https://doi.org/10.1007/s12043-024-02760-z

10 Fiase J.O., Devan K.R.S., Hosaka A. (2002) Mass dependence of M3Y-type interactions and the effects of tensor correlations. *Physical Review C*, 66(1), 014004. https://doi.org/10.1103/PhysRevC.66.014004

11 Ochala I., Fiase J.O. Gbaorun F., Bamikole J.A. (2021) A study of asymmetric nuclear matter with the B3Y-Fetal effective interaction. *International Research Journal of Pure and Applied Physics*, 8(2), 10 - 35. https://doi.org/10.37745/irjpap.13

12 Ochala I., Fiase J.O. (2021) B3Y-Fetal effective interaction in the folding analysis of elastic scattering of $^{16}O+^{16}O$. *Nuclear Science and Techniques*, 32(8), 81. https://doi.org/10.1007/s41365-021-00920-z

13 Ochala J. O. Fiase E. Anthony. (2017) Computation of nuclear binding energy and incompressibility with a new M3Y - type effective interaction. *International Research Journal of Pure and Applied Physics*, 5(3), 5 - 13.

14 Ochala I., Fiase J.O. (2018) Symmetric nuclear matter calculations: A variational approach. *Physical Review C*, 98(6), 064001. https://doi.org/10.1103/PhysRevC.98.064001

15 Khoa N.H.D., Tan N. H., Khoa D. T. (2022) Spin symmetry energy and equation of state of spin-polarized neutron star matter. *Physical Review C*, *105*(6), 065802. https://doi.org/10.1103/PhysRevC.105.065802

16 Hassanain M.A., Alqahtani F.M., Ibraheem A.A., Anwar M., Behary K.O., Mahmoud Z.M., El-Azab Farid M. (2018) Elastic and inelastic O16+C12 rainbow scattering within the coupled-channels mechanism. *Physical Review C*, *98*(1), 014621. https://doi.org/10.1103/PhysRevC.98.014621

17 Morzabayev A., Amangeldi N., Awad A. Ibraheem, Yergaliuly G., Mauyey B., Hamada Sh. (2024) Detailed analysis of the ^{6}Li breakup in the field of the ^{209}Bi nucleus. *Physica Sctripta,* 99. 025307. https://doi.org/10.1088/1402-4896/ad1d43

18 Khoa D. T., Loan D. T., Phuc N. H. (2024) Pauli nonlocality and the nucleon effective mass. *Physical Review C*, *110*(2), 024607. https://doi.org/10.1103/PhysRevC.110.024607

19 Khoa D.T., Von Oertzen W., Bohlen H.G., Ohkubo S. (2007) Nuclear rainbow scattering and nucleus–nucleus potential. *Journal of Physics G: Nuclear and Particle Physics*, *34*(3), R111. https://doi.org/10.1088/0954-3899/34/3/R01

20 De Vries H., De Jager C.W., De Vries C. (1987) Nuclear charge-density-distribution parameters from elastic electron scattering. *Atomic data and nuclear data tables*, 36(3), 495-536. https://doi 10.1016/0092-640X(87)90013-1

21 Thompson I.J. (1988) Getting started with FRESCO. *Comput. Phys. Rep*, *7*, 167-212. https://doi.org/10.1016/0167-7977(88)90005-6

AUTHORS' INFORMATION

Soldatkhan, D. - PhD, Senior Lecture, Department of Radio Engineering, Electronics and Telecommunications,L.N. Gumilyov Eurasian National University, Astana, Kazakhstan; Scopus Author ID: 57768566200; https://orcid.org/0000-0001-7981-4100; Soldathan.dauren@mail.ru

Baratova, A.A. – Candidate of Physical and Mathematical Sciences, Senior Lecturer, Department of Nuclear Physics, New Materials and Technologies, L.N. Gumilyov Eurasian National University, Astana, Kazakhstan; Scopus Author ID: 57217354220, https://orcid.org/0000-0002-1263-0734; aa.baratova@yandex.kz

EURASIAN PHYSICAL TECHNICAL JOURNAL

2025, Volume 22, No. 1 (51)

https://doi.org/10.31489/2025N1/28-36

Received: 05/11/2024 Revised: 10/02/2024 Accepted: 18/03/2025

Research Article

UDC 537.622.3:620.193.4:699.15

IMPACT OF POLYETHYLENE TEREPHTHALATE ON THE MECHANICAL PROPERTIES OF POLYIMIDE FILMS

Yar-Mukhamedova G.Sh.[1], Muradov A.D.[2], Mukashev K.[2], Umarov F.[3],
Imanbayeva A.K.[1*], Mussabek G.K.[1,4], Belisarova F.[1]

[1] Al-Farabi Kazakh National University, Almaty, Kazakhstan
[2] Energo University, Almaty, Kazakhstan
[3] Kazakh-British Technical University, Almaty, Kazakhstan
[4] Institute of Information and Computational Technologies, Almaty, Kazakhstan
**Corresponding author:* akmaral@physics.kz

Abstract. *This study focuses on analyzing the influence of varying concentrations of polyethylene terephthalate filler on both the tensile strength and elongation at break properties of polyimide films when subjected to uniaxial tension, aiming to determine how polyethylene terephthalate filler impacts the mechanical performance and durability of these films under stress. The mechanical behavior of polyimide films and their homogeneous composites with polyethylene terephthalate under uniaxial tension were investigated. The samples were prepared by mechanically mixing polyimide varnish solutions with polyethylene terephthalate, which serves as a reinforcing filler. The results demonstrate that, for all sample types, an initial mechanical load until induces a sharp ~3% increase in relative elongation, attributed to the rotation of globules and alignment of matrix macromolecules into extended chains along the load direction. The additive dependence of viscosity observed in the study further supports that no chemical bonds are formed between the polyimide and polyethylene terephthalate macromolecules, and that no conformational changes take place within the composite.*

Keywords: polyimide, polyethylene terephthalate, filler, uniaxial tension, IR spectroscopy, viscometry.

1. Introduction

The mechanical properties of polymers and polymer-based materials, such as chain flexibility, crystallinity, and intermolecular interactions, play a key role in determining their overall characteristics. These factors directly affect essential mechanical parameters, including deformation behavior and tensile strength [1-5]. In polyimides, the arrangement of macromolecular chains is governed by the imide groups within the aromatic backbone, contributing to a specific degree of crystallinity [6-8]. Disordered segments contribute to the amorphous phase, leading to a strong dependence between the polymer's properties and its structural organization. The mobility of chain segments, especially under external forces, also plays a significant role in determining mechanical behavior [9].

It is well known that polymers undergo chemical reactions under mechanical stress, leading to the disruption of structural order and affecting the extend, to which this order is preserved. Under mechanical impact, chemical bonds within the main polymer chain can break, resulting in mechanical degradation [10–13]. Among all polymers, polyimides exhibit the highest thermal stability, enduring temperatures up to 673 K while retaining flexibility even at liquid nitrogen temperatures [14]. This remarkable property is attributed to the presence of lone electron pairs on the heteroatom in the ring (nitrogen) and highly electronegative atoms (oxygen in carbonyl groups) [15]. At room temperature, polyimides exhibit high tensile strength (150–180 MPa) with an elongation at break of 70–90%, along with excellent electrical insulation, chemical resistance, and fire resistance [16].

The mechanical properties of polymer composite materials are largely determined by both the type and concentration of the filler [17–20]. According to [21], when fillers are introduced into a polymer solution through uniform mixing, they become evenly distributed within the polymer matrix, forming a molecular-level dispersion. This principle was fundamental in selecting fillers for the present study.

Different fillers influence the polymer matrix in distinct ways, affecting its physicochemical properties. Both the nature and content of the fillers significantly impact the strength and flexibility of polymer composites [22–27]. Research indicates that tensile strength is closely linked to factors such as cross-link density, crystallization tendency, filler characteristics, and the initial molecular weight of the polymer [18, 28]. However, the role of fillers in shaping the physico-mechanical properties of polymer composite materials (PCMs) and the mechanical and functional behavior of newly engineered polymer-based products remains insufficiently explored. A deeper understanding of these effects is critical for enhancing the durability of technological systems and optimizing industrial processes aimed at fine-tuning material properties.

The objective of this study is to investigate the effect of polyethylene terephthalate (PT) filler concentration on the tensile strength and elongation at break of polyimide films under uniaxial tension. The results of this study highlight the practical significance of incorporating polyethylene terephthalate fillers into polyimide composites, providing valuable insights for future material development.

2. Materials and methods

Polyimide (PI) films and their homogeneous compositions with polyethylene terephthalate (PT) filler were selected as the primary objects of study. The matrix polymer used was polyimide, a well-known member of the family of cyclolinear heterocyclic polymers. Polyimides belong to the class of rigid-chain, heat-resistant polymers with a high glass transition temperature, typically ranging from 600 to 800 K. Their macromolecular structure includes periodically repeating bulky polar groups (–O–C_6H_4–), which enhance intermolecular interactions—a key characteristic of rigid-chain polymers. These polar groups are integral components of the macromolecular structural unit, as shown in Fig. 1 [29].

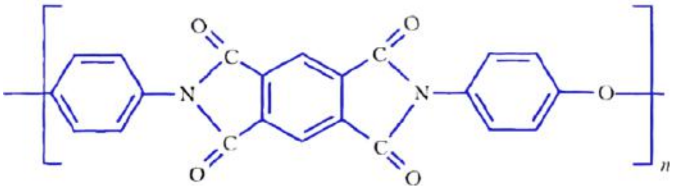

Fig.1. Structural Unit of a Polyimide Macromolecule [29]

The distinctive molecular architecture and strong intermolecular forces give polyimides exceptional thermal stability, making them highly suitable for demanding applications in high-temperature environments. Additionally, they exhibit resistance to radiation and weak acids, along with excellent electrical insulation properties [30]. Besides these advantages, polyimides maintain strong mechanical performance, retaining their strength across a wide temperature range.

2.1. Synthesis of the Polymer Composite

Composite samples were synthesized by mechanically mixing polyimide varnish with solutions containing various concentrations of fillers. The polyimide varnish used was a polyamic acid solution in dimethylformamide, produced by "Estrocom" (Russia).

A systematic approach was applied in the preparation of composite films: first, the mass of the filler corresponding to the desired concentration was measured. The mixture of polyimide varnish and polyester resin in a specific ratio was placed in a three-neck flask, where an inert gas atmosphere was maintained over the solution to prevent oxidation. The mixture was continuously stirred while gradually heating to 170°C.

The resulting viscous solution was then diluted with m-cresol to a concentration of 7%, followed by the introduction of the calculated amount of filler. Stirring continued for another two hours at 170°C to ensure homogeneity. The prepared composite mixture was poured onto a clean glass substrate, and the films were carefully spread and dried in a muffle furnace at 100°C. The resulting films were cut into parallelepiped-shaped samples, each with a working area of 50×50 mm. The thickness of pure polyimide films was 35 μm, while the thickness of composite films ranged from 40 to 140 μm.

As the reinforcing filler, polyethylene terephthalate (PT, also known as lavsan) with the chemical formula $(C_{10}H_8O_4)_n$ was selected. PT is a synthetic polymer containing a terephthalate group in its molecular structure. The structural unit of the polyethylene terephthalate macromolecule is shown in Figure 2 [31]. PT contains polar –O–CO– groups, which are evenly distributed along the polymer chain. These groups enhance intermolecular interactions, contributing to increased rigidity of the material. Compared to polyimide macromolecules, PT molecules exhibit a higher degree of structural crystallinity. The synthesized composite material contained PT fillers at concentrations of 0.25 wt.%, 0.50 wt.%, 2.00 wt.%, 5.00 wt.%, 10.00 wt.%, 15.00 wt.%, and 20.00 wt.%.

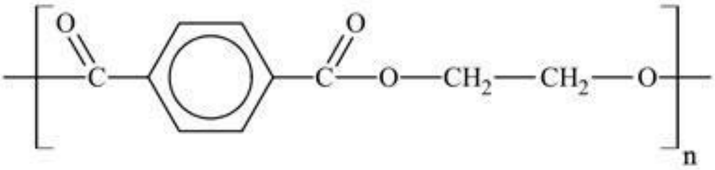

Fig.2. Structural unit of the polyethylene terephthalate (PT) macromolecule [31].

2.2 Samples Characterisation

Mechanical tests of the composite films were conducted using an Instron 5982 tensile testing machine (Instron, USA, manufactured in 2018) at a crosshead displacement speed of 0.05 mm/min [32]. The samples were secured using specialized clamps that ensured stable attachment to the machine's sliding mechanisms [32]. Mechanical loading was applied in a uniaxial tensile mode until the samples reached complete failure. All experiments were conducted under controlled conditions, with a constant load at a temperature of 20±2°C and a relative humidity of 45±5%. The measurement error for both force and film deformation was within ±0.5% of the recorded values. The study of mechanical properties followed GOST R 50583-93 (Russia) and ASTM D 3039/D 3039M - 00 (USA) standards.

The effect of the filler on changes in the polymer matrix's macromolecular structure was analyzed through FTIR spectroscopy, intrinsic viscosity measurements, and surface microphotography of the samples.

FTIR spectra of the samples were recorded using a Jasco IR-810 spectrophotometer (Japan) under standard conditions (20±2°C) within the wavenumber range of 400–4000 cm^{-1}.

Intrinsic viscosity of the polyimide solutions in m-cresol was measured using an Ubbelohde viscometer (Cannon Instrument Company, USA, model 2020), operating in a kinematic viscosity range of 6.0 to 30 m^2/s. The viscosity was determined at 20°C with a solution concentration of 0.5 dL/g.

Surface microphotographs of the samples were taken using a Jeol-ARM100F microscope (Japan) at 200x magnification. The visualization was performed on thin films cast from 7% m-cresol solutions, allowing for a detailed representation of the morphology of the synthesized composites.

3. Results and discussion

The results of experiments illustrating the change in relative elongation of the pure polyimide film without filler under various mechanical loads are presented in Fig. 3 (curve 1). Initially, in the applied load range σ = 0 to 1 MPa, there is a slight increase in relative elongation, up to about 3%. This can be explained by the development of elastic deformation, during which the globules and macromolecules inside the polymer rearrange into stretched chains in the direction of the applied load. As the load increases from 1 MPa to 40 MPa, the relative elongation (ε) of the polyimide film gradually increases. In this load range, the macromolecular chains straighten, aligning and stretching along the flow direction of the polymer matrix, forming fibrous structures. This behavior aligns with previous studies [29–31]. When the applied load exceeds 40 MPa, molecular bonds within the polyimide—particularly those between benzene rings—begin to break, resulting in structural degradation of the polymer. This process leads to a notable increase in relative elongation, ultimately causing film rupture at a stress level of approximately σr ≈ 70 MPa, with a corresponding relative elongation of εr ≈ 45%. The addition of 2 mass.% PT filler to the polyimide matrix significantly modifies the film's plasticity and mechanical properties. Like pure polyimide, the composite material demonstrates a linear increase in relative elongation in the load range from 1 MPa to 40 MPa (Fig. 3, curve 2). However, the elongation degree of the composite is noticeably higher. At an applied load of 40 MPa, the composite reaches a relative elongation of 30%, which is 26% better compared to the pure polyimide film (Fig. 3, curve 1).

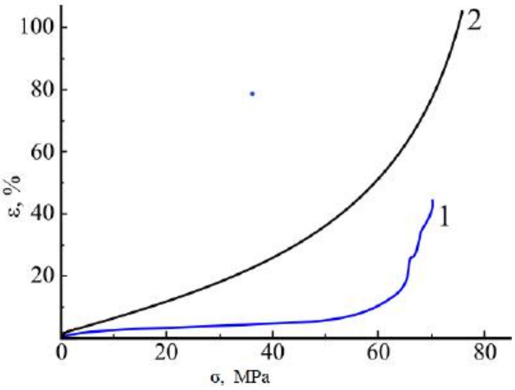

Fig. 3. The dependence of relative elongation (ε) on mechanical load (σ) for pure polyimide film (curve 1) and polyimide composites with PT filler (curve 2), measured at room temperature.

At loads exceeding 40 MPa, the relative elongation of the polyimide composite (PCM) sharply increases, ultimately leading to failure. Notably, the composite material demonstrates superior mechanical characteristics compared to pure polyimide: the strength limit of the composite reaches 80 MPa, and the ultimate elongation reaches 110% (Fig. 3, curve 2).

This improved mechanical behavior of the PCM can be explained by the molecular structure of the PT filler. PT macromolecules have regularly spaced polar groups (–O–CO–) along the polymer chain, which enhance intermolecular interactions both within the polyimide matrix and between polyimide and PT molecules. These interactions increase the rigidity and plasticity of the composite, leading to the observed improvement in both tensile strength and elongation at break.

Increasing the PT filler concentration to 5 mass.% results in a further significant increase in the plasticity of the composite material, with relative elongation (**ε**) reaching 250% without any noticeable changes in tensile strength. A distinctive feature of the ε = ε(σ) dependence in this case is that it reflects the behavior observed in pure polyimide films (see Fig. 3, curve 1). This indicates that the primary mechanisms determining the mechanical properties of this composite material remain the same as those of pure polyimide, despite the presence of the filler. However, the increased plasticity of the polyimide composite with PT filler is primarily due to the reinforcing effect of the filler, which strengthens the intermolecular interactions within the matrix and between the polyimide macromolecules and the filler.

Figure 4 shows the concentration-dependent changes in the plastic and strength properties of polyimide composite materials (PCM) containing PT filler. Changes in the physical-mechanical properties of the composite can be explained by the formation of boundary layers between the polyimide matrix and the PT filler molecules. Adding 0.5 mass.% PT to the polyimide matrix leads to a significant increase in both plasticity (Δα = 45%) and tensile strength (Δσ = 20 MPa) compared to pure polyimide. For the composite material with 2 mass.% PT filler, the elongation at break (εr) reaches approximately 78%, compared to ~37% for pure polyimide (C = 0 mass.%), with a corresponding strength limit Δσr ≈ 72 MPa (Fig.4).

Increasing the PT filler concentration to 5 mass.% leads to a noticeable improvement in the plasticity of the composite: the elongation at break (εr) reaches 250% (Fig. 4a), while the tensile strength remains stable around 75 MPa (Fig. 4b). This stabilization suggests that the reinforcing effect of PT is most pronounced in improving the plastic properties of the material without significantly altering its strength beyond a certain filler concentration.

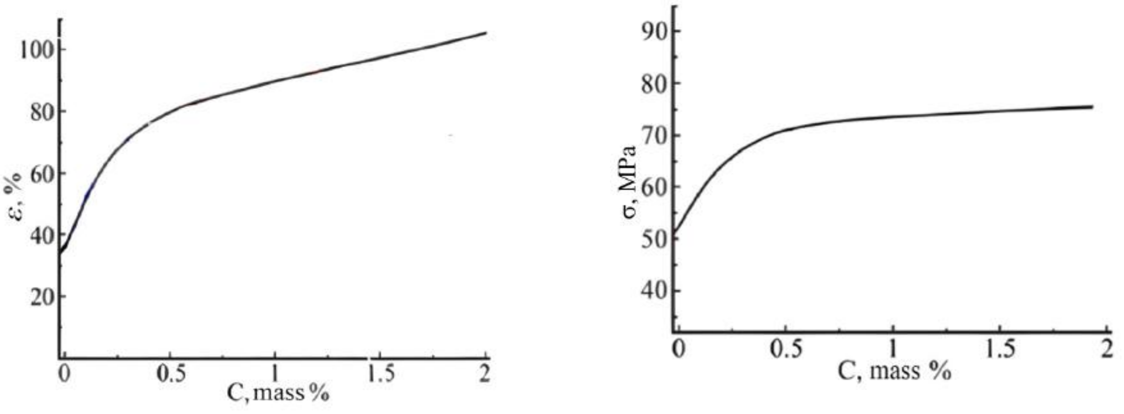

a) b)

Fig.4. a) Effect of PT filler concentration (C) on elongation at break (ε) of polyimide composite materials at room temperature. b) Effect of PT filler concentration (C) on tensile strength (σ) of polyimide composite materials at room temperature.

The observed additive viscosity dependence on the filler concentration suggests the absence of chemical bonding between the polyimide (PI) and PT macromolecules, as well as significant conformational changes (Fig. 5). As the PT concentration increases, the polyimide composite film acquires a more porous structure.

Figures 6 (a, b) show microphotographs demonstrating the microscopic structure of polyimide composite films with PT filler concentrations of 1 wt.% (a) and 10 wt.% (b). In the composite with 10 wt.% PT (Fig. 6b), the pore sizes are noticeably larger, reaching 40 nm, compared to the composite with 1 wt.% PT (Fig. 6a). At PT concentrations above 10–12.5 wt.%, thermodynamic incompatibility between the polymers becomes evident, leading to the formation of opaque film samples.

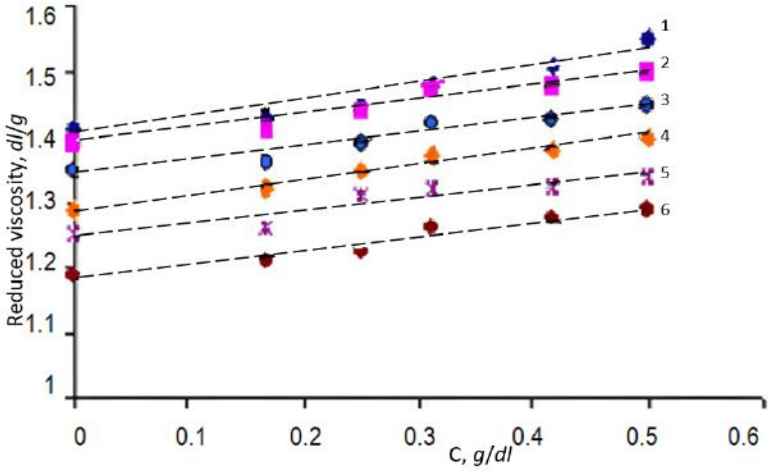

Fig.5. Change in the relative viscosity of polyimide composite material as a function of PT filler concentration (C): Line 1 – 5 wt.% PT; Line 2 – 10 wt.% PT; Line 3 – 15 wt.% PT; Line 4 – 20 wt.% PT; Line 5 – 25 wt.% PT; Line 6 – 30 wt.% PT.

To further verify the results of viscosimetric studies, infrared (IR) spectroscopic investigations were conducted on the composite materials (Figures 7 and 8). The influence of the PT filler and uniaxial mechanical load on the molecular configuration of the polyimide film after deformation was studied. The following maxima in the IR spectrum of the polyimide film after rupture were identified: 446.5; 492.5; 525.6; 605.7; 659.9; 728.3; 797.5; 835.8; 872.9; 950.3; 1008.2; 1065.5; 1107.5; 1161.7; 1252.4; 1297.5; 1378.8; 1508.2; 1626.0; 1721.6; 1771.1; 1899.0; 2028.1; 2578.8; 2950.7; 3053.0; and 3466.3 cm^{-1}.

The peak at 3466.3 cm^{-1} corresponds to the stretching vibrations of hydroxyl (OH) groups, indicating that during film rupture, atomic interactions weaken, leading to the formation of OH bonds as individual molecular bonds break. Additionally, the peak at 1297.5 cm^{-1} is associated with secondary, weak deformation vibrations of the OH group. After rupture, the intensity of this peak decreases, reflecting the weakening of these bonds as a result of material failure.

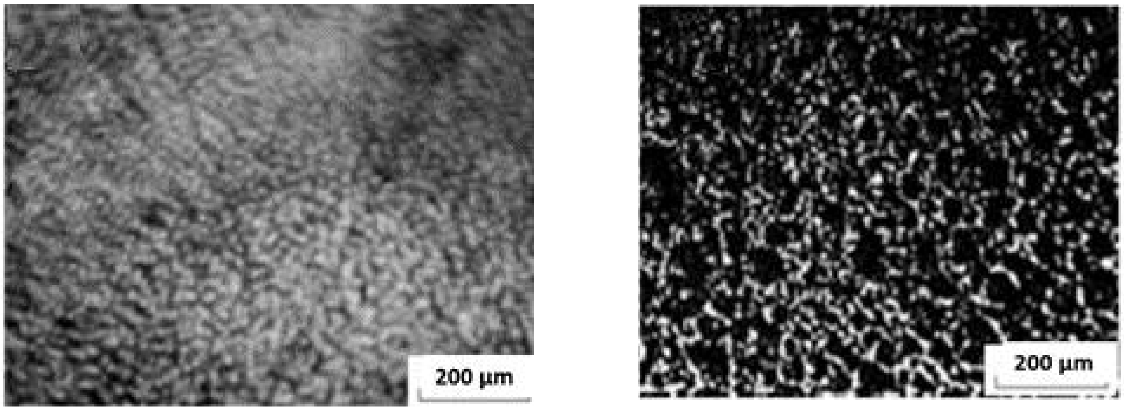

a) b)

Fig.6. Microscopic structure of polyimide composite films with PT filler content: a) 1 wt.% and b) 10 wt.%.

The presence of hydroxyl groups in the polyimide macromolecule is further confirmed by the appearance of absorption bands corresponding to C–O stretching vibrations at 950.3, 1008.2, 1161.7, and 1508.2 cm⁻¹ [37]. Deformation vibrations of Car–H bonds in the aromatic ring, observed in the 600–900 cm⁻¹ range, reveal structural changes after rupture: the peak at 728.3 cm⁻¹ indicates bond weakening, while peaks at 797.5 and 872.9 cm⁻¹ suggest enhanced bonding. The peak at 797.5 cm⁻¹ corresponds to m-displaced deformation vibrations of Car–H bonds.

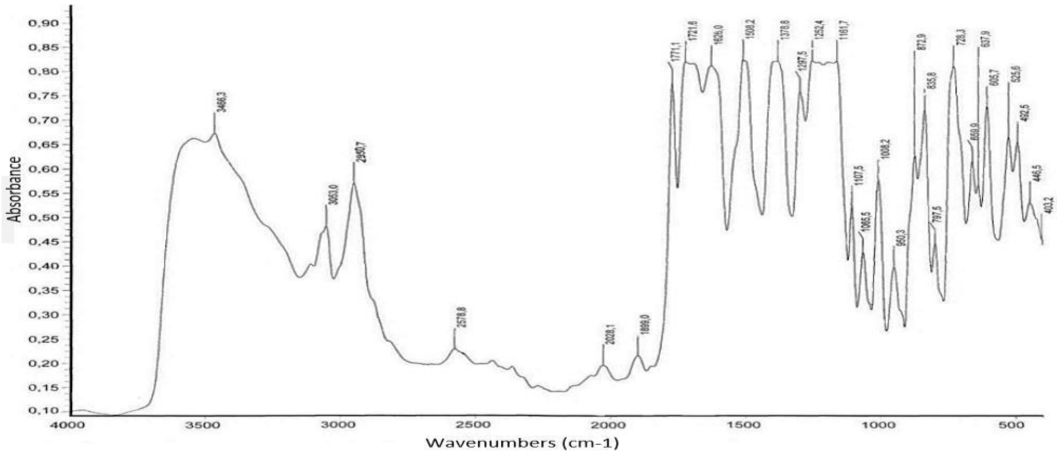

Fig.7. IR spectrum of polyimide film after film rupture

Film rupture also leads to the formation of new Car–H bonds, as evidenced by the emergence of a peak at 835.8 cm⁻¹ (m-displaced deformation vibrations), as well as peaks at 3053.0 cm⁻¹ and its overtone at 1899.0 cm⁻¹. The presence of these deformation vibrations in the Car–H bonds and aromatic ring after rupture suggests that some polyimide macromolecular bonds break, while others either weaken or strengthen. Film stretching weakens atomic bonds, and its rupture results in macromolecular chain shortening, leading to the formation of discrete structural units. Consequently, Car–H bonds strengthen, increasing their bond energy [31].

Fig. 8 shows the IR spectrum of polyimide containing 2 wt.% of PT filler, subjected to tensile stress until rupture. The following maxima were observed: 412.4, 439.2, 491.1, 523.3, 601.9, 636.3, 658.8, 700.0, 727.9, 797.6, 836.3, 879.1, 892.8, 920.1, 946.1, 1001.7, 1062.2, 1107.9, 1296.2, 1361.5, 1513.5, 1727.9, 1770.1, 1896.6, 2030.4, 2272.6, 2321.7, 2361.8, 2436.1, 2578.7, 2876.2, 2953.1, 3050.9, 3110.5, and 3587.0 cm⁻¹. The influence of the PT filler on the polyimide matrix manifests in the deformation processes (Figs. 4 and 5) and the resulting changes in the IR spectra of the deformed films (Figs. 7 and 8). Specifically, in the range of 400–1700 cm⁻¹, an increase in spectral intensity by up to 40% is observed, while in the range of 1700–3500 cm⁻¹, the increase is approximately 70% compared to the spectra of deformed pure polyimide films. These intensity changes occur without any noticeable shifts in the previously existing absorption bands, suggesting that the PT filler induces structural modifications within the polyimide matrix [33, 34].

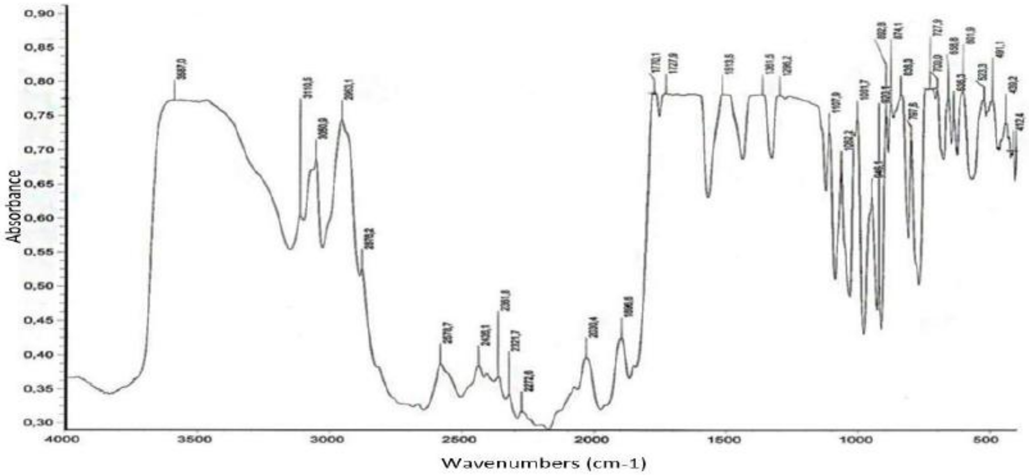

Fig.8. IR spectrum of polyimide film containing 2 wt.% PT filler, not subjected to deformation

The bands corresponding to the deformation vibrations of the C_{ar}–H bonds in the range of 600–900 cm^{-1} in the polyimide composite material (PCM) change significantly after stretching. The low-intensity peak at 727.9 cm^{-1} indicates a weak bond, while the increased intensity of the peaks at 797.5 and 874.1 cm^{-1} suggests an increase in the strength of the bond. The peak at 797.5 cm^{-1} is associated with m-disubstituted deformation vibrations of the C_{ar}–H bonds [14].

The rupture of the polyimide composite leads to the formation of new C_{ar}–H bonds. The peak at 835.3 cm^{-1} in the broken film corresponds to m-disubstituted deformation vibrations of the C_{ar}–H bonds, as well as the peak at 3053.9 cm^{-1} and its overtone at 1895.6 cm^{-1}.

4. Conclusions

The study results indicate that the addition of a polyethylene terephthalate filler significantly affects the physicochemical interactions between polyimide macromolecules, leading to noticeable changes in the composite material's mechanical properties:

– The PT filler at a concentration of 0.5 wt.% increases the plasticity of polyimide by $\Delta\varepsilon$ = 45% and the tensile strength by $\Delta\sigma$ = 20 MPa compared to the maximum changes of $\Delta\varepsilon \approx$ 37% and $\Delta\sigma \approx$ 72 MPa for pure polyimide.

– At a concentration of 2 wt.%, the PT filler enhances the tensile strength of the polyimide composite by 46% and increases its plasticity by a factor of 2.8. This concentration promotes structural organization within the polyimide matrix, resulting in a 40% increase in IR absorption intensity in the 400–1700 cm^{-1} range and a 70% increase in the 1700–3500 cm^{-1} range compared to pure polyimide. The improvement in mechanical properties is associated with the filling of the polymer matrix pores with the PT filler, which stabilizes the molecular chains and strengthens the polyimide structure with a flexible framework.

– The introduction of higher concentrations of PT (up to 10 wt.%) increases the porosity of the composite, reaching 40 nm. However, when the PT filler concentration exceeds 10–12.5 wt.%, thermodynamic incompatibility between the polymers becomes evident, leading to a decrease in compatibility. The additive dependence of viscosity on filler concentration indicates that no new bonds are formed or significant conformational changes occur between polyimide and PT macromolecules, as no new absorption bands or shifts in the IR spectra are observed.

– The observed additive viscosity dependence further confirms that no chemical bonds are formed between polyimide and PT macromolecules, and no conformational changes occur within the composite.

Conflict of interest statement

The authors confirm that they have no conflicts of interest – financial, personal, authorship-related, or any other – that could influence this research or the results presented in this paper.

CRediT author statement:
Yar-Mukhamedova G.Sh., Imanbayeva A.K.: Project Administration, Conceptualization, Methodology; **Muradov A.D., Mukashev K., Umarov F.**: Verification and Formal analysis; **Mussabek G.K., Belissarova F.**: Data Curation, Validation and Investigation. The final manuscript was read and approved by all authors.

Acknowledgements
This research was funded by the Science Committee of the Ministry of Science and Higher Education of the Republic of Kazakhstan (Grant No. AP23484310).

References

1 Tjong S.C. (2006) Structural and mechanical properties of polymer nanocomposites. *Materials Science and Engineering: R: Reports*, 53, 73-197. https://doi.org/10.1016/j.mser.2006.06.001

2 Al-Saleh M.H., Sundararaj U. (2011) Review of the mechanical properties of carbon nanofiber/polymer composites. *Composites Part A: Applied Science and Manufacturing*, 42, 2126-2142. https://doi.org/10.1016/j.compositesa.2011.08.005

3 Popescu D., Zapciu A., Amza C., Baciu F., Marinescu R. (2018) FDM process parameters influence over the mechanical properties of polymer specimens: A review. *Polymer Testing*, *69*, 157-166. https://doi.org/10.1016/j.polymertesting.2018.05.020

4 Bazli M., Abolfazli M. (2020) Mechanical properties of fibre reinforced polymers under elevated temperatures: An overview. *Polymers*, 12(11), 2600. https://doi.org/10.3390/polym12112600

5 Liaw D.-J., Wang K.-Li, Huang Y.-Chi, Lee K.-R., Lai J.-Yih, Ha Ch.-Sik. (2012) Advanced polyimide materials: Syntheses, physical properties and applications. *Progress in Polymer Science*, 37, 907-974. https://doi.org/10.1016/j.progpolymsci.2012.02.005

6 Ghaffari-Mosanenzadeh Sh., Tafreshi O.A., Karamikamkar S., Saadatnia Z., Rad E., Meysami M., Naguib H.E. (2022) Recent advances in tailoring and improving the properties of polyimide aerogels and their application. *Advances in Colloid and Interface Science*, 304, 102646. https://doi.org/10.1016/j.cis.2022.102646

7 Wu Z., He J., Yang H., Yang Sh. (2022) Progress in aromatic polyimide films for electronic applications: Preparation, structure and properties. *Polymers*, 14(6), 1269. https://doi.org/10.3390/polym14061269

8 Abadie M.J.M. (2012) *High performance polymers – polyimides based: From chemistry to applications*. Publisher: InTech Open, 258 p. https://doi.org/10.5772/2834

9 Meijer H.E.H., Govaert L.E. (2005) Mechanical performance of polymer systems: The relation between structure and properties. *Progress in Polymer Science*, 30, 915-938. https://doi.org/10.1016/j.progpolymsci.2005.06.009

10 Caruso M.M., Davis D.A., Shen Q., Odom S.A., Sottos N.R., White S.R., Moore J.S. (2009) Mechanically-induced chemical changes in polymeric materials. *Chem. Rev*., 109(11), 5755–5798. https://doi.org/10.1021/cr9001353

11 Li J., Nagamani Ch., Moore J.S. (2015) Polymer mechanochemistry: from destructive to productive. *Acc. Chem. Res*., 48(8), 2181–2190. https://doi.org/10.1021/acs.accounts.5b00184

12 Palomba D., Vazquez G.E., Díaz M.F. (2014) Prediction of elongation at break for linear polymers. *Chemometrics and Intelligent Laboratory Systems*, 139, 121-131. https://doi.org/10.1016/j.chemolab.2014.09.009

13 Liaw D., Wang K., Huang Y., Lee K., Lai J., Ha Ch. (2012) Advanced polyimide materials: Syntheses, physical properties and applications. *Progress in Polymer Science*, 37(7), 907-974. https://doi.org/10.1016/j.progpolymsci.2012.02.005

14 Ward I.M., Sweeney J. (2013) *Mechanical properties of solid polymers*. 3rd ed.; Publisher: John Wileyans Sons Ltd., 2013, 450 p.

15 Mahdi E., Dean A. (2020) The effect of filler content on the tensile behavior of polypropylene/cotton fiber and poly(vinyl chloride)/cotton fiber composites. *Materials*, 13, 753. https://doi.org/10.3390/ma13030753

16 Ogbonna, V.E., I. Popoola A.P., Popoola O.M., Adeosun S.O. (2022) A review on polyimide reinforced nanocomposites for mechanical, thermal, and electrical insulation application: challenges and recommendations for future improvement. *Polymer Bulletin*, 79, 663–695. https://doi.org/10.1007/s00289-020-03487-8

17 He X., Ou D., Wu Sh., Luo Y., Ma Y., Sun J. (2022) A mini review on factors affecting network in thermally enhanced polymer composites: filler content, shape, size, and tailoring methods. *Advanced Composites and Hybrid Materials*, 5, 21–38. https://doi.org/10.1007/s42114-021-00321-1

18 Yadav R., Singh M., Shekhawat D., Lee S., Park S.-J. (2023) The role of fillers to enhance the mechanical, thermal, and wear characteristics of polymer composite materials: A review. *Composites Part A: Applied Science and Manufacturing*, *175*, 107775. https://doi.org/10.1016/j.compositesa.2023.107775

19 Bashir M.A. (2021) Use of dynamic mechanical analysis (DMA) for characterizing interfacial interactions in filled polymers. *Solids*, 2(1), 108-120. https://doi.org/10.3390/solids2010006

20 Sanghvi M.R., Tambare O.H., More A.P. (2022) Performance of various fillers in adhesives applications: a review. *Polym. Bull*.**,** *79*, 10491–10553. https://doi.org/10.1007/s00289-021-04022-z

21 Antti P., Jukka, Vaari T., Verho O. (2019) Crystallization of cross-linked polyethylene by molecular dynamics simulation. *Polymer*, 171, 80-86. https://doi.org/10.1016/j.polymer.2019.03.040

22 Balasubramanian K.B. N., Ramesh Th. (2018) Role, effect, and influences of micro and nano-fillers on various properties of polymer matrix composites for microelectronics: A review. *Polymers Adv. Technol*., 29(6), 1568-1585. https://doi.org/10.1002/pat.4280

23 Liu Yi., Xing Zh., Jia S., Shi X., Chen Zh., Jian Zh. (2024) Research progress in special engineering plastic-based electrochromic polymers. *Materials*, 17(1), 73. https://doi.org/10.3390/ma17010073

24 Harito Ch., Bavykin D.V., Yuliarto B., Dipojono H.K., Walsh F.C. (2019) Polymer nanocomposites having a high filler content: synthesis, structures, properties, and applications. *Nanoscale*, 11, 4653-4682. https://doi.org/10.1039/C9NR00117D

25 Rueda M.M., Auscher M.-C., Fulchiron R., Périé T., Martin G., Sonntag Ph., Cassagnau Ph. (2017) Rheology and applications of highly filled polymers: A review of current understanding. *Progress in Polymer Science*, *66*, 22-53. https://doi.org/10.1016/j.progpolymsci.2016.12.007

26 Zhu Ch., Fu Yi., Liu Ch., Liu Y., Hu L, Liu J., Bello I., Li H., Liu N., Guo S., Huang H., Lifshitz,Ye., Lee Sh.-T., Kang Zh. (2017) Carbon dots as fillers inducing healing/self-healing and anticorrosion properties in polymers. *Adv. Mat.*, 29(32), 1701399. https://doi.org/10.1002/adma.201701399

27 Kharmoudi H., Lamtai A., Elkoun S., Robert M., Diez C. (2024) Effect of graphene on the mechanical properties of recycled high-density and high-molecular-weight polyethylene blends. *Materials*, 17(19), 4733. https://doi.org/10.3390/ma17194733

28 Wolf C., Angellier-Coussy H., Gontard N., Doghieri F., Guillard V. (2018) How the shape of fillers affects the barrier properties of polymer/non-porous particles nanocomposites: A review. *Journal of Membrane Science*, 556, 393-418. https://doi.org/10.1016/j.memsci.2018.03.085

29 Instron. Instron Model 5982 Floor-standing double-column testing machines. Manual M10-16250-RU. Editions D. Instron. – 2002. https://www.instron.com/en/search-results?ss360Query=5982

30 Zelele D.M., Rutkowska-Gorczyca M. (2024) Electrochemical synthesis and functional properties of metal and alloy-based composition coatings, *Recent Contributions to Physics*, 1(88), 41-48. https://doi.org/10.26577/RCPh.2024v88i1a06

31 Muradov A.D., Mukashev K.M., Yar-Mukhamedova G.Sh., Korobova N.E. (2017) Impact of silver metallization and electron irradiation on the mechanical deformation of polyimide films. *Technical Physics*, *62*, 1692-1697. https://doi.org/10.1134/S1063784217110226

32 Tomohiro O., Shinji A. (2016) Conformational characterization of imide compounds and polyimides using far-infrared spectroscopy and DFT calculations. *Polymer,* 86, 83-90. https://doi.org/10.1016/j.polymer.2016.01.037

33 Smith B.C. (2021) The Infrared Spectra of Polymers II: Polyethylene. *Spectroscopy*, 36, 24-29. https://doi.org/10.56530/spectroscopy.xp7081p7

34 Greshta V., Narivskyi O., Dzhus A., Vynar V., Yar-Mukhamedova G., Mukashev K., Beissen N., Mussabek G., Imanbayeva A., Zellele D., Atchibayev R., Kemelzhanova A. (2024) Corrosion behaviour of magnesium alloys NZ30K and NZ30K alloyed with silver in the model solution of the osteosynthesis process. *Eurasian Physical Technical Journal*, 21, 3 (49), 29-36. https://doi.org/10.31489/2024No3/29-36

AUTHORS' INFORMATION

Yar-Mukhamedova, Gulmira Sharipovna – Doctor of Phys. and Math. Sciences, Professor, Al-Farabi Kazakh National University, Almaty, Kazakhstan; Scopus Author ID: 6505954975; https://orcid.org/0000-0001-5642-3481; gulmira-alma-ata@mail.ru

Muradov, Abyl Darkhanovich – Candidate of Phys. and Math. Sciences, Associate Professor, Energo University, Almaty, Kazakhstan; Scopus Author ID:8270630100; https://orcid.org/0000-0003-1987-1167; abyl.muradov1@gmail.com

Mukashev, Kanat – Doctor of Phys. and Math. Sciences, Professor, Energo University, Almaty, Kazakhstan; Scopus Author ID: 10640069200; https://orcid.org/0000-0002-3568-7143; mukashev.kms@gmail.com

Umarov, Farid Fakhrievich – Doctor of Phys. and Math. Sciences, Professor, Kazakh-British Technical University, Almaty, Kazakhstan; Scopus Author ID: 6701387875; https://orcid.org/0000-0002-7475-0977; farid1945@yahoo.com

Imanbayeva, Akmaral Karimovna – Candidate of Phys. and Math. Sciences, Researcher, Al-Farabi Kazakh National University; Almaty, Kazakhstan; Scopus Author ID: 15054326000; https://orcid.org/0000-0001-9900-9782; akmaral@physics.kz

Mussabek, Gauhar Kalizhanovna – PhD (Sci.), Associate Professor, Al-Farabi Kazakh National University, Institute of Information and Computational Technologies, Almaty, Kazakhstan; Scopus Author ID: 37028867500; https://orcid.org/0000-0002-1177-1244; gauhar-mussabek@mail.ru

Belisarova, Farida Beksultanovna – Associate Professor, Candidate of Phys. and Math. Sciences, Al-Farabi Kazakh National University; Almaty, Kazakhstan; Scopus Author ID: 57189071061; https://orcid.org/0000-0003-0531-3818; farida.belisarova@kaznu.edu.kz

EURASIAN PHYSICAL TECHNICAL JOURNAL

2025, Volume 22, No. 1 (51)

https://doi.org/10.31489/2025N1/37-43

Received: 09/08/2024 Revised: 13/12/2024 Accepted: 18/03/2024

Research Article

UDC 539.232

FILMS OF POROUS ALUMINUM OXIDE OBTAINED BY TWO-STAGE ANODIZATION

Zhangbyrbay Ye.R.[1*], Aimukhanov A.K.[1], Zeinidenov A.K.[1], Gadirov R.M.[2],
Abeuov D.R.[1], Zhakanova A.M. [1]

[1] Buketov Karaganda University, Karaganda, Kazakhstan
[2] Tomsk State University of Control Systems and Radioelectronics, Tomsk, Russia
*Corresponding author: erkesh_zhan@mail.ru

Abstract. *Anodic aluminum oxide films are widely used to obtain many types of organic and inorganic nanomaterials and are of practical importance in studying the optical properties of nanomaterials synthesized from them. This work presents a method of two-sided and two-stage anodization for obtaining anodic aluminum oxide films with periodic and regularly spaced pores. The method of anodic oxidation of aluminum in solutions of acidic electrolytes makes it possible to quite easily vary the parameters of the porous structure of* Al_2O_3*. Oxalic acid was used as an electrolyte for "soft" anodizing of the aluminum plate, and ethyl alcohol and a solution of orthophosphoric acid and chromic anhydride were used to pre-clean and polish the aluminum plate. Anodization was carried out at low temperatures, as a result of which it was possible to obtain an aluminum oxide film with a high degree of ordering of pores, the sizes of which ranged from 60 to 110 nm, and the distance between the pores was in the range of 13–27 nm. Absorption and reflection spectra of a porous film of anodized aluminum were obtained, where good absorption of the films is observed in the short-wavelength region of the spectrum, and the maximum value of the refractive index is observed in the short- and long-wavelength regions of the spectrum.*

Keywords: Transparent anodic aluminum oxide films, double-sided anodizing, porous membranes, anodizing at low temperatures, barrier layer.

1. Introduction

Inorganic membranes, including dense membranes (nonporous) and microporous membranes, due to their good thermal and chemical stability, are one of the promising materials for the separation of gaseous H_2 [1-3]. During the last 30 years, many studies have been successfully conducted by various research groups to improve membrane transport/separation properties by modifying porous inorganic membranes using chemical vapor deposition (CVD), sol-gel and other methods [4, 5].

Anodic aluminum oxide (AAO) films with periodic and regularly spaced pores have a wide range of applications [6]. AAO is used to obtain many types of organic and inorganic nanomaterials, which are widely used in optics [7], energy storage [8], sensors [9], molecular sieves for gas separation [10], surface-enhanced Raman scattering [11], ion current rectification [12], biological antibacterial treatment [13], food industry [14] and many other areas. By changing the experimental conditions and preparation processes, it is possible to obtain AAO films with different porous structures [15]. Transparent AAO films are of practical importance in studying the optical properties of nanomaterials synthesized from them. Transparent AAO films with barrier layers separated from aluminum substrates have nonlinear diode-type current-voltage characteristics and ion rectification properties and are used in biosensing, bioseparation, nanofluidic electronics, etc. [16]. This paper presents the results of the development of technology and studying the properties of anodized aluminum oxide (AAO) films.

2. Experimental part

Films of porous aluminum oxide were prepared by two-sided and two-stage anodization. A 0.3 M solution of oxalic acid was used as an electrolyte.

To begin with, aluminum plates of 99.99% purity, 3.5x3.5 cm in size and 0.5 mm thick were prepared. Aluminum plates were pre-annealed in a muffle furnace at 500°C for 6 hours. Afterwards, the plate surface was cleaned with ethyl alcohol to degrease it. An important characteristic of metallic aluminum that affects the process of ordering of the porous structure is the roughness of its surface. The aluminum surface was leveled by electrochemical polishing in a pulsed mode. For electrochemical polishing of the aluminum surface, an electrolyte was used, which has the following composition: CrO_3 (185 g/l) and H_3PO_4 (1480 g/l). The solution was poured into a heat-resistant container and placed on a magnetic stirrer at a temperature of 80 °C. An aluminum plate (of the same composition and larger in area) was attached to the negative electrode and an aluminum plate for polishing to the positive electrode, then the aluminum plate was lowered into the solution with a special device and polished for 40 min. The aluminum plate was subjected to electrochemical polishing in a pulsed mode at a maximum voltage of 20 V, current - 11 A, pulse duration - 3 s, interval between pulses - 40 s, number of pulses - 40 pcs. The quality control of electrochemical polishing was assessed by the appearance of the aluminum surface.

A solution of oxalic acid $(COOH)_2$ with a concentration of 0.3 M was prepared for anodizing aluminum. The electrolyte was poured into a special container, as shown in Figure 1. Two platinum wires were used as a negative electrode. An aluminum plate was placed between the platinum wires and connected to the positive electrode. A stirrer was attached to the container lid to ensure uniform anodization. This entire structure was placed in a refrigerator to ensure anodic oxidation at a temperature of 0 °C.

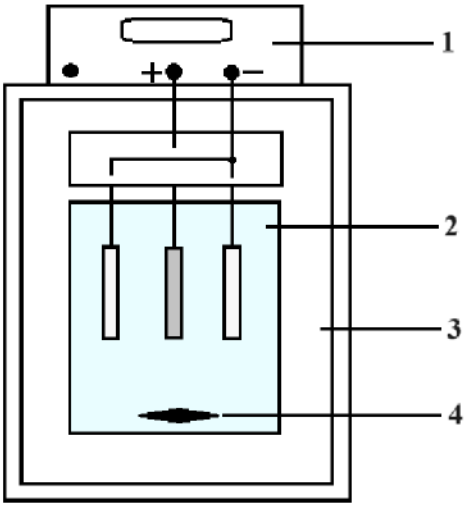

Fig.1. Installation for anodizing aluminum:
1 – power source, 2 – electrochemical cell, 3 – refrigeration chamber, 4 – magnetic stirrer.

The first anodizing stage was carried out at a voltage of 40 V. Then the plate was subjected to electrochemical etching in a solution of orthophosphoric acid (35 ml/l) and chromic anhydride (20 g/l) at 60°C for 15 min. After removing the oxide film, the second stage was carried out according to the same conditions as the first. The resulting transparent aluminum oxide film was washed in deionized water.

The absorption and reflection spectra of the anodic aluminum oxide film were measured on an AvaSpec-ULS2048CL-EVO spectrometer (Avantes). Graphs were built using the obtained data in the OriginPro application.

3. Results and discussion

Due to the fact that ordering of the structure occurs during film growth, the upper side of the membrane is characterized by a chaotic arrangement of pores. To obtain films with an ordered structure throughout the entire volume, two-stage anodization of the films was carried out. The method of anodic oxidation of aluminum in solutions of acidic electrolytes makes it possible to quite easily vary the parameters (pore diameter, distance between pores, film thickness) of the Al_2O_3 porous structure. The production of aluminum oxide layers was carried out under conditions of “soft” anodization using a two-sided method. The thickness of the films obtained by this method is directly proportional to the duration of electrochemical oxidation, and the rate of formation of the oxide layer varies from 2 to 5 μm/h. It should be noted that the temperature of the electrolyte is the most important parameter, since at a constant acid concentration it determines the rate of dissolution of the oxide layer at the oxide/electrolyte interface. After preliminary surface preparation, the first anodic oxidation of aluminum was carried out in a solution of 0.3 M $(COOH)_2$. After this, subsequent (second) anodic oxidation was carried out under the same conditions as during the first oxidation. In this case, it is possible to obtain an aluminum oxide film with a high degree of pore ordering. Figure 2 shows a chronoamperogram of the process of obtaining anodized aluminum films using a two-stage method.

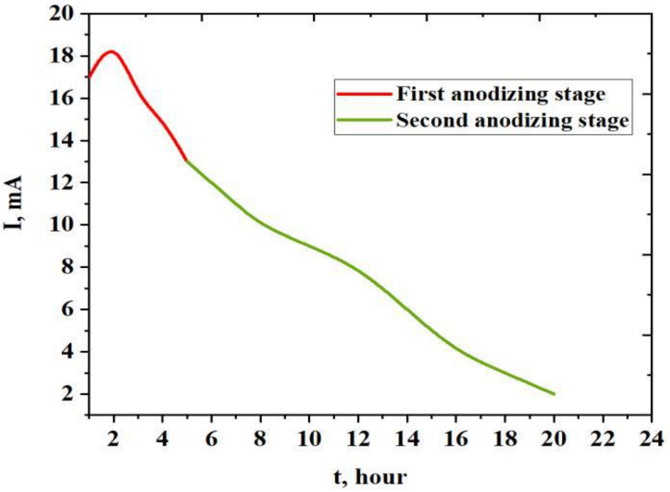

Fig.2. Chronoamperogram of the first and second stages of anodization.

In Figures 3 (a) and (b) are shown SEM images of one of the surfaces of a transparent alumina film. The pictures show a typical ordered porous structure. The size of the ordered pores varies in the range of 60–110 nm, as shown in Figure 3 (d). The distance between the pores was in the range of 13–27 nm. The SEM image of the transverse cleavage of the transparent AAO film is shown in the same Figure 3 c. The film thickness is about 291 μm. The transverse cleavage is divided into upper and lower layers, separated by a barrier layer whose size is on the order of 14 nm (Figure 3 b).

The absorption spectrum of a porous anodized aluminum film is shown in Figure 4. Anodized aluminum films are practically opaque in the spectral range of 400-700 nm. The observed good absorption of anodized aluminum films $\lambda<400$ nm in the short-wavelength region of the spectrum with the maximum at 380 nm corresponds to an interband transition from the valence band to the bottom of the conduction band. This region corresponds to transitions from final states of the valence band to broadened states of the conduction band in aluminum oxide [17]. In the long-wavelength part of the absorption spectrum of films at $\lambda>450$ nm, a broad band with a maximum at 570 nm is observed, which may be associated with light scattering in porous structures.

The diffuse reflectance coefficient of films is 27% at $\lambda<400$ and decreases as the wavelength of light increases. In the spectral range 470-700 nm it is 10%.

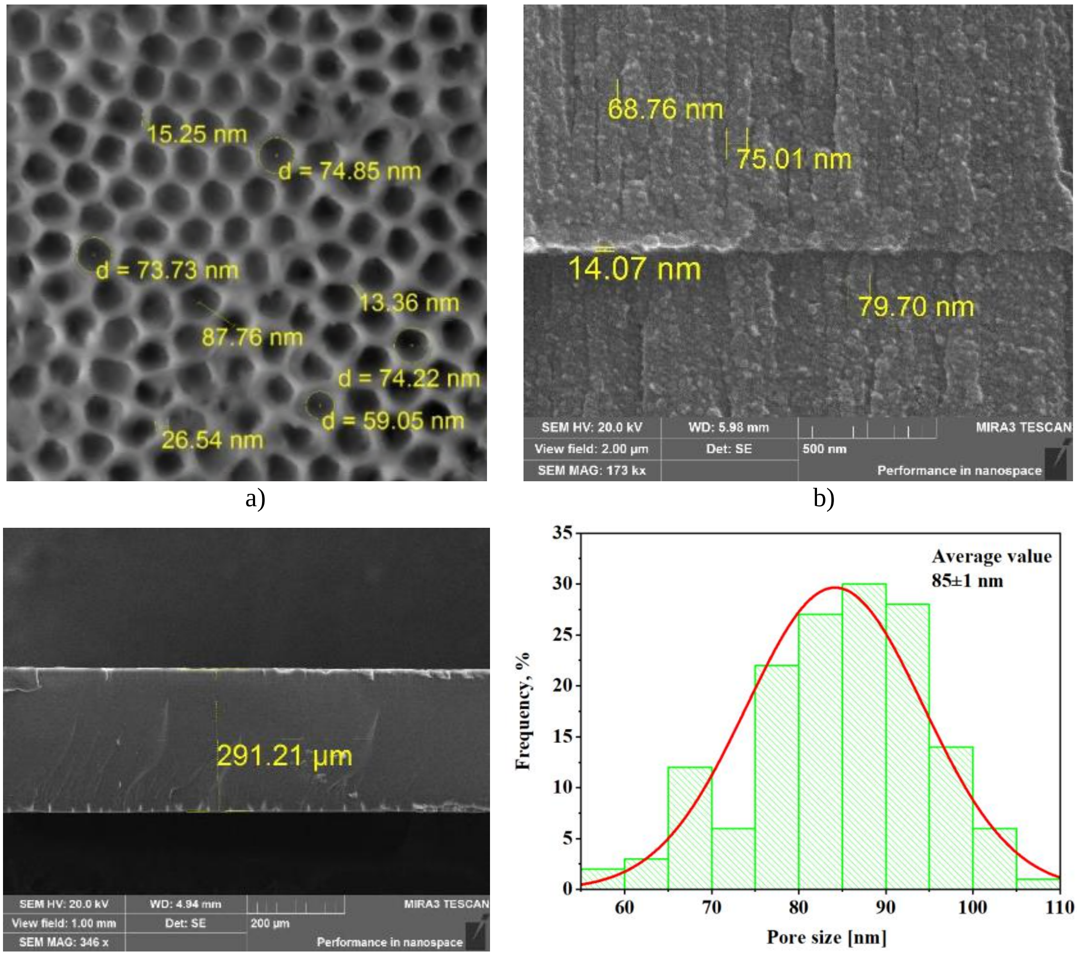

a) b)

c) d)

Fig.3. (a) SEM image of the surface of an aluminum oxide film; (b) SEM image of a transverse cleavage of a transparent AAO film; (c) size of a transverse cleavage; (d) histogram of pore size distribution.

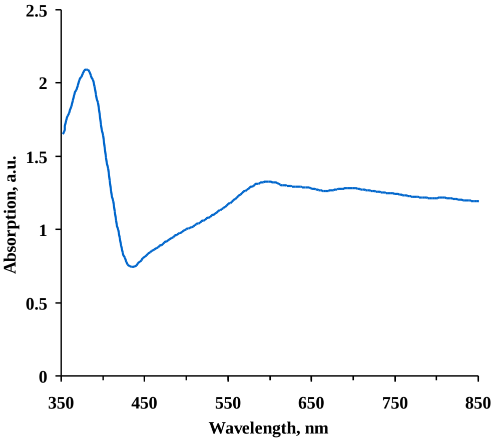

Fig.4. Absorption spectrum of a porous film of anodized aluminum.

The diffuse reflectance coefficient of films is 27% at 430 nm and decreases as the wavelength of light increases (Figure 5a). Such pronounced peaks are observed in thin AAO films, the thickness of which is comparable to the wavelength [18]. The appearance of such a peak in a thick AAO film is apparently associated with the presence of a barrier layer in the center of the oxide structure. In the range of 550-850 nm, the reflection is on average no more than 10%. The optical constants of thin films of anodized aluminum (k – extinction coefficient and n – refractive index) were determined according to the method [3]. As expected, the extinction coefficient given in Figure 5b for the resulting structure generally follows the absorption spectrum corrected for the reflection and refractive index.

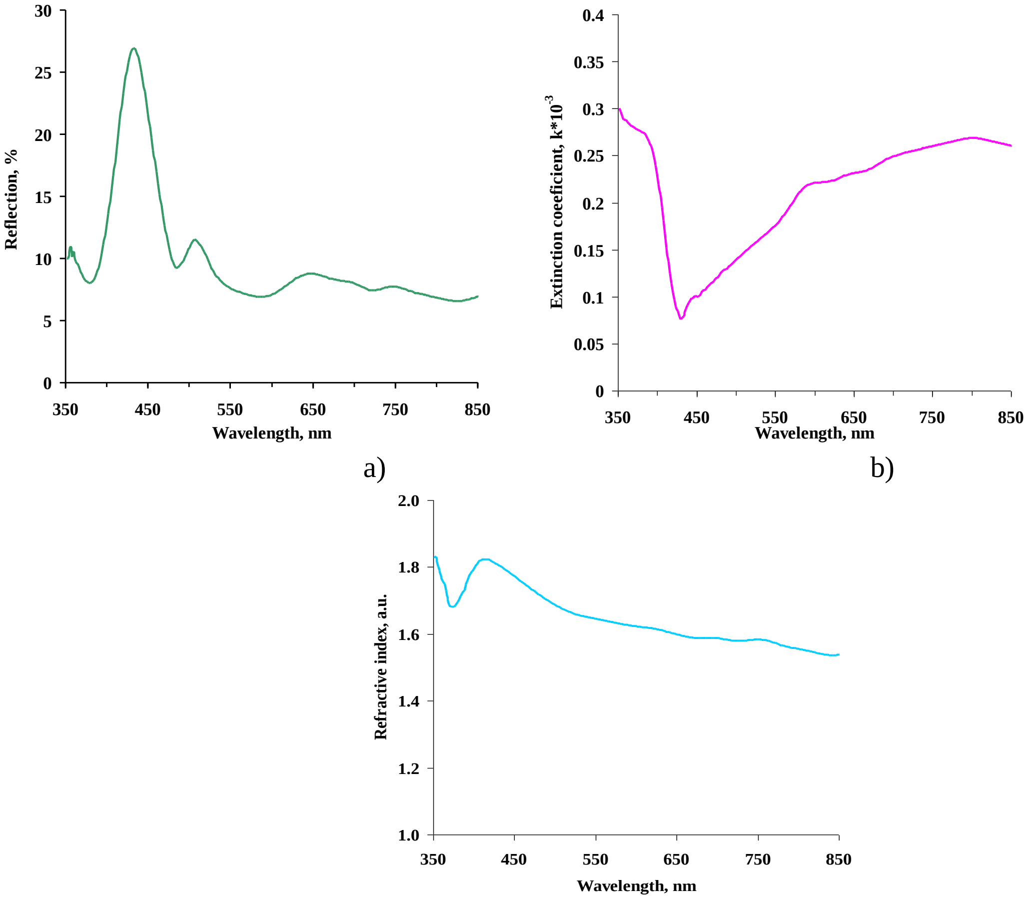

a) b)

c)

Fig.5. (a) Reflection spectrum; (b) dependence of the extinction coefficient on the wavelength; (c) dependence of the refractive index on the wavelength of anodized aluminum films.

The refractive index is one of the fundamental properties of an optical material, since it is closely related to the electronic polarization of ions and the local field within the material. The Figure 5 c shows that the maximum value of the refractive index (n=1.82) is observed in the short-wavelength λ=412 nm and gradually decreases in the long-wave part of the spectrum. These results are in good agreement with data obtained by other authors [19-21].

4. Conclusion

Using the method of two-sided and two-stage anodization, AAO films with periodic and regularly spaced pores were obtained. Anodization was carried out in oxalic acid at a voltage of 40 V at low temperatures. The aluminum plate was subjected to electrochemical polishing in orthophosphoric acid. As a result, an aluminum oxide film with a high degree of pore ordering was obtained, which is confirmed by the surface patterns of the transparent aluminum oxide film. The absorption and reflection spectra of a porous film of anodized aluminum were obtained. The ability to regulate the time of first and secondary anodization allows precise control of the thickness of the transparent AAO film, and the prepared film is a two-sided porous layer separated by a barrier layer, with subsequent use as molecular sieves in ion transport for photocatalytic reactions and hydrogen fuel cells. The proposed method is very easy to operate and does not require complex preparation processes. The advantage of the method we propose is that we have obtained a two-stage anodizing technology with through channels with adjustable dimensions formed towards each other. This method will allow the production of membranes and various types of filters for various applications. The results of the proposed solutions will allow developing technologies related to the development of new types of nanomaterials used as hydrogen fuel cells, which will expand the range of technologies in the field of “green energy”.

Conflict of interest statement

The authors declare that they have no conflict of interest in relation to this research, whether financial, personal, authorship or otherwise, that could affect the research and its results presented in this paper.

CRediT author statement

Zhangbyrbay Ye.R.: Writing – original draft, Investigation; **Aimukhanov A.K.:** Supervision, Methodology; **Zeinidenov A.K.**: Resources, Project administration, Conceptualization; **Gadirov R.M., Abeuov D.R.:** Formal analysis, Visualization; **Zhakanova A.M.:** Data curation. The final manuscript was read and approved by all authors.

Acknowledgements

This work was supported by the Ministry of Science and Higher Education
of the Russian Federation (State Assignment FEWM-2024-0001)

References

1 Ismail A.F., Khulbe K.C., Matsuura T. (2015) Gas Separation Membranes, *Switz. Springer, New York*, 10, 973–978. https://doi.org/10.1007/978-3-319-01095-3

2 Chiu W.V., Park I.S., Shqau K., White J.C., Schillo M.C., Ho W.S.W., Dutta P.K., Verweij H. (2011) Post-synthesis defect abatement of inorganic membranes for gas separation. *J. Membr. Sci*, 377, 182–190. https://doi.org/10.1016/j.memsci.2011.04.047

3 Poelman D., Smet P.F. (2003) Methods for the determination of the optical constants of thin films from single transmission measurements: a critical review. *J. Phys. D: Appl. Phys*., 36, 1850–1857. https://doi.org/10.1088/0022-3727/36/15/316

4 Cooper C.A., Lin Y.S. (2002) Microstructural and gas separation properties of CVD modified mesoporous γ-alumina membranes. *J. Membr. Sci*., 195, 35–50. https://doi.org/10.1016/S0376-7388(01)00508-7

5 Wang H., Zhang L., Gavalas G.R. (2000) Preparation of supported carbon membranes from furfuryl alcohol by vapor deposition polymerization. *J. Membr. Sci*., 177, 25–31. https://doi.org/10.1016/S0376-7388(00)00444-0

6 Lee W., Park S.J. (2014) Porous anodic aluminum oxide: anodization and templated synthesis of functional nanostructures. *Chem. Rev*., 114, 7487–7556. https://doi.org/10.1021/cr500002z

7 Iravani S. (2023) Surfactant-free synthesis of metal and metal oxide nanomaterials: a perspective. *RSC Sustainability*, 1, 72–82. https://doi.org/10.1039/d2su00088a

8 Li Z., Wei H., Chen D., Chang M., Hu H., Ye X., Zhang Y., Wen W., Wang M. (2021) Optical properties of multicolor, hierarchical nanocomposite films based on anodized aluminum oxide. *Opt. Mater.*, 111, 110557. https://doi.org/10.1016/j.optmat.2020.110557

9 Wei H., Xu Q., Chen D., Chen M., Chang M., Ye X. (2022) Lowered infrared emittance and enhanced thermal stability of solar selective absorption properties of anodic aluminum oxide photonic crystal coatings. *Sol. Energy*, 241, 592–600. https://doi.org/10.1016/j.solener.2022.06.041

10 Roslyakov I.V., Kolesnik I.V., Evdokimov P.V., Skryabina O.V., Garshev A.V., Mironov S.M., Stolyarov V.S., Baranchikov A.E., Napolskii K.S. (2021) Microhotplate catalytic sensors based on porous anodic alumina: operando study of methane response hysteresis. *Sensor. Actuator. B Chem*., 330, 129307. https://doi.org/10.1016/j.snb.2020.129307

11 Pan M., Cooper C., Lin Y.S., Meng G.Y. (1999) CVD modification and vapor/gas separation properties of nanoporous alumina membranes. *J. Membr. Sci*., 158, 235–241. https://doi.org/10.1016/S0376-7388(99)00016-2

12 Wang X., Wang J., Jiang Z., Tao D., Zhang X., Wang C. (2021) Silver loaded anodic aluminum oxide dual-bandgap heterostructure photonic crystals and their application for surface enhanced Raman scattering. *Appl. Surf. Sci*., 544, 148881. https://doi.org/10.1016/j.apsusc.2020.148881

13 Shi L., Jia F., Wang L., Jalalah M., Al-Assiri M.S., Gao T., Harraz F.A., Li G. (2021) Fabrication of an artificial ionic gate inspired by mercury-resistant bacteria for simple and sensitive detection of mercury ion. *Sensor. Actuator. B Chem.*, 326, 128976. https://doi.org/10.1016/j.snb.2020.128976

14 Zhang X., Zhang J., Han X., Wang S., Hao L., Zhang C., Fan Y., Zhao J., Jiang R., Ren L. (2023) A photothermal therapy enhanced mechano-bactericidal hybrid nanostructured surface. *J. Colloid Interface Sci*., 645, 380–390. https://doi.org/10.1016/j.jcis.2023.04.148

15 Thao D.T.V., Weng W.T., Hieu N.V., Chang C.C., Wang G.J. (2022) A flexible and stretchable photonic crystal film with sensitive structural color-changing properties for spoiled milk detection. *Food Chem. X*, 16, 100526. https://doi.org/10.1016/j.fochx.2022.100526

16 Ruiz-Clavijo A., Caballero-Calero O., Martin-Gonzalez M. (2021) Revisiting anodic alumina templates: from fabrication to applications. *Nanoscale*, 13, 2227–2265. https://doi.org/10.1039/D0NR07582E

17 Wangkasem P., Rojananan S. (2015) Mechanical and Electrical Properties of Aluminium Alloy by Cryorolling Process. *The International Journal of Advanced Culture Technology*, 3(1), 46-51. https://doi.org/10.17703/IJACT.2015.3.1.46

18 Liu Y., Wang H.H., Indacochea J.E., Wang M.L. (2011) A colorimetric sensor based on anodized aluminum oxide (AAO) substrate for the detection of nitroaromatics. *Sensors and Actuators B: Chemical*, 160(1), 1149-1158. https://doi.org/10.1016/j.snb.2011.09.040

19 Hierro-Rodriguez A., Rocha-Rodrigues P., Valdés-Bango F., Alameda J.M., Jorge P.A.S., Santos J.L., Araujo J.P., Teixeira J.M., Guerreiro A. (2015) On the anodic aluminium oxide refractive index of nanoporous templates. *Journal of Physics D: Applied Physics*, 48(45), 455105. https://doi.org/ 10.1088/0022-3727/48/45/455105.

20 Koushki E., Mousavi S.H., Jafari Mohammadi S.A., Majles Ara M.H., Oliveira P.W. (2015) Optical properties of aluminum oxide thin films and colloidal nanostructures. *Thin solid films*, 592, 81-87. https://doi.org/10.1016/j.tsf.2015.09.003

21 Seredin P.V., Lenshin A.S., Kashkarov V.M., Lukin A.N., Arsentiev I.N., Bondarev A.D., Tarasov I.S. (2015) Ultrathin nano-sized Al_2O_3 strips on the surface of por-Si. *Materials Science in Semiconductor Processing*, 39, 551-558. https://doi.org/10.1016/j.mssp.2015.05.067

AUTHORS' INFORMATION

Zhangbyrbay, Yerkesh Rashitkyzy – PhD student, E.A. Buketov Karaganda University, Karaganda, Kazakhstan; https://orcid.org/0009-0000-8491-8078; erkesh_zhan@mail.ru

Aimukhanov, Aitbek Kalievich – Candidate of Phys. and Math. Sciences, Professor, E.A. Buketov Karaganda University, Karaganda, Kazakhstan; Scopus Author ID: 5849300870; https://orcid.org/0000-0002-4384-5164, a_k_aitbek@mail.ru.

Zeinidenov, Assylbek Kalkenovich – PhD, Professor, E.A. Buketov Karaganda University, Karaganda, Kazakhstan; Scopus Author ID: 56386144000; https://orcid.org/0000-0001-9232-8406, asyl-zeinidenov@mail.ru.

Gadirov, Ruslan Magomedtakhirovich – Candidate of Chemical Sciences, Associate Professor, Tomsk State University of Control Systems and Radioelectronics, Tomsk, Russia; https://orcid.org/0000-0003-3953-3384; grm882@yandex.ru

Abeuov, Dosmukhammed Rashituly – Master student, E.A. Buketov Karaganda University, Karaganda, Kazakhstan; https://orcid.org/0009-0003-1434-6328; dsk-02@mail.ru

Zhakanova, Akerke Meirmkhanovna – Master (Eng), Junior Research Fellow, E.A. Buketov Karaganda University, Karaganda, Kazakhstan; https://orcid.org/0000-0002-3863-2682; zhakanova0@mail.ru

EURASIAN PHYSICAL TECHNICAL JOURNAL
2025, Volume 22, No.1 (51)
https://doi.org/10.31489/2025N1/44-51

Received: 14/10/2024 Revised: 04/02/2025 Accepted: 18/03/2025

Original Research Article

UDC: 535.24.022; 621.383.51; 621.565.45

STUDY OF THE EFFICIENCY OF PHOTOTHERMAL DEVICES OF DIFFERENT CAPACITIES WITH A NEW TYPE OF COOLING SYSTEM DESIGNED FOR DRY CLIMATES WITHOUT WATER

Tursunov M.N.[1], Sabirov Kh.[1], Alikulov R.B.[1], Kholov U.[2], Eshmatov M.[3]

[1] Physical-Technical Institute named after S. Azimov, Academy of Sciences of the Republic of Uzbekistan, Tashkent, Uzbekistan
[2] Karshi State Technical University, Karshi city, Uzbekistan
[3] Turan University, Uzbekistan, Karshi city, Uzbekistan
***Corresponding author**: muhammadtursunov1947@gmail.com

Abstract. *The article studies the efficiency of photovoltaic thermal of different capacities with a new type of cooling system designed for an arid dry climate. There are presented the results obtained on a 1 kW photovoltaic thermal device. To begin with, the article presents the efficiency of photovoltaic thermal based on 60 W and 180 W photovoltaic batteries and the results obtained on a 1 kW photovoltaic thermal. Several factors should be taken into account when using renewable energy sources in extremely dry regions of our republic including extremely high temperatures. At such high temperatures (40℃ and above in the shade) the efficiency of photovoltaic batteries decreases, some of the energy we need is lost. In order to decrease these losses, it is important that water is not constantly needed to cool the photovoltaic thermal. The new type of cooling system that we offer has no analogues in the world. In further scientific research, the goal is to further improve new type of cooling system and transfer it to work in an autonomous manner.*

Keywords: photovoltaic thermal device, new type of cooling system, collector, reflector.

1. Introduction

Modern industrial-scale monocrystalline and polycrystalline silicon solar cells have a flat construction and an absorption coefficient of 95 %, while their efficiency factor ranges between 18 and 20 %. In solar cells, about 80 % of the absorbed radiation energy is primarily spent on heating the element, which negatively affects its performance. When solar cells are placed on the surface of a heat collector absorber and ideal heat exchange is achieved, the overall efficiency of the system increases significantly [1].

Scientists at the Institute of Physics and Technology are conducting a series of scientific studies to improve the efficiency of photovoltaic-thermal (PV/T) batteries. In particular, the efficiency of photovoltaic-thermal (PV/T) batteries is being investigated using thermal collectors. For arid and water-scarce climates, an efficient, low-power, autonomous, and portable photothermal system helps supply rural households with the necessary electrical energy and partial hot water, reducing economic costs. The implementation of this system relies on a newly developed heat collector-integrated photo-thermal, a radiator, a pump, a water storage tank, a controller, an inverter, and a mobile supporting structure [2].

In the newly developed cooling system, water is used as the working fluid for cooling PV/Ts, and experimental studies are conducted to analyze the results. It is determined that the PV/Ts we developed produced 50–60 % more power than conventional photovoltaic panels [3]. In this study, a new cooling system has been introduced, utilizing water as the working fluid to improve the efficiency of PV/Ts.

PV/Ts systems generate both electrical and thermal energy simultaneously, increasing overall efficiency while minimizing environmental impact [4–6]. In arid and water-scarce climates, researchers are addressing cooling challenges by exploring heat transfer fluids with significantly improved thermal conductivity [7–10]. Advanced materials such as nanofluids are widely used by researchers worldwide to enhance heat transfer rates and improve the efficiency of photovoltaic systems, including PV/Ts [11–14]. Innovative designs of thermal collectors optimize heat dissipation from photovoltaic cells, which is crucial to preventing overheating and reducing efficiency losses.

2. Materials and methods.

The methods of cooling PV/Ts are very diverse, and many scientists are conducting research in this direction. Some studies have found that PV/Ts cannot be used in extremely dry areas, and a constant amount of water is needed to cool the PV/Ts. Considering these shortcomings, the PV/T with new type of cooling system (NTCS) has been created. The photovoltaic thermal device (PV/TBD) with NTCS is designed for use in extremely dry areas without water, self-cooling and providing electricity and hot water without of efficiency. The parts that make up the PV/TBD with NTCS perform the following tasks.

- a new type of heat collector ensures reduction of energy losses of the photo-thermal;
- the radiator serves to cool the hot water collected in the heat collector;
- the fan is installed above the radiator and serves to increase the efficiency of the radiator with the help of wind;
- the pump passes the heated water through the radiator in the new type of collector, and ensures that the cooled water enters the collector and circulates the water;
- the water tank is used for storing hot water and for good operation of the pump;
- mobile construction.

Placing and switching together the radiator, fan, pump, water storage tank, controller and inverter in the PV/T, and ensuring that the portable structure performs the function of mechanical protection when moving them from one place to another.

The new type of PV/T cooling system is based on the principle of the cooling system of internal combustion engines, and cooling is provided by the circulation of water through the radiator. The heat accumulated in the rear part of the PV/T is transferred to the water in the collector, and the heated water is transferred to the cooling radiator using a pump. This process continues continuously. And the liquid that has passed through the cooling radiator is returned to the collector. A fan is installed on it for better cooling of the liquid that has passed through the cooling radiator. The pump and fan in the cooling system of this device are low-power and do not negatively affect the energy produced by the PV/T.

Figures 1 and 2 show the front and rear views of the PV/TBD made on the basis of a 60 W PV. Figure 2 shows the components of PV/TBD: 1) photothermal, 2) accumulator battery, 3) inverter, 4) controller.

Fig.1. Fig. 1. Front view of the device with PV/T.

Fig.2. Rear view of the device with PV/T.

Table 1 shows the characteristics of photovoltaic cells with different capacities and the equipment of the new type of cooling system.

Figures 3 and 4 show the front and rear views of the PV/TBD made on the basis of the 180W PV. Figure 4 shows the components of PV/TBD with a new type of cooling system: 1) controller, 2) amperemeter, 3) inverter, 4) radiator, 5) fan, 6) Accumulator battery, 7) reserve water storage (capacity 20 liters), 8) pump, 9) Electronic thermometer 10) switch.

Table 1. Physical and technical characteristics of different power photothermal devices with a new type of cooling system.

Name	PV/T 1	PV/T 2	PV/T 3
Maximum power of PV, $П_{max}$	60 W, 1 pc.	180 W, 1 pc.	350 W, 2 pc.
Efficiency factor of PV, η	19.9%	19.9%	19.9%
The operating voltage of the PV, $У_{oc}$	21,6 V	22.80 V	22,3
Short circuit current of PV, $И_{sc}$	3.53 A	10.34A	8.6 A
Fill factor of the VAC of PV, *ff*	0,71-0,73	0,71-0,73	0,71-0,73
Reflection coefficient of the reflector R, size in cm, pieces.	05, width 67, height 54, 2 pc.	0,5 , width 145, height 60, 2 pc.	0,5 , width 180, height 80, 2 pc.
Water capacity of the polycarbonate heat collector	3 l	10 l	7x2=14 l
The radiator is made of which material, size in sm	Aluminium, width 15, height 15	Aluminium, width 30, height 60	Aluminium, width 30, height 60, 2 pc.
Fan power W, pc.	3,6 , 1 pc.	3,6 , 5 pc.	3,6 , 12 pc.
Pump power, W	5	5	60
BB, A/h	20, 1 pc.	65, 1 pc.	200, 2 pc.
Inverter, W	300,	300	3000
Controller, A	10	20	-

Fig. 3. Front view of the new type of PV/TBD.

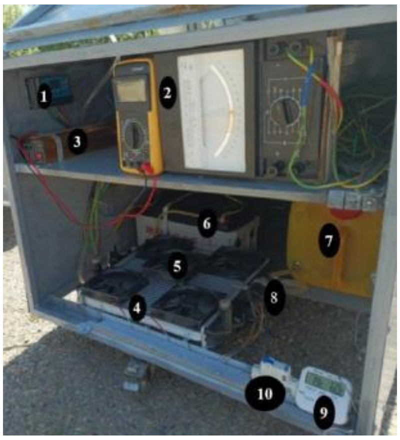

Fig. 4. Rear view of the new type of PV/TBD.

Figures 5 and 6 show the external view of a large capacity PV/TBD with a new type of cooling system. A large-capacity PV/TBD with a new type of cooling system was created to meet the needs of rural residents for electricity and hot water.

Fig. 5. Front view of a 1kW PV/TBD with a new type of cooling system.

Fig. 6. Rear view of a 1kW PV/TBD with a new type of cooling system.

3. Results and analysis

This paper presents the power efficiency of PV/TBDs with NTCS based on 60 W and 180 W PVs. These results were obtained in May and June, respectively. On September 7, 2024, experimental tests were carried out at the high-power PV/TBD with NTCS at the Helio polygon of the Institute of Physics and Technology. Figure 7 shows the time variation of the power values of 60 W PV based on PV/T. The black line of PV1 is the maximum power that the 60 W PV can deliver. The PV/T red line is the power results obtained on a typical 60 W PV. It can be seen from Figures 7 and 8 that due to external influences, PV cannot reach the values indicated in the nominal data. The PV/T blue line shows the power values of a PV/T based on a 60 W PV with NTCS. Reflectors are installed on the side of the PV/T, aiming to increase the solar radiation flux density. Since the short-circuit current (SCC) is directly proportional to the solar radiation current density (SRCD), the SCC of the PV/T is increased [15]. At 10:20, two reflectors were installed on the sides of the PV/T and the NTCS was launched. As a result, the power of the PV/T increased from 46 W to 69 W, as shown in Figure 7. When the solar radiation current density (SRCD) reaches its maximum value, the power of the PV/T reaches 84 W.

The power values of PV/T are always below the PV1 line, that is, they never reach the maximum value. 60 W and 180 W PV-based PV/Ts require 9.6 W and 24 W of additional power to power the NTCS for cooling, respectively. It was mentioned above that the additional useful power provided by PV/T is 2-3 times greater than these powers. Figure 8 shows the time variation of power values of PV/T and PV. It can be seen from Figure 8 that the power values of PV are below the black line of PV1, that is, they have reached values smaller than the maximum power of PV. To increase the efficiency, it is necessary to increase the SCC with the help of reflectors to the PV/T, to prevent a sharp decrease in the operating voltage (OV) with the help of NTCS. Figure 8 shows that the power of PV/T reaches values greater than the maximum power of PV. Solar radiation is absorbed in the surface area of the solar cell. The greater the amount of Sunlight absorbed, that is, in the broad wavelength range of radiation, the greater the efficiency of the element [16-17]. The SCC increase of PV/T using reflectors is shown in Fig. 9. The increase of SRCD through the reflectors also causes an increase in heat in the rear part of the PV/T.

A sharp increase in SRCD leads to an increase in temperature in the back of the PV/T. This causes a decrease in OV, because the parameter most dependent on temperature change is OV. This phenomenon is explained as follows. A solar cell (SC) based on crystalline silicon decreases OV by 0.002 V (0.4 %/degree) at a temperature of 1 degree above 25^{o} C (certification AM 1 reference temperature). Heating of SC on an open sunny day (in the summer months) can reduce OV by 0.07 - 0.09 V. This is the main reason why SC has reduced the efficiency factor (EF). The temperature reduction of the voltage obtained from the SC has been observed in scientific research [18]. A new type of self-cooling, i.e., a new type of cooling system was used to prevent the reduction of the OV of the PV/T. Figure 10 shows the increase in OV of PV/T.

Figures 9 and 10 show the change of PV/T SCC and OV over time. Results started at 10:00 a.m. At 12:00, reflectors were installed on the side of the PV/T. Figure 9 shows that the value of SCC has been increased from 15 A to 22 A. Through reflectors, the SCC has been increased to 50%. Figure 10 shows the decrease of

PV/T OV under the influence of heat. OV values of PV/T have been increased since 12:00 when the new type of cooling system was put into operation. PV/T's OV was 44 V at 11:40 a.m., and 46.5 V at 12:00 p.m. when the new cooling system was put into operation.

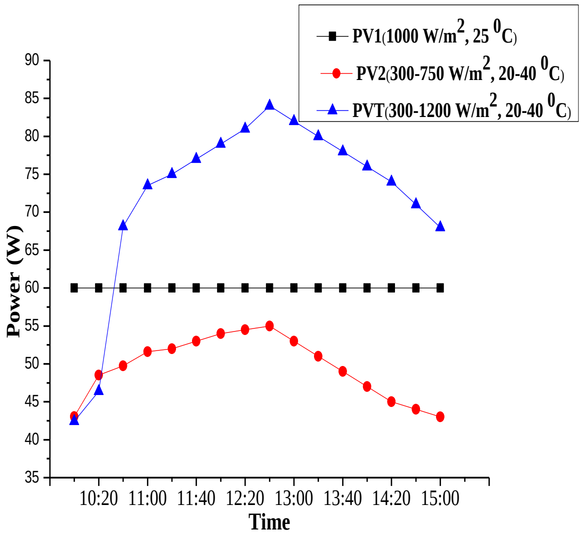

Fig. 7. Power values of 60 W PV based on PV/T with NTCS and 60 W PVB depending on time.

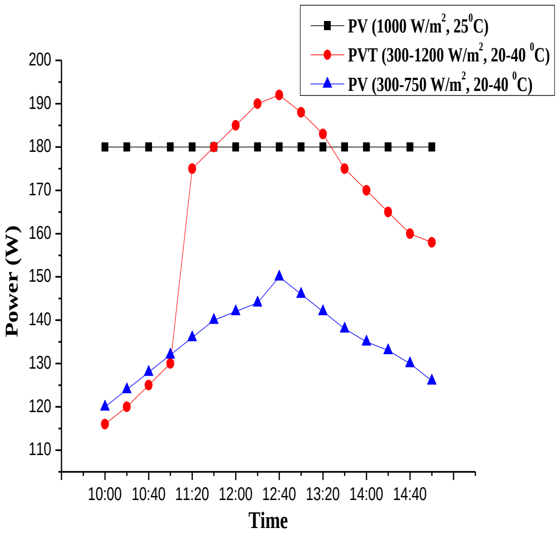

Fig. 8. Power values of 180 W PV based on PV/T with NTCS and 180 W PVB depending on time.

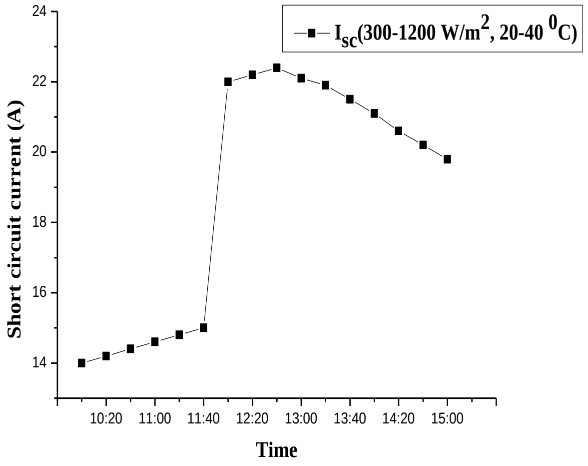

Fig. 9. Time variation of PV/T TB SCC per 1 kW power.

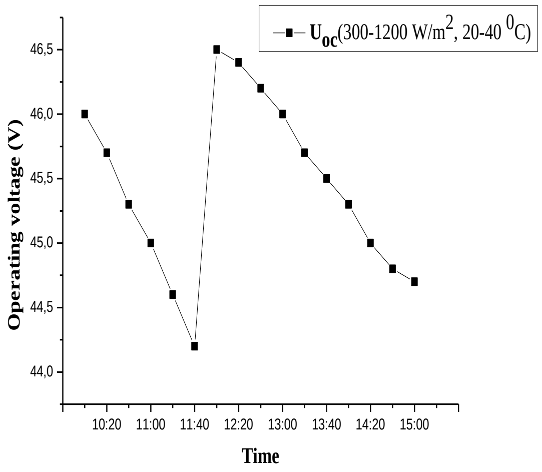

Fig. 10. Time variation of PV/T OV per 1 kW power.

Figure 11 compares the power values of PV/T with the maximum values of PV. Figure 11 shows that the power of PV/T is greater than the maximum power of PV up to 152 W. 100 W of additional energy is required to power the new type of cooling system. Our proposed PV/TBD provides additional useful energy along with providing energy to NTCS. Since the results are received in September, the efficiency of PV/T is slightly less. Because in Based on this, in the summer months, the efficiency of PV/Ts with large capacity NTCS reaches even greater values. The decrease in SRCD is shown in Figure 12. this month, SRCD is slightly lower than in the summer months.

Figure 12 shows the values of SRCD. At 11:40 a.m. SRCD was increased by reflectors to PV/T. That is, up to 30% increase in radiation has been achieved. But these increased values were smaller than AM 1.

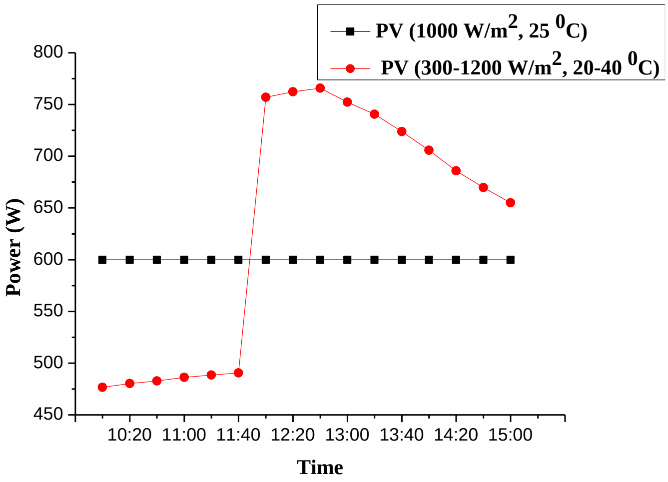

Fig. 11. Time variation of PTB power values with NTCS providing power up to 1 kW.

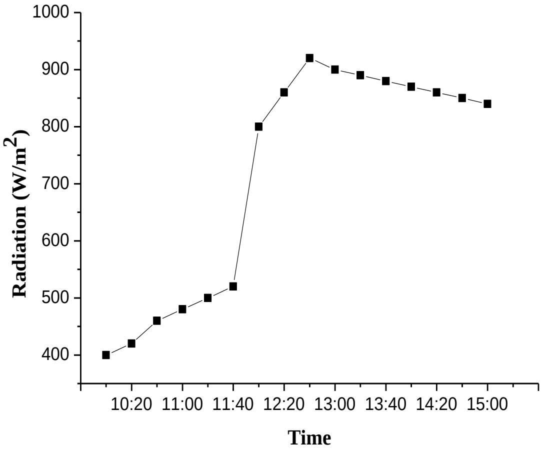

Fig. 12. Time variation of the value of SRCD.

4. Conclusion

In this research work, it was found that the efficiency of PV/TBDs with NTCS based on 60 W and 180W PV was increased to 50% and 30%, respectively. And a new type of cooling system was tested to improve the efficiency of high-power PV/Ts. The experiments showed that the SCC of PV/T was up to 50%, and a sharp decrease in the values of OV was prevented. With a large-capacity new type cooling system, PV/TBD can provide electricity and hot water for rural residents and extremely dry areas. The PV/TBD we offer provides power to water pumps and similar equipment. This device can be used to get up to 100 l of hot water for household needs of villagers. In further scientific research, it was aimed to develop new, more convenient and more efficient versions of PV/TBDs with a new type of cooling system with a large capacity.

The power consumption of the water pump and fan in the new PV/T cooling system is 5 W and 0.36 W, respectively. Under natural conditions, a 60 W PV generates 40–50 W, while a 180 W PV produces 110–140 W. In contrast, PV/Ts with the same power ratings generate 70–80 W and 170–190 W, respectively. Thus, the useful energy output of PV/Ts is several times greater than the energy consumed by the new cooling system. Further scientific research aims to evaluate the efficiency of the cooling system's working fluid by testing nanofluids alongside water.

Conflict of interest statement

The authors declare that they have no conflict of interest in relation to this research, whether financial, personal, authorship or otherwise, that could affect the research and its results presented in this paper.

CRediT author statement
Tursunov M.N.: Conceptualization, Methodology, Validation, Writing - Original Draft; **Sabirov Kh.:** Conceptualization, Methodology, Data Curation, Investigation, Writing – Review & Editing; **Alikulov R.B.**: Methodology, Software, Investigation, Writing - Original Draft; **Kholov U.R.**: Data Curation, Visualization; **Eshmatov M.M.**: Formal analysis, Funding acquisition, Writing-Review & Editing. The final manuscript was read and approved by all authors.

References

1 Murodov M.Kh., Murodov R.N., Abduraimov R. (2000) Solar energy device is a thermophotoelectric device combining social energy. *Economy and Economics*. 6(97), 2, 163 - 164. Heat Island Group Home Page. Lawrence Berkeley National Laboratory. https://cyberleninka.ru/article/n/quyosh-energetik-qurilmasi-samaradorligini-oshirish-uchun-kombinatsiyalashgan-termofotoelektrik-qurilma. [in Uzbek]

2 Tursunov M., Sabirov Kh., Alikulov R., Kholov U., Shohimardonov J., Eshmatov M. (2024) Testing the Energy Efficiency of a New Type of Photothermal Device in Dry Climate Conditions. *Proceedings of Intern. Conf. on Applied Innovation in IT*, 12 (2), 139 – 144. https://doi.org/10.25673/118126

3 Tursunov M.N.,. Sobirov H., Alikulov R.B. (2024) Testing of new generation photothermal batteries that work effectively in dry climate conditions in the summer months. *Newsletter of Young Scientists*, 3, 37 – 41.. https://cyberleninka.ru/article/n/suvsiz-ekstremal-iqlim-sharoiti-uchun-yuqori-samarali-o-zini-sovutadigan-fotoissiqlik-batareyani-sinovdan-o-tkazish

4 Hussein A. Kazem, Ali H.A. Al-Waeli, Miqdam T. Chaichan, Karrar H. Al-Waeli, Anwer Basim Al-Aasam, K Sopian (2020) Evaluation and comparison of different flow configurations PVT systems in Oman: A numerical and experimental investigation. *Solar Energy*, 208, 58 – 88. https://doi.org/10.1016/j.solener.2020.07.078.

5 Joshi Sandeep S., Dhoble Ashwinkumar S. (2018) Photovoltaic-thermal systems (PV/T): technology review and future trends. *Renew. Sustain. Energy Rev*., 92, 848 – 882. https://doi.org/10.1016/j.rser.2018.04.067

6 Maseer M.M., Firas Basim I., Hannun Rafid M., Lim Chin W., Kumail A.H.A., Salim O.M. (2022) A review of the characters of nanofluids used in the cooling of a photovoltaic -thermal collector. *Mater. Today: Proc*., 57, 329 – 336. https://doi.org/10.1016/j.matpr.2021.09.214

7 Maseer Muayad M., Firas B.I., Kazem H.A., Dhafer M.H., Kumail Abdulkareem H.A., Chaichan Miqdam T. (2024) Performance enhancement of photovoltaic/thermal collector semicircle absorber tubes using nanofluid and NPCM. *Renewable Energy*, 233, 121152. https://doi.org/10.1016/j.renene.2024.121152

8 Mohammadreza M., Akbar Abbasian A.A. (2024) Experimental evaluation of photovoltaic thermal (PV/T) system using a modular heat collector with flat back shape fins, pipe, nanofluids and phase change material. *Solar Energy Materials and Solar Cells*, 280, 113294. https://doi.org/10.1016/j.solmat.2024.113294

9 Thamir A., Hakim S., Aljibori S., Jasim M., Mahdi. D. (2024) Optimization and performance evaluation of a photovoltaic/thermal collector with porous twisted tape inserts: A comprehensive energy and exergy analysis, International *Communications in Heat and Mass Transfer*, 159 (B), 108104. https://doi.org/10.1016/j.icheatmasstransfer.2024.108104

10 Zainab M.M., Ali N.A.Sh., Ahmed M., Hazim A., Raed R., Sopian K., Alahmer A. (2024) Enhancing photovoltaic thermal (PV/T) performance with hybrid solar collector using phase change material, porous media, and nanofluid. *Solar Energy*, 283. 112983. https://doi.org/10.1016/j.solener.2024.112983

11 Al-Aasam Anwer B., Ibrahim A., Sopian K., Bassam Abdulsahib M., Dayer M. (2023) Enhancing the performance of photovoltaic thermal solar collectors using twisted absorber tubes and nanofluids with optimal design parameters. *Int. J. Renew. Energy Resour*., 13 (3), 1277 – 1284. https://doi.org/10.20508/ijrer.v13i3.14163.g8799

12 Al-Waeli Ali H.A., Hussein A. Kazem H.A., Jabar H. Yousif J.H., Miqdam T.M.T., Sopian K. (2020) Mathematical and neural network modeling for predicting and analyzing of nanofluid-nano PCM photovoltaic thermal systems performance. *Renew. Energy*, 145, 963 – 980. https://doi.org/10.1016/j.renene.2019.06.099n

13 Sofiah A.G.N., Rajamony R.K., Samykano M., Pandey A.K., Pasupuleti J., Sulaiman N.F. (2024) Assessment on thermophysical properties of nano enhanced heat transfer fluid with hexagonal boron nitride nanoparticles for thermal management of photovoltaic thermal (PV/T) system. *Process Saf. Environ. Prot*., 189, 1087 – 1102. https://doi.org/10.1016/j.psep.2024.06.097

14 Muminov R. A., Tursunov M. N., Sabirov X., Eshmatov M. M., Xolov U. R. (2023) Comparison of the Efficiency of Autonomous Water Release Systems Based on Photovoltaic and Photothermal Batteries. *Applied Solar Energy*, 59 (3), 305 – 310. https://doi.org/10.3103/S0003701X2360100X

15 Khamrayev O. (2022) Sources of energy for solar photovoltaic power plants. *Education News: Research in the 21st Century*, 1(4), 60–64. Available at: https://nauchniyimpuls.ru/index.php/noiv/article/view/1283 [in Russian]

16 Abilfayziyev Sh.N., Yuldoshov B.A., Abilfayziev Sh.N. (2022) Testing of different material type photoelectric and photothermal batteries composed. *Eurasian Physical Technical Journal*, 19(4), 44–50. https://doi.org/0.31489/2022No4/44-50

17 Jurayev I., Yuldoshev I., Jurayeva Z. (2023) Effects of Temperature on the Efficiency of Photovoltaic Modulesю *Proceedings of International Conference on Applied Innovation in IT*, 11 (1), 199 – 206. https://doi.org/10.25673/101938

18 Elbreki A.M., Sopian K., Fazlizan A., Ibrahim A. (2020) An innovative technique of passive cooling PV module using lapping fins and planner reflector. *Case Studies in Thermal Engineering*, 19. 100607. https://doi.org/10.1016/j.csite.2020.100607

AUTHORS' INFORMATION

Tursunov, Muhammadjon – DSc., Chief scientist, Physical-Technical Institute, Tashkent, Uzbekistan; Scopus Author ID: 6701492181; https://orcid.org/0000-0002-7559-8479; muhammadtursunov1947@gmail.com

Sabirov, Habibullo – PhD, Professor, Chief scientist, Physical-Technical Institute, Tashkent, Uzbekistan; https://orcid.org/0009-0004-5325-6015; sabirovhabibullo1954@gmail.com

Alikulov, Ramazon - Doctoral Student, Physical-Technical Institute, Tashkent, Uzbekistan; https://orcid.org/0009-0000-8237-9461; ramazonalikulov209@gmail.com

Kholov, Uygun - PhD, Head of laboratory, Karshi State Technical University, Karshi, Uzbekistan, https://orcid.org/0000-0002-6675-5479, uygunshams@mail.ru

Eshmatov, Mansur - PhD, Senior researcher, Turan University, Karshi, Uzbekistan, https://orcid.org/0009-0004-1097-8579; meshmatov2811@mail.ru

EURASIAN PHYSICAL TECHNICAL JOURNAL

2025, Volume 22, No. 1 (51)

https://doi.org/10.31489/2025N1/52-58

Received: 30/10/2024 Revised: 06/02/2024 Accepted: 18/03/2025 Published online: 31/03/2025
Original Research Article

UDC 536.722

THE EFFICIENCY DEPENDANCE OF A SINGLE-CIRCUIT POWER UNIT WITH A HELIUM-COOLED REACTOR AND A HYDROGEN MODULE ON THE DEGREE OF REGENERATION

Nurym K.A.[1], Antonova A.M.[2], Sakipov K.E.[1]*, Vorobyev A.V.[2], Stetsov N.V.[2]

[1] L.N. Gumilyov Eurasian National University, Astana, Kazakhstan
[2] Tomsk Polytechnic University, Tomsk, Russia
***Corresponding author**: sakamer2100@gmail.com

Abstract. *The most attractive single-circuit scheme of the power unit was chosen. Helium at the outlet of the reactor core enters the steam generator, where it gives part of the heat to generate highly superheated steam for the electrolysis plant. Next, helium operates in a closed gas turbine cycle with heat recovery. A gas-cooled reactor with a turbine and compressor allows the use of a thermodynamic cycle with high efficiency. A series of design calculations of the regenerator for various degrees of regeneration have been performed. A series of assessments of the effect on the real resistance of the regenerator from the high- and low-pressure sides have been carried out. The thermal scheme of energy production is calculated in accordance with a series of design calculations of the regenerator.*

Keywords: reactor, helium, gas-turbine installation, regenerator, hydraulic resistance, aerodynamics resistance.

1. Introduction

In recent years, there has been a significant development in gas turbine construction worldwide, in particular, the expansion of their application areas, an increase in energy efficiency parameters, and the improvement of units and circuits in order to increase efficiency and take into account compliance with environmental requirements [1 - 4]. Studies have been conducted that include coupling a high-temperature gas-cooled nuclear reactor with a closed-cycle helium gas turbine energy conversion system [1]. In [2] the accumulated experience from the operation of helium gas turbine units and associated test facilities is considered in order to determine the conditions and factors for more efficient and safe operation. It has been established that a helium turbine with liquid characteristics allows operation between normal temperatures of the exhaust gas of the upper turbine and temperatures of liquid hydrogen [3]. The results of a study of coupling a high-temperature gas-cooled nuclear reactor with solid oxide electrolyzers for large-scale hydrogen production are shown in [4]. The combined system can achieve sufficiently high efficiency values.

A single-circuit power unit with a helium-cooled reactor and a hydrogen module is being created on the basis of a closed gas turbine unit (GTU), in which the use of regeneration is a necessary condition for achieving a sufficiently high efficiency. The temperature of the exhaust gases after the turbine is high and when working on a simple Brighton cycle, a large amount of heat is released into the environment. In a regenerative cycle, part of the heat can be returned to the cycle by transferring it from the helium spent in the turbine to the helium compressed in the compressor before it enters the nuclear reactor. The degree of regeneration (σ) can vary in a certain range, the value of which is determined by the values of the helium temperature at the outlet of the turbine and at the outlet of the compressor, which, in turn, depend on the degree of pressure increase in the compressor. According to [5] "there are 2 types of GTU regenerator designs: plate and tubular. Regenerator heat exchangers must meet the following requirements: be compact and durable enough to be used in cycles with a high degree of compression, have a high coefficient of heat transfer on the gas side, ease of manufacture, and low cost of these heat exchangers. Tubular heating surfaces have been most fully studied and presented, the advantages of which include: the possibility of use at high pressures, simpler layout, reliability, ease of manufacture and maintenance. Tubular regenerators have tube boards, housings, and other parts that sometimes exceed the weight of the active part of the heating surface in terms of their weight and dimensions. Reducing the diameter of the tubes, which is a significant factor affecting the reduction of the dimensions of the heat exchanger, is possible only up to the known practically permissible limits. In order to increase the efficiency of tubular heating surfaces, transverse and longitudinal fins are used [6 – 13].

The purpose of this study is to determine the maximum efficiency of the heat exchange process of the unit, taking into account the degree of regeneration and the hydrodynamic characteristics of the regenerator. In this case, preference is given to the design of a tubular counter-current heat exchanger with transverse finning of heat exchange pipes, due to the widespread use of these devices, compactness and ease of maintenance.

2. Main part

2.1 Theoretical approach

In the considered single-circuit installation, the working fluid of the GTU and the coolant of the reactor is helium, which operates in a closed gas turbine cycle with heat regeneration (Fig. 1). The regenerator is a helium-helium countercurrent tubular heat exchanger, the blocks designations in it are shown in Fig. 1. Part of the heat obtained in the reactor core; helium is given in the steam generator to generate highly superheated steam for the electrolysis installation of the hydrogen module. The supply and removal of heat in the apparatus (reactor, steam generator, regenerator, cooler) occurs in isobaric processes with some pressure losses; the processes of expansion and compression of helium in the turbine and compressor are adiabatic in nature.

To study the parameters of the installation in a wide range of changes in the initial parameters, the method of calculating the thermal circuit of the GTU was used, implemented in the form of a model and a program in the Excel and COOLPROP spreadsheet package. The model is based on the equations of energy balances and patterns of adiabatic processes of expansion and compression of helium gas using relative internal efficiencies to account for non-isotropy in real processes. The reliability of the model and calculation method was checked by manual calculations, the calculation error did not exceed 2.5%.

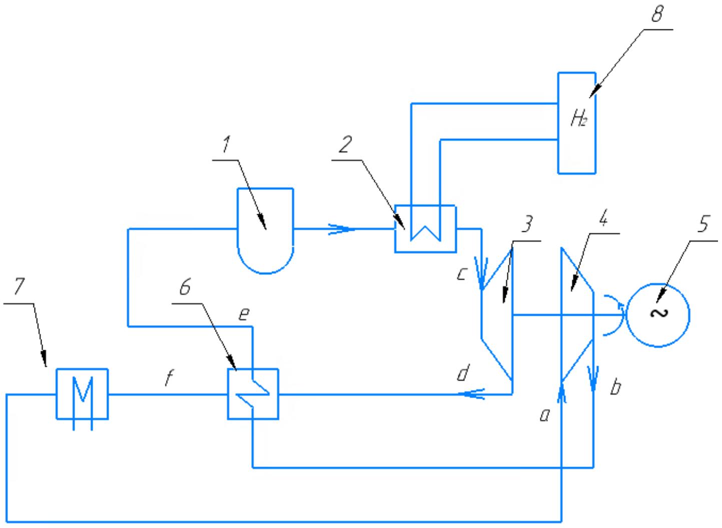

Fig.1. Diagram of a closed nuclear power plant with heat recovery and a hydrogen complex [9]: 1 – reactor, 2 – steam generator, 3 – turbine, 4 – compressor, 5 – generator, 6 – electric generator, 7 – cooler, 8 – electrolyzer.

Regenerator resistance values are calculated for different values of the regeneration degree. Calculation results of the regenerator resistance coefficient on the degree of regeneration are shown on Fig.2. Further, according to the previously used algorithm [6] variant calculations of the thermal circuit were carried out taking into account the increase in regenerator resistance with increasing σ.

As an assumption, it is assumed that when the degree of regeneration changes, only the resistance of the regenerator changes, and the resistance of the other elements (core, steam generator, compressor-gas turbine tract, heat exchanger-cooler, nozzles and pipelines) remain unchanged and can be excluded from consideration. With an increase in the degree of regeneration, the value of the heat transfer surface of the regenerator increases not linearly, but much faster. The deeper the regeneration, the larger the surface is required to transfer heat to the unit. Therefore, the degree of regeneration has a limited value, determined by a technical and economic analysis, which will have to be performed in the future.

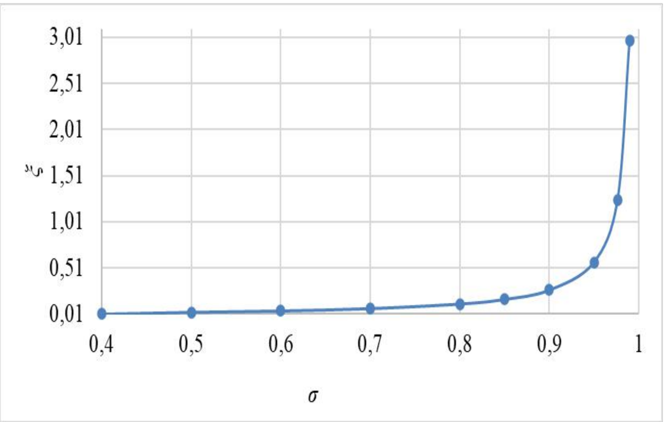

Fig.2. Dependence of the regenerator resistance coefficient on the degree of regeneration *ξ*, *σ*

The paper [10] the results of a calculated assessment of the dependence of the characteristics of a hydrogen complex HTU on changes in the resistance of the regenerator based on its hyperbolic dependence on the degree of regeneration were presented [11]. In this paper, the aim is to establish the effect of the hydraulic resistance of the regenerator on the efficiency of the installation based on the design calculation of the regenerator. For various values of the degree of regeneration, the main characteristics of a shell-and-tube regenerative heat exchanger are calculated, such as the heat transfer coefficient, the heat exchange surface area, the length of heat exchange tubes, the diameter of the pipe board, and hydraulic resistance. There are main parameters in theoretical process are presented in Table 1.

Table 1. GTU's indicators for theoretical process

No.	σ	ξ_{p1}	λ_1	p_c, MPa	*G, kg/s*	H_T, kJ/кg	H_K, kJ/кg	$N_э$, MW	$\Delta\eta$, %	Efficiency
1	0.4	0.01	0.96	69.12	62.96	1315	899	25.16	-24.13	0.210
2	0.5	0.015	0.955	68.76	67.57	1299		26.01	-26.72	0.220
3	0.6	0.0225	0.9475	68.22	72.90	1276		26.43	-30.74	0.238
4	0.7	0.035	0.935	67.32	79.16	1236		25.68	-37.74	0.259
5	0.8	0.06	0.91	65.52	86.586	1154		21.26	-52.63	0.284
6	0.85	0.068	0.90	64.92	90.84	1068		14.77	-68.52	0.297

Note: λ_1 – coefficient of losses along the high-pressure path, p_c – pressure in front of the turbine, G – coolant consumption, H_T – heat transfer on the turbine, H_K – heat transfer on the compressor, $N_э$ – electrical power, $\Delta\eta$ – relative efficiency difference, Efficiency – efficiency coefficient, when determining the values, an algorithm was used in [6].

2.2 Real approach

When designing the device, in order to increase the efficiency of the heat exchange process in gas-gas media, annular finning was used, (Fig. 3). Below schematically shows the transverse and longitudinal sections of the heat exchange tube bundle with characteristics values (diameters, lengths, etc.) that were used in the calculations.

Figure 4 shows a model of the movement of the coolant and working fluid in the regenerator. The heated medium is high-pressure helium in the tubes at a temperature of T_b and the heating medium is hot helium from the turbine at a temperature of T_d ($T_d > T_d$). Exhaust temperatures are indicated by T_f (at the exit from the intertubular space) and T_e (before entering the reactor).

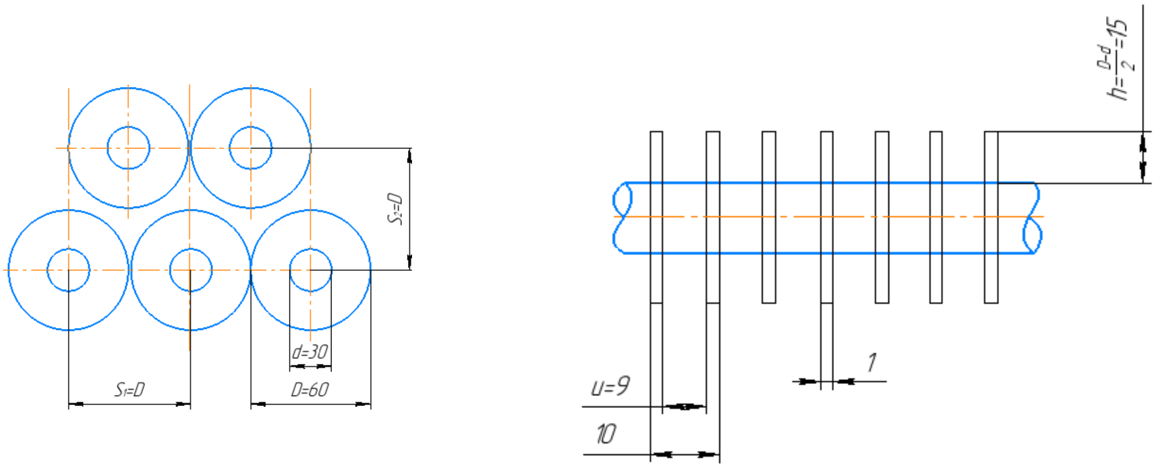

top view side view

Fig.3. Characteristics of the fins of the heat exchange bundle of pipes: S_1, S_2 – the distance between the tube centers; D – diameter of the ribs, U – the distance between adjacent edges, h – edge height

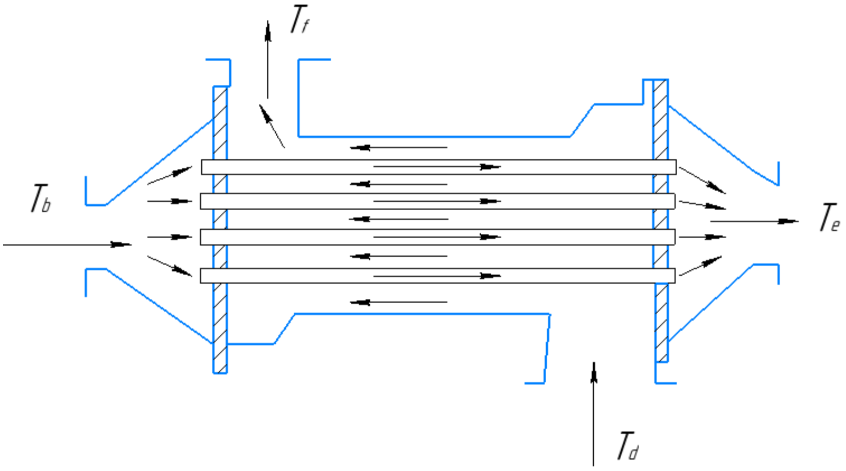

Fig. 4. Model of the movement of the coolant and the working fluid in the regenerator.

Calculations were carried out using Excel spreadsheets and the COOLPROP module for thermophysical parameters of gases. The initial data are assumed to be the same as in [11]: the temperature of helium at the inlet to the gas turbine is 1123 K; the temperature of helium at the outlet of the reactor is 1223 K, at the inlet to the turbine is 1123 K; the pressure of helium at the inlet to the compressor is assumed to be 3.0 MPa; the degree of pressure increase is 2.4. Calculations were carried out for the thermal power of the reactor is equal to 200 MW. Parameters of steam generated for the electrolysis plant of the hydrogen module: pressure 1 MPa, temperature 800°C. The range of changes in the degree of regeneration: from 0.7 to 0.9 in accordance with the results of the work [11]. For clear understanding (red – theory, blue – reality).

Having obtained the values of pressure resistances in design calculations and having constructed the dependence of pressure losses on the degree of regeneration, it is worth noting that the nature of the dependence has been preserved (hyperbolic), which indicates the correctness of the calculations. However, the real resistances turned out to be slightly lower than those accepted in the theoretical approach. Figure 5-7 demonstrate parameters which reflect the real influence of aerodynamic resistance on cycle performance indicators. In the real cycle, the temperature of point *e* is lower due to pressure losses in the tube space of the regenerator. Since the temperature behind the reactor is constant, the ΔT of the reactor increases.

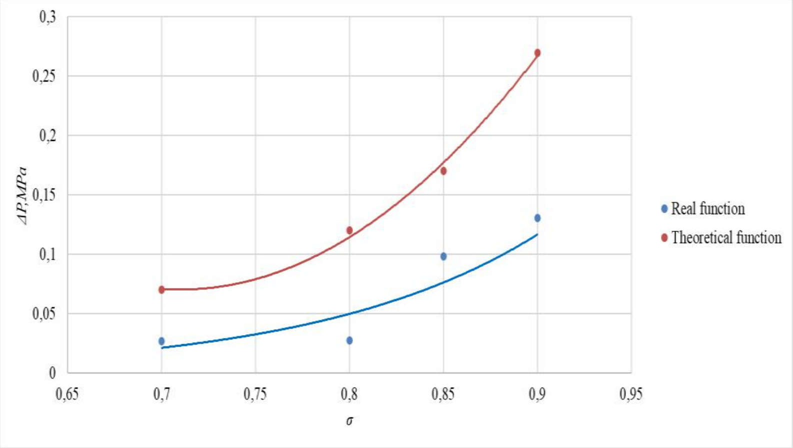

Fig.5. Dependence of the pressure loss value on the degree of regeneration

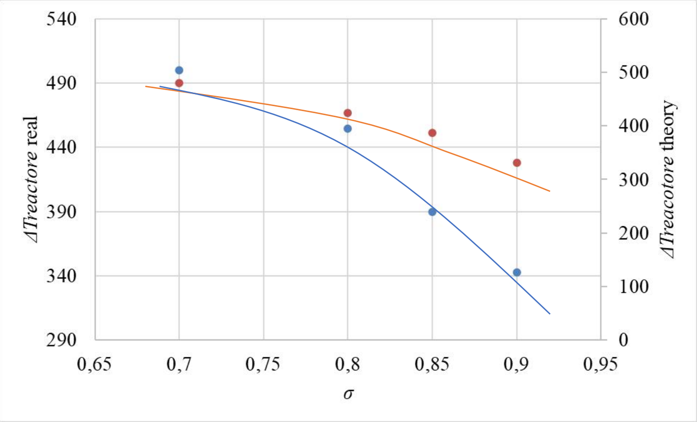

Fig.6. Dependence of helium heating in the reactor on the degree of regeneration

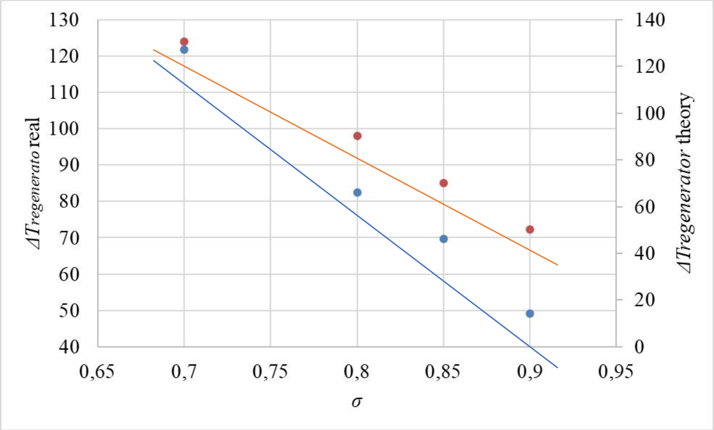

Fig.7. The dependence of the temperature difference on the degree of regeneration

3. Results and discussion

Evaluation the aerodynamic resistance let recalculate main parameters for scheme (Fig. 1). As for the comparison it can be state with certainty that resistance in the theoretical process turned out to be higher, which significantly affected the efficiency of the cycle. This is due to the low resistance along the low-pressure path and low flow rates of heating helium at the inlet to the regenerator. The main results are in table 2 below.

Table 2. GTU's and regenerator indicators for real process

No.	*σ*	*Efficiency, %*	Q_{reg}, MW	*ΔT, K*	*G, kg/s*	*w1, m/s*	*Δp, MPa*	*l, m*	*D, m*	*ε*
1	0.70	28	120	121	77	5	0.02	6.9	4.15	2.4
2	0.80	29	150	82	84	5	0.03	11.7	4.44	3.7
3	0.85	25	168	69	98	5	0.09	18.8	4.63	5.8
4	0.90	17	186	49	112	5	0.13	32.0	4.84	9.3

As for the efficiency (Fig. 9) of the cycle itself, the area of an acceptable degree of regeneration lies in the range from 0,7 to 0,8, since after a value of 0,9 we get superhigh resistance and high speeds, which negatively affects the efficiency of the cycle as a whole. With an optimal degree of regeneration, the consumption reaches a value of 98 kg/s (Fig. 8).

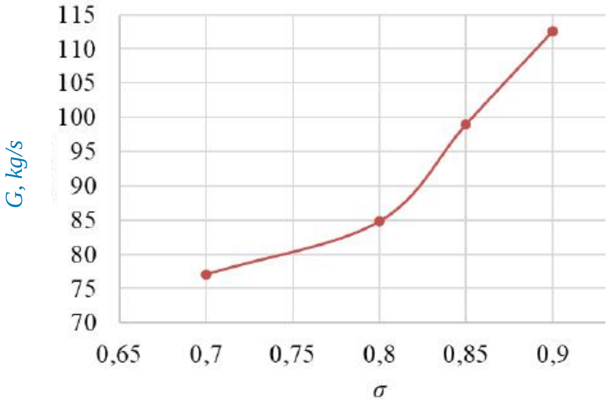

Fig.8. Dependence of the coolant flow rate on the degree of regeneration

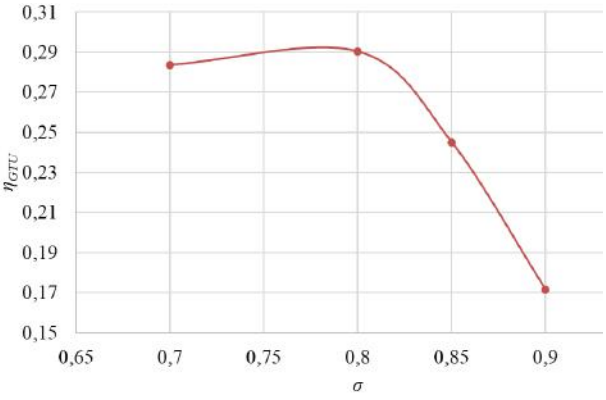

Fig.9. Dependence of the efficiency of the GTU of the real cycle on the degree of regeneration

4. Conclusion

Summing up the work done, it should be noted that the purpose of the study has been achieved. 2 series of design calculations were carried out for the regenerator and the GTU circuit. The highest efficiency turned out to be equal to 29% with a degree of regeneration of 0.8, while the resistance along two pressure paths was 0.03 MPa at a coolant velocity of 5 m/s. As the resistance *ΔP* increases, the heating in the reactor and regenerator decreases, which is associated with a deterioration in the heat exchange process due to energy losses to overcome the resistance. The efficiency of the unit has a maximum with a degree of regeneration of 0.9 – which is the boundary value. With higher degrees of regeneration, we have large dimensions of the regenerator and high resistance values, which negatively affects the investment and efficiency of the device. The decisions made in the development of the power unit are justified: the parameter level is the temperature of the coolant T_e=530^{0}C, T_p=950^{0}C and the working fluid T_c=850^{0}C, p_c=6.81 MPa, taking into account the process of high-temperature electrolysis T_p=800^{0}C. The optimal controlled parameters of the thermal circuit have been established: ε=2.4 (degree of pressure increase in the compressor), σ=0.8–0.9 (degree of regeneration). An analysis of the effect of the degree of regeneration on the resistance of the regenerator was carried out, during which a hyperbolic dependence $\xi=f(\sigma)$ was obtained.

Conflict of interest statement

The authors declare that they have no conflict of interest in relation to this research, whether financial, personal, authorship or otherwise, that could affect the research and its results presented in this paper.

CRediT author statement

Nurym K.A.: Investigation, Modeling; **Antonova A.M.:** Supervision; Conceptualization, Methodology; **Sakipov K.E.:** Formal analysis, Review & Editing; **Vorobyev A.V.:** Data Curation, Writing - Original Draft; **Stetsov N.V.:** Calculations, Visualization. The final manuscript was read and approved by all authors.

References

1 McDonald C.F. (2012) Helium turbomachinery operating experience from gas turbine power plants and test facilities. *Applied Thermal Engineering*, 44(2), 108–142. https://doi.org/10.1016/j.applthermaleng.2012.02.041

2 Frutschi H.U. (2005) Closed-Cycle Gas Turbines: Operating Experience and Future Potential. ASME Press, 294. https://doi.org/10.1115/1.802264

3 Bisio G., Massardo A., Agazzani A. (1996) Combined Helium and Combustion Gas Turbine Plant Exploiting Liquid Hydrogen (LH_2) Physical Exergy. *J. Eng. Gas Turbines Power*., 118(2), 257 – 264. https://doi.org/10.1115/1.2816586

4 Kupecki J., Hercog J., Motyliński K., Malesa J., Muszyński D., Skrzypek E., Skrzypek M., Boettcher A., Tchorek G. (2024) Advancing production of hydrogen using nuclear cycles – integration of high temperature gas-cooled reactors (HTGR) with solid oxide electrolyzers (SOE). *International Journal of Hydrogen Energy,* 53, 40 – 48. https://doi.org/10.1016/j.ijhydene.2023.12.017

5 Gelfenbein L.G. (1963) Regenerators of gas turbine units. Moscow, 180. Available at: www.gornitsa.ru/item.php?id=15544612 [in Russian]

6 Kostyuk A.G., Frolov V.V., Bulkin A.E., Trukhny A.D. (2016) *Steam and gas turbines for power plants textbook for universities.* Moscow, Publ.House of MEI, 556. Available at: https://obuchalka.org/2017111297430/parovie-i-gazovie-turbini-dlya-elektrostancii-kostuk-a-g-frolov-v-v-bulkin-a-e-truhnii-a-d-2016.html [in Russian]

7 Grebennik V.N., Kukharkin N.E., Ponomarev-Stepnoy N.N. (2008) High-temperature gas-cooled reactors - an innovative direction in the development of nuclear energy. Energoatomizdat, 136. Available at: https://cyberleninka.ru/article/n/vysokotemperaturnye-gazoohlazhdaemye-reaktory/viewer [in Russian]

8 Goryunova I.Y., Larionov I.D. (2017) GTU regenerators: a methodological manual. Yekaterinburg : Ural University Publishing House, 80. Available at: http://elar.urfu.ru/handle/10995/54034 [in Russian]

9 Lipin A.A., Romanenko Yu.E., Shibashov A.V., Lipin A.G. - Calculation of heat exchangers. Shell-and-tube heat exchangers. Ivanovo, 76. Available at: https://e.lanbook.com/book/171826 [in Russian]

10 Stetsov N.V. (2023) Effect of changing the regenerator resistance on the characteristics of a closed nuclear gas turbine with a hydrogen complex. *Butakovskie readings: articles collection of the III All-Russian youth conference with international participation*, Tomsk: TPU Publishing House, 249 – 252. Available at: http://earchive.tpu.ru/handle/11683/77631

11 Stetsov N.V. (2023) Analysis of the influence of controlled parameters on the operation of a closed GTU with a hydrogen complex. *Butakovskie readings: articles collection of the III All-Russian youth conference with international participation*, Tomsk: TPU Publishing House, 427 – 430. Available at: http://earchive.tpu.ru/handle/11683/76052 [in Russian]

12 Antonova A.M., Vorobyov A.V., Stetsov N.V. (2022) Analysis of the influence of controlled parameters on the efficiency of a closed GTU with a hydrogen complex. *Proceedings of the XIII All-Russian Scientific and Technical Conference*, Orenburg State University, 51 - 57. Available at: https://www.elibrary.ru/item.asp?id=50174542&pff=1

13 Guidance document on standardization rules for thermal and hydraulic calculation of heat exchange equipment of NPP OKSTU 3103 (1990) Available at: https://docs.cntd.ru/document/1200085786 [in Russian]

AUTHOR'S INFORMATION

Nurym K.A. - PhD student, Department of Thermal Power Engineering, L.N. Gumilyov Eurasian National University, Astana, Kazakhstan; https://orcid.org/0000-0003-3822-5697; kazedu23@gmail.com

Antonova A.M. – Candidate of Techn. Sciences, Associate Professor, Butakov research center, Tomsk Polytechnic University, Tomsk, Russia; SCOPUS Author ID: 56950262800; https://orcid.org/0000-0002-5230-9750; anton@tpu.ru

Sakipov K.E. — Candidate of Techn. Sciences, Associate Professor, Power Engineering Department, L.N. Gumilyov Eurasian National University, Astana, Kazakhstan; https://orcid.org/0000-0003-2477-3879; sakamer2100@gmail.com.

Vorobyev A.V. – Candidate of Techn. Sciences, Associate Professor, Butakov research center, Tomsk Polytechnic University, Tomsk, Russia; SCOPUS Author ID 56950140400; https://orcid.org/0000-0003-4149-0387; worob@tpu.ru.

Stetsov N.V.– Student of Butakov's research center, Tomsk Polytechnic University, Tomsk, Russia; https://orcid.org/0009-0006-7968-9403; nikolay.stecov@mail.ru

EURASIAN PHYSICAL TECHNICAL JOURNAL

2025, Volume 22, No.1 (51)

https://doi.org/10.31489/2025N1/59-66

Received: 30/12/2024 Revised: 06/02/2025 Accepted: 18/03/2025 Published online: 31/03/2025
Original Research Article

UDC 53.08 + 621.039.9

APPLICATION OF A COAXIAL HPGe DETECTOR AND FRAM CODE FOR DETERMINING THE ENRICHMENT OF SHIELDED URANIUM SAMPLES

Medetbekov B.S.*, Popov Yu.A., Prozorova I.V., Sabitova R.R., Syssaletin A.V.

Institute of Atomic Energy, Branch of the National Nuclear Center of the Republic of Kazakhstan,
Kurchatov, Kazakhstan
*Corresponding author: medetbekov@nnc.kz

Abstract. *The determination of uranium enrichment is a critical aspect of nuclear material control, essential for assessing potential safety threats and detecting unauthorized material transfers. Gamma spectrometry using a High-Purity Germanium detector offers a non-destructive method for isotope ratio analysis. However, standard equipment often lacks precision, particularly when samples are shielded. This study aims to evaluate the capability of a portable coaxial High-Purity Germanium detector in conjunction with the FRAM software for determining uranium enrichment under both shielded and unshielded conditions. To achieve this goal, a series of gamma spectrometric measurements was performed on fuel rod samples with low uranium content. The results demonstrated that the method provides reliable and rapid enrichment estimation with an error margin of up to 10%, which is particularly significant for nuclear forensics, where timely and accurate isotope analysis is crucial.*

Keywords: nuclear forensics, uranium enrichment, shielded source, gamma spectrometry, coaxial High-Purity Germanium detector, FRAM software.

1. Introduction

Determining the isotope ratio of uranium (enrichment) is one of the key characteristics of nuclear materials, requiring prompt and accurate assessment. Such evaluations are essential for decision-making regarding whether the material poses a threat to national security and for identifying instances of unauthorized material transfers. In cases where the threat is directly associated with nuclear materials, such as enriched uranium compounds, the National Nuclear Center of the Republic of Kazakhstan (NNC RK) can provide substantial technical support through preliminary analysis of material characteristics using gamma spectrometry. It is well known that equipment used during initial inspections often lacks sufficient precision to determine the isotope ratio (e.g., the degree of enrichment or uranium type). A solution to this issue could be a non-standard gamma spectrometry method requiring the use of a high-sensitivity detector based on High-Purity Germanium (HPGe), which provides high resolution [1–3].

The NNC RK laboratory staff has extensive experience using a coaxial HPGe detector in various studies. This detector has been employed for neutron activation analysis and for measuring gamma-emitting radionuclides, such as fission and activation products, in the coolant of the IVG.1M reactor. These studies have effectively determined the composition and concentrations of radionuclides in various samples [4–6].

Gamma spectrometry is a non-destructive analytical method that can be used to measure the enrichment of nuclear materials and obtain rapid and satisfactory results on the isotopic composition of uranium or plutonium in unknown samples. This is particularly important in nuclear forensics, where prompt provision of data on the isotopic composition of nuclear materials is required. When nuclear material is placed in a protective container (e.g., active samples or spent nuclear fuel), gamma lines in the low-energy range (90–100 keV) may not be detected by the detector. Namely, this range of photon energies is used to determine uranium enrichment by the multigroup analysis of uranium (MGAU) method. Under such conditions, calculation algorithms using the MGAU code [7] become ineffective for enrichment assessment. To solve this problem, it is advisable to use a coaxial HPGe detector in combination with the FRAM code for spectral analysis. A feature of the coaxial HPGe detector compared to the planar detector is a higher efficiency of photon registration in the high energy range of 1.2 MeV. In our work, a coaxial HPGe detector was used in tandem with the FRAM program to determine uranium enrichment. The FRAM code, unlike the MGAU program, uses gamma lines with energies in the range from 121 to 1001 keV to determine uranium enrichment, which can penetrate steel shielding up to 10 mm thick [8,9].

This study aimed to investigate the feasibility of applying gamma spectrometry to determine the enrichment of uranium samples, both unshielded and shielded with steel of varying thickness, using a portable coaxial HPGe detector and the FRAM software.

2. Methodology and equipment

To determine the enrichment of ^{235}U, eight segments of fuel rods from water-cooled technological channels with low-enriched uranium (WCTC-LEU) of the IVG.1M reactor were provided. These WCTC-LEU fuel rods, measuring 49 to 60 mm in length, are hereinafter referred to as "samples." The samples are spiral rods with a two-blade profile, consisting of a metallurgically bonded cladding and a fuel core. The fuel core comprises a zirconium alloy E110 matrix with evenly distributed uranium filaments enriched to 19.75% in ^{235}U. The appearance of the WCTC-LEU sample is shown in Figure 1.

The declared uranium enrichment in ^{235}U is 19.75%, while the ^{235}U content in the sample is 2.18% by mass, equivalent to 0.23 g. Such low uranium content complicates the enrichment determination process due to reduced gamma radiation activity, which decreases the intensity of the detectable lines, making accurate isotopic analysis challenging. To minimize errors and improve measurement accuracy, various measurement geometries were employed to assess the effects of shielding and the distance between the sample and the detector. The parameters of these measurements are summarized in Table 1.

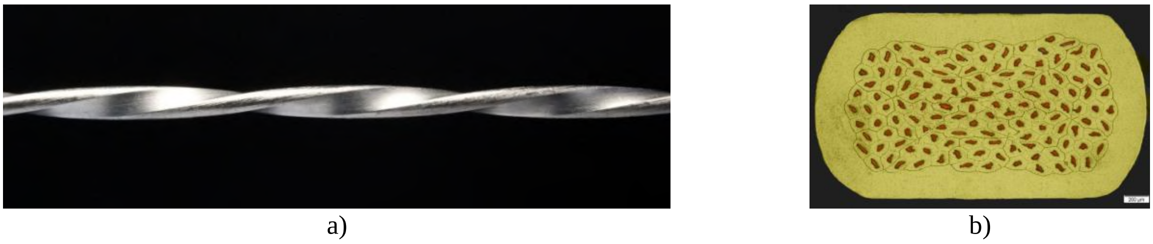
a) b)

Fig.1. The appearance of the WCTC-LEU fuel rod sample (a) and cross-sectional view of the WCTC-LEU fuel rod (b).

The research methodology involved measuring the gamma spectra of the sample in four different geometries. In three geometries, the distance from the sample to the detector cap was fixed at 16 mm. The difference between these geometries was as follows: the first measurement was conducted without shielding; the second used a steel shield with a thickness of 2.5 mm; and the third used a steel shield with a thickness of 8 mm. In the fourth geometry, the sample was placed directly on the detector cap. The measurement duration was adjusted so that the peak area at energy E = 1001 keV was approximately $4.3 \cdot 10^3$ counts for all measurements (statistical uncertainty was estimated at 1.6 –1.8%). The shield for the second geometry consisted of a steel plate measuring 90×30×2.5 mm, and for the third geometry, a steel plate measuring 80×40×8 mm. Additionally, background measurements were conducted in the laboratory, and no uranium isotope peaks were detected in the background spectrum.

Table 1. Measurement Parameters

Measurement Geometry Number	Distance Detector-Sample, mm	Shield Thickness, mm	Exposure Time, s	Shield Dimensions, Length×Width, Thickness, mm
1	16	-	5000	-
2	16	2,5	5500	90×30×2,5
3	16	8	7500	80×40×8,0
4	0	-	2200	-

Spectrometric studies were conducted using the GC1518 coaxial germanium semiconductor detector, which has a gamma radiation detection efficiency of 15% and an energy resolution of 1.8 keV at 1332 keV. The measurements were carried out using the DSA-LX pulse analyzer with an 8182-channel scale. The amplification of the channel was set to 0.125 keV/channel. The energy calibration of the gamma spectrometer was performed using the Eu-152 calibration source. The measurement process and the geometry of the sample placement, both without shielding and with shielding, are shown in Figures 2a and 2b, respectively.

а) б)

Fig.2. Geometry of sample measurement without shielding (a) and with a 2.5 mm thick shield (b).

The spectra of the samples were processed using the FRAM code. Unlike the MGAU code, the FRAM code offers several different algorithms for result processing, which can be configured through an editable parameter file. The FRAM package includes a recommended set of input parameters, which vary depending on the enrichment of the sample. These parameters include specific settings for analyzing low-enriched uranium (enrichment less than 40% for ^{235}U) and highly enriched uranium (enrichment greater than 10% for ^{235}U) [8-10].

Table 2. Standard Parameter Sets Embedded in the FRAM Code.

Parameter name	Description
ULEU_Plnr_060-250	U Only, Enrichment ≤40%, 0.075 keV/ch, Planar detector
UHEU_Plnr_060-250	U Only, Enrichment ≥10%, 0.075 keV/ch, Planar detector
ULEU_Cx_120-1001	$^{235}U < 40\%$ or high thorium background, 0.125 keV/ch, Coaxial detector
UHEU_Cx_120-1001	$^{235}U > 10\%$, 0.125 keV/ch, Coaxial detector

For the analysis of the spectra, the parameter ULEU_Cx_120-1001 was used**,** which is oriented for low-enriched uranium and utilizes energy peaks in the range from 121 keV to 1001 keV for a coaxial detector type.

For each measurement geometry, 18 spectra were recorded. The results of processing those spectra were subjected to statistical analysis. For each data set obtained, the mean enrichment value (Enr) was calculated using formula (1), and the standard deviation (SD) was calculated using formula (2):

$$\overline{Enr} = \frac{1}{n}\sum_{i=1}^{n} Enr_i , \tag{1}$$

$$SD = \left(\frac{1}{n-1}\sum_{i=1}^{n} \left(Enr_i - \overline{Enr} \right)^2 \right)^{1/2} , \tag{2}$$

where *n* is the number of measurements; *Enr* is the enrichment value obtained from the i-th spectrum.

3. Results of the study

As a result of gamma spectrometric measurements of the sample, 72 spectra were obtained (18 for each of the four measurement geometries) and processed using the FRAM code. The average enrichment values of ^{235}U in the sample (Enr) and the standard deviation (SD) for the unshielded sample at a distance of 16 mm from the detector were 20.1% and 1.8%, respectively. For the shielded sample with a 2.5 mm thick screen, these values were 20.3% and 1.2%. For the shielded sample with an 8 mm thick screen, the values were 19.65% and 1.21%. For the unshielded sample placed directly on the detector cap, the enrichment values were 20.4% and 0.8%. Table 3 presents the statistical distributions of the results for determining the enrichment of ^{235}U for both unshielded and shielded samples.

Table 3. Results of Statistical Analysis.

Interval No.	Unshielded sample		Shielded sample, d=2.5 mm	
	Enrichment % by mass	Number of Measurements	Enrichment % by mass	Number of Measurements
1	17.10 ± 0.63	1	18.44 ± 0.45	2
2	18.36 ± 0.63	5	19.34 ± 0.45	5
3	19.62 ± 0.63	5	20.24 ± 0.45	5
4	20.88 ± 0.63	1	21.14 ± 0.45	2
5	22.15 ± 0.63	6	22.04 ± 0.45	4
	Shielded sample, d=8 mm		Unshielded sample on cap	
1	18.15 ± 0.45	3	18.94 ± 0.30	2
2	19.05 ± 0.45	5	19.55 ± 0.30	5
3	19.95 ± 0.45	5	20.16 ± 0.30	2
4	20.85 ± 0.45	3	20.77 ± 0.30	5
5	21.75 ± 0.45	2	21.38 ± 0.30	4

When constructing histograms of statistical distributions, consisting of five intervals, the interval width was calculated using the formula (3):

$$w = \frac{Enr_{max} - Enr_{min}}{5} \tag{3}$$

The values for the first and subsequent intervals were calculated using formulas (4) and (5):

$$Enr_1 = Enr_{min} + \frac{w}{2} \tag{4}$$

$$Enr_i = Enr_{i-1} + w \tag{5}$$

The statistical distributions of the ^{235}U enrichment results for the FRAM code are also presented in histograms shown in Figure 3. The point with the error interval on the abscissa axis corresponds to the average enrichment value (Enr) and the standard deviation (SD) obtained from formulas (1) and (2).

The spectra of the sample were analyzed to study the ability of shielding materials to attenuate gamma radiation intensity at various energies. The exposure time for the measurements was selected such that the area of the 1001 keV peak was approximately $4.4 \cdot 10^3$ impulses. Table 4 shows the results of measuring the peak areas of gamma radiation at different energies (121, 143, 163, 185.7, 205, and 1001 keV) in four different geometries and exposure times. Analysis of the data in the table highlights the property of the absorbing screens to attenuate the low-energy part of the gamma spectrum more significantly, as well as the ability of the coaxial detector to efficiently register high-energy gamma quanta from uranium-238 at 1001 keV, which penetrate well through shielding materials. This makes the coaxial detector especially effective for analyzing samples with a high-energy component in the gamma spectrum and those shielded by steel screens.

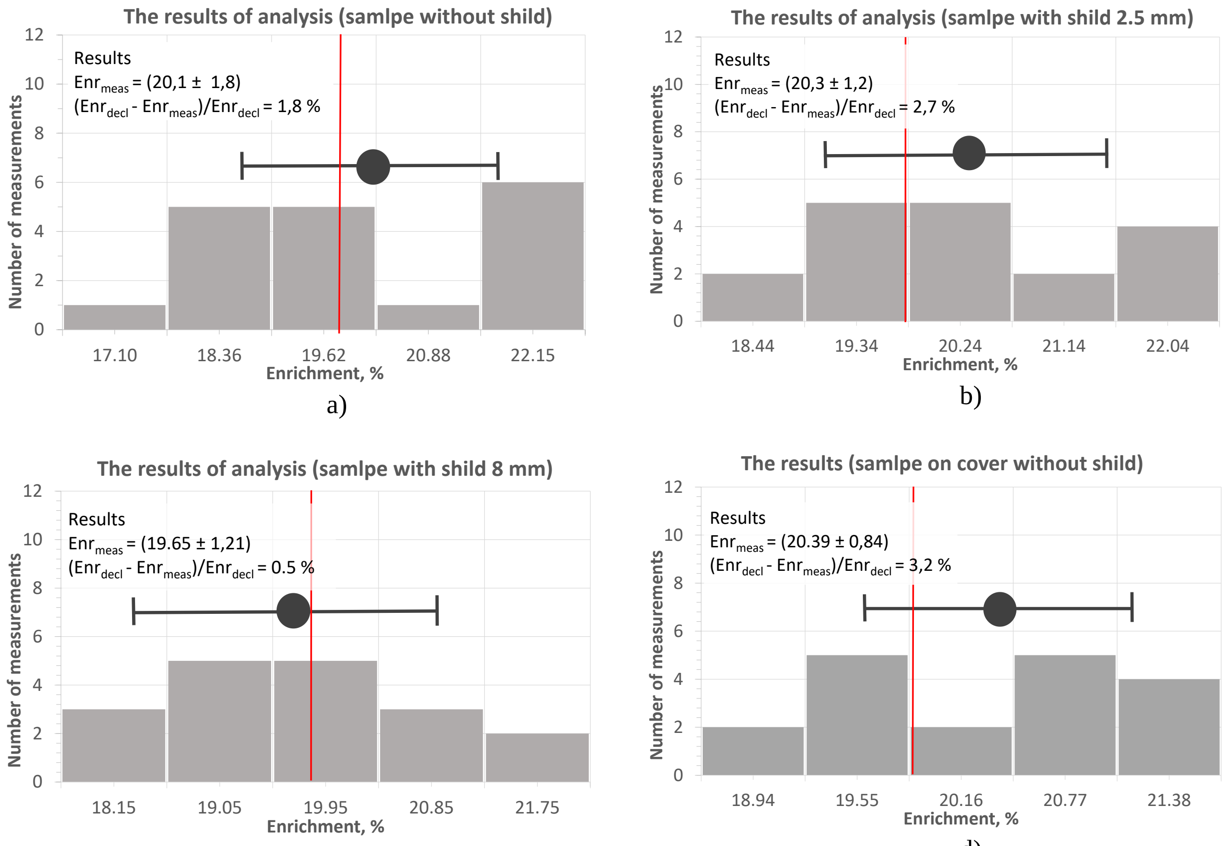

a) b) c) d)

Fig.3. Statistical distribution of the results of the determination of ^{235}U enrichment in the unshielded sample (a), the shielded sample with 2.5 mm steel (b) and 8 mm steel (c), and the sample placed on the detector lid (d).

Table 4. Results of Peak Area Measurements for Various Energies, Geometries, and Exposure Times.

Measurement Conditions	Energy, keV					
	121	143	163	185.7	205	1001
Without shield (t=2200 s)	2.74(4)E+04	3.72(6)E+05	1.87(14)E+05	2.10(2)E+06	1.78(4)E+05	4.44(9)E+03
Without shield (t=5000 s)	3.19(6)E+04	4.17(8)E+05	2.04(8)E+05	2.26(3)E+06	1.89(6)E+05	4.39(7)E+03
Shield 2.5 mm (t=5500 s)	2.10(6)E+04	3.10(7)E+05	1.61(7)E+05	1.86(2)E+06	1.59(5)E+05	4.40(7)E+03
Shield 8.0 mm (t=7500 s)	8.30(26)E+03	1.59(7)E+05	9.34(7)E+04	1.19(2)E+06	1.08(4)E+05	4.27(5)E+03

4. Discussion of results

For the FRAM code, the algorithm used for processing results was focused on low-enriched uranium, utilizing energy peaks in the range from 121 keV to 1001 keV for the coaxial detector type. It is important to note that when measuring a shielded nuclear material source, longer exposure times are required to achieve the necessary statistical accuracy of the full absorption peak area.

The study obtained statistical distributions of ^{235}U enrichment results for both unshielded and shielded samples. The distributions were divided into five intervals based on enrichment values. During the result processing, varying numbers of measurements fell into each interval, which were subsequently presented in histograms. These intervals allow for evaluating the distribution of enrichment results and how closely they align with the declared enrichment value of 19.75%.

Upon analyzing the results, it is observed that the histogram with the maximum shielding thickness and exposure time exhibits a normal distribution. The enrichment value in this case most closely matches the declared value of 19.75%. For other histograms, the distribution is uneven, likely due to an insufficient number of measurements and short exposure times. Overall, it can be stated that the results of enrichment determination using the coaxial detector are sufficiently reliable.

The count rate in the peak with energy Ei depends on the shield thickness. As shown in Table 4, gamma quanta with a "low" energy of 121 keV are attenuated to a greater extent, while gamma quanta with a "high" energy of 1001 keV are attenuated to a lesser extent. For clarity, the measurement results of the count rate as a function of steel shield thickness for various gamma-ray energies are presented in Fig. 4.

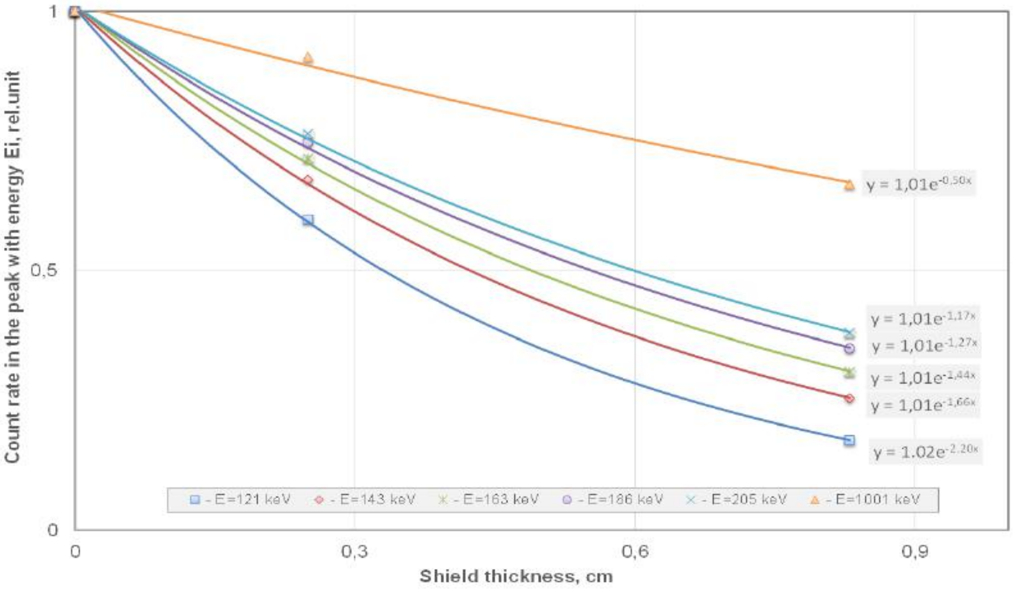

Fig.4. Results of count rate measurements as a function of steel screen thickness.

As observed, the count rate in the E=1001 keV peak with a 0.8 cm thick shield decreased by 1.5 times compared to the unshielded sample, while the count rate in the E=121 keV peak decreased by 5.8 times. This confirms the advantages of using the FRAM method compared to the MGAU method for samples shielded with thick materials. It is well-known that the MGAU method analyzes uranium enrichment using the low-energy region of the gamma spectrum in the range of 90–100 keV.

The measurements, conducted in four different geometries, indicated that the enrichment values calculated using the FRAM code had a maximum relative deviation of 3.2%. This confirms the method reliability even with changing measurement conditions such as shielding and detector distance. The use of the coaxial HPGe detector and the FRAM software code proved to be effective for analyzing uranium samples under various conditions, including shielding. The average ^{235}U enrichment value obtained from all measurements lies within the statistical error and corresponds to the declared value of 19.75%.

5. Conclusion

Gamma spectrometry measurements were performed to determine the uranium enrichment in both unshielded and shielded samples with low uranium content. Despite the low uranium content (1.2% of the total mass of 10.9 g), sufficiently reliable data on the isotopic composition of ^{235}U were obtained.

The measurements carried out in four different geometries, showed that the enrichment values calculated using the FRAM code had a maximum relative deviation of 3.2%. This confirms the method reliability even when the measurement conditions, such as shielding and detector distance, change.

The use of the coaxial HPGe detector and the FRAM software code proved effective for analyzing uranium samples in various conditions, including shielding. The average ^{235}U enrichment value, derived from all measurements, lies within the statistical error and corresponds to the declared value of 19.75%.

In perspective, gamma spectrometry using a coaxial HPGe detector with FRAM software may be an alternative method in nuclear forensics for determining uranium enrichment, where samples can be shielded (e.g. in containers with ~10 mm thick steel shielding). It allows for obtaining relatively fast and satisfactory results on the isotopic composition of uranium, which makes it an effective tool for express analysis.

Conflict of interest statement.
The authors declare that they have no conflict of interest in relation to this research, whether financial, personal, authorship or otherwise, that could affect the research and its results presented in this paper.

CRediT author statement
Medetbekov B.: Conceptualization, Methodology, Writing Review & Editing; **Popov Yu.:** Writing- Original draft preparation, Supervision; **Sabitova R.**: Data Curation, Investigation; **Prozorova I.**: Writing- Original draft preparation and Editing; **Syssaletin A.**: Project administration. The final manuscript was read and approved by all authors.

Acknowledgments (Funding)

This work was supported financially by the Committee of Science of the Ministry of Science and Higher Education of the Republic of Kazakhstan under the result-oriented funding project BR21882185-OT-24, titled "Research in Support of the Creation and Safe Operation of a Nuclear Power Plant in the Republic of Kazakhstan."

Additionally, the research on WCTC-LEU fuel elements was conducted with support from the international project ISTC KZ-2540, titled "Development of a National Library for Nuclear Forensics in the Republic of Kazakhstan as a System for Identifying Nuclear and Other Radioactive Materials and Sample Exchange."

References

1 Zsigrai J., Frigerio A., Bagi J., Mühleisen A., Berlizov A. (2017) Using FRAM to determine enrichment of shielded uranium by portable electrically cooled HPGe detectors. *IProceeding of the 39th ESARDA Annual Meeting - Symposium, Düsseldorf, Germany* 80 – 86. Available at: https://jeodpp.jrc.ec.europa.eu/ftp/public/JRC-OpenData/UPu-Gamma/UraniumDetective/LATEST/ESARDA2017-Dusseldorf-FRAM-U.pdf

2 Kim W., Jang J. (2021) A study on the uranium enrichment determination using the standard-less gamma spectrometry technique. *In Transactions of the Korean Nuclear Society Virtual Spring Meeting*, 3. Available at: https://www.kns.org /files/pre_paper/45/21S-281-%EA%B9%80%EC%9A%B0%EC%A7%84.pdf

3 Nguyen C.T., Zsigrai J. (2006) Basic characterization of highly enriched uranium by gamma spectrometry. *Nuclear Instruments and Methods in Physics Research Section B: Beam Interactions with Materials and Atoms*, 246(2), 417 - 424. https://doi.org/10.1016/j.nimb.2006.01.011

4 Medetbekov B. S., Vurim A. D., Prozorova I. V., Popov Y.A. (2023) Fission product release from high and low-enriched uranium fuels of the IVG. 1M research reactor. *Eurasian Physical Technical Journal*, 20, 4(46), 54-60. https://doi.org/10.31489/2023No4/54-60

5 Aleynikov Y.V., Popov Y.A., Medetbekov B.S., Kozhakhanov S.B. (2016) Adaptation of the k0-INAA method for the IVG. 1M reactor. Izvestiya Tomskogo Politekhnicheskogo Universiteta. 327(4), 16 - 22. Available at: https://earchive.tpu.ru/bitstream/11683/22649/1/bulletin_tpu-2016-v327-i4-02.pdf [in Russian]

6 Sabitova R.R., Popov Y.A., Irkimbekov R.A., Bedenko S.V., Prozorova I.V., Svetachev S.N., Medetbekov B.S. (2023) Experimental studies of power distribution in LEU-fuel of the IVG. 1M reactor. *Applied Radiation and Isotopes*, 200, 110942. https://doi.org/10.1016/j.apradiso.2023.110942

7 Genie 2000 (2002) Software. MGA-U, Model S507, Version 4.3. User Manual. Available at: http://depni.sinp.msu.ru/~hatta /canberra/S507%20MGAU%20for%20Genie-2000%20User's%20Manual.pdf [in Russian]

8 Model S575 PC/FRAM. Isotopics Software, 9231022D V5.2. User’s Manual. (2011). Available at: https://www.ortec-online.com/-/media/ametekortec/manuals/f/fram-mnl.pdf?la=en&revision=0bd69175-033e-4d18-990b-2d186cca0178

9 Darweesh M., Shawky S. (2019) Study on the performance of different uranium isotopic codes used in nuclear safeguards activities. *Heliyon*, 5(4), e01542. Available at: https://doi.org/10.1016/j.heliyon.2019.e01542

10 Sampson T. E., Croft S. (2015) Making quality HPGe gamma ray spectrum measurements for uranium: The role of FRAM for analysis, quality control and enrichment measurements, and opportunities for improved quantification documentation. Oak Ridge National Laboratory, 55. Available at: https://info.ornl.gov/sites/publications/Files/Pub58137.pdf

AUTHORS’ INFORMATION

Medetbekov, Berik Sakenovich – Master (Sci), Junior researcher, Laboratory of Neutron Physics, Institute of Atomic Energy Branch of NNC RK, Kurchatov, Kazakhstan. SCOPUS Author ID: 57194243464; https://orcid.org/0009-0005-7232-0235, medetbekov@nnc.kz

Popov, Yuri Anatol’evich – Specialist, Deputy Head of the Laboratory, Laboratory of Neutron Physics, Institute of Atomic Energy Branch of NNC RK, Kurchatov, Kazakhstan. SCOPUS Author ID: 57194237762; https://orcid.org/0009-0004-2617-2262, popov@nnc.kz

Sabitova, Radmila Radikovna – graduated PhD student, Tomsk Polytechnic University (Russia); junior researcher, Laboratory of Neutron Physics, Institute of Atomic Energy Branch of NNC RK, Kurchatov, Kazakhstan. SCOPUS Author ID: 57211189530, https://orcid.org/0000-0002-0958-7923; sabitovar@nnc.kz

Prozorova, Irina Valentinovna – PhD student, Tomsk Polytechnic University (Russia); Head of the Laboratory of Neutron Physics, Institute of Atomic Energy Branch of NNC RK, Kurchatov, Kazakhstan. Scopus Author ID: 57220986470, https://orcid.org/0000-0001-8701-9756; prozorova@nnc.kz

Syssaletin, Andrey Valerievich – Specialist, Head of Security Division, NNC RK, Kurchatov, Kazakhstan; Scopus ID: 57820636900; https://orcid.org/0000-0003-1873-4160; syssaletin@nnc.kz

EURASIAN PHYSICAL TECHNICAL JOURNAL

2025, Volume 22, No.1 (51)

https://doi.org/10.31489/2025N1/67-75

Received: 20/08/2024 Revised: 28/02/2025 Accepted: 18/03/2025

Original Research Article

UDC 536.8; 621.434.49

IMPROVING PRODUCTIVITY AND REDUCING EMISSIONS OF SOLAR-BIOGAS DUAL-FUEL DIESEL ENGINES

Ridhuan K, Mafruddin, Irawan D.*, Handono S.D.

Department of Mechanical Engineering, Universitas Muhammadiyah Metro, Lampung, Indonesia
*Corresponding author: Irawan.ke10@gmail.com

Abstract. *Global energy needs continue to increase, which have been met by fossil fuels, resulting in significant environmental damage. Alternative energy such as biogas is an effective solution to reduce the use of fossil fuels because it has a high auto-ignition temperature (±650°C), making it suitable for use in engines with high compression ratios. This research aims to evaluate the effect of using biogas in dual-fuel diesel engines on performance and exhaust emissions. Experiments were carried out on diesel engines with single and dual-fuel, using variations in biogas flow rates of 3, 4, and 5 l/minute. The research results show that the use of biogas in dual-fuel engines produces higher torque and brake power values compared to single fuel at flow rates of 3 and 4 l/min. In addition, single-fuel diesel engine exhaust emissions show the highest values for CO (0.29%) and CO_2 (5.67%), while dual-fuel engines produce CO (0.27%) and CO_2 (5.51%). These findings show that biogas as a dual-fuel can improve engine performance while reducing harmful emissions, making it a sustainable energy alternative.*

Keywords: Biogas, dual-fuel, diesel, performance, exhaust emissions.

1. Introduction

The world's energy needs continue to increase along with human population growth and sustainable industrial needs. It is estimated that energy demand will increase by 30% until 2040, with most of this need still being met by fossil fuels [1] . Using of fossil fuels as the main energy source has caused significant environmental damage, including air pollution and climate change [2], [3]. Exhaust gas emissions from burning fossil fuels, such as gasoline, diesel, and LPG in internal combustion engines (ICE), contribute greatly to acid rain, global warming, and increased greenhouse gas concentrations [4], [5]. Diesel engines produce large amounts of particulate matter (PM) and nitrogen oxides (NOx) emissions [6]. The most widely used energy source in the machinery and transportation industry is the use of diesel fuel for diesel engines [7], [8].

To reduce environmental impacts, many countries have adopted policies and regulations that encourage using renewable energy [9]. In Indonesia, for example, the government has developed various initiatives to increase the use of renewable energy as part of its commitment to global climate agreements. One promising alternative energy source is biogas [10]. Biogas is produced from agricultural waste, industrial waste, livestock waste, and household waste through anaerobic fermentation which produces methane gas (CH_4) 50-70%, Carbon Dioxide (CO_2) 25-50%, Hydrogen (H_2) 1-5%, and Nitrogen (N_2) 0.3-3% [11]. The potential for biogas as a renewable fuel is very large, because it can reduce dependence on fossil fuels and greenhouse gas emissions.

The use of biogas in diesel engines as a dual-fuel has shown significant potential. Previous research shows that biogas-diesel mixtures can reduce diesel use by up to 63% and even replace up to 90% of diesel consumption [12]. Biogas, with its high auto-ignition temperature (±650°C), is suitable for use in engines with high compression ratios [13]. However, the use of biogas in diesel engines still faces several obstacles, such as decreased thermal efficiency and increased exhaust emissions of carbon monoxide (CO) and hydrocarbons (HC) [14]. On the other hand, the use of biogas can provide economic benefits, including reduced operational costs and increased energy sustainability. Biogas can be mixed homogeneously with air, allowing better ignition thanks to its wide flame range [15]. The biogas used should contain more than 50% CH_4 and be free from hydrogen sulfide, water and siloxane to ensure quality and efficiency [16]. The latest innovations in biogas processing technology and the development of dual-fuel engines continue to be developed to overcome these obstacles [17].

Various researchers have studied dual-fuel diesel engines by examining parameters such as timing variation [18], [19], optimization of pilot injection timing [20], and variation of air flow rate into the combustion chamber. The timing and duration of biogas injection fundamentally affect the combustion process, as it is related to the volume of biogas fuel entering the combustion chamber during the intake stroke. In dual-fuel diesel engines, a variable fuel supply is required according to changes in engine load, so a constant biogas supply can reduce the percentage of biogas substitution as the load increases [21].

Research by Liu et al. (2020) [22] on a dual-fuel diesel engine fuelled by diesel-CNG found that the mass flow rate of CNG affects the combustion process and emissions produced. In the context of a dual-fuel diesel engine, the fuel supply parameter is very important for the combustion process, which makes the combustion more spread and closer to the cylinder wall. This study aims to evaluate the combustion reaction, engine performance, fuel consumption, and exhaust emission characteristics of a dual-fuel diesel engine fuelled by diesel-biogas. The results of this study are expected to provide information related to the use of biogas as an alternative fuel for diesel engines and efforts to reduce environmental damage.

2. Materials and research method

To study the performance and combustion process of a dual-fuel diesel engine, modifications were made to a single-cylinder diesel engine by adjusting the fuel input to regulate the flow of biogas fuel into the combustion chamber. The test scheme of a dual-fuel system diesel engine is shown in Figure 1.

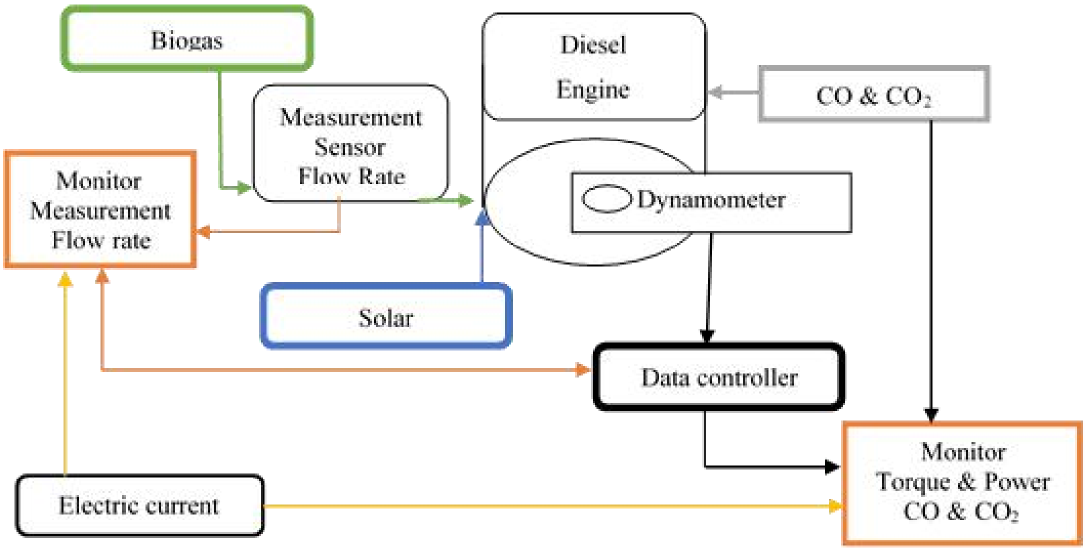

Fig.1. Test Scheme.

2.1. Fuel Characteristics and Fuel Supply Systems

This research uses diesel fuel supplied from PT Pertamina Indonesia. Biogas is produced anaerobically by using cow dung as raw material in a fixed dome type biogas digester with a capacity of 2 m^3 which is accommodated in a biogas storage balloon. Diesel and biogas fuel specifications are shown in Table 1.

Table 1. Fuel properties [23]

Properties	**Diesel**	**Biogas**
Lower heating value (MJ/kg)	42	20.958*
Density (kg/m^3)	840	1.12*
Auto ignition temperature (°C)	280	650
Stoichiometric air-fuel ratio	14.60	17
Cetane number	49	-
Octane number	-	130
Laminar burning velocity (m/s)	0.5	0.2

The study used diesel and biogas fuels, diesel fuel was injected directly into the combustion chamber using a mechanical injection pump, and biogas fuel was injected into the intake manifold using a gas injector whose gas volume was controlled by a flow meter with variations of 3 lpm (B3), 4 lpm (B4), and 5 lpm (B5). The biogas flow rate was kept constant at each variation of flow rate and combustion load at each engine speed.

2.2. Test Machines and Test Procedures

The test used a diesel engine with a single cylinder capacity, four strokes, and direct injection fuel system. Detailed specifications of the test engine are shown in Table 2. The test engine was modified to accommodate a dual-fuel system of diesel solar - biogas. Diesel fuel is injected mechanically and biogas is injected using a pump into the intake manifold to the combustion chamber.

Table 2. Diesel engine specifications

Parameter	**Mark**
Machine capacity	0.296 L
Number of cylinders step	Single cylinder four steps
Liner diameter	78mm
Stride length	62mm
Combustion system	direct injection
Power factor	1.0
Count output	5.5 kW

The diesel engine is connected to a dynamometer to measure torque and brake power. The CO_2 and CO sensors are connected to the data controller and the results are displayed on the monitor screen. Diesel fuel is prepared in a measuring cup to measure fuel consumption. Biogas is prepared in a biogas storage balloon with the addition of a flow meter to measure the flow rate injected into the intake manifold towards the combustion chamber. Before evaluating engine performance and emission results, the engine is turned on until it reaches the highest working temperature and engine speed, experiments are carried out at the maximum throttle position with additional braking load until the specified engine speed is reached (2700, 2600, 2500, 2400, 2300, 2200, 2100, and 2000 rpm). All test equipment is set up and recalibrated to ensure the data obtained is valid and accountable. Instrument calibration refers to adjusting an instrument to ensure that the measurement results are in accordance with established standards. This process improves data accuracy and minimizes measurement errors that may occur due to drift or environmental changes since the last calibration was performed [24].

3. Results and Discussion

This section discusses the performance of diesel engines, namely fuel combustion reactions, engine torque, engine power, and specific fuel consumption, as well as exhaust emissions with single fuel and dual-fuel. The exhaust gas emissions analyzed are CO and CO_2 emissions.

3.1 Combustion Reaction

Burning fuel in a diesel engine in this study involves a reaction between hydrocarbons (in diesel and biogas) with oxygen from the air, producing the main products in the form of carbon dioxide (CO_2) and water

(H_2O), as well as by-products such as carbon monoxide (CO), nitrogen oxides (NOx), and unburned hydrocarbons (HC). Biogas, with its main content being methane (Ch_4), mixes easily with air, producing a more homogeneous fuel-air mixture than diesel. This can increase fuel combustion efficiency, the methane in biogas helps create a fast initial combustion, thereby increasing the combustion chamber temperature.

Initial reaction of methane combustion:

$$CH_4+2O_2 \rightarrow CO_2+2H_2O \quad (1)$$

The combustion reaction increases the temperature to help evaporation so that the octadecane in diesel burns more quickly. Combustion reaction of octadecane in diesel:

$$2C_{16}H_{34}+49O_2 \rightarrow 32CO_2+34H_2O \quad (2)$$

This more efficient combustion increases pressure in the cylinder, which translates into higher torque. The biogas-diesel mixture produces more uniform and intense combustion, increasing the mechanical energy produced per engine cycle [18]. Thus, increasing the flow of biogas in the fuel mixture directly contributes to increasing engine torque and power, resulting in more optimal engine performance.

3.2 Brake Torque

Engine performance in brake torque shows an increase in brake torque on diesel-biogas fuel compared to single diesel fuel. Increasing the biogas flow rate contributed to an increase in brake torque, with a flow rate of 5 lpm (B5) showing the most significant increase. The test results are presented in Figure 2. On single diesel fuel, brake torque increases with increasing load and decreasing engine speed. At an engine speed of 2700 rpm, the brake torque is initially around 4 Nm, and increases to around 18 Nm at an engine speed of 2000 rpm. At the B3 biogas flow rate, the brake torque produced is higher than single fuel at engine speeds above 2500 rpm, but slightly lower at engine speeds below 2400 rpm.

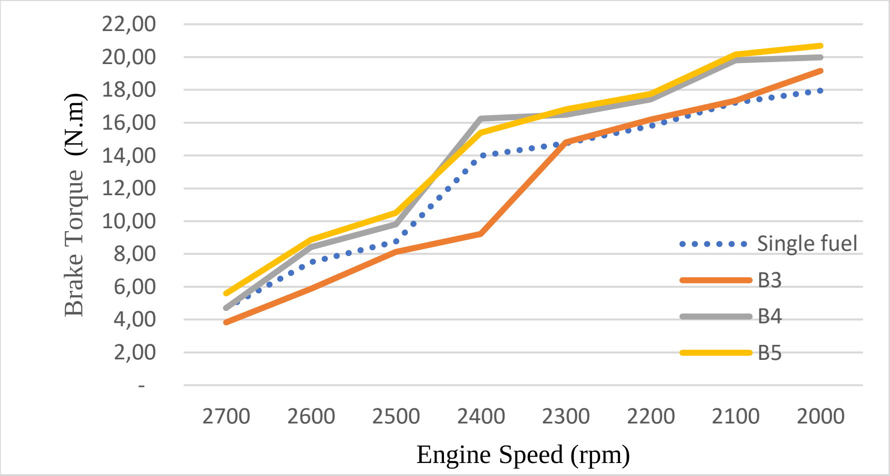

Fig. 2. Brake torque graph at each engine speed.

This indicates that at lower biogas flow rates, combustion may not be optimal at high loads. At the B4 biogas flow rate, the resulting brake torque is consistently higher than single fuel throughout the engine speed range. Brake torque increases from around 8 Nm at 2700 rpm to around 19 Nm at 2000 rpm. At biogas flow rate B5, the brake torque produced is the highest compared to all other variations. Brake torque increases from around 10 Nm at 2700 rpm to around 22 Nm at 2000 rpm. This shows that higher biogas flow rates significantly improve combustion efficiency and engine performance [14]. This phenomenon can be explained by the fact that biogas, which has a high methane component, allows more efficient combustion and increased energy output. However, it is important to note that the optimal biogas flow rate must be adapted to the machine characteristics and operating conditions to achieve the best performance. The use of dual-fuels not only increases brake torque but also shows potential to increase engine thermal efficiency, which could contribute to reduced fossil fuel consumption and greenhouse gas emissions [25].

3.3 Brake Power

The brake power test results show that the use of biogas can increase brake power compared to diesel fuel, which is presented in Figure 3. Brake power increases with increasing braking load and decreasing engine speed. The best biogas flow rate is B5 biogas flow rate, with the highest brake power produced compared to all other variations.

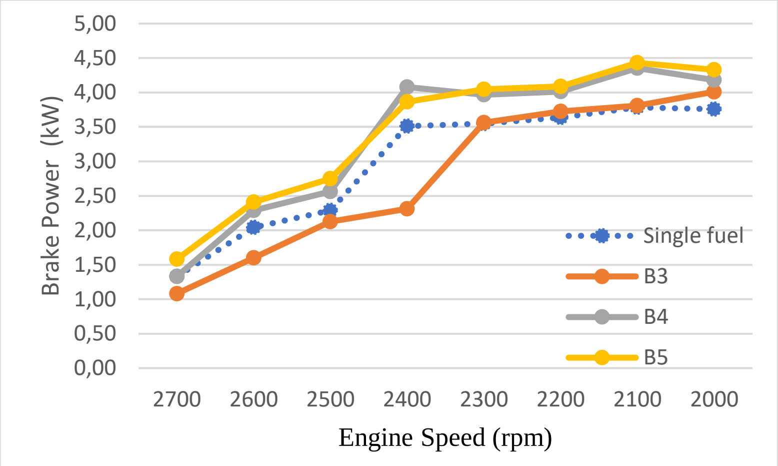

Fig. 3. Graph of brake power at each engine speed

Braking power increases from around 2.2 kW at 2700 rpm to around 4.4 kW at 2000 rpm. The addition of biogas to the combustion chamber produces a more homogeneous biogas-air mixture, increases the formation of ignition kernels, and improves the combustion of the diesel fuel premix [1]. This can improve the thermal efficiency and power output of the diesel engine.3.4 Brake Specific Fuel Consumption (BSFC).

The BSFC test results show that the dual-fuel system can reduce BSFC compared to single diesel fuel. A decrease in BSFC indicates an increase in combustion efficiency, as less fuel is used to produce the same power. The BSFC test results are presented in Figure 4. BSFC tends to be higher at higher engine speeds and decreases as the engine speed decreases on single fuel.

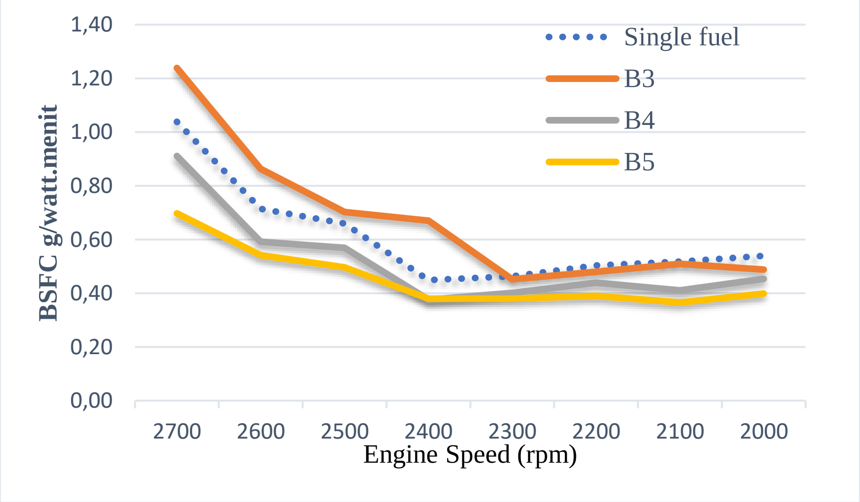

Fig. 4. BSFC graph at each engine revolution.

On dual-fuel, BSFC results at high engine speed (2700-2600 rpm) are higher than with single fuel, but decrease more significantly at lower engine speed. Higher biogas flow rates (B4 and B5) resulted in lower

BSFC compared to lower flow rates (B3). This shows that at higher biogas flow rates, combustion is more effective and fuel efficiency increases [23], [26].

3.5 Exhaust gas emissions

The test results show that the concentration of carbon monoxide (CO) is higher in the combustion reaction, this can result in a low combustion temperature resulting in incomplete combustion. With the addition of biogas, the combustion temperature increases because methane can help the combustion reaction run faster [27]. The CO concentration produced in this study is presented in Figure 5. The use of a diesel-biogas mixture in a diesel engine has been proven to reduce carbon monoxide (CO) emissions compared to the use of single diesel. Biogas, especially methane (CH_4), mixes more easily with air, producing a more homogeneous mixture and increasing combustion efficiency. Methane burns faster, increasing the temperature of the combustion chamber, which facilitates more complete combustion of diesel fuel and reduces CO formation [28]. Test results show that biogas flow rates of 4 Lpm and 5 Lpm significantly reduce CO emissions. This research is in line with previous studies, such as Mohsin et al. 2014 [29] and Yoon and lee. 2011 [23], who also found that blending biogas in diesel engines increased combustion efficiency and reduced CO emissions.

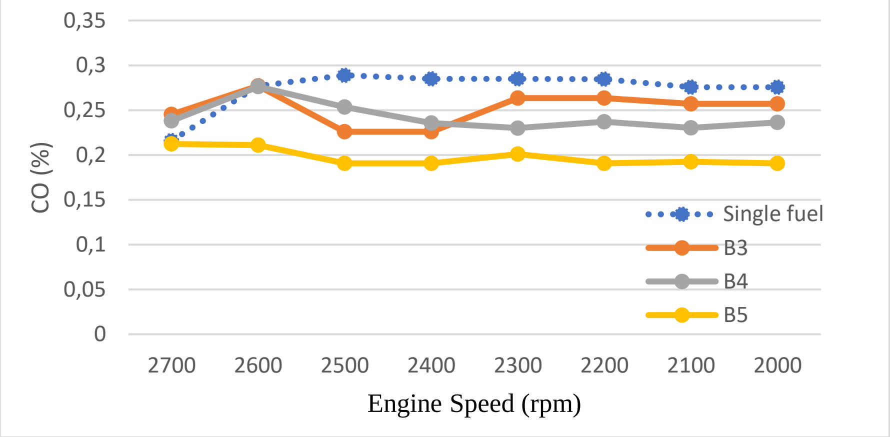

Fig. 5. Graph of CO concentration at each engine speed

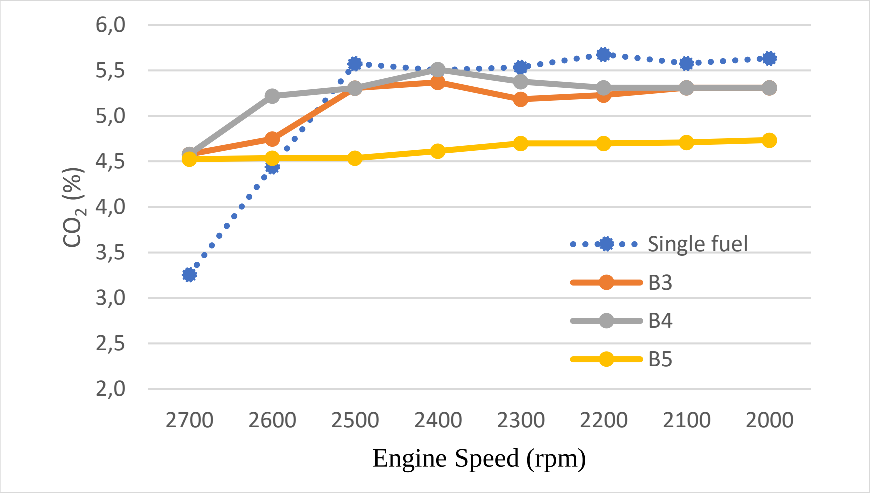

Fig. 6. Graph of CO_2 concentration at each engine speed

CO_2 is the most important gas that causes the greenhouse effect, which is generally produced from burning fossil fuels for transportation [30]. The results of CO_2 emissions can be seen in Figure 6, CO_2 emissions increase as the load increases, the temperature inside the cylinder increases. CO_2 increases when using a single fuel engine as the engine load increases [28]. The difference in CO_2 content when using single fuel and dual-fuel diesel-biogas. In the picture, it can be seen that CO_2 for single fuel reaches 5.67%, while for dual-fuel it is around 5.51%. The results are due to more complete combustion and reduced fuel consumption.

This study offers a novelty compared to previous studies examining biogas use in a dual-fuel diesel system. Several previous studies, such as those conducted by Ambarita (2017) [8] and Barik & Murugan (2014) [6], showed that biogas can reduce CO emissions and improve engine efficiency. However, this study tested variations in biogas flow at three levels (3, 4, and 5 lpm), which has not been widely done before, providing new insights into the effect of biogas flow on engine performance and exhaust emissions. In addition, this study measured the reduction in CO_2 emissions in more detail, with results showing a decrease in CO_2 from 5.67% in single diesel to 5.51% in dual-fuel. These findings indicate that biogas reduces CO emissions and CO2 and improves engine performance, especially at higher biogas flows, which has not been widely discussed in previous literature.

Based on the research results, the best proportion for biogas mixture in a dual-fuel diesel system is at a biogas flow of 5 pm. This flow significantly improves engine torque and braking power compared to 3 and 4 lpm flows. In addition, using biogas with a flow of 5 lpm results in better CO and CO_2 emissions reduction. Although higher biogas flow improves performance and emission reduction, it is essential to consider operational cost and efficiency. Therefore, a biogas flow of 5 lpm is the optimal proportion to balance engine performance and emissions.

4. Conclusion

The use of biogas as an additional fuel increases the homogeneity of the fuel-air mixture, resulting in more efficient and complete combustion. The results show an increase in engine torque and power, as well as a decrease in specific fuel consumption (BSFC). Carbon monoxide (CO) and carbon dioxide (CO_2) emissions are significantly reduced with the use of biogas mixtures. This research shows that biogas-biodiesel blends in diesel engines reduce emissions due to higher combustion efficiency. Overall, diesel-biogas blends offer an environmentally friendly and efficient solution for diesel engines.

Conflict of interest statement

The authors declare that they have no conflict of interest in relation to this research, whether financial, personal, authorship or otherwise, that could affect the research and its results presented in this paper.

CRediT author statement

Ridhuan, K.: Conceptualization, Writing - Original Draft; **Mafruddin**: Data Curation, **Irawan, D.**: Conceptualization Writing - Original Draft, Methodology; **Handono, S.D.:** Writing - Review & Editing.

The final manuscript was read and approved by all authors.

Funding

This work was carried out with financial support from Universitas Muhammadiyah Metro
("Performance Improvement and Emission Reduction of Solar-Biogas Dual-Fuel Diesel Engines")

References

1 Abanades S., Abbaspour H., Ahmadi A., Das A., Ehyaei M.A., Esmaeilion F., El Haj Assad M., Hajilounezhad T., Jamali D.H., Hmida A., Ozgoli H.A., Safari S., Al Shabi M., Bani-Hani E.H. (2022) A critical review of biogas production and usage with legislations framework across the globe. *Int. J. Environ. Sci. Technol.*, 19, 3377 – 3400. https://doi.org/10.1007/s13762-021-03301-6

2 Aydın M., Uslu S., Bahattin Çelik M. (2020) Performance and emission prediction of a compression ignition engine fueled with biodiesel-diesel blends: A combined application of ANN and RSM based optimization. *Fuel*, 269. https://doi.org/10.10.1016/j.fuel.2020.117472

3 Simsek S., Ozdalyan B. (2018) Improvements to the composition of fusel oil and analysis of the effects of fusel oil-gasoline blends on a spark-ignited (SI) engine's performance and emissions. *Energies*, 11 (3). https://doi.org/10.3390/en11030625

4 Simsek S. (2020) Effects of biodiesel obtained from Canola, sefflower oils and waste oils on the engine performance and exhaust emissions. *Fuel*, 265, 117026. https://doi.org/10.1016/j.fuel.2020.117026

5 Uslu S. (2020) Optimization of diesel engine operating parameters fueled with palm oil-diesel blend: Comparative evaluation between response surface methodology (RSM) and artificial neural network (ANN). *Fuel*, 276, 117990. https://doi.org/10.1016/j.fuel.2020.117990

6 Barik D., Murugan S. (2014) Investigation on combustion performance and emission characteristics of a DI (direct injection) diesel engine fueled with biogas-diesel in dual fuel mode. *Energy*, 72, 760–771. https://doi.org/10.1016/j.energy.2014.05.106.

7 Ali R., Raheemah S., Al-Mayyahi N.N. (2020) Numerical Analysis of Combustion Characteristics and Emission of Dual and Tri-Fuel Diesel Engine under Two Engine Speeds. *Jordan Journal of Mechanical and Industrial Engineering*, 14 (2), 205 - 213. Available at: https://www.researchgate.net/publication/343769901

8 Ambarita H. (2017) Performance and emission characteristics of a small diesel engine run in dual-fuel (diesel-biogas) mode. *Case Stud. Therm. Eng.*, 10, 179 – 191. https://doi.org/10.1016/j.csite.2017.06.003

9 Møller H.B., Sørensen P., Olesen J.E., Petersen S.O., Nyord T., Sommer S.G. (2022) Agricultural Biogas Production—Climate and Environmental Impacts. *Sustainability*, 14 (3), 1 - 24. https://doi.org/10.3390/su14031849

10 Abilmazhinov E., Akimzhanov A., Shaiakhmetov E., Anibaev S., Nurgaliyev N., Shakerkhan K., Sailauov D. (2021). Development of the biogas industry and prospects for the implementation of biogas plants in kazakhstan. *Eurasian Physical Technical Journal*, 18, 3(37), 76–82. https://doi.org/10.31489/2021No3/76-82

11 Ali S., Qin Y., Razzaq A., Khan I., Irfan M. (2022) Modeling Factors of Biogas Technology Adoption: A Roadmap Towards Environmental Sustainability and Green Revolution. *Environ. Sci. Pollut. Res.*, 30 (5), 11838–11860. https://doi.org/10.1007/s11356-022-22894-0

12 Kumar A., Daw P., Milstein D. Homogeneous Catalysis for Sustainable Energy: Hydrogen and Methanol Economies. Fuels From Biomass, and Related Topics. *Chem. Rev.*, 122 (1), 385 – 441. https://doi.org/10.1021/acs.chemrev.1c00412

13 He L., Chen L., Dong X., Zhang S., Zhang M., Dai X., Liu X., Lin P., Li K., Chen C., Pan T., Ma F., Chen J., Yuan M., Zhang Yu., Chen L., Zhou R., Han Yu., Chai Z., Wang S.(2021) A nitrogen-rich covalent organic framework for simultaneous dynamic capture of iodine and methyl iodide. *Chem,* 7 (3). 699 - 714. https://doi.org/10.1016/j.chempr.2020.11.024

14 Ga B.V., T.M.T. Bui, Hoang A.T., Nižetić S., Thi T.X.N., Vo A.V. (2021) Hydrogen-Enriched Biogas Premixed Charge Combustion and Emissions in Direct Injection and Indirect Injection Diesel Dual Fueled Engines: A Comparative Study. *J. Energy Resour. Technol.*, 143 (12) , 120907. https://doi.org/10.1115/1.4051574

15 Fop S., McCombie K.S., Wildman E.J., Skakle J.M.S., Irvine J.T.S., Connor P.A., Savaniu C., Ritter C., & Mclaughlin A.C. (2020) High Oxide Ion and Proton Conductivity in a Disordered Hexagonal Perovskite. *Nat. Mater.*, 19 (7), 752–757. https://doi.org/10.1038/s41563-020-0629-4

16 Golmakani A., Nabavi S.A., Wadi B., Manović V. Advances, Challenges, and Perspectives of Biogas Cleaning, Upgrading, and Utilisation. *Fuel*, 317, 123085. https://doi.org/10.1016/j.fuel.2021.123085

17 Dahlgren S. Biogas-Based Fuels as Renewable Energy in the Transport Sector: An Overview of the Potential of Using CBG, LBG and Other Vehicle Fuels Produced From Biogas. *Biofuels*, 13 (5), 587 – 599. https://doi.org/10.1080/17597269.2020.1821571

18 Nayak S.K., Hoang A.T., Nižetić S., Nguyen X.P., Le T.H. (2022) Effects of advanced injection timing and inducted gaseous fuel on performance, combustion and emission characteristics of a diesel engine operated in dual-fuel mode. *Fuel*, 310, 122232. https://doi.org/10.1016/j.fuel.2021.122232

19 Kurniawan M.A., Yuvenda D., Sudarmanta B. (2019) The Effects CNG Injection Timing on Engine Performance and Emissions of A Diesel Dual Fuel Engine. *Journal for Technology and Science*, 30 (2), 64 - 67. https://doi.org/http://dx.doi.org/10.12962/j20882033.v30i2.4996

20 Wang Z., Zhang F., Xia Y., Wang D., Xu Y., Du G. (2021) Combustion phase of a diesel/natural gas dual fuel engine under various pilot diesel injection timings. *Fuel*, 289, 119869. https://doi.org/10.1016/j.fuel.2020.119869

21 Arbi Trihatmojo, A., Sudarmanta B. Muraza O. (2023) Performance and Combustion Process of a Dual Fuel Diesel Engine Operating with CNG-Palm Oil Biodiesel. *Journal of Railway Transportation and Technology*, *2*(1), 10–20. https://doi.org/10.37367/jrtt.v2i1.22

22 Liu J., Ma B., Zhao H. (2020) Combustion Parameters Optimization of a Diesel/Natural Gas Dual Fuel Engine Using Genetic Algorithm. *Fuel*, 260, 16365. https://doi.org/10.1016/j.fuel.2019.116365

23 Experimental investigation on the combustion and exhaust emission characteristics of biogas–biodiesel dual-fuel combustion in a CI engine. *Fuel Process. Technol.*, 92 (5), 992–1000. https://doi.org/10.1016/j.fuproc.2010.12.021.

24 Liu Y., Chen Y., Tian Y., Sakthivel T., Liu H., Guo S., Zeng H., Dai Z. (2022) Synergizing hydrogen spillover and deprotonation by the internal polarization field in a MoS2/NiPS3 vertical heterostructure for boosted water electrolysis. *Adv. Mater.,* 34, 2203615. https://doi.org/10.1002/adma.202203615

25 Yousefi A., Guo H., Dev S., Lafrance S., Liko B. (2022) A study on split diesel injection on thermal efficiency and emissions of an ammonia/diesel dual-fuel engine. *Fuel*, 316, 123412. https://doi.org/10.1016/j.fuel.2022.123412

26 Papagiannakis R.G., Hountalas D.T. (2004) Combustion and exhaust emission characteristics of a dual fuel compression ignition engine operated with pilot Diesel fuel and natural gas. *Energy Conversion and Management,* 45, 2971–2987. https://doi.org/10.1016/j.enconman.2004.01.013

27 Leykun M.G., Mekonen M.W. (2022) Investigation of the Performance and Emission Characteristics of Diesel Engine Fueled with Biogas-Diesel Dual Fuel. *Fuels*, 3 (1), 15 – 30. https://doi.org/10.3390/fuels301000

28 Simsek S., Uslu S. (2020) Investigation of the impacts of gasoline, biogas and LPG fuels on engine

performance and exhaust emissions in different throttle positions on SI engine. *Fuel*, 279, 118528. https://doi.org/10.1016/j.fuel.2020.118528

29 Mohsin R., Majid Z.A., Shihnan A.H., Nasri N.S., Sharer Z. (2014) Effect of biodiesel blends on engine performance and exhaust emission for diesel dual fuel engine. *Energy Convers. Manag.*, 88, 821 – 828. https://doi.org/10.1016/j.enconman.2014.09.027

30 Ridhuan K., Mafruddin, D.W., Wawan A.Ya., Rusman T.P., Asroni and Irawan D. (2023) The Effect of Gasoline Fuel and Biogas on Engine Performance and Exhaust Emissions. *ARPN J. Eng. Appl. Sci.*, 18 (10), 1089–1094. https://doi.org/10.59018/0523142

AUTHORS’ INFORMATION

Ridhuan, Kemas – Master (Eng.), Lecturer, Department of Mechanical Engineering, Universitas Muhammadiyah Metro, Lampung, Indonesia. Scopus Author ID: 58489991900; https://orcid.org/0009-0003-3291-2469; kmsridhuan@yahoo.co.id.

Mafruddin – Master (Eng.), Lecturer, Department of Mechanical Engineering, Universitas Muhammadiyah Metro, Lampung, Indonesia; Scopus Author ID: 58553788800; https://orcid.org/0009-0001-1327-8410; mafruddinmn@gmail.com.

Irawan, Dwi – Master (Eng.), Lecturer, Department of Mechanical Engineering, Universitas Muhammadiyah Metro, Lampung, Indonesia. Scopus Author ID: 58489732600; https://orcid.org/0009-0007-9019-2884; Irawan.ke10@gmail.com.

Handono, Sulis Dri – Master (Eng.), Lecturer, Department of Mechanical Engineering, Universitas Muhammadiyah Metro, Lampung, Indonesia. Scopus Author ID: 59489842300; https://orcid.org/0009-0000-2647-4309; esdehaa@gmail.com

EURASIAN PHYSICAL TECHNICAL JOURNAL

2025, Volume 22, No. 1 (51)

https://doi.org/10.31489/2025N1/76-82

Received: 30/07/2024 Revised: 23/12/2024 Accepted: 18/03/2025 Published online: 31/03/2025

Research Article

UDC 537.322

DETECTION ALGORITHM FOR FAULTY CONTACT JOINTS IN ELECTRICAL NETWORK

Soldatov A.I.[1], Soldatov A.A.[1], Kostina M.A.[1], Abouellail A.A.[2], Bortalevich S.I.[3]

[1] Tomsk State University of Control Systems and Radioelectronics, Tomsk, Russia,
[2] Sphinx University, New Asyut, Egypt,
[3] Market Economy Institute, Russian Academy of Sciences, Moscow, Russia
*Corresponding author: mariyakostina91@mail.ru

Abstract. *The article proposes a thermoelectric method for monitoring the contact resistance of contact joints in power grids. It describes an algorithm to detect faulty contact joints with resistance exceeding the value specified in regulatory standards. The algorithm is considered using the example of a circuit containing five contact joints and three electrical installations. The algorithm is based on calculating contact resistance from the measured values of thermoelectromotive force and flowing current only at the moment the electrical installation is turned on, which makes it possible to calculate the resistance of the contact through which the electrical installation is connected. By the number of electrical installations being turned on or off, the numbers of the contact joints that make up the power supply circuit of this installation are determined.*

Keywords: contact joint, power supply network, thermoelectromotive force, algorithm.

1. Introduction

Power grids are integral to any technological process, where electricity is supplied to consumers via networks of power lines, whose length may reach thousands of kilometers. This creates certain complications due to conductor connections, which become inevitable. There are two types of connections: detachable and permanent. Permanent connections include crimping, soldering, and welding. Detachable connections include twisting, bolted connection, terminal block connection, plug-socket connection, etc. When operating such connections, malfunctions may occur in the form of high electrical contact resistance (ECR), which is one of the main causes of fires in electrical installations. The number of fires that occurred as a result of violations of the rules for operating electrical equipment is steadily increasing. Thus, in Russia, for instance, the number of fires increased from 41,317 in 2016 to 51,930 in 2021 [1]. The death toll was 2,289 people in 2021 alone, and the number of injured was 2,545. The material damage caused amounted to over 15 billion Russian Rubles [2]. A similar trend is observed in America, where the number of fires caused by faulty electrical installations in the residential sector alone increased from 43.5 thousand in 2016 to 48.4 thousand in 2021 [3]. In 2019 alone, property damage amounted to about $15 billion [4]. One of the causes of fires in electrical installations is the ignition of contact joints due to increased contact resistance, which leads to excessive heating. The value of contact resistance is regulated by documents RD 34.45-51.300-97 and PTEEP and should not exceed 0.05 Ohm. For explosive premises, the contact resistance should not exceed 0.03 Ohm. The reasons for high ECR occurrence have been investigated [5-9], and various methods to reduce it have been proposed and developed in recent years [10-15]. However, none of these approaches meet modern requirements for monitoring contact resistance or allow monitoring during the operation of electrical installations.

2. Problem Specification

To control the ECR value of a contact joint, the authors proposed using the thermoelectric method [16-19], which consists in the appearance of a thermoEMF signal in contact pairs of dissimilar conductors, due to an increase in temperature when the load current flows through the contact resistance.

It should be noted that the thermoelectric method has not been used previously to monitor contact resistance and was proposed by the authors for the first time. The thermoelectric method is traditionally used to sort finished products by grades of steels and alloys, to testing the quality of heat treatment, to testing the quality of electron beam welding, to testing plastic deformation and to measure temperature [20-23]. More recently, it has been used to monitoring the thermal resistance of the contact pair transistor housing-cooling radiator [24]. Laboratory tests confirmed the feasibility of using the thermoelectric method for real-time monitoring of contact resistance in live power supply networks [17].

However, the power supply system of even one room contains several contact joints, and the appearance of a thermoEMF signal in the power supply network does not allow one to unambiguously determine a faulty contact joint.

It is not economically feasible to use a thermoelectric monitoring device on each contact joints to monitor its resistance, in addition, as a rule, most contact joints that make up the power supply circuit of an electrical installation are located in hard-to-reach places: in distribution boxes, in hidden channels of wall panels, etc., so connecting a contact resistance monitoring device to these contact joints is extremely difficult. A possible solution to this problem would be to use one thermoelectric monitoring device to monitor a group of contact joints. The purpose of this study is to develop a method for detecting faulty contact joints among those being monitored in a power supply network, using one thermoelectric monitoring device. Considering that the thermoelectric monitoring method is used for the first time to monitor the resistance of a contact joint, there are currently no methods for detecting faulty contact joints.

3. Problem-Solving Approach

To detect the contact resistance of the contact joints, the moment of switching on and the number of the electrical installation (loads) are determined by the presence of current flowing through this electrical installation, the obtained data about the switched-on electrical installation and the amount of flowing current is transferred to the microcontroller, and the change in thermoEMF is analyzed when each electrical installation is turned on and off. By the number of the electrical installation being turned on or off, the numbers of the contact joints that make up the power supply circuit of this installation are determined. For example, consider the power supply circuit of three electrical installations with a system for monitoring the contact resistance of the contact joints (Fig. 1).

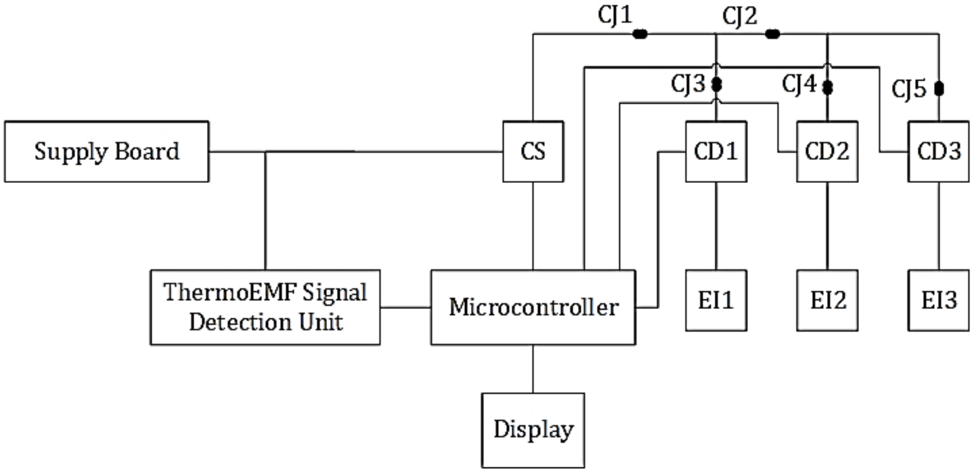

Fig.1. Power supply diagram of three electrical installations with a contact resistance monitoring system

The circuit contains an input panel, a current sensor (CS), contact joints CJ1...CJ5, current detectors CD1...CD3, three electrical installations EI1, EI2 and EI3, a thermoEMF signal detection unit, a microcontroller and a display. The first electrical installation is connected to the input panel through a current sensor (CS), contact joints CJ1 and CJ3, and a current detector CD1. The second electrical installation is connected to the input panel through a current sensor (CS), contact joints CJ1, CJ2, and CJ4, and a current detector CD2. The third electrical installation is connected to the input panel through a current sensor (CS), contact joints CJ1 and CJ5, and a current detector CD3.

When the first electrical installation is turned on, current flows through the current sensor (CS), contact joints CJ1 and CJ2, current detector CD1, and the first electrical installation. The thermoEMF signal detection unit separates the thermoEMF signal from the total signal of the power supply network and transmits it to the microcontroller. The microcontroller reads this signal only when the first electrical installation starts. The moment the electrical installation is turned on is determined by the start of current flow detected by the current detector CD1. The microcontroller also receives data from the current sensor. The microcontroller determines the current flowing through the first electrical installation by subtracting the current before switching on from the current after switching on. The resulting value is stored in the memory of the microcontroller. A similar procedure is carried out when turning off the first electrical installation. Based on the received data on the current value and thermoEMF, the microcontroller calculates the contact resistance. Since the first electrical installation is connected to the input panel through two contact joints CJ1 and CJ3, two options are possible: first - only the current of the first electrical installation flows through the contact joints CJ1, i.e. the second and third electrical installations are not turned on. In this case, the microcontroller can only calculate the total resistance of the two contact joints. In the second case, the second or third electrical installation, or both together, may be turned on. In this case, the resistance of the contact joint CJ1 does not affect the value of thermoEMF and the microcontroller calculates the resistance of the contact joint CJ3.

When the second electrical installation is turned on, current flows through the current sensor (CS), contact joints CJ1, CJ2, CJ4, current detector CD2 and the second electrical installation. The thermoEMF signal detection unit separates the thermoEMF signal from the total signal of the power supply network and transmits it to the microcontroller. The microcontroller reads this signal only when the second electrical installation starts. The moment the electrical installation is turned on is determined by the start of current flow detected by the current detector CD2. The microcontroller also receives data from the current sensor. The microcontroller determines the current flowing through the second electrical installation by subtracting the current before switching on from the current after switching on. Considering the fact that the second electrical installation is connected to the input panel through the contact joints CJ1, CJ2, and CJ4, four options are possible for calculating the contact resistance. First case: only the second electrical installation is turned on. In this case, the microcontroller can only calculate the total resistance of the three contact joints. The second case is when the first electrical installation is turned on. In this case, the total resistance of the contact joints CJ2 and CJ4 is calculated. The third case is when the third electrical installation is turned on. In this case, the resistance of the contact joint CJ4 is calculated. Fourth case: the first and third electrical installations are turned on. In this case, the resistance of the contact joint CJ4 is calculated. The resulting value is stored in the memory of the microcontroller. A similar procedure is carried out when turning off the second electrical installation.

When the third electrical installation is turned on, current flows through the current sensor (CS), contact joints CJ1, CJ2, and CJ5, current detector CD3 and the third electrical installation. The thermoEMF signal detection unit separates the thermoEMF signal from the total signal of the power supply network and transmits it to the microcontroller. The microcontroller reads this signal only when the third electrical installation starts. The moment of switching on the third electrical installation is determined by the start of current flow detected by the current detector CD3. The microcontroller also receives data from the current sensor. The microcontroller determines the current flowing through the third electrical installation by subtracting the current before switching on from the current after switching on. Taking into account the fact that the third electrical installation is connected to the input panel through the contact joints CJ1, CJ2, and CJ5, four options are possible for calculating the contact resistance. First case: the first and second electrical installations are not turned on. In this case, the total resistance of the three contact joints CJ1, CJ2 and CJ5 is calculated. Second case: the first electrical installation is turned on. In this case, the total resistance of the two contact joints CJ2 and CJ5 is calculated. The third case is when the second electrical installation is turned on. In this case, the resistance of the contact joint CJ5 is calculated. Fourth case: the first and second electrical installations are turned on. In this case, the resistance of the contact joint CJ5 is calculated. The resulting value is stored in the memory of the microcontroller. A similar procedure is carried out when turning off the second electrical installation. The operating algorithm of the contact joint resistance monitoring system is presented in Fig. 2.

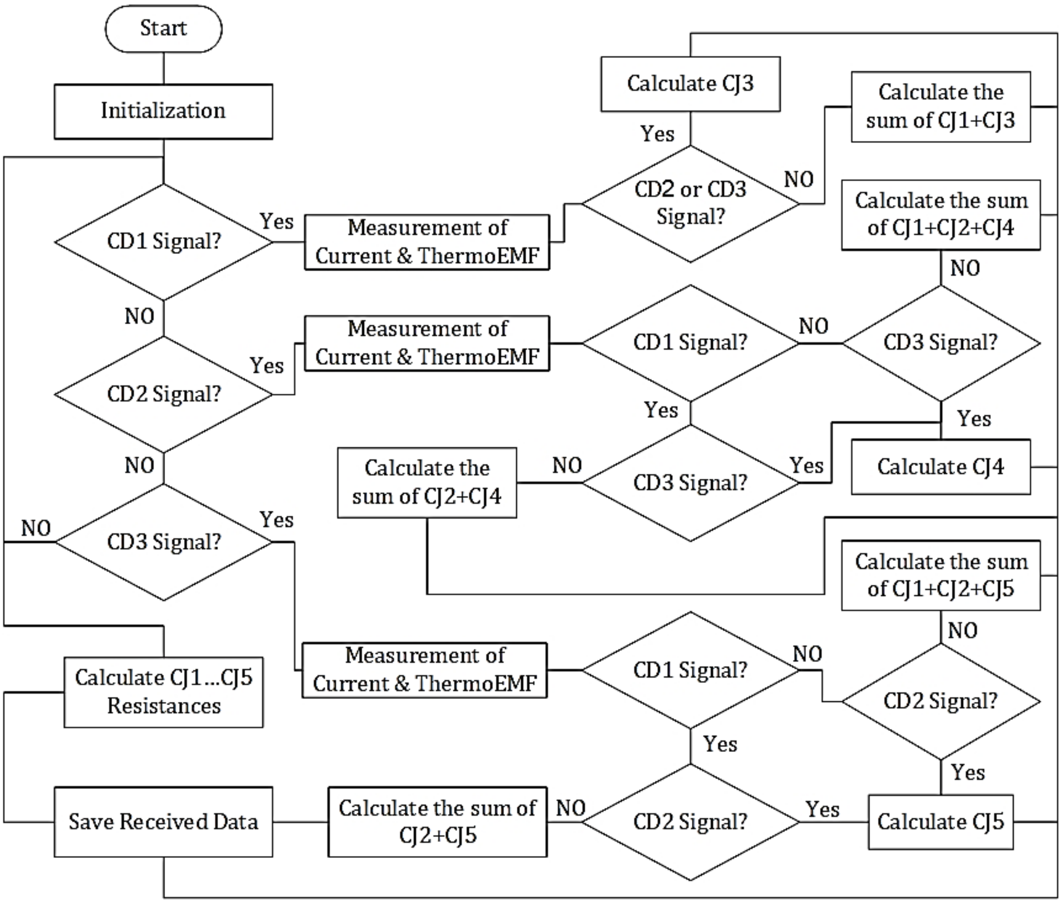

Fig.2. Algorithm of operation of the contact-joint resistance monitoring system

The process of calculating the resistances of contact joints CJ1, CJ2, CJ3, CJ4, and CJ5 from the obtained data includes solving several equations. When the first electrical installation is turned on and the second and/or third are turned on, the contact resistance of CJ3 is determined. When the second electrical installation is turned on and the first and/or third are turned on, the contact resistance of CJ4 is calculated. When the third electrical installation is turned on and the first and/or second are turned on, the contact resistance of CJ5 is calculated. For other combinations of switching on electrical installations, the total resistance of several contacts is calculated, and then the unknown contact resistance is calculated, for example:

$$R_{CJ1} = (R_{CJ1} + R_{CJ3}) - R_{CJ3}$$
$$R_{CJ2} = (R_{CJ2} + R_{CJ4}) - R_{CJ4}$$

For a different wiring diagram for electrical installations, the algorithm is written similarly, considering the presence of specific contact joints. The method for calculating contact resistance was described in detail by the authors [17], where the following expression was obtained for calculating contact resistance from the measured values of thermoEMF and current flowing through the contact joint:

$$R = \frac{K \cdot S \cdot \dfrac{E}{(S_1 - S_2)}}{I^2} \quad (1)$$

where E is the thermoEMF value, S_1 and S_2 are the Seebeck coefficients of the contact pair, I is the current through the contact pair, K is the general heat transfer coefficient, taking into account all its types; S – contact cooling surface area.

4. Experimental Procedure

A practical test of the algorithm's operation was carried out on a device prototype (Fig. 3).

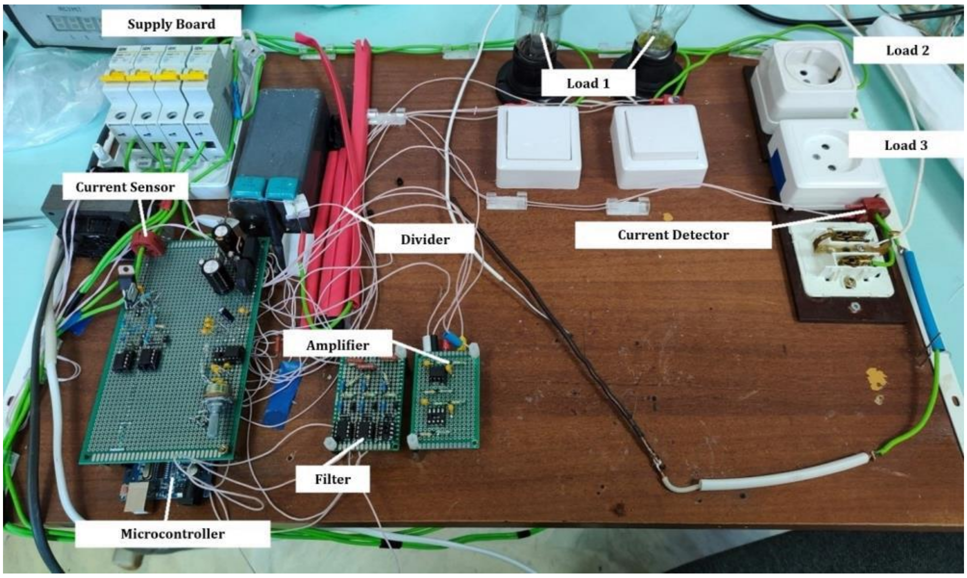

Fig.3. Experimental model of the contact joint resistance monitoring system

The layout contains an input panel, three electrical installations (loads): two incandescent lamps (load 1 with a contact joint in the form of a switch (CJ3)) and two sockets (Cariva 773659 from Legrand) for connecting an electric kettle and an iron (load 2 (CJ4) and load 3 (CJ5)), a current detector, current sensor (ACS758LCB-100B from Allegro), microcontroller, thermoEMF signal detection unit, including a divider, filter and amplifier. Also, two contact joints, CJ1 and CJ2, were artificially introduced in the form of twisting two conductors made of copper and aluminum to correspond to the structural diagram shown in Fig. 1. To increase the contact resistance of CJ1, it was placed in a heat chamber and heated at a temperature of 150 °C for 20 hours. At the same time, an oxide film formed on the surface of the copper conductor and the contact resistance became about 0.4 Ohm. The measurement was carried out with a Rigol DM3068 multimeter. When three electrical installations were turned on and off sequentially, the monitoring system detected the first contact joint CJ1 with a resistance exceeding the permissible value of 0.05 Ohm.

5. Results and Discussion

The presented example, which involves detecting the resistance of contact joints in three electrical installations connected to the power grid via five contact joints, demonstrates a general approach to developing an algorithm for detecting a faulty contact joint. For each room, such an algorithm will be unique, in which it is necessary to take into account the number of electrical installations, the number of contact joints used to connect each electrical installation to the input panel, the number of common contact joints for all electrical installations, the number of common contact joints for several electrical installations. For the system to accurately detect faulty connections, each installation needs a current alarm to pinpoint switching events. These events are crucial because they induce thermoEMF changes in the connecting joints. ThermoEMF changes at other times are likely to be due to switching activity in other installations. Crucially, precise faulty joints detection requires knowledge of the Seebeck coefficient of the metals used in the contact joints.

6. Conclusion

The use of the proposed algorithm for detecting a faulty contact joint in the presented example of a power supply network can be implemented in continuous monitoring of contact joints in the power supply network of an office building or other separate premises. Timely detection of a faulty contact joint will eliminate failures in power grids, ensure trouble-free operation of electrical equipment, eliminate the fire hazard of contact joints, and thereby prevent man-made accidents. The article discusses a general approach to developing an algorithm for monitoring a faulty contact joint. For a specific power supply network, it is necessary to develop a specified algorithm for detecting a faulty contact joint based on the approach proposed by the authors.

Conflict of interest statement
The authors declare that they have no conflict of interest in relation to this research, whether financial, personal, authorship or otherwise, that could affect the research and its results presented in this paper.

CRediT author statement
Kostina M.A.: Formal analysis, Data Curation; **Soldatov A.I.:** Conceptualization, Methodology, Project administration; **Soldatov A.A.:** Investigation, Validation; **Abouellail A.A.:** Software; **Bortalevich S.I.:** Resources.
The final manuscript was read and approved by all authors.

References

1 Pronin S.V. (2021) Analysis of statistical data on fires resulting from emergency operating modes of electrical equipment. *Actual Research*, 38 (65). 11-14. [in Russian]. Available at: https://apni.ru/article/2930-analiz-pozharov-po-prichinam-svyazannim.

2 Chechetkina T.A., Goncharenko V.S., Sibirko V.I., Zagumennova M.V. (2022) The situation with fires in the Russian Federation in 2021. *Fire safety*, 1 (106). 98-115. [in Russian] Available at: https://elibrary.ru/download/elibrary_48100502_ 59795205.pdf.

3 Residential Building Fire Causes (2013-2022). Available at: https://www.usfa.fema.gov/statistics/residential-fires/causes.html (Jan22, 2020).

4 U.S. Fare Statictics. Available at: https://www.usfa.fema.gov/statistics/data-sets/ (Dec16, 2023).

5 Titkov V.V., Bekbaev A.B., Sarsenbaev E.A. (2017) On the possibilities of monitoring non-stationary thermal processes in the contacts of power electrical installations. *Scientific and Technical Bulletin of SPbPU. Natural and engineering sciences*, 23(1). 168-178. [in Russian] Available at: https://engtech.spbstu.ru/userfiles/files/articles/2017/1/16_titkov.pdf.

6 Chaly A.M., Dmitriev V.A., Pavleino M.A., Pavleino O.M. (2013) Heating of high-current electrical contacts by short-circuit shock currents. *Electronic processing of materials*, 49(5). 81–88. [in Russian] Available at: https://cyberleninka.ru/article/n/nagrev-silnotochnyh-elektricheskih-kontaktov-udarnymi-tokami-korotkogo-zamykaniy

7 Chaly A.M., Dmitriev V.A., Pavleino M.A., Pavleino O.M., Safonov M.S. (2016) On the peculiarities of welding and destruction of the surface of high-current contacts by pulsed currents. *Electronic processing of materials*. 52(6). 12-18. [in Russian] Available at: https://cyberleninka.ru/article/n/ob-osobennostyah-svarivaniya-i-razrusheniya-poverhnosti-silnotochnyh-sloistyh-kontaktov-impulsnymi-tokami/viewer

8 Troitskiy O.A., Stashenko V.I., Skvortsov O.B. (2018) Vibrations of conductors during transmission of pulsed electric current and non-destructive testing. *Engineering Journal: Science and innovation electronic scientific and technical publication*. 3. 1-16. [in Russian] Available at: https://doi.org/10.18698/2308-6033-2018-3-1741

9 Chuprova L.V., Ershova O.V., Mullina E.R. (2013) Chemical and technological aspects of the problem of oxidation of copper contacts of electrical equipment operated in water purification workshops. *Young Scientist*, 9 (56). 77-80. [in Russian] Available at: https://moluch.ru/archive/56/7712/

10 Wang J., Wu Z., Mao C., Zhao Y., Yang J., Chen Y. (2018) Effect of electrical contact resistance on measurement of thermal conductivity and wiedemann-franz law for individual metallic nanowires. *Scientific Reports*, 8(4862). https://doi.org/10.1038/s41598-018-23291-9

11 Ren W., Chen Y., Cao S., Cui L., Liang H. (2013) A new automated test equipment for measuring electrical contact resistance of real size rivets. *Holm*, 1-7. https://doi.org/10.1109/HOLM.2013.6651396.

12 Mozgalin N.F. (2010) Electrically conductive lubricants – a reliable measure to reduce the emergency in networks and reduce losses in electrical contacts. *Industrial power engineering*, 11. 13-16. [in Russian] Available at: https://elibrary.ru/item.asp?id=20600601

13 Belyaev V.L., Shalaginov A.A. (2014) Investigation of the effect of electrically conductive lubricants on the resistance of high-current contact systems of electrolyzers and electrical apparatus. *Industrial power engineering*, 5. 34-37. [in Russian] Available at: https://labhcs.narod.ru/prom_energetika5-2014.pdf

14 Sivkov A.A., Shanenkova Y.L., Saygash A.S., Shanenkov I.I. (2016) High-speed thermal plasma deposition of copper coating on aluminum surface with strong substrate adhesion and low transient resistivity. *Surface and Coatings Technology*, 292. 63-71. https://doi.org/10.1016/j.surfcoat.2016.03.029

15 Sivkov A.A., Saigash A.S., Kolganova Yu.L. (2013) The influence of the properties of a copper coating on an aluminum contact surface on the transient resistance. *Electrical engineering*, 8. 11-14. [in Russian] Available at: https://elibrary.ru/download/elibrary_19405835_44481637.pdf.

16 Soldatov A.I., Soldatov A.A., Kostina M.A., Bortalevich S.I., Loginov E.L. (2018) Method of non-destructive testing of faults in the electrical network. Patent of the Russian Federation No.2656128. [in Russian] Available at: https://elibrary.ru/download/elibrary_37372302_67574899.PDF.

17 Abouellail A.A., Chang T., Soldatov A.I., Soldatov, Soldatov, A.A., Kostina M., Bortalevich S. (2022) Laboratory substantiation of thermoelectric method for monitoring contact resistance. *Russian Journal of Nondestructive Testing*, 58(12). 1153-1161. https://doi.org/10.1134/S1061830922700152

18 Obach I.I., Abouellail A.A., Soldatov A.I., Soldatov A.A., Sorokin P.V., Shinyakov Y.A., Sukhorukov M.P. (2019) Monitoring of power supply. *SIBCON 2019 - Proceedings*. 8729572. https://doi.org/10.1109/СИБКОН.2019.8729572

19 Obach I.I., Soldatov A.A. (2018) Monitoring of the electric network using a thermoelectric component. *Collection of selected articles of the scientific session of TUSUR*. 1-2. 60-62. [in Russian] Available at: https://elibrary.ru/download/elibrary_36415407_25063302.pdf.

20 Carreon H. (2000) Thermoelectric detection of spherical tin inclusions in copper by magnetic sensing. *Journal of Applied Physics*, 88(11). 6495. https://doi.org/10.1063/1.1322591

21 Nagy P.B. (2010) Non-destructive methods for materials' state awareness monitoring. *Insight: Non-Destructive Testing and Condition Monitoring*, 52(2). 61-71. https://doi.org/10.1784/insi.2010.52.2.61

22 Li J.F., Liu W.S., Zhao L.D., Zhou M. (2010) High-performance nanostructured thermoelectric materials. *Npg Asia Mater.*, 2(4). 152-158. https://doi.org/10.1038/asiamat.2010.138

23 Carreon H., Medina A. (2007) Nondestructive characterization of the level of plastic deformation by thermoelectric power measurements in cold-rolled Ti–6Al–4V samples. *Materials Science, Nondestructive Testing and Evaluation*, 299-311. https://doi.org/10.1080/10589750701546960

24 Abouellail A.A., Chang J., Soldatov A.I., Soldatov A.A., Kostina M.A., Vasiliev I.M. (2023) Thermoelectric monitoring of thermal resistance in electronic systems. *Eurasian Physical Technical Journal*, 20(3(45) 52-61. https://doi.org/10.31489/2023No3/52-61

AUTHORS' INFORMATION

Soldatov, A.A.– Candidate of techn. sciences, Associate Professor, Tomsk State University of Control Systems and Radioelectronics, Tomsk, Russia; https://orcid.org/0000-0003-0696-716X; soldatov.88@bk.ru

Soldatov, A.I.– Doctor of techn. sciences, Professor, Tomsk State University of Control Systems and Radioelectronics, Tomsk, Russia, Tomsk, Russia; https://orcid.org/0000-0003-1892-1644; asoldatof@mail.ru

Kostina, M.A. – Candidate of techn. sciences, Associate Professor, Tomsk State University of Control Systems and Radioelectronics, Tomsk, Russia; https://orcid.org/0000-0003-2626-6002; mariyakostina91@mail.ru

Abouellail, A.A. - Candidate of techn. sciences, Lecturer, Sphinx University, New Asyut, Egypt; https://orcid.org/0000-0002-9357-6214; ahmed.abouellail@sphinx.edu.eg

Bortalevich S.I. - Doctor of econ. sciences, Professor, Market Economy Institute, Russian Academy of Sciences, Moscow, Russia; https://orcid.org/0000-0002-2978-7797; 680097@inbox.ru

EURASIAN PHYSICAL TECHNICAL JOURNAL

2025, Volume 22, No. 1 (51)

https://doi.org/10.31489/2025N1/83-92

Received: 05/10/2024 Revised: 04/12/2024 Accepted: 18/03/2025 Published online: 31/03/2025

Research Article

UDC53.043

CHOICE RATIONALE OF MATERIALS FOR ROAD MARKING IN ORDER TO DEVELOP ITS PRODUCTION TECHNOLOGY

Merkulov V.V. [1], Ulyeva G.A. [1,2], Yakovleva D.A. [1], Volokitina I.E.[1,*]

[1] Karaganda Industrial University, Temirtau, Kazakhstan
[2] JSC ‘Qarmet’, Temirtau, Kazakhstan
**Corresponding author:* irinka.vav@mail.ru

Abstract. *The article is devoted to the study of coating for road markings. Because road marking coatings are highly weatherproof, resistant to temperature extremes, moisture resistance, and good anti-corrosion properties, they can be used to protect exposed steel structures, but their main purpose is to apply road markings. When choosing the type of materials for marking, it is important to take into account their technical characteristics. It is very important that the markings are clearly visible at any time of the day. During the day, visibility is affected by the size and brightness of the markup. This work describes a series of laboratory experiments with samples coated with paints and reveals their protective properties in contact with water and acid. The highest quality coverage was also identified. Work in this direction continues. Thus, the authors are currently conducting experiments to develop a polymer coating for the protection of concrete and concrete products.*

Keywords: coating, road markings, corrosion resistance, polymer, polymer coating.

1. Introduction

Everything in the world does not stand still, new technologies are constantly being developed, both in metallurgy [1- 5], engineering [6 - 8] and construction [9, 10]. One of the main problems is road surfaces and the durability and wear resistance of road markings. For the first time marking as a method of road traffic organization was applied in the early XIX century in Great Britain. In Shrewsbury, a row of white stones was laid on a small width of a bridge, marking the central line. In the XX century (1911) road markings began to be practiced in the United States of America.In Russia, the use of highway graphics began in 1933, when "piece-lines" made of nitro paint began to appear on Moscow streets. The first were Teatralnaya square and exits from Neglinka and Petrovka to Kuznetsky bridge [11, 12].

In the age of high speeds, the main reason for the accelerated pace of development of new technologies for pavements has been people's need for efficient transportation routes [13]. Infrastructure provision in the city needs to start with transportation routes. For this reason, special services pay special attention to signage on roads that are responsible for the safety of all road users. Road markings remain one of the most important elements in this system. It is used to ensure the regulation of traffic on the road. Road markings remain visible even in the dark through the use of special paint. The paint allows you to create distinct lines that are visible to the driver and signal to him how to behave on a particular section of the road [14].

The main functional purpose of quality road markings is to provide effective visual information to motorists and other road users in various conditions [15-18]. Traffic safety and road capacity depend to a large extent on the quality and condition of road markings. Road markings occupy a significant place within the technical means of traffic organization and are an integral part of the normal optical perception of a modern highway. Most importantly road markings shall be durable in terms of functionality [19].

The functional durability of road markings does not exceed two years, the cost of marking works is a significant part of the operational costs of road maintenance, and the time of their implementation is limited to the warm season of the year, especially in the northern regions of the Republic of Kazakhstan. During marking works, traffic conditions are significantly deteriorated, traffic safety is reduced, the cost of transportation is increased, and the environmental situation on adjacent road sections is worsened due to congestion. For these reasons, the problem of improving the functional durability of road markings is very relevant.

For example, the practical experience of using thermoplastic materials for markings in domestic and some CIS countries shows that a significant part of the destruction of markings made of thermoplastics is cracking with subsequent detachment of the material from the road surface. This is largely due to the imperfection or complete lack of methods for assessing the quality parameters of the materials used for road markings. These circumstances indicate the relevance of the development and improvement of methods of obtaining, testing and standardization of requirements for materials used for road markings [20]. The performance of coatings for road markings has been established through a series of laboratory experiments. An important research objective is to select the best quality pavement to improve the performance of road markings. Purpose of the work. Selection and formulation of initial components for road markings. The materials for pavements currently in existence are summarized in Table 1 [21 - 29].

Table 1. Road marking materials

Name	Advantage	Disadvantage	Note
Paints (Figure 1)	low cost of material per unit area of marking compared to the use of plastic materials; technological equipment for its application, short drying time; the possibility of stencil application of complex in configuration marking elements; brightness; easy to apply and use.	availability of non-ecological, flammable organic solvents (up to 60%); lack of light fastness and reflective effect (does not glow in the dark); rapid abrasion (service life is 3-8 months); at the same time, not suitable for busy federal high ways.	
Thermo-plastics (Figure 2)	does not contain solvents; has much greater functional durability than in the case of paints; brightness; layer thickness; ease and speed of application.	the need to heat up the material before use with special devices for infrared heating of asphalt concrete pavements; precise compliance with the plastic heating temperature and time for its melting and mixing.	flow properties of thermoplastics necessary for marking are acquired as a result of melting at 150-220°C.
Cold-plastics (Figure 3)	do not require heating for their application; as a result of their mixing, a material is formed that creates elements of horizontal road markings; have a good prospect of use in various climatic conditions; frost resistant; economical; has high adhesion and homogeneity of the layer.	high cost and small number of machines; use of marking machines with a special unit for mixing hardener and plastic; complete release of the node from plastic within a short period of time (30-60 minutes).	they are an alternative to plas-tics; in its original form it is a fluid mixture of basic components and a separately supplied hardener
Polymer-tapes (Figure 4)	high and consistent quality.	have not found wide application; the cost is very high and exceeds the cost of cold plastics.	are used on an experimental basis; careful compliance with the marking technology is required.
Light reflectors (cataphotes) (Figures 5, 6)	clearly visible in bright sunlight and dark night, which increases safety in any weather; increased service life by 10-15% due to the presence of glass beads; significantly increase the grip of car tires with the surface of the highway; does not contain organic solvents in contrast to paint, so it is not flammable and absolutely safe in terms of the environment.	fixed artificial lighting, when the significance of retro reflective parameters is reduced to a certain extent; precise compliance with the application technology; dependence on weather conditions; long drying time; rapid abrasion and high cost; moreover; the service life does not exceed 3-9 months.	glass beads with a diameter of (0.05-1.50 mm) are used to give the markings retro reflective properties.

Scientific novelty consists in the fact that in the proposed formulation of road markings there is a polymer matrix coating consisting of vinyl-n-butyl ether (VBE), which is a low-temperature additive at the molecular level, that is, provides elasticity of the coating at low temperatures and improves adhesive properties, which leads to an increase in the service life of road marking compositions. The presence of titanium and zinc metal oxides in the composition increases the corrosion resistance of these road markings.

The most important characteristics of road markings are the parameters that determine their visibility. During daylight hours, the visibility of the marking is characterized by its size, contrast of color and brightness (brightness factor) of the marking and the pavement on which it is applied (GOST R 51256-99), to which is also normalized the value of the brightness factor (or visibility factor in diffuse daylight and artificial illumination) depending on the characteristics of the road - its category, the material of the top layer of the pavement and the color of the marking.

Fig. 1. Road markingpaint.

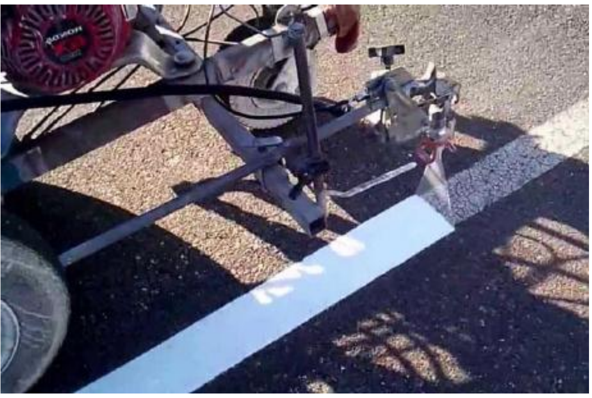

Fig. 2. Thermoplastic.

Fig. 3. Cold-useplastic.

Fig. 4. Polymertape.

Fig. 5. Glassmarbles.

Fig. 6. Glassbeadcoating.

It is now possible to use "structural" markings consisting of separate fragments or having a certain shape in the form of a checkerboard, comb, etc. Such markings provide better visibility of the markings at night when the pavement is wet in the reflected light of vehicle headlights. Another important property of "structural" markings is that when a vehicle wheel collides with it, the driver receives additional information in the form of vibration, which allows the driver to take timely action to return to the lane limits. Such markings are very promising given the country's climatic peculiarities [30].

Table 1 shows that paints and cold plastic are the most popular pavement marking materials for pavement markings. Their main difference is in the application technology. Paints, road enamels and cold plastics are applied at ambient temperature. These materials are applied by the so-called "cold method". The paint is applied to the road surface using a stencil. Road markings developed on the basis of a fluorescent surface and intended for use as directional, warning and/or side markings on roads, streets, embankments or parking lots are discussed in [31]. The markings contain a binder material that fluoresces when irradiated with UV(A) light, and translucent glass granules arranged in the binder material at 50-75% of their size. The size of the glass granules is 0.4-1.0 mm. Such a road marking material should resist water and tire wear during operation.

The authors of the paper propose a technology for road markings containing basic resins - n-butyl acrylate and methyl methacrylate, hardener, reactive resin on the basis of acrylic resins, gas pedal of the curing reaction; in this case the ratio of basic resins and reactive resin is in the range from 1:3 to 3:1. This technology will expand the possibility of using road markings in climatic conditions with reduced temperatures [32].

After analyzing the existing materials for road markings, the authors of this article offer their own technology for creating polymer coating for road markings.

2. Materials and Methods

All countries use white paint for permanent markings, so the university's chemistry lab used white components that were used as pigments. Reflective material (crushed glass) was also incorporated into the pavement to improve the visibility of the markings.

St.3 steel plates were used as samples (according to GOST 5272-82, in which steel plates are the analog samples). This underlayment was chosen because of its low porous permeability compared to asphalt-concrete; if the pavement performs well on steel, the quality performance on asphalt-concrete will be better compared to the experimental performance. (The porous structure of asphalt-concrete allows for improved adhesion properties of the proposed material, which in turn will affect performance). Coatings of different compositions were applied on degreased steel plates; quality control was performed by visual inspection after drying, and samples were tested in aggressive media such as water/NaCl (10% wt.), water/HCl (10% wt.). [35]

The main component of coatings is varnish (copolymer of methyl methacrylate/vinyl butyl ether, copolymer of methyl methacrylate/vinyl butyl ether, maleic anhedride ethyl acetate (solvent), adhesion additives, emulsifying agents), having a liquid or semi-liquid consistency and drying in a thin layer on an object to form a strong film, well resisting various external physical and chemical influences.

Methyl methacrylate and vinyl butyl ether (copolymer 1) were poured into a three-neck flask. After loading 100 g of solvent - ethyl acetate. Then dinitrilazoisobutyric acid polymerization initiator was added. To obtain varnish to coating #1, the components were heated to a temperature of 90 °C, during heating the components should be stirred constantly for their complete dissolution. Copolymerization occurs at slow heating to a temperature of 70-80 °C for 1-2 hours. The retention time after heating was 16 hours. [35]

Similarly, the synthesis of copolymer 2 (methyl methacrylate, vinyl butyl ether, maleic anhydride) with different ratio of initial components was carried out. After dissolution of maleic anhydride, 100 g of solvent, ethyl acetate, was loaded. Pigment powder was obtained by thoroughly abrasion from 5-40 μm using mortar and pestle. The obtained copolymers were mixed with fillers and crushed glass in order to change their technological and operational properties. Coating compositions containing pigments, fillers, retroreflective component and base are given in Table 2. The obtained coatings of different compositions were applied on degreased steel plates made of St.3 steel (according to GOST 5272-68, in which steel plates are the reference samples). This substrate was chosen because of its low porous permeability compared to asphalt concrete; if the coating performs well on steel, the qualitative performance on asphalt concrete will be better compared to the experimental performance. (The porous structure of asphalt concrete can improve the adhesion properties of the proposed material, which in turn will affect the performance properties) [34].

The drying time of the coating on the plates was 24 h. After drying of the coatings, quality control was carried out by visual method. Samples were weighed on analytical scales before and after coating (Table 3).

Table 2. Coating compositions

Component	Coating No. 1	Coating No. 2
Glass	20 g	40 g
Zinc oxide	60 g	20 g
Titanium dioxide	-	20 g
Components for varnish:		
Methylmethacrylate	100 ml	100 ml
Vinylbutylether	40 ml	40 ml
Ethylacetate/solvent	300 ml	
Dinitrilazobisisobutyricacid (DAA)	1.4 g	1 g
Dioxane	-	200 ml
Maleican hydride	-	50g

The purpose and description of the used components included in the polymer coating is given in Table 4.

Table 3. Difference in weight of samples before and after staining, g

Sample weight before staining	Sample weight after staining
$M_1 = 13.4$	$M_1=29.94$
$M_2= 14.2$	$M_2=29.41$

Table 4. Characteristics of varnish components

Material	Description and purpose
Zinc oxide	Has good optical properties and leads to a reduction in material consumption; used to save expensive titanium oxide.
Methylmethacrylate	Complex methyl ester of methacrylic acid; colorless; oily liquid with aromatic odor; easily evaporated and flammable.
Vinylbutylether	Used to produce polymer.
Solvent	A mixture of aromatic hydrocarbons with a small content of naphthenes, paraffins and unsaturated cyclic hydrocarbons; used for dissolving oils, bitumens, rubbers, etc.
Dinitrilazobisisobutyricacid (DAA)	Organic substance of nitrogen compounds and nitriles class; used as an initiator of radical polymerization and other radical reactions.
Dioxane	Good solvent for mineral and vegetable oils, paints; hygroscopic and miscible with water.
Maleican hydride	Raw material for the production of polyester resins; is an important component of varnish [24, 35].

To obtain the varnish for coating No.1, the components (see Table 2) were heated to a temperature of 90°C, during heating the components had to be stirred constantly to dissolve them completely. The settling time after heating was 16 hours. Pigment powder was obtained by thoroughly abrasion from 5-40 μm using mortar and pestle. [35]

3. Results and discussion

After drying of samples exposed to aggressive media (10% aqueous solutions of NaCl and HCl) for 10 days, the corrosion resistance of protective coatings was determined by calculating the corrosion severity and adhesion by the scratch grid method according to GOST 5272-82 (Table 5).

Table 5. Test results

Sample	After 10% aqueous NaCl solution	Corrosion severity	After 10% aqueous HCl solution	Corrosion severity
No.1	After the test, the coating on the sample partially peeled off	3	After the test, the coating peeled off completely	2
No.2	After testing, there was only slight crumbling of the coating, but the coating itself held tightly to the sample and did not peel off	4	After the test there was a typical crumbling of the coating, the coating itself even at light contact leaves white prints. It should be noted that this coating has a good adhesion ability	3

According to Table 5, coating No.2 withstood the effects of aggressive environments, maintaining continuity, unlike polymer coating No.1 (Figures 7) [24, 35, 36].

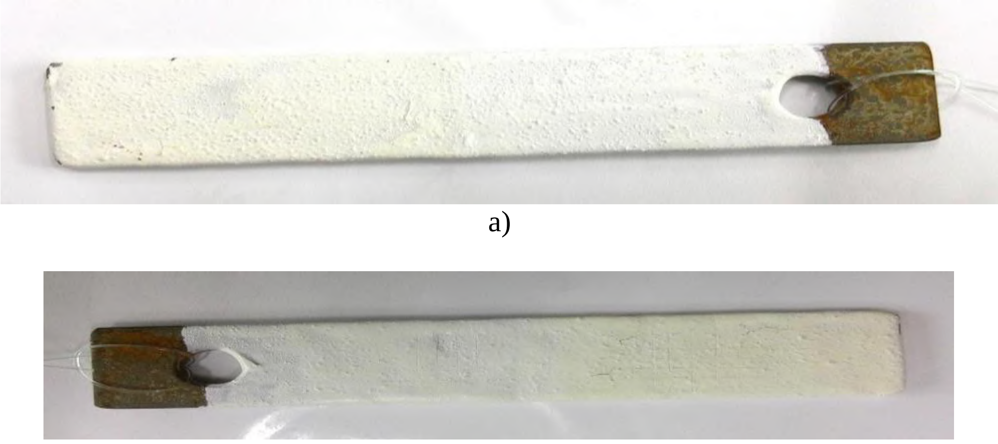

a)

b)

Fig. 7. Coating of sample No. 2 after exposure to a - 10% aqueous NaCl solution, b - 10% aqueous HCl solution

On the scanning electron microscope of the German brand "Zeiss" (JSC "Qarmet") the surfaces of the obtained protective coatings were investigated before and after exposure to aggressive media (Fig. 8-11).

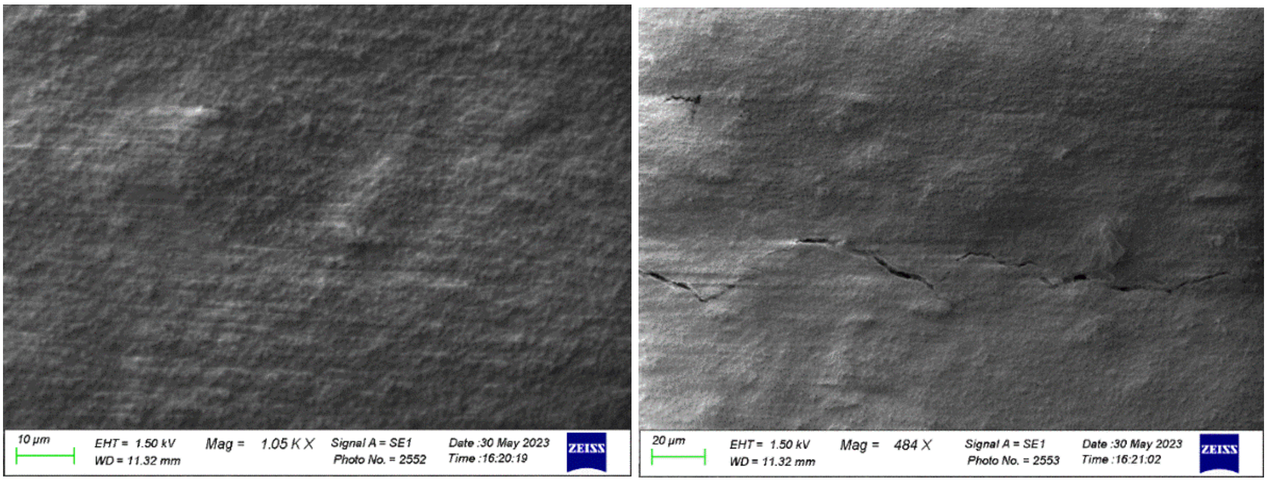

a b

Fig. 8. Polymer coating No.1 before (a, 1000x) and after (b, 480x) exposure to aggressive medium (10% aqueous NaCl solution)

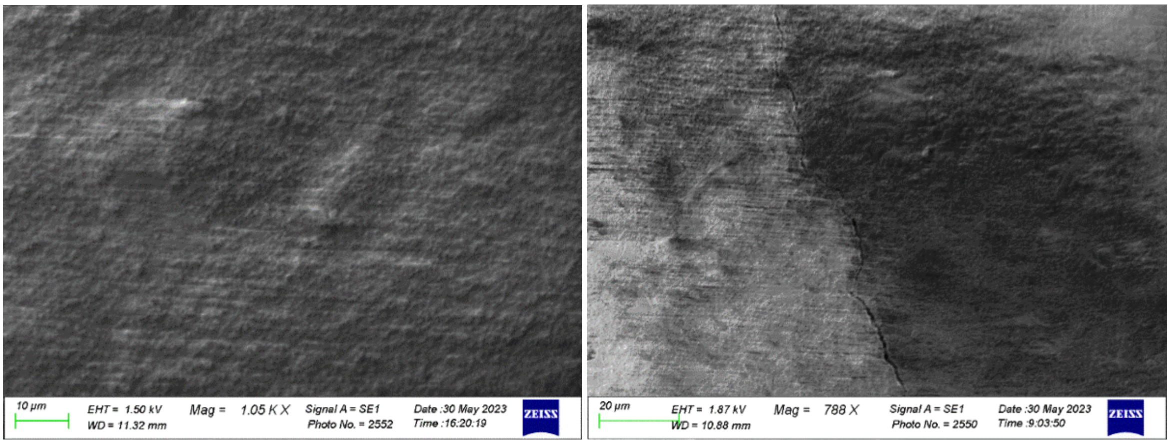

a b

Fig. 9. Polymer coating No.1 before (a, 1000x) and after (b, 780x) exposure to aggressive environment (10% aqueous solution of HCl)

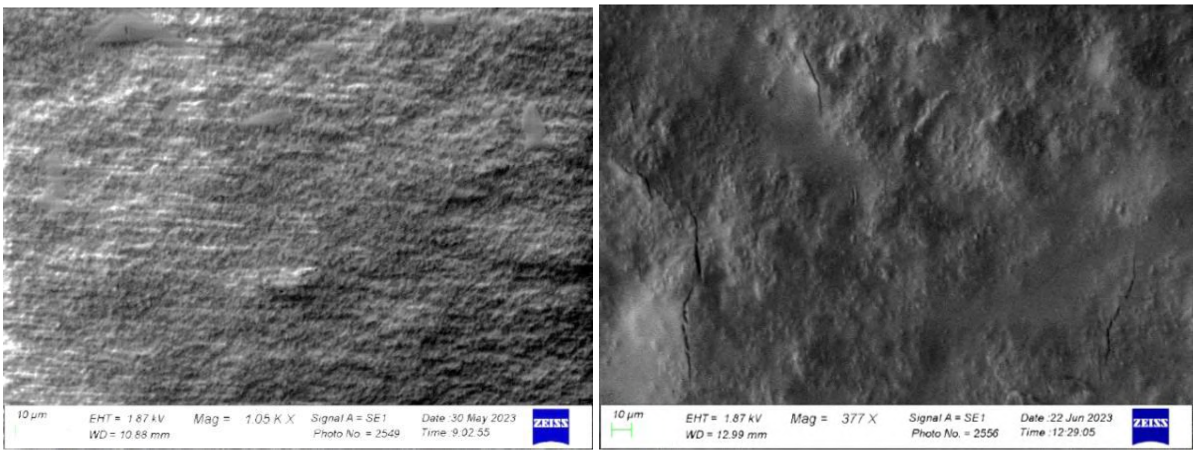

a b

Fig. 10. Polymer coating No.2 before (a, 1000x) and after (b, 380x) exposure to aggressive medium (10% aqueous NaCl solution)

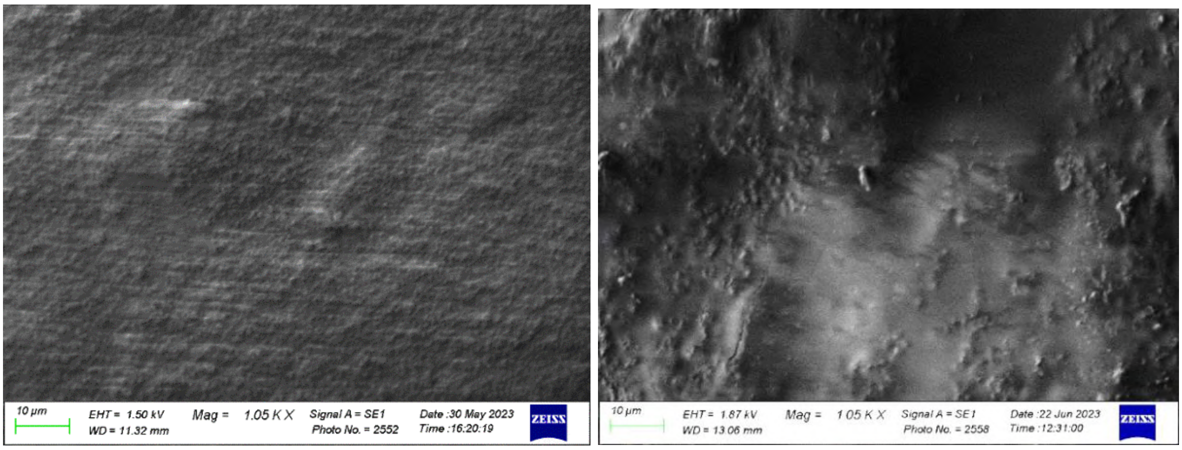

a b

Fig. 11. Polymer coating No.2 before (a, 1000x) and after (b, 1000x) exposure to aggressive environment (10% aqueous HCl solution)

As can be seen from Figures 8-11, the developed coatings No. 1 and No. 2 are homogeneous and solid before exposure to aggressive media. Similar structure has polymer coating No. 2 after exposure to aggressive medium of 10% aqueous solution of HCl (Fig. 11a, b). After exposure to 10% aqueous NaCl solution, polymer coating No.2 has small non-continuities (Fig. 10b). In polymer coating No. 1 after exposure to aggressive medium already at low magnification microcracks are observed in some places, and the coating itself is smooth, homogeneous (Fig. 8b and Fig. 9b).

4. Conclusion

Thus, coating No.2 withstood the exposure to aggressive media of 10% NaCl and HCl aqueous solutions (corrosion score of 3 and 2, respectively), compared to coating No.1 in the same media (corrosion score of 4 and 3, respectively). In this regard, the authors of this work plan to carry out approbation of the obtained results of the laboratory experiment by experimental-industrial means.

Conducting such research will solve the problem of selection of durable, corrosion-resistant, cheap and reliable pavement marking coatings, given the large supply of different materials on the market.

Currently, there are no production facilities for the creation of new polymer systems in Kazakhstan. Creation of such production will allow to receive own protective polymer coatings, solve the problem of choosing durable, corrosion-resistant, cheap and reliable coating for road markings, guarantees the expansion of the raw material base of the country, increase import substitution and, thus, increase the competitiveness of Kazakhstan.

Conflict of interest statement

The authors declare that they have no conflict of interest in relation to this research, whether financial, personal, authorship or otherwise, that could affect the research and its results presented in this paper.

CRediT author statement

Conceptualization, G.U.; Methodology, V.M.; Software, I.V.; Validation, G.A., D.Y and I.V.; Formal Analysis, I.V. and V.M.; Investigation, V.M.; Resources, G.U.; Data Curation, I.V. and V.M.; Writing – Original Draft Preparation, V.M; Writing – Review & Editing, I.V.; Visualization, I.V.; Supervision, D.Y. and V.M.
The final manuscript was read and approved by all authors.

References

1 Volokitina I.E., Volokitin A.V., Latypova M.A., Chigirinsky V.V., KolesnikovA.S. (2023) Effect of Controlled Rolling on the Structural and Phase Transformations. *Progress in Physics of Metals*, 24 (1), 132–156. https://doi.org/10.15407/ufm.24.01.132

2 Ulyeva G.A., Akhmetova G.E., Tuyskhan K. (2021) On the issue of alloying ang modification of alloys: using the waste products for creation of novel materials. *Progress in Physics of Metals*, 22, 2, 271-289. https://doi.org/10.15407/ufm.22.02.271

3 Avelar R.E., Carlson P.J. (2014) Link between pavement marking retro reflectivity and night crashes on Michigan two-lane high ways.*Transportation Research Record: Journal of the Transportation Research Board*, 2404, 59-67. https://doi.org/10.3141/2404-07

4 Carlson P.J., Park E., Kang D.H. (2013) Investigation of longitudinal pavement marking retro reflectivity and safety. *Transportation Research Record: Journal of the Transportation Research Board*, 2337, 59-66. https://doi.org/10.3141/2337-08

5 Kostina M.A., Soldatov A.I., Soldatov A.A., Abouellail A.A. (2024) Simulation of multipoint contact under thermoelectrictesting.*Eurasian Physical Technical Journal*, 21, 1(47). https://doi.org/10.31489/2024No1/93-103

6 Mirabedini S.M., Zareanshahraki F., Mannari V. (2019) Enhancing thermoplastic roadmarking paints performance using sustainable rosin ester. *Progress in Organic Coatings,* 139. https://doi.org/10.1016/j.porgcoat.2019.105454

7 Sersembekov B.K., Kadyrov A.S., Kunayev V.A., Issabayev M.S., Kukesheva A.B. (2024) Experimental comparison of methods for cleaning gas exhaust by exposure using ultrasoung and laser radiation. *Material and mechanical engineering technology*, 3, 44-53. https://doi.org/10.52209/2706-977X_2024_3_44

8 Georgiadi I., Kadyrov A., Kunayev V. (2023) Development of the universal working equipment of the exavator for preparation of materials based on waste during the road building.*Communications. Scientific Letters of the University of Žilina*, 25(2), B62-B76. https://doi.org/10.26552/com.C.2023.022

9 Sapargaliyeva B., Agabekova A., Syrlybekkyzy S., Kolesnikov A., Yerzhanov A., Kozlov P. (2023) Study of changes in microstructure and metal interface Cu/Al during bimetallic construction wire straining. *Case Studies in Construction Materials*. 18, e02162. https://doi.org/10.1016/j.cscm.2023.e02162

10 Kadyrov A., Kunayev V., Georgiadi I., Khaibullin R. (2019) Advanced methods for solving the problems of road construction in central Kaxakhstan.*Techniki Vjesnik*, 26(4), 1159-1163. https://doi.org/10.17559/TV-20170225144013

11 Volokitina I., Bychkov A., Volokitin A., Kolesnikov A. (2023) Natural Aging of Aluminum Alloy 2024 After Severe Plastic Deformation, *Metallography Microstructure, and Analysis*, 12(3), 564-566. https://doi.org/10.1007/s13632-023-00966-y

12 Volokitina I.E. (2021) Effect of Preliminary Heat Treatment on Deformation of Brass by the Method of ECAP. *Metal Science and Heat Treatment*, 63, 163-167. https://doi.org/10.1007/s11041-021-00664-y

13 Ulyeva G.A. (2024) Requirements on carbon-based reducing agents for electrothermal processes. *Coke and chemistry*, 67, 10, 596-606. https://doi.org/10.3103/S1068364X24600982

14 Tomasz E. Burghardt, PashkevichA. (2020) Materials selection for structured horizontal road marking: financial and environmental case studies.*Journal European Transport Research Review*, 11. https://doi.org/10.1186/s12544-020-0397-x

15 Greenhalgh J., Mirmehdi M. (2015) Detection and Recognition of Painted Road Surface Markings.*In Proceedingsof the 4th International Conference on Pattern Recognition Applications and Methods*, 1-9.10.5220/0005273501300138

16 Albert M., Schilling K. (2015) The line coating robot – An automated mobile system for high precision powder coating, 2nd IFAC Conference on Embedded Systems. *Computer Intelligence and Telematics*, 28, 10, 58-62. https://doi.org/10.1016/j.ifacol.2015.08.108

17 Babić D., Burghardt T., Babić D. (2015) Application and characteristics of waterborne road marking paint. *InternationalJournal for Traffic and Transport Engineering*, 5, 150-169. https://doi.org/10.7708/ijtte.2015.5(2).06

18 Burghardt T., Pashkevich A., Mosböck H. (2019) Yellow pedestrian crossings: From innovative technology for glass beads to a new retroreflectivity regulation. *Case Studies on Transport Policy*, 7(4), 862-870. https://doi.org/10.1016/j.cstp.2019.07.007

19 Burghardt T., Pashkevich A., Fiolić M., Żakowska L. (2019) Horizontal road markings with high Retroreflectivity: Durability, environmental, and financial considerations. *Advances in Transportation Studies*, 47, 49-60. https://doi.org/10.13140/RG.2.2.35798.14405

20 Burghardt T.E., Pashkevich A., Żakowska L. (2016) Influence of volatile organic compounds emissions from road marking paint song round-level ozone formation. *Case study of Kraków, Poland. Transportation Research Procedia*, 14, 711-723. https://doi.org/10.1016/j.trpro.2016.05.338

21 Albalate D., Fernández L., Yarygina A. (2013) The road against fatalities: Infrastructure spending vs. regulation. *Accident Analysis and Prevention*, 59, 227-239. https://doi.org/10.1016/j.aap.2013.06.008

22 Cruz M., Klein A., Steiner V. (2016) Sustainability assessment of road marking systems. *Transportation Research Procedia*, 14, 869-875. https://doi.org/10.1016/j.trpro.2016.05.035

23 Burghardt T.E., Pashkevich A., Zakowska L. (2016) Influence of Volatile Organic Compounds Emissions from Road Marking Paints on Ground-level Ozone Formation. *Transportation Research Procedia*, 14, 714-723. https://doi.org/10.1016/j.trpro.2016.05.338

24 Asainova D.A., Merkulov V.V., Akhmetova G.E., Ulyeva G.A. (2021) Secondary Processing of Metallurgical Production Waste to Obtain Refractory Materials. *Inorganic Materials: Applied Research*, 12, 1066-1069. https://doi.org/10.1134/S2075113321040031

25 Yari H., Mohseni M., Messori M. (2015) Toughened acrylic/melamine thermosetting clear coats using POSS molecules: Mechanical and morphological studies. *Polymer*, 63, 19-29. https://doi.org/10.1016/j.polymer.2015.02.040

26 Li H., Ma F., Sun S.-Q. (2015) Tri-level infrared spectroscopic identification of hot melting reflective road marking paint. *Spectroscopy and Spectral Analysis*, 35, 12, 3339-3343. https://doi.org/10.3964

27 Rastiveis H., Shams A., Sarasua W.A., Li J. (2020) Automated extraction of lane markings from mobile LiDAR point clouds based on fuzzy inference. *Journal of Photogrammetry and Remote Sensing*, 160, 149-166. https://doi.org/10.1016/j.isprsjprs.2019.12.009

28 Diamandouros K., Gatscha M. (2016) Rain vision: The impact of road markings on driver behaviour-wet night visibility. *Transportation Research Procedia*, 14, 4344-4353. https://doi.org/10.1016/j.trpro.2016.05.356

29 Calvi A. (2015) A study on driving performance along horizontal curves of rural roads. *Journal of Transportation Safety and Security*, 7(3), 243-267. https://doi.org/10.1080/19439962.2014.952468

30 Burghardt T.E., Ščukanec A., Babić D. (2017) Durability of Waterborne Road Marking Systems with Various Glass Beads, Proceedings of International Conference on Traffic Development. *Logistics and Sustainable Transport*, 51-58. Available at: https://www.esearchgate.net/publication/326587824_Durability_of_waterborne_road_marking_systems_with_ vario

31 Hadizadeh E., Pazokifard S., Mirabedini S.M., Ashrafian H. (2020) Optimizing practical properties of MMA-based cold plastic road marking paints using mixture experimental design. *Progress in Organic Coatings*, 147. https://doi.org/10.1016/j.porgcoat.2020.105784

32 Andrés Coves-Campos, Luis Bañón , José Andrés Coves-García, Salvador Ivorra. (2018) In-Situ Study of Road Marking Durability Using Glass Microbeads and Antiskid Aggregates as Drop-On Materials.*Reseach Gate*, https://doi.org/10.20944/preprints201809.0401.v2

33 Volokitina, I.E., Volokitin, A.V. (2023) Changes in Microstructure and Mechanical Properties of Steel-Copper Wire During Deformation. *Metallurgist*. 67(1-2), 232–239. https://doi.org/10.1007/s11015-023-01510-7

34 Rehna P.C., Harikrishna M., Anjaneyu M.V. (2020) Evaluation of centre line marking on driver behaviour. *Lecture Notes in Civil Engineering*. 45, 607-619. https://doi.org/10.1007/978-981-32-9042-6_48

35 Merkulov V., Ulyeva G., Akhmetova G., Volokitin A. (2024) Synthesis of copolymers for protective coatings. *Journal of Chemical Technology and Metallurgy*. 59(3), 639-646. https://doi.org/10.59957/jctm.v59.i3.2024.18

36 GOST 5272-68 "Corrosion of metals. Terms" - M.: IPK Publishing House of Standards, 1999. [in Russian] Available to: https://echemistry.ru/assets/files/gost/5272-68.pdf

AUTHORS' INFORMATION

Merkulov, Vladimir Vitalievich - Candidate of Chemical Sciences, Department of Chemical Technology and Ecology, Karaganda Industrial University, Temirtau, Kazakhstan, Scopus Author ID: 57751157700, https://orcid.org/0000-0003-0368-3890; smart-61@mail.ru

Ulyeva, Gulnara Anatolievna - Candidate of Technical Sciences, Associate Professor, Department of Metallurgy and Materials Science, Karaganda Industrial University, Temirtau, Kazakhstan, Scopus Author ID: 57211983028, https://orcid.org/0000-0002-3600-1318; g.ulyeva@tttu.edu.kz

Yakovleva, **Diana Amangeldievna** - Master, Researcher, Karaganda Industrial University, Temirtau, Kazakhstan; https://orcid.org/0009-0008-3791-6692; asainova97.da @gmail.com

Volokitina, Irina Evgenievna - PhD, Professor, Department of Metallurgy and Materials Science, Karaganda Industrial University, Temirtau, Kazakhstan, Scopus Author ID: 55902810800, https://orcid.org/0000-0002-2190-5672; irinka.vav@mail.ru

EURASIAN PHYSICAL TECHNICAL JOURNAL

2025, Volume 22, No. 1 (51)

https://doi.org/10.31489/2025N1/93-102

Received: 04/12/2024 Revised: 19/02/2024 Accepted: 18/03/2025

Research Article

UDC 534.8.081.7+669

INVESTIGATION OF SOME PHYSICAL AND STRUCTURAL PROPERTIES OF MELTS BY ULTRASOUNDS

Kazhikenova S.Sh., Shaikhova G.S., Shaltakov S.N.

Karaganda Saginov Technical University, Karaganda, Kazakhstan
*Corresponding author: sauleshka555@mail.ru

Abstract. *A modern effective way of influencing molten metal is ultrasonic treatment - a type of dynamic influence on liquid and crystallizing metal. At certain parameters of the intensity of ultrasonic treatment, which causes acoustic cavitation of the liquid metal, the refining process actively occurs. Moreover, powerful ultrasound allows, during the modification process, to introduce various composite elements and refractory alloys into the metal, acting directly on the crystal lattice. The calculations carried out on the properties of elastic waves make it possible to identify such features in the behavior of the sound absorption coefficient polytherms, which with sufficient certainty indicate the absence or presence of structural changes when the melt is heated, and establish the possibility of implementing various mechanisms of structural changes in the same melt in different temperature ranges. The conducted studies of elastic wave energy absorption as well as ultrasound velocity allow us to identify such features in the behavior of sound absorption coefficient polyterms that indicate the absence or presence of structural changes during melt heating. The comparative analyses make it possible to conclude that there is not a single mechanism of structural changes The possibility of implementing various mechanisms of structural changes in the same melt in different temperature ranges is shown.*

Keywords: viscous, liquid metals, ultrasound propagation speed, structural changes, melt.

1. Introduction

Ultrasonic melt processing attracts considerable interest from both academic and industrial communities as a promising route improving melt quality. The significance of this problem is predetermined by the matter liquid state problem. The application of power ultrasound during liquid to solid transformation is believed to be an effective way to improve the solidification microstructures and mechanical properties [1]. In fact, the entire arsenal of modern experimental and theoretical physics is connected to the research of the physicochemical behavior of melts [2]. Acoustic methods are the most promising among experimental methods for research of the matter liquid state. They are simple, reliable, highly sensitive to changes of matter structure and the interatomic interaction. The results of this research make it possible to predict the melts elastic properties of simple substances and extend it to complex substances.

At present, the electrophysical, thermophysical, thermodynamic and viscous properties of liquid semimetals and semiconductors based on the electronics industry have been widely studied. However, the ongoing research in the field of studying these properties is not sufficient to solve the problem of the liquid semimetals and semiconductor’s structure. It is also impossible to obtain an unambiguous result by only structural research. In this aspect, it is known that «modern acoustic research methods are a powerful tool for obtaining information about the structure of melts and semiconductors» [3]. Melts and semiconductors were not widely also studied, since the high-temperature acoustic experiments technology with aggressive melts of semimetals and semiconductors complicated the research process [1–5]. Our research includes: development liquid semimetals and semiconductor's structure model; experimental and theoretical studies of the propagation speed and absorption coefficient of ultrasound temperature dependences in liquid semimetals and semiconductors; regularities generalization of liquid metals, semimetals and semiconductors structural properties.

2. Theory of the Method

The conducted studies of elastic wave energy absorption as well as ultrasound velocity allow us to indicate the absence or presence of structural changes during melt heating.

This work demonstrated the practical importance of acoustic measurements in metal melts. We performed calculations of ultrasonic treatment of molten systems, investigated the physical and chemical effects of ultrasound on the structural properties of liquid molten systems. We found that the chemical effect is an irreversible and permanent change in the atomic weight and atomic-weight distribution due to ultrasound. Calculations showed that with an increase in the ultrasound intensity, the atomic weight of molten metals decreases, while the orientation of atoms along the flow direction decreases. Ultrasonic vibration increases the motion of atoms, a change in the structure of atoms occurs, which makes them more disordered. Ultrasonic vibration affects the relaxation process of molten metals, resulting in a weakening of the elastic effect.

2.1 The practical value of direct acoustic measurements in liquid metals

A hypothesis about the micro-inhomogeneous structure of liquids arose in connection with Stuart's research using X-rays in the 1920. Micro-inhomogeneity extends to any melts from alkali metals to semiconductors. But the hypothesis remained a hypothesis, since there were no interpreted experimental data. The experiments were performed with a solidification apparatus incorporated with ultrasonic generator. The propagation of elastic waves is associated with the fundamental properties of material media, including the mass of particles, their space, the bonds between particles of matter.

Let's consider the Stokes-Kirchhoff formula (1) [7], and transform (1) to (2), (3):

$$\beta = \frac{2\pi^2 f^2}{\rho \mathrm{v}_S^3}\left[\frac{4}{3}\eta + \frac{\chi}{C_P}(\gamma - 1)\right] \tag{1}$$

$$\frac{\beta \mathrm{v}_S}{f^2} = 2\pi^2 \alpha_S \left[\frac{4}{3}\rho\upsilon + \frac{\chi}{\left(\frac{dQ}{dT}\right)_P} m(\gamma - 1)\right]. \tag{2}$$

$$\frac{\beta \mathrm{v}_S}{f^2} = \sigma M_A. \tag{3}$$

$$\gamma = \frac{C_P}{C_V}, \qquad \sigma = 2\pi^2 \alpha_S \left[\frac{4}{3}\frac{\upsilon}{V_A} + \frac{\chi}{\left(\frac{dQ}{dT}\right)_P} N_A(\gamma - 1)\right].$$

χ - is the thermal conductivity coefficient, C_V is the heat capacity at constant volume, C_P - is the heat capacity at constant pressure, υ is the kinematic viscosity, $\frac{1}{\rho \mathrm{v}_S^2} = \alpha_S$ is the adiabatic compressibility, $C_P = \frac{dQ}{dT}\frac{1}{m}$ is the melt heat capacity, N_A is the Avogadro number, M_A is the atomic mass, V_A is the atomic volume,.

These indicators, namely, the inertial factor (mass of particles), the spatial factor (volume per particle), the stiffness factor between particles (compressibility), are sufficient fora general description of elastic waves absorption and propagation speed [6].

2.2 Algorithm of the method

The obtained equation (3) makes acoustic parameters monitoring in simple substances melts more accessible. Experimental measurements monitoring by value using reference data [8-12] is shown in Fig.1.

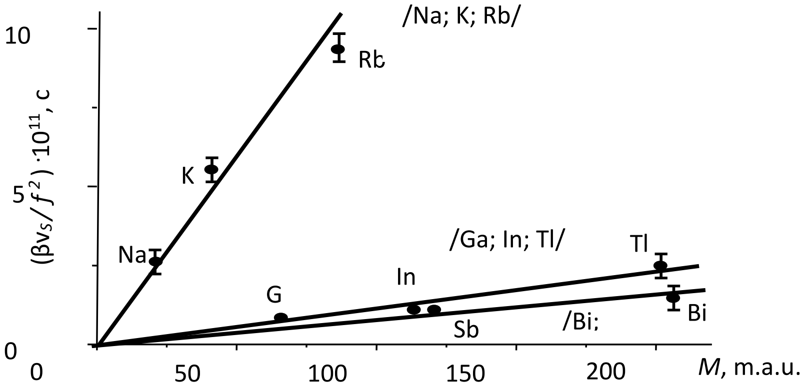

Fig.1. $\frac{\beta \mathrm{v}_S}{f^2}$ – M simple substances dependence at crystallization temperatures

We have established the correlation dependence between measurement results $\frac{\beta \mathrm{v}_S}{f^2}$ and the parameter values M_A, where σ is a constant value for each group. The bonding factors intragroup similarity not only observed in condensed bodies, but also diatomic molecules it. Highest value of the dissociation energy is observed for five electrons in the outer shell, the most rigid bonds exist in diatomic molecules [13].

In the Fig. 1 that the parameter $\frac{\beta \mathrm{v}_S}{f^2}$ increases from *Na* to *Rb* in the alkali metal series is shown. This is confirmed by the fact that these groups of metals tend to loosen the structure with increasing atomic mass M_A. The $\frac{\beta \mathrm{v}_S}{f^2}$ temperature dependence is quite complex. Immediately after melting, there is a decrease in the absorption coefficient of ultrasonic waves, which increases monotonically with increasing temperature. This includes the alkali metals and further all other simple metals that are densely packed in the solid state. Such behavior is natural for all other simple metals and for two-component liquid metal solutions. Metallic melts in which the polytherms of absorption of ultrasonic waves do not increase with increasing temperature belong to the second class, containing semimetals and semiconductors, in which significant changes in their structural properties occur during melting. For example, bismuth, antimony, tellurium are characterized by anomalous behavior of the polytherms of absorption and propagation velocities, therefore structural changes in them continue in a certain temperature range after melting. The experimental results are shown in Fig. 2 - 19 for *Ga, Bi, Sb, Ge, Se, Te, GaSb, InSb,* $Bi_{0,25}Sb_{0,75}$, $Bi_{0,5}Sb_{0,5}$, $Bi_{0,75}Sb_{0,25}$, *Bi-Sb*, $Sn_{0,30}Te_{0,70}$, $Sn_{0,5}Te_{0,5}$, $Sn_{0,70}Te_{0,30}$,, *Sn-Te* compounds. The solid lines are the result of the experimental data approximation by the equation

$$v_S\left(T\right)=v_{SL}-\beta\left(T-T_L\right),$$

$\beta=\frac{dv_S}{dT}$ is the ultrasound propagation speed temperature coefficient, T_L is melting point, v_{SL} is ultrasound propagation speed at T_L.

3. Practical approbation and results

Thus, the acoustic analysis in electron melts experimental measurements shows that the absorption polytherms and the propagation velocity behavior of ultrasonic waves depends on the semimetals and semiconductors acoustic properties. This was the reason for separating these melts into an electron melts separate class. A straight-line relationship between $\frac{\beta \mathrm{v}_S}{f^2}$ and M_A inertial factor has been established.

Ultrasonic vibrations were introduced into the melt continuously during the entire time of exposure perpendicular to the surface, which corresponded to the longitudinal scheme of their introduction in relation to the beam direction and the predominant heat removal from the melt zone. The frequency and intensity of ultrasonic vibrations are selected depending on the specific melt. At an ultrasound intensity of more than $105\frac{W}{m^2}$, the kinetic energy of collapsing bubbles, concentrated in an extremely small volume, is transformed partly into a force impulse and partly into thermal energy. In liquid, when exposed to ultrasonic vibrations, electrokinetic phenomena also arise, caused by the directed movement of charged particles, which affect the diffusion processes and structural properties, in particular the orientation of atoms.

Experimental measurements of the velocity and absorption of ultrasound in liquid were carried out using ultrasonic Doppler velocimetry. To obtain sufficient Doppler signals, the problems of ultrasonic beam passage through a channel wall made of stainless steel, acoustic coupling between the transducer and the channel wall, and wetting of the inner wall surface with liquid metal were studied, respectively. Measuring the sound speed The DOP3000 allows to measure the sound speed in a liquid by measuring with precision the time that is taken by an ultrasonic burst to propagate over a define distance.

The DOP3000 Velocimeter

The propagation of elastic waves is associated with the fundamental properties of material media, including the mass of particles, their space, the bonds between particles of matter. These indicators, namely, the inertial factor (mass of particles), the spatial factor (volume per particle), the stiffness factor between particles (compressibility), are sufficient fora general description of elastic waves absorption and propagation speed [13]. First of all, this is the relationship of the selected factors with the absorption coefficient of ultrasonic waves. For the occurrence of such observations in the behavior of the melts elastic properties, one can use the system analysis methods based on the D.I. Mendeleev Periodic phenomenon.

Gallium has a low melting point, is rather easily supercooled and is a convenient object for studying the structural correspondence of liquids at temperatures above and below the melting point. Fig. 2 show the results of investigations of the absorption coefficient temperature dependence, ultrasound propagation velocity and β_S theoretical values in liquid gallium at 30, 50, 70 MHz frequencies. For comparison, the data on the ultrasound velocity in liquid gallium obtained in [14] are given. The results obtained correlate well with those of the authors [14-16] in Fig. 2.

The polyterm of the ultrasound absorption coefficient in liquid gallium at temperatures 370 K and 545 K has extrema. This indicates structural changes occurring in liquid gallium and noted in [14]. It should be noted that such behavior of the $\frac{\beta}{f^2}$ and v_S polyterms was not observed in metal melts. The totality of these experimental facts indicates the complexity of the structure of liquid gallium. The $\frac{\beta}{f^2}$ and v_S polyterms behavior for liquid gallium is explained by the two-structure liquid model proposed in [14]. The research results of ultrasound absorption and velocity temperature dependence as well as theoretical values obtained using the density functional, in bismuth melt from five different melts are presented in Fig. 3 in comparison with the authors data [17]. It can be seen that even in this case the results of $\frac{\beta}{f^2}$ and v_S measurements correlate well with the data of other authors. On the polyterm $\frac{\beta}{f^2}$ at temperature T=650K, the extremum of the ultrasonic absorption coefficient is observed. Fig. 4 shows the results of temperature dependence of ultrasound absorption and velocity in antimony melt of six different melts in comparison with the authors' data [18]. We used the functional in calculating β_S by $\rho_n = N_n \frac{\lambda^{\chi_n+1}}{\chi_n!} r^{\chi_n} e^{-\lambda r}$.

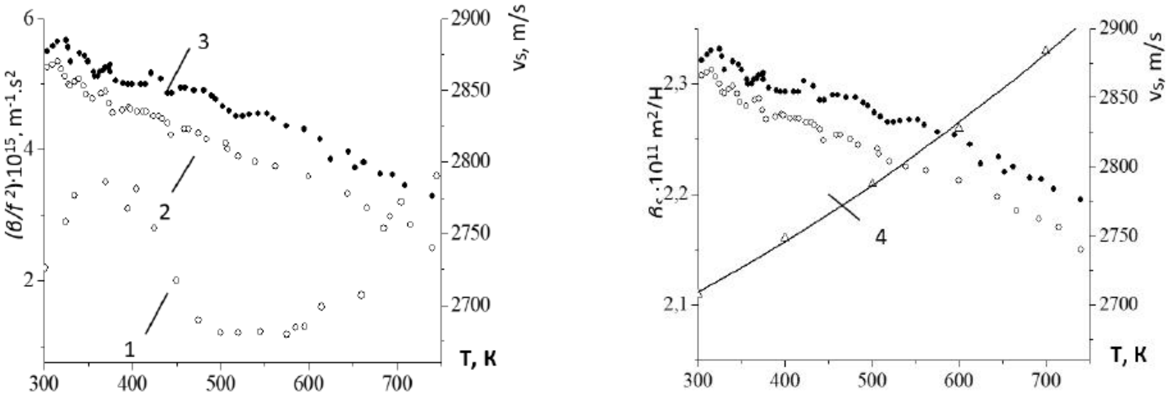

Fig. 2. Absorption, ultrasound propagation velocity and compressibility in liquid gallium: 1 - $\frac{\beta}{f^2}$ data of present work, 2 - v_S data of present work, 3 - v_S data of [14-16], 4 - β_S

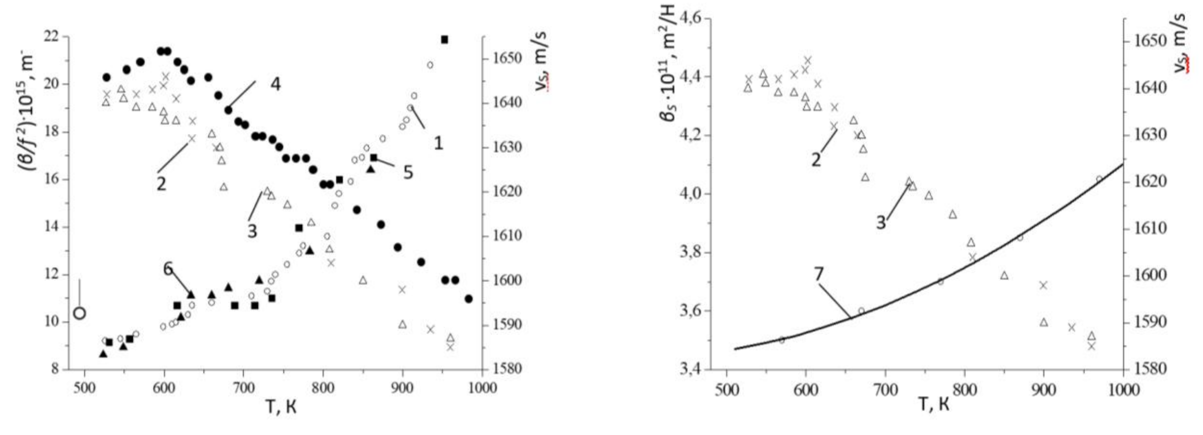

Fig.3. Absorption coefficient, ultrasound velocity and compressibility in bismuth melt: 1 - $\frac{\beta}{f^2}$, 2 - v_S at f = 53.1 MHz and 3 - v_S at f = 31.9 MHz data of present work, 4 - v_S , 5 - $\frac{\beta}{f^2}$ and 6 - $\frac{\beta}{f^2}$ data of [17-18], 7 – β_S

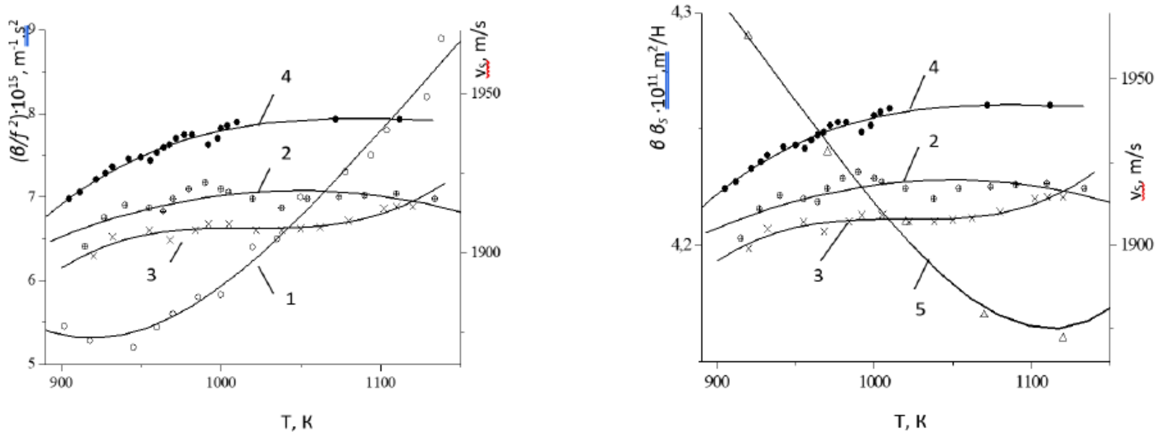

Fig. 4. Absorption coefficient, ultrasonic velocity and compressibility in antimony melt:

1- $\frac{\beta}{f^2}$ data of present work, 2- v_S at f = 52.0 MHz, 3 - v_S at f = 31.0 MHz and 4- v_S data of [18], 5 - β_S

Despite the fact that germanium belongs to the most studied semiconductor substances, interest to it does not weaken, as germanium serves as a key «type-setting» object, with which the properties and behavior of complex semiconductor materials are compared [19]. The research results are presented in Fig. 5. In the interval T_{ml} - 1000K there is a pronounced extremum of the absorption value, and at further heating the ultrasound absorption in liquid germanium noticeably increases as in most liquid metals [19]. The noted anomalies of absorption polytherms and ultrasound velocity in this case in the period after melting directly indicate the process of structural rearrangement in the direction of the melt described two-structure cluster model formation in this paper.

In accordance with this model, the melt near the melting point is a «solution» of two components: atomic matrix with metallic chemical bonds and larger associations of atoms - clusters, in which the chemical bond between atoms is realized mainly by covalent type. Obviously, during heating the clusters are disaggregated and at the same time their content in the total volume of the melt decreases. Both of these processes can lead to a decrease in the absorption of ultrasonic waves. Further heating of the germanium melts leads to the usual thermal loosening of its structure, due to which the absorption of ultrasound increases. The study of viscosity, density and electrical conductivity of selenium and tellurium melts shows features in the behavior of these properties as heating [14,16,20,21].

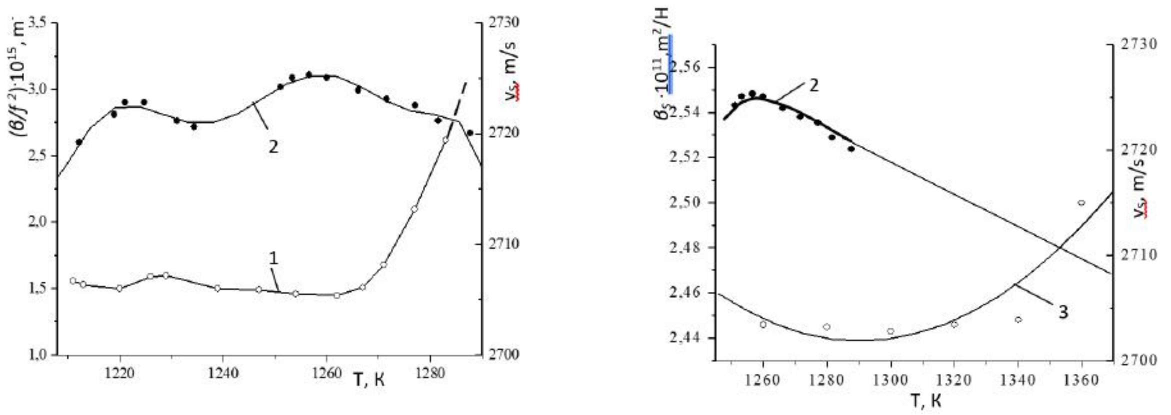

Fig.5. Absorption coefficient, ultrasound velocity and compressibility in liquid germanium:

1 - $\frac{\beta}{f^2}$ data of present work, 2 - v_S data of [19], 3 - β_S

Fig. 6 shows the results of studies of absorption coefficient, ultrasonic velocity and theoretical values of β_S in liquid selenium at temperatures from the melting point to 700 K. Data from [14,16,20,21] are plotted in the same figure (curves 3,2,6,5, respectively). The ultrasound velocity data presented in [20,21] correspond to a frequency of 5 MHz. Nevertheless, the results up to 680 K agree quite satisfactorily. At higher temperatures, our data show that the v_S polyterm decreases steeper with temperature. According to the character of the change in the steepness of the v_S polytherm, we divided the whole temperature interval of the study into three sections. At the first site $\frac{dv_s}{dT} = 0.975 m/s\cdot K$, at the second site $\frac{dv_s}{dT} = 0.675 m/s\cdot K$,at the third site $\frac{dv_s}{dT} = 1.125 m/s\cdot K.$ It is interesting to note that at the temperature T = 580 K in Fig. 6 the steep change in the temperature dependence of the viscosity coefficient is completed [16] and it is at this temperature that there is the first kink in the ultrasonic velocity polyterm and a minimum in the $\frac{\beta}{f^2}$ curve.

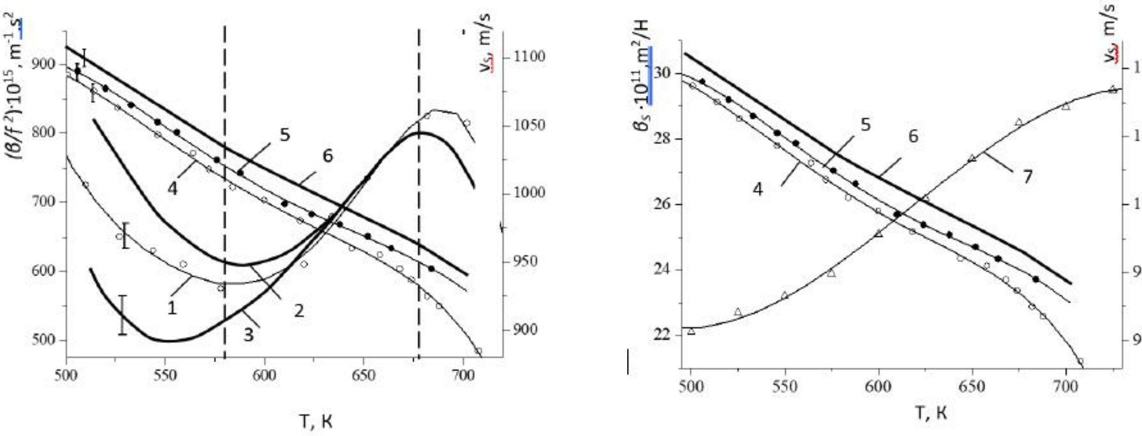

Fig.6. Absorption coefficient, ultrasound velocity and compressibility in liquid selenium:
1- $\frac{\beta}{f^2}$ and 4 - v_S data of present work, 2 - $\frac{\beta}{f^2}$, 3 - $\frac{\beta}{f^2}$, 5 - v_S, 6 - v_S data of [14, 20], 7 - β_S

Fig.7 shows our results on the elastic properties of the tellurium melt together with the data of [21] on the absorption (curve 3) and ultrasound velocity (curve 5).

According to the character of the $\frac{\beta}{f^2}$ polytherm, the whole temperature range can be divided into three sections. In section 1 from the melting point up to about 790 K, the ultrasound absorption decreases with increasing temperature. A decreasing $\frac{\beta}{f^2}$ polyterm was not found by the authors [20]. It should be noted that they did not start their measurements from the melting point, but at 45 degrees above the latter. At site II, a very slight increase in absorption with temperature is observed and, finally, at site III, a substantial increase in absorption commensurate with that in liquid metals [21].

Gallium and indium antimonide compounds are the closest electronic analogues of germanium [14-16,19]. The melting of GaSb and InSb compounds results in a dramatic change in the near-order structure and the nature of chemical bonding. Fig. 8 and 9 show the results of ultrasound absorption $\frac{\beta}{f^2}$ in GaSb and InSb melt together with the data [22] on the ultrasound propagation velocity v_S and the value of β_S. It can be seen that the polyterm of the absorption coefficient normalized by the square of the carrier frequency $\frac{\beta}{f^2}$, near the melting temperature, decreases with temperature and, only after passing through a pronounced minimum (for GaSb), increases with further heating.

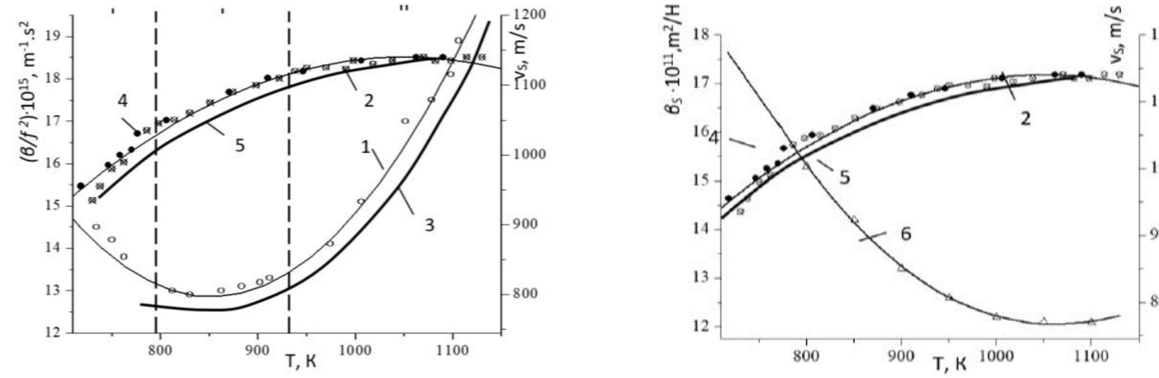

Fig.7. Absorption coefficient, ultrasound propagation velocity and compressibility in tellurium melt: 1- $\frac{\beta}{f^2}$ and 2-v_S data of present work, 3 - $\frac{\beta}{f^2}$, 4-v_S and 5-v_S data of [21], 6-β_S

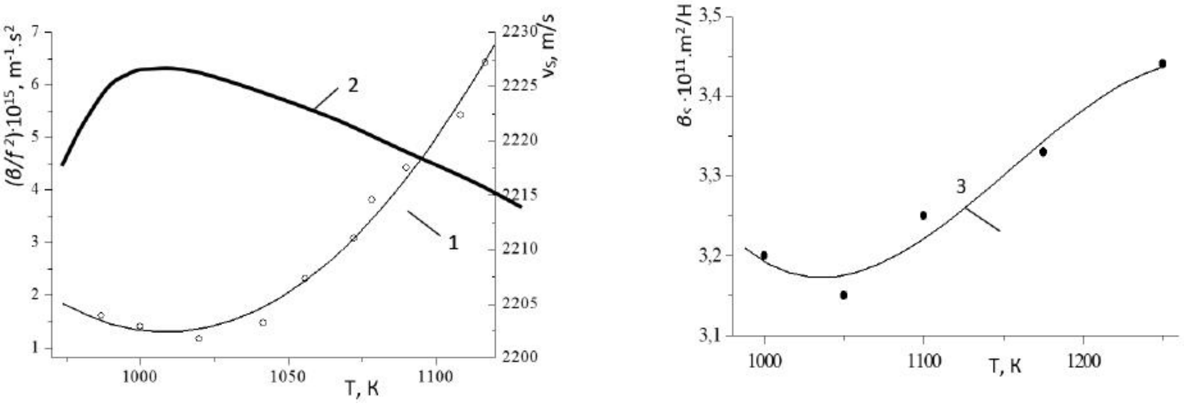

Fig.8. Absorption coefficient, ultrasonic velocity and compressibility in gallium antimonide melt [14-16]: 1 - $\frac{\beta}{f^2}$ and 2 - v_S data of present work, 3 - β_S

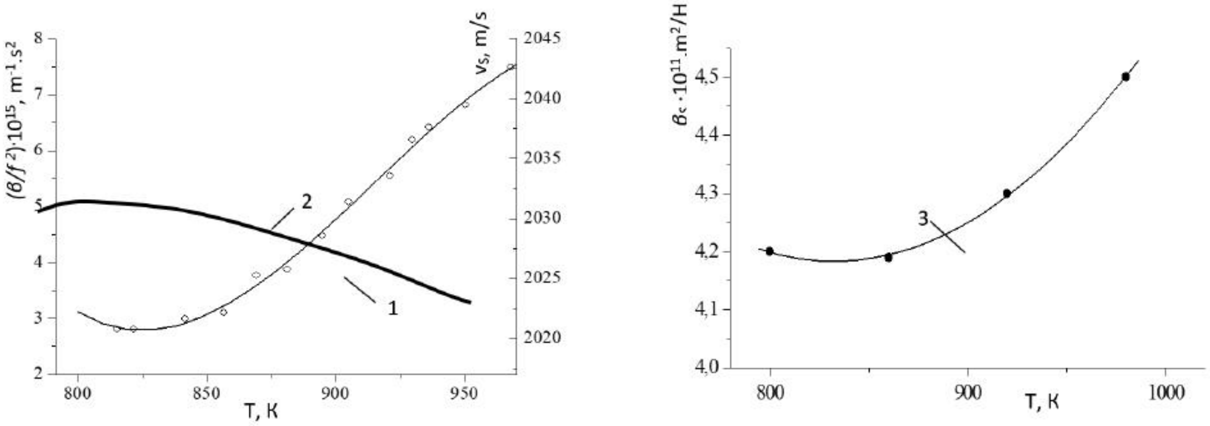

Fig.9. Absorption coefficient, ultrasonic velocity and compressibility in indium antimonide melt [14-16]: 1 - $\frac{\beta}{f^2}$ and 2 - v_S data of present work, 3 - β_S

4. Conclusion

Thus, the conducted studies of elastic wave energy absorption as well as ultrasound velocity allow us to identify such features in the behavior of sound absorption coefficient polyterms that:

1. With sufficient certainty indicate the absence or presence of structural changes during melt heating.

2. In comparative analyses make it possible to conclude that there is not a single mechanism of structural changes.
3. Show the possibility of different mechanisms realization of structural changes in the same melt in different temperature ranges.

This work demonstrated the practical importance of acoustic measurements in metal melts. We performed calculations of ultrasonic treatment of molten systems, investigated the physical and chemical effects of ultrasound on the structural properties of liquid molten systems. We found that the chemical effect is an irreversible and permanent change in the atomic weight and atomic-weight distribution due to ultrasound. Calculations showed that with an increase in the ultrasound intensity, the atomic weight of molten metals decreases, while the orientation of atoms along the flow direction decreases. Atomic orientation is an effect caused by the excitation of atoms by ultrasound. Ultrasonic waves propagate in a straight line. The wavelength and intensity of the ultrasonic vibrations determine the resolution and attenuation of the signal. High frequency of ultrasonic vibrations (short wavelength) is characterized by an improvement in spatial resolution, while the penetration depth decreases. Low frequency (long wavelength) is characterized by an increase in the wave depth, but the resolution decreases. Ultrasonic vibration increases the motion of atoms, a change in the structure of atoms occurs, which makes them more disordered. Ultrasonic vibration affects the relaxation process of molten metals, resulting in a weakening of the elastic effect. The relaxation process is attributed to the slow establishment of equilibrium between the atoms of the melts. The $\frac{\beta}{f^2}$ polytherms behavior in the «post-melting» temperature range is associated with relaxation mechanisms in the high-temperature region, where viscosity has a maximum value and the ultrasound absorption coefficient is minimal. At higher temperatures, despite the fact that viscosity has a minimum value, the sound absorption coefficient remains virtually unchanged. Relaxation occurring in alloys under the action of periodic stresses is a structural relaxation associated with a change in the average number of nearest neighbors surrounding a given atom. Relaxation is characterized by diffusion rates.

Conflict of interest statement.
The authors declare that they have no conflict of interest in relation to this research, whether financial, personal, authorship or otherwise, that could affect the research and its results presented in this paper.

CRediT author statement
Kazhikenova S.Sh.: conceptualization, methodology; writing – review and editing; **Shaikhova G.S.:** formal analysis, investigation; **Shaltakov S.N.:** resources, supervision. All authors have read and agreed to the published version of the manuscript.

Acknowledgments

This research was funded by the Science Committee of the Ministry of Science and Higher Education of Kazakhstan Republic (Grant No. AP23486482): «Development of information models for managing technological processes of metallurgical production, monitoring their functioning».

References

1 Chinnam R.K., Fauteux C., Neuenschwander J., Janczak-Rusch J. (2011) Evolution of the microstructure of Sn–Ag–Cu solder joints exposed to ultrasonic waves during solidification. *Acta Materialia*, 59, 1474-1481. https://doi.org/10.1016/j.actamat.2010.11.011

2 Kazhikenova S.Sh., Shaltakov S.N., Nussupbekov B. (2021) Difference melt model. *Archives of Control Sciences*, 31 (LXVII), 607–627. https://doi.org/10.24425/acs.2021.138694

3 Kazhikenova S.Sh. (2021) The unique solvability of stationary and non-stationary incompressible melt models in the case of their linearization. *Archives of Control Sciences*, 31(LXVII), 307-302. https://doi.org/10.24425/acs.2021.137420

4 Hackett L., Miller M., Weatherred S. (2023) Non-reciprocal acoustoelectric microwave amplifiers with net gain and low noise in continuous operation. *Nat Electron*., 6, 76–85. https://doi.org/10.1038/s41928-022-00908-6

5 White D.L. (1962) Amplification of ultrasonic waves in piezoelectric semiconductors. *J. Appl. Phys.*, 33, 2547–2554. https://doi.org/10.1063/1.1729015

6 Eskin D.G., Tzanakis I., Wang F., Lebon G.S.B., Subroto T., Pericleous K. (2019) Fundamental studies of ultrasonic melt processing. *Ultrasonics Sonochemistry*, 52, 455-467. https://doi.org/10.1016/j.ultsonch.2018.12.028

7 García-Colín L.S., De La Selva S.M.T. (1973) The Stokes-Kirchhoff relation in chemically reacting fluids. *Chemical Physics Letters*, 23 (4), 611-613. https://doi.org/10.1016/0009-2614(73)89041-4

8 Shekaari H., Golmohammadi B. (2021) Ultrasound-assisted of alkali chloride separation using bulk ionic liquid membrane. *Ultrasonics Sonochemistry*, 74, 105549. https://doi.org/10.1016/j.ultsonch.2021.105549

9 Liu Y., Yu W., Liu Y. (2019) Effect of ultrasound on dissolution of *Al* in *Sn*. *Ultrasonics Sonochemistry*, 50, 67-73. https://doi.org/10.1016/j.ultsonch.2018.08.029

10 Zheng Y., Tan X.Yi, Xiaojuan W., Cheng X., Liu Zh., Yan Q. (2020) Thermal stability and mechanical response of Bi_2Te_3 - based materials for thermoelectric applications. *ACS Applied energy materials*, 3 (3), 2078-2089. https://doi.org/10.1021/acsaem.9b02093

11 Chiba A., Ohmasa Y., Yao M.. (2013) Vibrational, single-particle-like, and diffusive dynamics in liquid *Se*, *Te*, and $Te_{50}Se_{50}$. *J. Chem. Phys*., 119, 9047 – 9062. https://doi.org/10.1063/1.1615234

12 Inui M., Kajihara Y., Tsuchiya Y. (2020) Peculiar temperature dependence of dynamical sound speed in liquid $Se_{50}Te_{50}$ by inelastic x-ray scattering. *Journal of Physics Condensed Matter*., 21, 214003. https://doi.org/10.1088/1361-648X/ab6d8e

13 Pak Yu., Pak D., Kazhikenova S.Sh., Shaikhova G.S., Abayeva N.F., Imanbayeva S.B. RK Patent No 35901(14 October 2022)

14 Bitong Wang, Douglas H. Kelley. (2021) Microscale mechanisms of ultrasound velocity measurement in metal melts. *Flow Measurement and Instrumentation*, 81, 102010. https://doi.org/10.1016/j.flowmeasinst.2021.102010

15 Cramer A., Zhang C., Eckert S. (2024) Local flow structures in liquid metals measured by ultrasonic Doppler velocimetry. *Flow Measurement and Instrumentation*, 15, 145-153. https://doi.org/10.1016/j.flowmeasinst.2003.12.006

16 Syla N., Ahmeti H., Aliaj F., Dalipi B. (2024) The determination of some sizes and physical characteristics of metals by ultrasound. *International Journal of Computational and Experimental Science and Engineering*, 10 https://doi.org/10.22399/ijcesen.315

17 Kazhikenova S.Sh., Shaltakov S.N., Belomestny D., Shaihova G.S. (2020) Finite difference method implementation for Numerical integration hydrodynamic equations melts. *Eurasian Physical Technical Journal*, 17, 1(33). https://doi.org/10.31489/2020NO1/145-150

18 Greenberg Y., Yahel E., Ganor M., Hevronib R., Koroverb I., Dariela M., Makov G. (2008) High precision measurements of the temperature dependence of the sound velocity in selected liquid metals. *Journal of Non-Crystalline* 354(34), 4094-4100. https://doi.org/10.1016/j.jnoncryso1.2008.05.038

19 Gauthier M., Lheureux D., Decremps F., Polian A. (2003) High-pressure ultrasonic setup using the Paris–Edinburgh press: Elastic properties of single crystalline germanium up to 6 GPa. *The Review of scientific instruments*, 74(8), 3712-3716. https://doi.org/10.1063/1.1593791

20 Kozhevnikov V., Payne W.B., Olson J., Allen A., Taylor P.C. (2004) Sound velocity in liquid and glassy selenium. *Journal of Non-Crystalline Solids*, 353(32), 3254-3259. https://doi.org/10.1016/j.jnoncrysol.2007.05.062

21 Knyazev G.A., Voloshinov V.B. (2008) Diffraction of IR radiation by ultrasound in tellurium single crystals. *Bulletin of the Russian Academy of Sciences Physics*, 72(12), 1643-1647. https://doi.org/10.3103/S1062873808120149

22 Kuleyev I.G., Kuleyev I.I., Arapova Yu I. (2007) Transverse ultrasound absorption in cubic crystals with positive and negative anisotropies of second-order elasticity moduli. *Journal of Physics*, 19(40), 406216. https://doi.org/10.1088/0953-8984/19/40/406216

AUTHORS' INFORMATION

Kazhikenova, Saule Sh. - Doctor of Engineering Sciences, Associate Professor , Karaganda Saginov Technical University, Karaganda, Kazakhstan; https://orcid.org/0000-0002-6937-1577, sauleshka555@mail.ru

Shaikhova, Gulnazira - Candidate of Engineering Sciences, Karaganda Saginov Technical University, Karaganda, Kazakhstan; https://orcid.org/0000-0002-1186-1178, shaikxova_2011@mail.ru

Shaltakov, Sagyndyk - PhD, Karaganda Saginov Technical University, Karaganda, Kazakhstan, https://orcid.org/0000-0002-2036-3023, sagyndyk613@mail.ru

EURASIAN PHYSICAL TECHNICAL JOURNAL

2025, Volume 22, No. 1 (51)

https://doi.org/10.31489/2025N1/103-114

Received: 29/11/2024 Revised: 24/02/2024 Accepted: 18/03/2025 Published online: 31/03/2025

Research Article

UDC 536.495; 539.52; 539.1.043

STUDY OF THE EFFECT OF HEAT TRANSFER DURING MOLDING OF TERMOPLASTIC BERYLLIUM OXIDE CERAMICS

Yesbol Zh.[1], Sattinova Z.K.[2], Turalina D.E.[1], Mussenova E.K.[3]*

[1]Al-Farabi Kazakh National University, Almaty, Kazakhstan
[2] L.N. Gumilyev Eurasian National University, Astana, Kazakhstan
[3] Karaganda Buketov University, Karaganda, Kazakhstan
**Corresponding author:* emusenova@mail.ru, jalynesbol@gmail.com

Abstract. *Beryllium oxide (BeO) ceramics formed with the use of ultrasound exhibit more intense sintering, lower shrinkage, and a reduced sintering temperature compared to ceramics produced without ultrasound. The effectiveness of ultrafast sintering is dependent on the cohesion of ceramic agglomeration and the proper arrangement of particles. Rheological properties thermoplastic slurry changed as a result of ultrasound activation. These changes are related to dispersion phase processes and mass transfer. Ultrasonic activation also slightly enhances the properties of the castings. The increase in the density and strength of castings is explained by the effective reduction of shrinkage under the influence of ultrasound during hardening. That is, compensation for the deposition of the Ingot is determined by filling with a liquid slurry and its compaction under the influence of pressure. For ultrasonic injection of thermoplastic beryllium oxide slurry, formulations with a binder content ranging from 9,5 to 11,7% are recommended. Because these binder compositions are mixed with beryllium powder, turning into a high-strength slurry, forming ceramics that can withstand large temperatures.*

Keywords: ultrasonic activation, beryllium oxide, thermoplastic slurry, molding process, viscous plastic state.

1. Introduction

Beryllium oxide powder is used to prepare thermoplastic slurry which is obtained using standard technology in serial production from beryllium hydroxide [1]. Beryllium oxide powder has a granulometric composition by fractions. This composition of BeO powder (Table 1) shows satisfactory casting properties of the slurry when the mass fraction of the binder changes from $\omega = 9.5\ to\ \omega = 11.7\%$. case of an increase in the finer fractions BeO in the powder composition, the required amount of binder increases. With an increase in the composition of larger fractions BeO in the powder, the ceramics become stained, which indicates the presence of micropores and cracks [2]. On the edges of beryllium oxide microcrystals and important physical and chemical processes occur in the layers, such as adsorption, changes in surface energy, etc. Therefore, the dispersion of beryllium oxide powder significantly affects the casting process of beryllium ceramics. All types of ceramic dispersed systems intended for molding are classified as coagulation structures. Coagulation structures are characterized by contacts between particles that are comparatively weak in terms of interaction strength. In dispersion systems, boundary layers of considerable extent are recorded. These layers, possessing specific deformation properties, are responsible for the thixotropic nature of the suspension flow. With regard to the dispersed system - thermoplastic slurry, the following main features of their structure can be formulated:

relatively high viscosity of the dispersion medium and low value of its dielectric constant; complex structure of the dispersion medium, the presence of supramolecular formations and low diffusion mobility of individual structural elements; weak lyophilic interaction at the phase boundary and absence of dissolution of the solid phase; significant dependence of the density and viscosity of the dispersion medium on temperature. The slurry is assumed to have certain rheological properties when studying its deformation behavior. Complete information in determining the relationship between the rheological properties of the dispersed system and the intensity of the ultrasonic effect on the slurry was obtained by constructing a complete rheological flow curve [1-5]. The flow curve allows to describe the viscous plastic and elastic properties of coagulation structures in the range of changes in these properties under ultrasound exposure.

The physical essence of the use of ultrasonic activation for processing slurry is reduced to the intensification of physical and chemical processes that facilitate the flow of mass and heat exchange processes throughout the entire volume, as well as the sound-capillary effect, which actively influences the processes occurring at the interface between the solid and liquid phases [3, 6-7]. As a result of the action of ultrasound, a whole series of secondary effects arise, accompanying the propagation of ultrasonic waves in the liquid slurry, depending on the rheological behavior. The most significant effect is structural destruction, which is expressed in a sharp decrease in the viscosity of the slurry due to the deep destruction of the coagulation structures [1-3].

The article [8-9] presents the results of calculations under the influence of ultrasonic vibrations and a comparison with the results of experimental data, the change in viscosity and ultimate stress depending on the temperature and duration of ultrasonic treatment.

The volume-phase characteristics of the highly heat-conducting dispersed system change during the casting process at a temperature of 59–40 ºC and the volume of the liquid phase increases. Increasing the volume of the liquid phase, which gives the slurry the necessary casting properties, does not allow achieving the desired effect, since during firing the “additional” amount of binder leads to the appearance of structural defects and deformation of the products. The migration mechanism of shrinkage compensation will work only in the liquid slurry layer, and at the interface between the liquid and solid phases, incomplete compensation of internal shrinkage is the cause of internal defects. Complete compensation of internal shrinkage is achieved using the mechanism of plastic deformation of the hardening layer of slurry in the forming volume of the casting mold under the action of a pressure gradient arising as a result of ultrasonic vibrations [1-3].

Ultrasonic activation has brought significant changes to thermoplastic slurry casting systems [3-5]. The intensity of ultrasonic processing allows you to effectively influence the Rheology of the thermoplastic Slurry. The mechanism of action involves managing the parameters that govern the relationship between the solid and liquid phases [3-5]. Optimal conditions for the interaction of casting systems were found within a temperature range of 63 - 68°C and with 7 - 10 minutes of ultrasonic processing [1, 3-5]. Ultrasonic processing with thermoplastic slurry showed a change in the properties of the microstructure of ceramics. Compared to samples made without ultrasound, ultrasonic samples have a uniform structure and have higher structural-mechanical and electrophysical parameters [1, 3-5]. The conducted comparative analysis of the thermal-physical characteristics of the slurry in the range of phase transformations in combination with experimental data reveals a detailed method of physicochemical analysis of the solidification depending on the cooling rate and the change in the position of the crystallization interval of the slurry in the cavity of the casting plant.

At the molding stage, the castability of the slurry depends on its viscosity, and the solidification temperatures and cooling rates are determined by its thermal conductivity. It has been established that the high thermal conductivity of beryllium oxide slurry at elevated temperatures is linked to the temperature-dependent variations in its viscosity and shear stress output. The changes in the structural and mechanical properties of the beryllium oxide slurry are determined by the relationship between the solid phase and the binder, as well as the stages of the casting process [1,6].

The article uses mathematical modeling to investigate distributions of velocity and temperature fields showing the dynamics, to track the change in temperature-phase fields during the solidification process, calculation and prediction of cooling and solidification of the casting system of ceramic products, necessary for the study of thermal processes and analysis of the formation of shrinkage defects.

2. Materials and methods

The movement and heat exchange of the thermoplastic slurry occur in flat configuration. Fig.1 shows a diagram of a flat forming cavity. The thickness of the flat cavity is 2H = 0,0015 m, width b = 0,03 m, length L = 0,071 m. the cooling circuit (Fig. 1) consists of two parts. A liquid slurry with an initial temperature of $t_0 = 75°\mathrm{C}$ is introduced into the cavity. During the casting phase, the thermoplastic slurry undergoes cooling and hardening through heat exchange. As the slurry solidifies, its density increases. The movement of the thermoplastic slurry is laminar, with a Reynolds number Re < 1. Due to the high viscosity of the thermoplastic slurry, the Prandtl number $\mathrm{Pr} = \mu c_p/\lambda$ is greater than one.

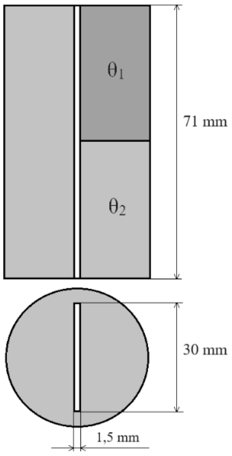

Fig.1. Diagram of a flat cavity die.

The thermoplastic slurry is a two-phase dispersion system, where the solid phase consists of beryllium oxide powder, and the liquid phase comprises organic compounds (binders) [1, 5]. The organic compounds are made up of three components: paraffin (0,82%), wax (0,15%), and oleic acid (0,03%). The beryllium oxide powder possesses a granulometric composition categorized by fractions (Table 1). The mass fraction of the organic binders varies between ω = 10% and 11,7% [6,7].

Table 1. Key properties of beryllium oxide powder [1]

Bulk Density ρ_0 × 10^3 kg/m^3		0.75
Surface Area per Unit Mass, S × 10^{-3} m^2/kg		1.72
Granulometric Composition by Particle Size Fractions of Beryllium Oxide	Fraction, μm	Fraction, %
	up to 1.4	35.2
	1.4 - 4.1	52.7
	4.1 - 7.0	9.6
	7.0 - 9.7	1.7
	9.3 - 12.5	0.4
	12.6 - 15.3	0.3
	15.3 - 18.2	0.1

The composition of BeO powder (Table 1) demonstrates satisfactory flow properties of the slurry when the mass fraction of the binder ranges from ω = 9.5 % to ω = 11.7 %. An increase in smaller fractions of BeO in the powder necessitates a higher binder content. Conversely, an increase in larger BeO fractions in the powder results in ceramics exhibiting microcracks and defects. Viscoplastic slurry can be classified as a Bingham liquid, which has a thixotropic nature of the flow of $0.005 - 1200\ s^{-1}$, within the limits of a change in the shear rate [8,9]. The effective molecular viscosity of a liquid μ_{eff} is defined as [10-12]:

$$\mu_{eff} = \begin{cases} \mu_p + \tau_0 |\dot{\gamma}|^{-1}, & \text{if } |\tau| > \tau_0 \\ \infty, & \text{if } |\tau| \le \tau_0 \end{cases}, \tag{1}$$

where τ_0 - yield strength, μ_p - plastic viscosity coefficient, $\tau = \mu_{eff} \cdot S$ - shear stress tensor, $S \equiv \sqrt{2S_{ij} \cdot S_{ij}}$ - strain rate tensor, $S_{ij} = \frac{1}{2}\left(\frac{\partial U_i}{\partial x_j} + \frac{\partial U_j}{\partial x_i}\right)$- second principal invariant of the strain rate tensor. The Shvedov–Bingham model is a viscous plastic fluid model that linearly relates the shear stress of a simple viscous liquid to the viscosity [13 -15]. Ultrasonic treatment affects the rheological properties of the slurry. Experimental data of plastic viscosity and yield strength for mass fraction $\omega = 11.7\%$ of the slurry after treatment can be described as follows [1,3-5]:

$$\mu_p(t) = 293{,}6259 \cdot \exp(-0{,}05816 \cdot t), \text{ Pa·s} \tag{2}$$

$$\tau_0(t) = 11{,}4 + 11{,}41 \cdot \exp(-(t - 70{,}05)/5{,}47), \text{ Pa} \tag{3}$$

Density of the slurry taking into account the concentration of beryllium oxide powder and organic binder:

$$\rho = \frac{\rho_{BeO} \cdot \rho_{bin}}{(1-\omega)\rho_{bin} + \omega \cdot \rho_{BeO}}, \tag{4}$$

where ω - volume fraction of the binder, ρ_{bin} - density of the binder, ρ_{BeO} - density of BeO. The density of the binder for $\omega = 11.7\%$ is determined by the formula:

$$\rho_{bin}(t) = 0{,}852 + 0{,}0725 \cdot cos(0{,}05612 \cdot (t + 273{,}15) - 16{,}7361), \text{ kg/m}^3 \tag{5}$$

The density of organic binder in temperature range $t = 74 - 52°\text{C}$ varies from 779.7 kg/m^3 to 901.0 kg/m^3 and at $\omega = 11.7\%$ the density of the slurry increases from 2260 kg/m^3 to 2370 kg/m^3.

The density of thermoplastic slurry is determined by the content of the solid phase of the studied dispersed system. The volume content of the solid phase, depending on the composition and temperature, varies in the liquid slurry 5% by volume and does not exceed 71%. In this case, the increment of the binder density during the cooling process is 1.20 including due to cooling to 55°C - 1.02, during crystallization 55÷40°C-1.03, in a solid-plastic state below 55°C-1.17. Based on the calculation results and in comparison with the experimental data presented in the article [5,16-17], it's possible conclude that the effect of ultrasound affects the change in the density of ceramics and shows the solidification front depending on the casting modes, the structure of the casting mass and the features of the configuration of the products.

The slurry's rheological characteristics undergo changes based on temperature variations, and heat release occurs during phase transitions involving shifts in the material's state. When the slurry cools, it can lead to non-uniform temperature distribution, influencing the mold's rheological properties. Solidification typically initiates from the walls, while the central portion of the cavity might remain liquid. As a result, slurry may flow into the cooled areas to compensate for internal volume shrinkage. Full control over the cooling of the slurry mass during forming products in a molding cavity is of great importance, since the solidification process inside the mass depends on the temperature distribution. Also, the change in the temperature field at the cooling process depends on the heat release in the phase transition region and the determination of boundary conditions. The experimentally established liquidus and solidus temperatures of the slurry make it possible to identify the nature of the phase distribution at different stages of crystallization and calculate the rate of solid phase release necessary for studying thermal processes [1,3,6]. The amount of heat released per unit mass during the phase transition is calculated based on the enthalpy ΔH in the transition zone [13].

In this phase, the slurry's heat capacity changes, and the increase in enthalpy can be measured through the apparent heat capacity method [14-20]. The specific heat capacity of the slurry is calculated by the equation [14,21]:

$$c_p = c_s \cdot \left(1 - \alpha(\bar{t})\right) + c_l \cdot \alpha(\bar{t}) + H_{1\to 2} \frac{d\alpha}{dt} \tag{6}$$

where c_s, c_l - represent the heat capacities of the slurry in its solid and liquid states, respectively, $\alpha(\bar{t}) = 0$ for the solid-state slurry, and $\alpha(\bar{t}) = 1$ for the liquid-state slurry. Here, $\bar{t}$ denotes the dimensionless temperature of the slurry.

For the binder content, the function at $\omega = 11.7\%$ is expressed as follows. This heat capacity method is advantageous because the transition zone does not need to be predefined; it is instead determined by calculating the temperature of the slurry [20 - 23]. The thermal conductivity of the slurry is temperature-dependent and can be calculated using the following formula when the binder content is $\omega = 11.7\%$ [7]:

$$\lambda = 1{,}6 + 4{,}8 \cdot exp(-0{,}017 \cdot t),\ \text{W/(m·K)} \tag{7}$$

The aggregate change of the liquid slurry during the molding process, the transition of the slurry to a viscous-plastic state is governed by temperature-dependent formulas (2) - (7), which define the properties of the slurry. Thermal conductivity, heat capacity and melting heat are the main parameters for calculating the model of the process by injection casting ceramic products [24]. In scientific literature, the data on thermophysical properties of the dispersed system are limited, and they theoretically confirm that mechanical failures of the dispersed system structure do not affect thermophysical properties, i.e., the value of c_p heat capacity and λ thermal conductivity [5]. The change of thermal conductivity before (1) and after (2) ultrasonic treatment of the slurry in the temperature range of 20 - 80 °C are given (Fig. 2a).

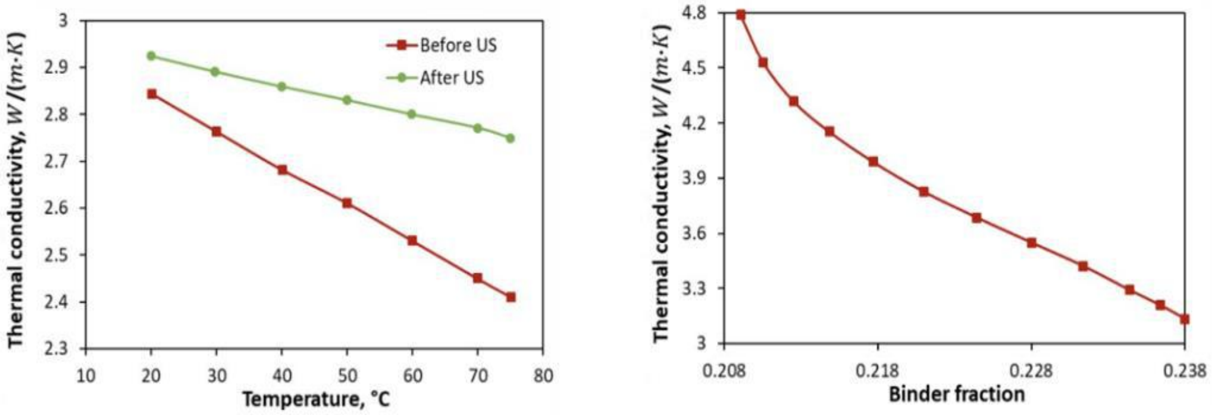

a) b)

Fig.2. The dependence of the thermal conductivity of the slurry on the temperature (a) and the volume fraction of the binder (b).

With an increase in the content of the binder, the thermal conductivity of the slurry decreases, that this is natural, given the large difference in the thermal conductivity of the binder. A comparison of the high thermal conductivity of beryllium oxide with the low thermal conductivity of the the binder indicates that when considering the slurry as a structured dispersed system, its thermal conductivity depends, first of all, on the thermal conductivity of the binder, especially free, unsolvated, since the particles of the dispersed phase practically do not contact each other and cannot have a significant effect on the thermal conductivity of the system. This phenomenon is clearly visible when considering the dependence of thermal conductivity on the volume fraction of the binder content in slurry (Fig.2b).

As well as density, the thermal conductivity of slurry in the solid state is higher than in the liquid state, which is entirely consistent with the idea of higher thermal conductivity of substances [1-5]. With a decrease in the volume content of the binder below 40%, the thermal conductivity of the slurry begins to increase sharply due to the increase in the possibility of direct contact between particles [1-5, 26]. In the work [7,16] the results of studies of heat transfer in suspensions under shear flow are published. It follows from them that for a viscoelastic dispersed system, the linear dependence of thermal conductivity and heat capacity on temperature is preserved. This dependence is not observed only more in a homogeneous liquid state of the dispersed phase. The thermal conductivity coefficient of the casting was determined at a temperature of 20-25°C using the one-dimensional heat flow method according to the industry standard (OCT 48-91-7-75) on the IT-02Ts device. The measurement method is based on comparing heat flows through the sample under study and standards with known thermal conductivity. The measurement error in this method is known to be $\pm 10\%$.

The heat capacity of beryllium oxide slurry with an increase in temperature and binder content naturally increases [13]. The graphs show that the heat capacity of the slurry depends only on density and does not depend on viscosity and shear stress (Fig.3).

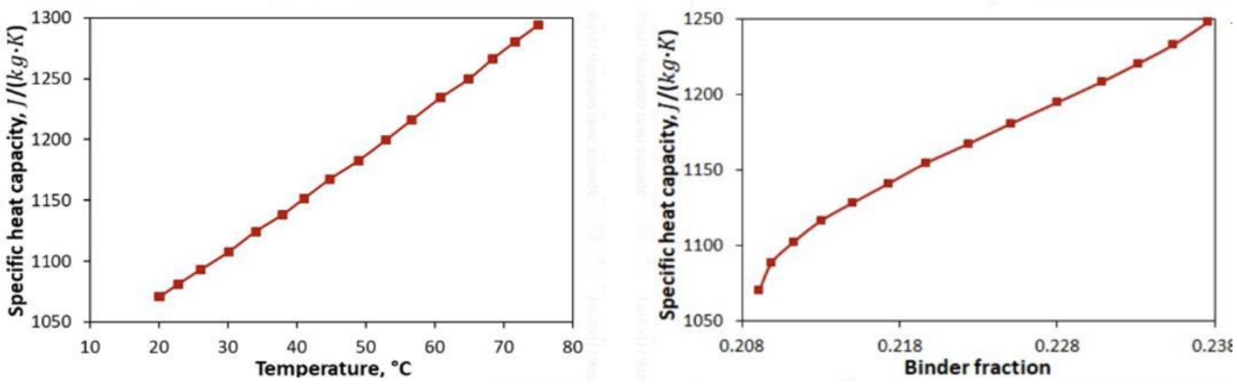

a) b)

Fig.3. The dependence of the heat capacity of the slurry on the temperature (a) and the volume fraction of the binder (b)

In the structure of the slurry on the surface of solid particles, the adsorbed molecules of liquids significantly change some physical properties, in particular, the melting point and density increase. The slurry mass has a higher heat capacity than other liquids, due to the latent heat of phase transition, it can increase the volume of heat transfer at an equivalent volume flow rate in the mold cavity.

3. Mathematical model

The casting speed is directed vertically downwards along the axis OX, and there is also a transverse velocity component due to the addition of liquid slurry from the wall side until the casting has completely solidified (Fig.1). The mathematical model of the flow process includes equations of motion, continuity and energy, taking into account the dissipation of kinetic energy, temperature dependence of rheological properties and heat of crystallization:

$$\begin{gathered}
\rho u\frac{\partial u}{\partial x}+\rho v\frac{\partial u}{\partial y}=-\frac{dp}{dx}+\frac{\partial}{\partial y}\left(\mu\frac{\partial u}{\partial y}\right)+\frac{\partial}{\partial y}(\tau)+\rho g \\
\frac{\partial \rho u}{\partial x}+\frac{\partial \rho v}{\partial y}=0 \\
\rho u c_p\frac{\partial T}{\partial x}+\rho v c_p\frac{\partial T}{\partial y}=\frac{\partial}{\partial y}\left(\lambda\frac{\partial T}{\partial y}\right)+L_k\frac{d\rho}{dt}(\tau)+\mu\left(\frac{\partial u}{\partial y}\right)^2
\end{gathered}\tag{8}$$

Based on the results of the experiments, the thermophysical properties of the thermoplastic beryllium oxide slurry were found using ultrasonic activation at $30\ ^\circ\mathrm{C}\le T\le 80\ ^\circ\mathrm{C}$, which are described by empirical formulas (2-7). The pressure gradient in the equation of motion is determined from the condition of conservation of mass flow rate:

$$\int_0^h \rho_j^{n+1}u_j^{n+1}dy=\dot{m}\tag{9}$$

The values of velocity and temperature at the inlet section of the cavity are constant, and accordingly all thermophysical characteristics of the slurry are constant:

Boundary conditions

at $x=0$: $u=u_0,\ v=0,\ T=T_0$

$$\text{at } x > 0,\ \ y = 0:\ \ \frac{\partial u}{\partial y} = \frac{\partial T}{\partial y} = v = 0. \tag{10}$$

when the thermoplastic slurry moves, the wall sliding of the solid phase is observed. It is practically known that a layer of dispersion medium is formed near the wall, along which the dispersed system moves. At the same time, the condition of adhesion of the slurry mass complied with the wall, but only for its continuous phase [27-29]. And for the entire casting system, the actual conditions at the cavity wall combine the effects of internal and boundary friction. At calculating the velocity profile and flow rate, the slurry condition on the wall is as follows:

$$\text{at } x > 0,\ \ y = h:\ \ \frac{dp}{dx} = \left(\tau_{ow} + \left(\mu_0 \frac{\partial u}{\partial y}\right)_w\right)$$

The heat exchange on the outer wall is determined in accordance with the temperature in the cooling circuits of the channel. Specifying the water temperatures in the hot, warm and cold circuits $T_1,\ T_2,\ T_3$, respectively, there are boundary conditions for the temperature on the outer wall:

$$\begin{aligned} &\text{at } 0 \le x < l_1,\ -\lambda\frac{\partial T}{\partial y} = k'(T_m - T_1),\\ &\text{at } l_1 \le x < l_2,\ -\lambda\frac{\partial T}{\partial y} = k'(T_m - T_2),\\ &\text{at } l_2 \le x < l_3,\ -\lambda\frac{\partial T}{\partial y} = k'(T_m - T_3) \end{aligned} \tag{11}$$

To determine the average mass temperature, the distribution of temperature and longitudinal velocity over the cross section of a flat cavity is used

$$T_m = \frac{\int \rho u T dA}{A\rho_m u_m} \tag{12}$$

where $dA -$ cross-sectional area, $A\rho_m u_m$- mass flow. Product of $\rho_m u_m$ is expresses the average mass flux density, u_m- average velocity, which is determined by the expression

$$u_m = \frac{\int u dA}{A} \tag{13}$$

Heat exchange calculations were considered using the boundary condition of the third kind in the form of expression (11) for a flat forming cavity. This means that the heat flux density is taken to be proportional to the difference between the temperatures of the coolant T_w and the average mass temperature of the slurry T_m. In the stationary mode, heat flux density q_w can be represented as

$$q_w = \alpha_1(T_m - T_w) = k'(T_w - T) = k(T_m - T) \tag{14}$$

where k'- heat transfer coefficient from the inner surface of the wall to the coolant; k – heat transfer coefficient from the slurry flowing in the cavity to the cooling liquid; α_1- coefficient of heat transfer from the slurry flowing in the cavity to the inner surface of the wall.

The coefficients $\alpha_1, k,\ k'$are related by the relation

$$\frac{1}{k} = \frac{1}{\alpha_1} + \frac{1}{k'} \tag{15}$$

For flat forming cavities:

$$\frac{1}{k'} = \frac{d_e}{\lambda_s} + \frac{1}{\alpha_2} \tag{16}$$

where $d_e = \frac{4A}{s}$ - equivalent diameter; s - cavity perimeter; λ_s - thermal conductivity coefficient of the wall material; α_2- coefficient of heat transfer from the outer surface of the wall to the coolant:

$$\alpha_2 = \frac{2\lambda_b}{d_3 ln(4d_3/d_e)} \tag{17}$$

Numerical methods are used to solve the model of motion and heat transfer of thermoplastic slurry in a flat cavity [25].

4. Calculation results and discussion

The effect of ultrasonic treatment on the properties of the casting was assessed by changes in apparent density and mechanical strength. Ultrasonic treatment allows us to obtain castings with a finer grain structure and apparent density compared to samples obtained without ultrasound. According to experimental data, it is known that castings with maximum density are obtained with an ultrasound power of 60-80% from $\mathrm{N_{max}}$, which corresponds to an ultrasound intensity $0.4 - 1.6\frac{\mathrm{W}}{\mathrm{cm}^2}$. A decrease of the density of castings at a level above 60-80% from $\mathrm{N_{max}}$ leads to the formation of shrinkage and cracks in castings during the process of forming their structure [3-4]. The increase in the density of the casting indicates a change in the volume-phase relationships during the structure formation of the casting under the influence of ultrasound. Considering the insignificance of the gas phase content in the liquid slurry and equal cooling of the casting in all experiments, the increase in the density of castings formed with ultrasound is a more effective compensation for shrinkage during casting hardening. In this case, compensation for shrinkage is achieved both by adding liquid slip and by deformation compaction during the structure formation of the casting. A comparative analysis of the structural and mechanical properties of products, with and without the use of ultrasound, showed that castings with ultrasound had a 7-10% higher apparent density. The universal strength limit for flexible products obtained using ultrasound exposure is 1.3-1.7 times greater than for products obtained without ultrasound.

Dynamic viscosity of slurry $\mu_p(t)$, density ρ(t), and shear stress $\tau_0(t)$ the temperature increases as it decreases. In the second cooling circuit, the water temperature is set at θ_2 = 40 ^{0}C. Through the heat exchange process between the slurry and the water, the slurry's temperature is reduced to 40 ^{0}C (Fig.4 a,b,c), and the density increases from 2270 kg/m^3 to 2370 kg/m^3 (Fig.5 a,b,c).

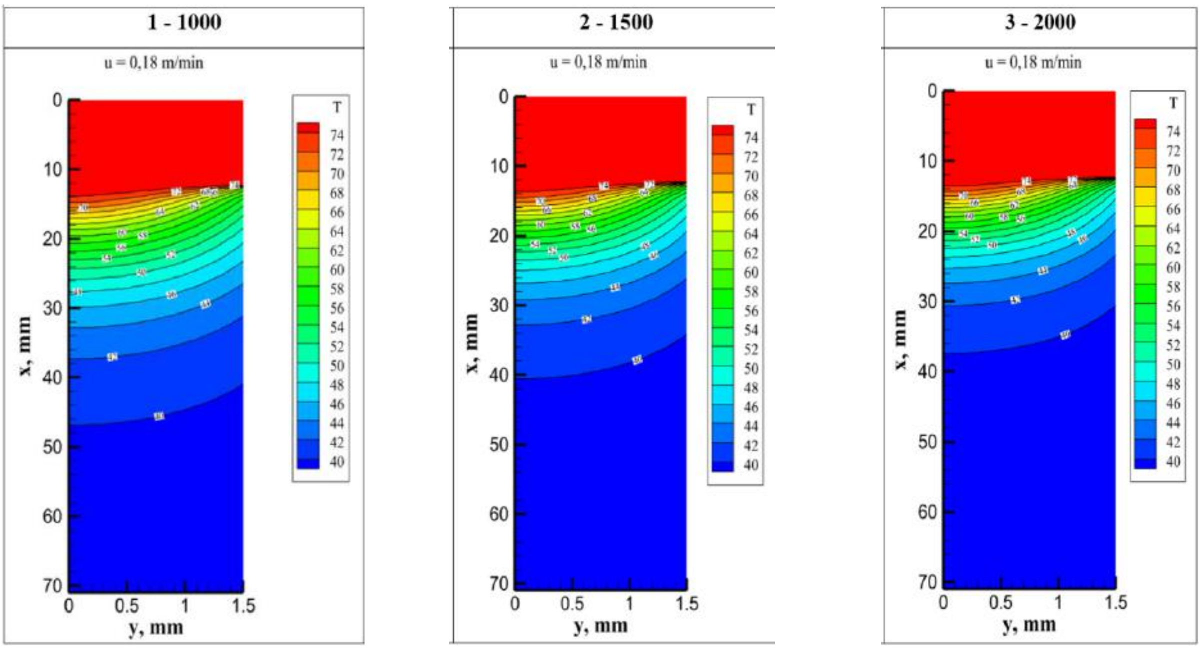

a) b) c)

Fig.4 Changing the temperature of the slurry depending on the value of the heat exchange coefficient: $a)\ k = 1000\, J/(m^2 \cdot ℃),\ b)\ k = 1500\, J/(m^2 \cdot ℃),\ c)\ k = 2000\ \ J/(m^2 \cdot ℃)$

After ultrasound exposure, calculations were made for slurry with rheological properties. The computation results for the slurry movement in a planar die, given a cavity thickness of 2h = 0.0015 m, a casting speed of $\vartheta = 0.18$ m/min, and an initial temperature of $t_0 = 75℃$, are illustrated in figure 4. In the initial cooling circuit, the temperature of the water is θ_1 = 75 ^{0}C. The temperature field shows a decrease in temperature to 72 °C (Fig. 4 a, b, c), and the density increases from 2260 kg/m^3 to 2270 kg/m^3 (Fig.5 a, b,c).

Transitioning from the first to the second region involves a shift from an amorphous state to a viscous-plastic state, during which the temperature and density fields change, eventually stabilizing to uniform values. Experimental data [1,6] indicate that an increase in the transition zone between states can lead to shrinkage of the slurry, the formation of cavities and voids, and a decrease in casting strength. The smaller the transition zone between states, the less the slurry will shrinkage. Ultrasonic treatment, by improving rheological properties, results in a reduction in the transition zone and consequently a decrease in the shrinkage of the beryllium oxide casting.

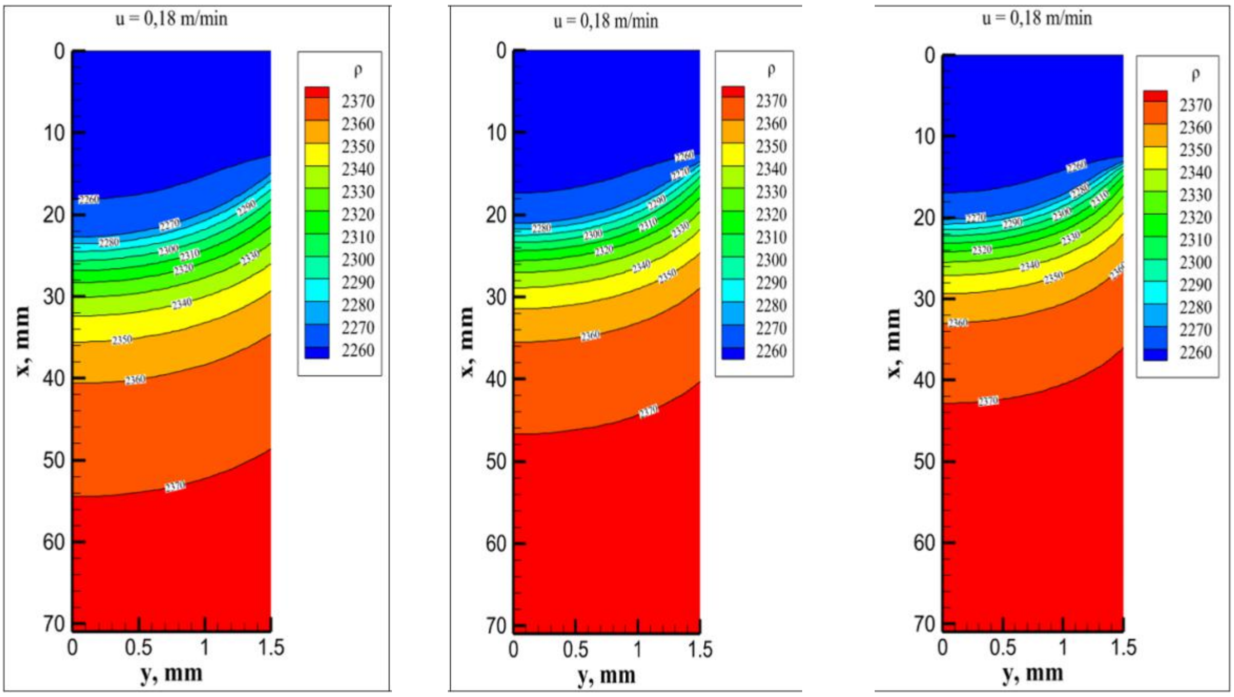

a) b) c)

Fig.5 Changing the density of the slurry depending on the value of the heat exchange coefficient: $a)\ k = 1000\,J/(m^2\cdot{}^\circ\mathrm{C}),\ b)\ k = 1500\,J/(m^2\cdot{}^\circ\mathrm{C}),\ c)\ k = 2000\ \ J/(m^2\cdot{}^\circ\mathrm{C})$

Table 2 presents experimental data on the casting performance and mechanical strength of the cast, as a function of binder composition and casting speed.

Table 2. The dependence of the strength of ceramics on the velocity of casting in a flat cavity [1].

Mass fraction of mass	Slurry's viscosity, Pa*s at $T_0 = 75°C$	Slurry casting ability, mm	Casting velocity, mm / min	Mechanical strength of the casting at bending, mPa
0.117	4.16	88	165	8.18

The calculation data were obtained at the experimental values of the filling velocity $u_0 = 0.165\ m/min$ at ω = 0.117 in a flat cavity (Fig. 6). In the initial configuration, the cooling water temperature is set at θ_1= 75 ^{0}C, while in the second configuration it is θ_2= 59 ^{0}C, and in the third configuration, it is θ_3= 40 ^{0}C. The liquid slurry flows into the uniform cavity at an initial temperature of t_0 = 75 ^{0}C. As depicted in Fig. 4, the transition between one cooling circuit and the next shows fewer voids. The casting speed ensures a uniform temperature distribution across the cross-section of the cavity. This even temperature distribution results in uniform rheological and thermophysical properties of the slurry across its cross-section. Consequently, the shrinkage of the thermoplastic slurry is consistent, preventing the formation of voids and defects that could compromise the strength of the beryllium oxide casting. The slurry solidifies within the molding cavity, indicating that the beryllium oxide (BeO) ceramic product acquires a structural shape suitable for further processing.

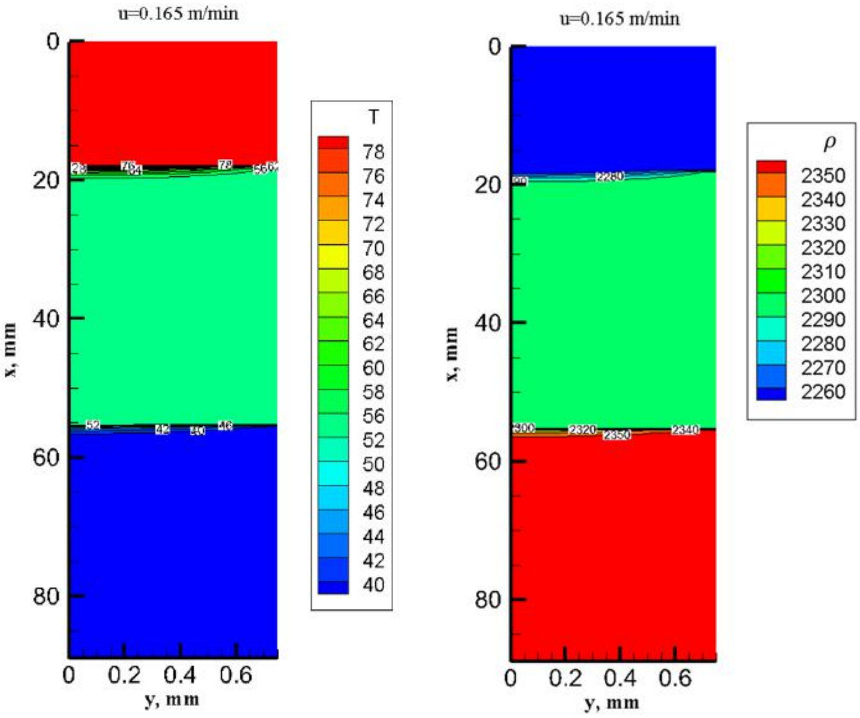

a) b)

Fig.6 The temperature and density field of a Slurry in a flat cavity: u_0 = 0.165 m/min, ω = 0,117 %

5. Conclusion

Ultrasonic treatment improves the rheological properties and enhances the fluidity of the thermoplastic beryllium oxide slurry within the molding cavity. The maximum values of apparent density and mechanical strength were obtained at an ultrasound intensity of 0.4÷1.6 W/ cm^2. A further increase in the impact power leads to a decrease in density due to the formation of porosity in the castings due to an increase in the size of the cavitation region, the number of newly formed cavitation cavities and the entry of part of the cavitation region into the cooling zone of the die. The increase in density and strength of castings is an effective compensation for shrinkage under the influence of ultrasound during pressing. In this case, shrinkage compensation occurs both according to the classical scheme by feeding with liquid slip, and by means of deformation compaction under the action of static and radiation pressure.For ultrasonic casting of thermoplastic slips based on beryllium oxide, it is advisable to use compositions with a binder content of 11.0-11.7% by weight, since these compositions achieve better shrinkage compensation and, accordingly, a denser casting.

Through the analysis of experimental data, empirical formulas were developed to relate the plastic viscosity and the critical shear stress of the slurry to temperature. It was established that the phase transition of the thermoplastic beryllium oxide slurry occurs within a defined temperature range. The heat generated during the phase transition was accounted for by considering the increased heat capacity over this temperature range.

Based on the calculation results, the following main conclusions can be made:

- a mathematical model of the formation of ceramic processes by the hot casting method includes a system of equations of motion of a non-Newtonian fluid, continuity and energy, taking into account the release of heat during the state of aggregation changes as the slurry cools in the mold cavity;

- the calculations received distributions of velocity, temperature and rheological properties, showing the internal structure of the slip in the mold cavity. The change of temperature and density of the slurry depending on the value of the heat exchange coefficient at a given value of the casting velocity is uniform across the cross-section of the mold cavity. This is explained by the fact that the conduction mechanism plays a predominant role in heat transfer due to the high thermal conductivity of beryllium oxide.The heat of crystallization released during this process is quickly dissipated due to the high thermal conductivity of beryllium oxide;

- the density of the slurry mass increases with a change in the state of aggregation, the calculation explains the mechanism for compensating for volumetric changes during the formation of ceramics by the hot casting method and is in satisfactory agreement with experiment.

Comparative calculations with experimental results help define the conditions for the hot molding process, facilitating the production of hardened beryllium oxide ceramics with a uniform structure.

Conflict of interest statement

The authors declare that they have no conflict of interest in relation to this research, whether financial, personal, authorship or otherwise, that could affect the research and its results presented in this paper.

CRediT author statement

Sattinova Z.: Conceptualization, Funding acquisition, Supervision; **Turalina D**.: Methodology, Data curation, Validation, Editing; **Yesbol Zh.:** Investigation, Analysis of results, Writing- Reviewing and Editing; **Mussenova E.:** Writing Reviewing and Editing, Resources, Data curation. The final manuscript was read and approved by all authors.

Funding

This work is funded by the Science Committee of the Ministry of Science and Higher Education of the Republic of Kazakhstan (Grant #BR24992907) for 2024-2026.

References

1 Shakhov S, Bitsoev G. (1999) *Application of Ultrasound in the Manufacture of High Thermal Conductivity Ceramic Articles.* Ust-Kamenogorsk: EKTU? 145. Available at: http://lib.ektu.kz/CGI/irbis64r_15/cgiirbis_64.exe?LNG=kz&Z21ID=&I21DBN=TRRR&P21DBN=TRRR&S21STN=1&S21REF=&S21FMT=fullwebr&C2 [in Russian]

2 Kiiko V, Makurin Yu, Ivanovsky A. (2006) *Beryllium Oxide Ceramics: production, physico-chemical properties, application.* Yekaterinburg, 440. https://www.centrmag.ru/catalog/product/keramika-na-osnove-oksida-berilliya-poluchenie-fiziko-him/?srsltid=AfmBOoo1AO3bkXmtHHBv5fD [in Russian]

3 Shakhov S. (2007) Controlling the deformation behavior of thermoplastic slurries with ultrasound. *Glass and Ceramics*, 64, 354–356. https://doi.org/10.1007/s10717-007-0088-2

4 Shakhov S. (2008) Use of ultrasound in order to intensify molding of high-temperature thermocouple sheaths. *Refract. Ind. Ceram.*, 49,261–263. https://doi.org/10.1007/s11148-008-9074-7

5 Shakhov S, Gagarin A. (2008) Rheological characteristics of thermoplastic disperse systems treated with ultrasound. *Glass and Ceramics*, 65, 122–124. https://doi.org/10.1007/s10717-008-9030-5

6 Akishin G, Turnaev S, Vaispapir V., Kiiko V. S., Shein I. R., Pletneva E. D., Timofeeva M.N., Ivanovskii A.L. (2011) Composition of beryllium oxide ceramics. *Refractories and Industrial Ceramics,* 51, 377–381. https://doi.org/10.1007/s11148-011-9329-6

7 Akishin G, Turnaev S, Vaispapir V., Gorbunova M.A., Makurin Yu.N., Kiiko V.S., Ivanovskii A. L. (2009) Thermal conductivity of beryllium oxide ceramic. *Refractories and Industrial Ceramics,* 50, 465–468. https://doi.org/10.1007/s11148-010-9239-z

8 Zhapbasbayev U., Sattinova Z., Ramazanova G. (2024) Simulation of Hot Casting Shrinkage of Thermoplastic Beryllium Oxide Slurries with Ultrasonic Activation. *Engineered Science*, 32, 1294. https://doi.org/10.30919/es1294

9 Sattinova Z.K., Ramazanova G.I., Zhapbasbayev U.K., Assilbekov B.C., Musenova E.K. (2018) Investigation of thermal conditions of the molding process slurry beryllium oxide. *Eurasian Physical Technical Journal*, 15(2), 30. https://phtj.buketov.edu.kz/index.php/EPTJ/article/view/528/240

10 German R, Bose A. (1997) *Injection molding of metals and ceramics.* New Jersey: Princeton, 413. https://books.google.kz/books/about/Injection_Molding_of_Metals_and_Ceramics.html?id=jXINAAAACAAJ&redir_e

11 Bingham E.C. (1922) *Fluidity and Plasticity.* New York: McGraw-Hill? 463. https://archive.org/details/fluidityandplast007721mbp

12 Wilkinson W.L. (1960) *Non-Newtonian Fluids. Fluid Mechanics, Mixing and Heat Transfer.* London: Pergamon Press, 138. https://www.amazon.com/Non-Newtonian-Fluids-Mechanics-Mixing-Transfer/dp/0080092683

13 Pakhomov M.A., Zhapbasbayev U.K., Bosinov D.Zh. (2023) Numerical simulation of the transition of a Newtonian fluid to a viscoplastic state in a turbulent flow. *Journal King Saud University Science*, 35(2), 102522. https://doi.org/10.1016/j.jksus.2022.102522

14 Zhapbasbayev U.K., Bekibayev T.T., Pakhomov M.A., Ramazanova G.I. (2024) Heat transfer of crude waxy oil with yield stress in a pipe. *Energies*, 17, 4687. https://doi.org/10.3390/en17184687

15 Dvinskikh Yu, Popil'skii R, Kostin L, Kulagin V. (1979) Thermophysical properties of thermoplastic casting slurries of some high-refractory oxides. *Ogneupory*, 12, 37 – 4. [in Russian]

16 Zhapbasbayev U, Ramazanova G, Kenzhaliyev B., Sattinova Z., Shakhov S. (2016) Experimental and calculated data of the beryllium oxide slurry solidification. *Appl. Therm. Eng.*, 96, 593–599. https://doi.org/10.1016/j.applthermaleng.2015.11.114

17 Sattinova Z., Assilbekov B., Bekenov T., Ramazanova G. (2024) Computational investigation of the influencing parameters on the solidification of thermoplastic beryllium oxide slurry in a cylindrical shell. *Ceramics*, 7(3), 906-925.https://doi.org/10.3390/ceramics7030059

18 Voller V, Prakash C. (1987) A fixed grid numerical modeling methodology for convection-diffusion mushy region phase-change problems. *Int. J. Heat Mass Transfer*, 30, 1709–1719. https://doi.org/10.1016/0017-9310(87)90317

19 Voller V, Swaminathan C, Thomas B. (1990) Fixed grid techniques for phase change problems: a review. *Int. J. Numer. Methods Fluids*, 30, 875–898.https://doi.org/10.1002/nme.1620300419

20 Hu H., Argyropoulos S. (1996) Mathematical modeling of solidification and melting: a review. *Modelling Simul. Mater. Sci. Eng.*, 4, 371–396. https://doi.org/10.1088/0965-0393/4/4/004

21 Moraga N, Andrade M, Vasco D. (2010) Unsteady conjugated mixed convection phase change of power law non-Newtonian fluid in a square cavity. *Int. J. Heat Mass Transfer*, 53, 3308-3318. https://doi.org/10.1016/j.ijheatmasstransfer.2010.02.044

22 Carmona M, Cortes C. (2014) Numerical simulation of a secondary aluminum melting furnace heated by a plasma torch. *J. Mater. Process. Technol.*, 214, 334-346. https://doi.org/10.1016/j.jmatprotec.2013.09.024

23 Bannach N. (2014) Phase Change: Cooling and Solidification of Metal. Available to: https://www.comsol.com/blogs/phase-change-cooling-solidification-metal/

24 COMSOL Inc. (2014) Available at: http://www.comsol.com/

25 Chung T. (2002) *Computational Fluid Dynamics.* Cambridge: Cambridge University Press. https://doi.org/10.1017/CBO9780511606205

26 Kiiko V.S., Vaispapir V.Ya. (2014) Thermal conductivity and prospects for application of BeO ceramic in electronics. *Glass and Ceramics*, 11, 12–16. https://doi.org/10.1007/s10717-015-9694-6

27 Zhao-Hui R., Xiu-Yan G., Yuan Y., He-Ping T. (2021) Determining the heat transfer coefficient during the continuous casting process using stochastic particle swarm optimization. *Case Stud. Therm. Eng.*, 28, 101439. https://doi.org/10.1016/j.csite.2021.101439

28 Tannehill J.C., Anderson D.A., Pletcher R.H. (2012) Computational Fluid Mechanics and Heat Transfer, 763. https://www.iust.ac.ir/files/mech/ayatgh_c5664/files/Computational_Fluid_Mechanics_and_Heat_Transfer_Anderson__Main_Reference.pdf

29 Cebeci T., Bradshaw P. (1988) *Physical and Computational Aspects of Convective Heat Transfer.* https://doi.org/10.1007/978-1-4612-3918-5

AUTHORS' INFORMATION

Yesbol Zh. – Master (Sci.), Researcher, al-Farabi Kazakh National University, Almaty, Kazakhstan; https://orcid.org/0009-0006-7166-261X; jalynesbol@gmail.com

Sattinova, Zamira Kanaevna – Candidate of phys. and math.sciences, Professor, Department of Electrical Power Engineering, L.N. Gumilyev Eurasian National University, Astana, Kazakhstan; SCOPUS Author ID: 54400166600; https://orcid.org/0000-0002-2990-6581; sattinova.kz@gmail.com

Turalina, Dinara Eleusizovna – Candidate of phys.-math. sciences, Associate Professor, Head of the Mechanics Department, al-Farabi Kazakh National University, Almaty, Kazakhstan; SCOPUS Author ID: 56728873900; https://orcid.org/0000-0003-0762-2657; dinara.turalina@kaznu.kz

Mussenova, Elmira Kuanaravna – Candidate of phys.-math. Sciences, Associate Professor, Physics and Nanotechnology Department, Karaganda Buketov University, Karaganda, Kazakhstan; SCOPUS Author ID: 56242227100; https://orcid.org/0000-0001-5458-3641; emusenova@mail.ru

30

EURASIAN PHYSICAL TECHNICAL JOURNAL
2025, Volume 22, No.1 (51)
https://doi.org/10.31489/2025N1/115-126

Received: 25/09/2024 Revised: 18/02/2025 Accepted: 18/03/2025

Original Research Article

UDC: 524.7; 52; 52-16/-17; 520.88; 520.2/.8

SPECTRAL AND PHOTOMETRIC STUDIES OF MRK6 AND MRK1040 IN THE OPTICAL RANGE

Shomshekova S.A.*, Denissyuk E.K., Kondratyeva L.N.,
Serebryanskiy A.V., Aimanova G.K., Aktay L.

Fesenkov Astrophysical Institute, Almaty, Kazakhstan
**Corresponding author*: shomshekova@fai.kz

Abstract. *This paper is dedicated to the study of variability in active galactic nuclei, which play a key role in understanding the physical processes occurring in their central regions. This research focuses on the analysis of photometric and spectral variability of two Seyfert galaxies, MRK 6 and MRK 1040, based on archival and modern observations. For the first time, the results of photometric observations of MRK 6 have been processed, with special attention given to the profiles of emission lines and the identification of additional spectral components that may indicate gas outflows. The velocity dispersions of each emission-line component have been determined for the studied galaxies. In some profiles of Hα and Hβ, their velocity dispersions and corresponding line-of-sight velocities have been estimated, which may indicate the outflow of matter from the central regions of the galaxies.*

Keywords: active galactic nuclei, Seyfert galaxies, photometry, spectroscopy, light curves, emission lines.

1. Introduction

This work is dedicated to the study of selected Seyfert galaxies from the Markarian list. Spectral and photometric studies of Seyfert galaxies from the Markarian list have been conducted at Fesenkov Astrophysical Institute (FAI) for several decades. A significant factor that has increased the efficiency of studies on active nuclei of poorly studied Seyfert galaxies is the implementation of an innovative spectral instrument developed at FAI in 2022. This instrument enables the acquisition of spectra from distant, hence faint and less studied Seyfert galaxies. Due to the large number of Seyfert galaxies discovered to date, both ground-based and space observatories dedicated to studying Active Galactic Nuclei (AGN) cannot cover all these Seyfert galaxies with systematic observations, which are crucial due to the unpredictable photometric and spectral variability of AGNs. Therefore, systematic observations and studies of poorly studied Seyfert galaxies remain a relevant task.

The paper [1] presents the results of a 22-year study of the galaxy MRK 6 using X-ray data from 2001 to 2022. Changes in the spectral and temporal behavior of the galaxy were detected in both X-ray and optical ranges. In another study [2], the morphology and kinematics of ionized gas in the galaxy MRK 6 were investigated, revealing extended filaments of ionized gas. Analysis of the kinematics and ionization state of gas in these filaments suggests that the hard radiation from the active nucleus illuminates externally accreted material, which rotates nearly perpendicular to the stellar disk of MRK 6. In the study [3], a new method is presented for measuring the radius of the equatorial scattering region in Type 1 active galaxies using the polarization of broad lines, indicating a scattering region size of approximately 100 light-days in MRK 6. The kinematics of gas and emission line profiles of Hβ in active galaxies were investigated in the study [4]. Observations, exemplified by MRK 6, revealed complex structures, providing an opportunity to search for close binary supermassive black holes. In the study [5], the analysis of X-ray reverberation in six active galactic nuclei using Granger causality analysis was conducted. Granger causality delays and their variations over time were analyzed for each individual light curve. Significant delays correlating with the light curve were observed in all active galactic nuclei except MRK 1040. It is suggested that the spread of the obtained delays may be related to the expansion of the corona. It is suggested that in IZw1, MRK 704, and MRK 1040, the corona may be more compact. The paper [6] presents the results of high-resolution X-ray spectroscopy of warm absorption in the galaxy type MRK 1040. The observations were conducted from 2013 to 2014 with a total exposure of 200 ks. The spectrum revealed the presence of warm absorption, including absorption lines of Ne, Mg, and Si ions, as well as H-like lines of S and Ar. The profiles indicate low outflow velocities of the absorbing gas, which may suggest possible attenuation of outflowing gas on large scales in the galaxy MRK 1040. The results from all authors indicate the complexity and diversity of physical processes occurring in AGNs, contributing to a better understanding of the underlying mechanisms.

2. Photometric and spectral observations

Photometric observations of the studied objects at FAI have been conducted since 2015. The observations are carried out at the Tien Shan Astronomical Observatory (TShAO) using the Zeiss-1000 "East" telescope with a modified optical system and equipped with an Apogee Alta U9000 CCD camera, with a field of view of 20'×20'. Spectral observations were conducted using the AZT-20 telescope at the Assy-Turgen Observatory. This is the largest telescope in Kazakhstan, capable of detecting extremely faint objects (up to 21-22 stellar magnitudes). Currently, the AZT-20 is equipped with a spectrograph based on dispersing elements VPHG (Volume Phase Holographic Gratings) using fiber optic technologies. An electron-multiplying CCD-camera with high-speed image readout at minimal noise level (EMCCD) is used as the radiation receiver.

2.1 Methodology of photometric and spectral studies

The galaxies Mrk 6 and Mrk 1040 belong to the class of active galactic nuclei of the Narrow-Line Seyfert 1 galaxies (NLSy1), known as Seyfert galaxies (Table 1). This subclass of galaxies was discovered by Osterbrock and is characterized by narrow Balmer lines (Hβ line profile width less than 2000 km/s), intense FeII lines, and weak forbidden lines [7]. The methodology and processing of photometric observational data consist of standard operations using calibration Dark and Flat frames. Brightness measurements are conducted using the differential photometry methods (standard software package MaximDL Pro6). The stars with known brightness values in the vicinity of the object are selected as the standard stars (Table 2). To convert the obtained instrumental brightness estimates to the standard B V Rc system, corresponding transformation equations are applied [8].

Table 1. Seyfert galaxies for the study

Object	α(2000)	δ(2000)	V
Mrk 6 (IC450)	06 52 12.33	74 25 37.12	14.19
Mrk 1040 (NGC 931)	02 28 14.46	31 18 41.46	14.74

Table 2. Properties of standard stars for photometric studies

Object	Referent stars			
	Object	B	V	R
Mrk 6 (IC450)	GSC 04371-00113	15.06	14.44	14.33
Mrk 1040 (NGC 931)	Tycho-2323-1484-1	11.47	10.49	10.16

2.2 Methodology of Spectral Analysis

Accurate measurement of the velocity dispersion of broad components of spectral emission lines and their distribution plays a key role in estimating the masses of supermassive "black holes" in active galactic nuclei. Therefore, it is important to have an idea of the most accurate shape of the broad component profile, especially in the Hα region, where narrow components of the Hα and NII emission lines blend. To describe the shape of the profile, several separate components are used. However, in this case, the question arises of an adequate choice of the number of such components. For example, in [9], it is said that to correctly describe the line profiles, it was necessary to use several Gaussians. At the same time, the authors tried to use as few of them as possible, but at the same time they tried to ensure an adequate fitting of the observed line profiles. The criterion for adding additional components was a significant reduction in the root-mean-square error and $\chi 2$ during the fitting. This approach is somewhat subjective. The problem of determining the required number of components in the broad emission lines of Hα or Hβ can be solved within the concept of Bayesian analysis:

$$P(\Theta|D,M) = \frac{P(D|\Theta,M)P(\Theta|M)}{P(D|M)} \equiv \frac{L(\Theta)\pi(\Theta)}{Z} \qquad , \tag{1}$$

where $P(\Theta|D,M)$ is the posterior (updated, taking into account the new data obtained) information (conditional probability) for the parameters Θ, taking into account the data D and the used model M. $P(D|\Theta,M) = L(\Theta)$ is the likelihood function (how probable the obtained data are, taking into account the chosen model and the its optimal parameters), $P(\Theta|M) = \pi(\Theta)$ is the prior (before the experiment, observations) probability for the parameters of the adopted model M, and $P(D|M) = Z$ is the marginal likelihood, otherwise called the model evidence, which is the integral over all possible model and parameter spaces. $P(D|M)$ determines the highest probability among all possible models:

$$P(D|M) \equiv Z \int_{\Omega_\theta} L(\Theta)\pi(\theta)\, d\Theta \tag{2}$$

It is clear that it is often not possible to estimate $P(D|M)$ (since we will need to consider all possible models and parameters for a given problem), but it can be used to estimate which of the models under consideration is more probable compared to other models. For the analysis of the spectra of Seyfert galaxies with the choice of the most probable model among the considered model (for example, in the case of different number of components in a wide profile), we use the nested sampling method [10], which, in addition to estimating the reliability of the model, gives us posterior distributions. The latter, in turn, can be used to estimate the model parameters and their error range:

$$\bar{\Theta}_i = E[\Theta_i] = \int \Theta_i\, P(\Theta_i|D,M) d\Theta_i \tag{3}$$

$$P(\Theta_i|D,M) \sim \int_{\forall\Theta_j \in (\Theta_j \neq \Theta_i)} L(\Theta_j)\, \pi(\Theta_j) d\Theta_j \tag{4}$$

To implement the nested sampling method, we use the DYNESTY package [11,12]. As prior information for each parameter in the model, we use a so-called 'non-informative' approach where the probability of values for the selected parameter is uniform over a range of accepted values (these constraints are known from previous studies of Seyfert galaxies). Unfortunately, this significantly increases computation time. However, in the future, this will allow us to analyze individual galaxies (or specific types of galaxies), using posterior information as prior for subsequent iterations (e.g., when new observational data is available). Additionally, in our models, we assume that the amplitudes in the [OIII] doublet are related by Aλ5007Å/Aλ4959Å = 2.99 [13] and the amplitudes in the [NII] doublet are related by Aλ6585Å/Aλ6550Å = 3.05 [14]. The widths of narrow emission lines are assumed to be identical (in terms of velocity dispersion) for all lines in the considered range, and the widths of broad profiles are also identical for all components of the broad emission spectrum. Doppler shifts of the 'red' and 'blue' components of the broad profile are also assumed to be identical (in the case of choosing a model with such components). To compensate for possible errors in wavelength calibration, as well as inaccurate account of redshift, we introduce an additional parameter for each set of spectral lines. For precise determination of velocity dispersion values, we approximated the spectra with composite models. For the Hα region, these models consist of narrow emission lines of [OI], [SII], [NII] doublets, and the narrow Hα emission line, along with a broad Hα component. For the Hβ region, models include narrow emission lines of the [OIII] doublet and the narrow Hβ emission line, as well as a broad Hβ component. To complete the analysis, it is necessary to account for the stellar component of galaxies in both spectral regions. This can be achieved, for example, using the methodology implemented in the STARLIGHT package [15]. To incorporate the stellar contribution (continuum spectrum), we additionally included a power-law flux distribution in each composite model. In addition to approximating observed spectra with composite models to estimate parameters and analyze the broad components of Hα and Hβ, there is also the task of selecting the number of profiles (sub-components) in the broad Hα and Hβ profiles, as well as determining the shapes of the narrow emission line profiles. In our studies, we analyzed the result using both Gaussian profiles and profiles modeled as Voigt functions. The total number of parameters for the Hα region, using Voigt profiles for narrow components, three sub-components in the broad component of emission line Hα, and the additional assumptions mentioned earlier, was 18. For the Hβ region, the number of parameters was 14. For the model where all line profiles are described by Gaussians, the number of parameters was 17 and 13 respectively. Models with fewer broad emission line components (two or one) had fewer parameters.

3. Results of photometric and spectral analysis of the studied objects

MRK 6 (IC 450) is a Seyfert galaxy of the Sy1.0-1.5 class. Redshift $z=0.018676\pm0.000834$. The distance to the galaxy is 79 Mpc. The mass of the galaxy's central body (CB) is, $MBH = (1\text{-}2)*10^{8}$ Mc [16]. Active spectral and photometric studies of MRK 6 were carried out between 1990 and 2015 [17-20]. At FAI, MRK 6 observations in the BVRc photometric system have been carried out since 2016 [21]. Table A (Appendix) presents the results of photometric studies from November 25, 2019 to February 22, 2024. For general comparison, the results are presented as light curves (Figure 1) for the galaxy MRK 6 from 2016 to 2024.

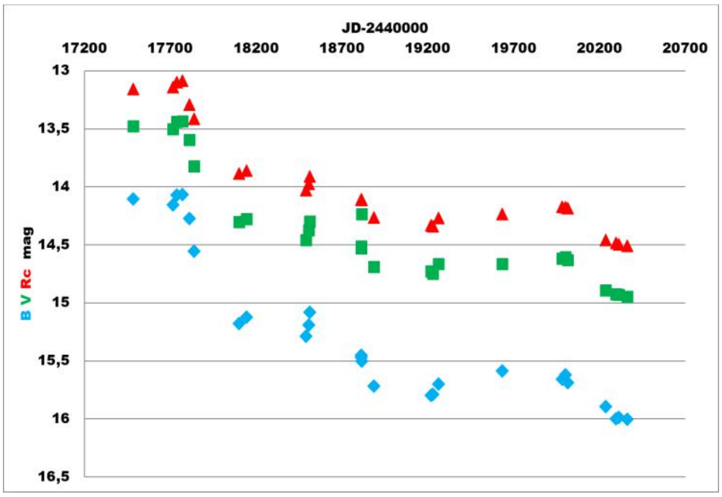

Fig.1. Light curves of MRK6 obtained in 2016-2024.
On the X-axis: Julian date - 2440000, and on the Y-axis: stellar magnitude

There was a unique opportunity to compare archival observational data with contemporary data over an extended time interval for the galaxy MRK 6. In previous works [22, 23] the digitization process and analysis of proprietary spectral data from the archive is described. In the spectra of MRK 6 obtained on February 4, 1976, on the left wing of the Hα line, an additional component is visible, shifted from the line center by 45 Å. Its radial velocity corresponds to 2450 km/s. In the spectra from 2023 and 2024, this detail appears in the Hα profile as a broad blue wing (Figure 2). Presumably, this additional component is created by a powerful jet (gas flow) moving towards the observer. Our modeling estimates indicated the radial velocity of this jet to be 2525^{+45}_{-49} km/sec (Figure 4). Additionally, a combined profile of the H_{β} region is presented (Figure 5), consisting of both narrow emission lines and profiles of the broad component.

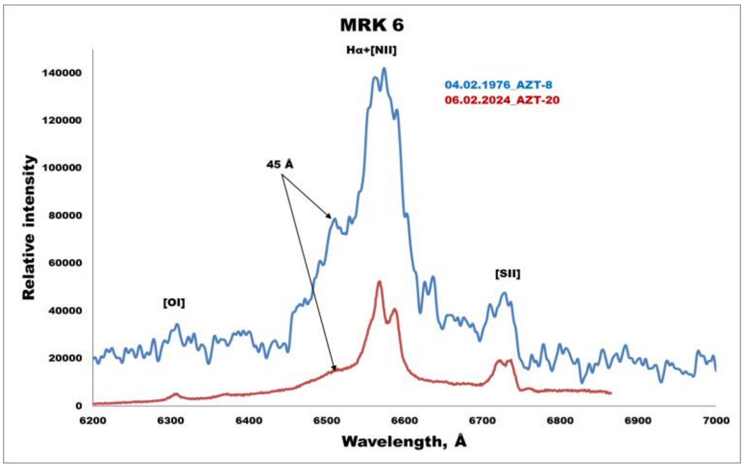

Fig. 2. Comparison of data obtained from digitizing archival spectra with results from 2024 (AZT-20)

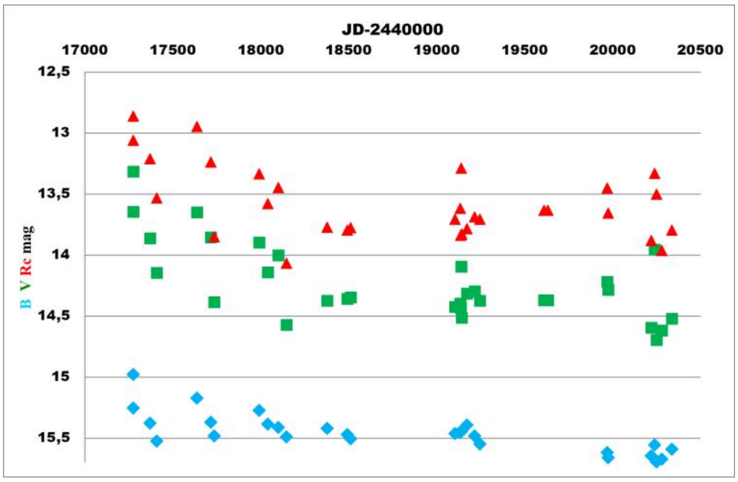

Fig.3. Light curves of MRK1040 obtained in 2015-2024. On the X-axis: Julian date - 2440000, and on the Y-axis: stellar magnitude.

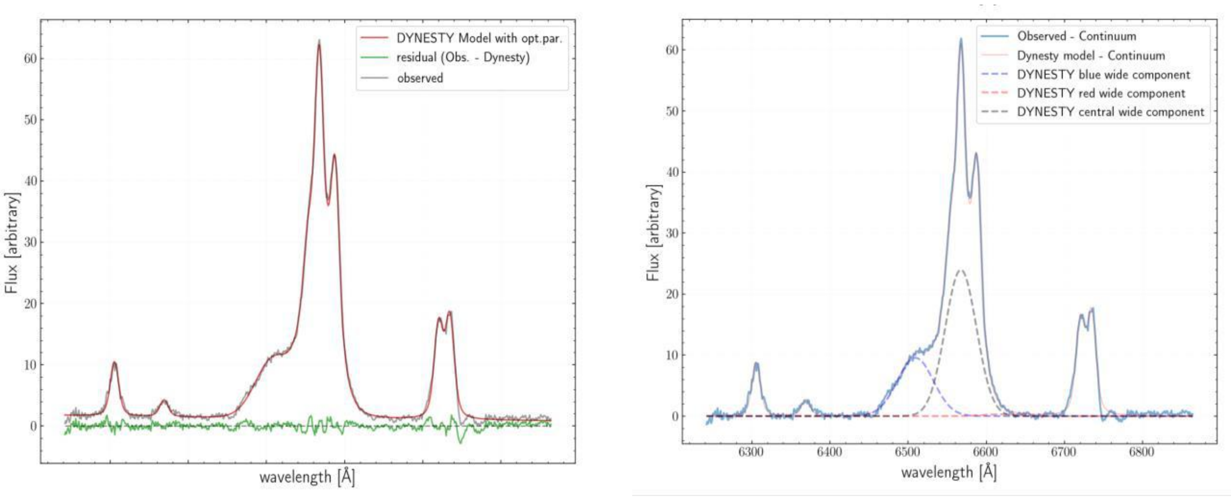

a) Hα, 3- component model

b) Hα, 3- component model

Fig.4. The result of the model approximation with three components of the broad Hα line spectrum of MRK 6 obtained on AZT-20 06.02.2024

Table 3. The results of processing spectral data for the galaxy MRK6 obtained in 2023-2024

Emission line of the spectrum of Seyfert galaxies	λ (Å)	Continuum flux (erg s^{-1} cm^{-2} $Å^{-1}$)	Line flux (erg s^{-1} cm^{-2})	Equivalent width (Å)	Telescope
Mrk6 (16.01.2015)					
Hα+[NII]	6562	1.3E-14	5,562E-12	428	AZT-8
[SII]	6720	1.1E-14	2,44E-13	22	
Mrk6 (25.01.2023)					
[OI]	6300	6.284E-15	5.344E-14	8.498	AZT-20
Hα+[NII]	6562	9.102E-15	1.042E-12	111.8	
[SII]	6720	7.575E-15	1.909E-13	25.32	
Mrk6 (16.11.2023)					
Hα+[NII]	6562	1.083E-14	8.828E-13	81.98	AZT-20
[SII]	6720	7.035E-15	2.324E-13	33.55	
H_β	4861	1.363E-14	1.677E-13	12.31	
[OIII]	4959	1.039E-14	6.074E-13	58.33	
[OIII]	5007	1.178E-14	1.801E-12	149.5	
Mrk6 (06.02.2024)					
[OI]	6300	9.611E-15	1.405E-13	14.62	AZT-20
Hα+[NII]	6562	1.241E-14	3.258E-12	261.1	
[SII]	6720	1.229E-14	4.659E-13	38.24	
H_β	4861	2.712E-14	3.654E-13	13.49	
[OIII]	4959	2.678E-14	1.300E-12	48.46	
[OIII]	5007	2.678E-14	4.003E-12	148.3	

MRK 1040 (or NGC 931) is a bright Seyfert 1 spiral galaxy. It has a redshift of z=0.016338±0.000314 and is located at a distance of 340 Mpc. At FAI, photometric observations of MRK 1040 in the BVRc photometric system have been conducted since 2015 [21]. Table B (Appendix) presents the results of photometric studies from September 13, 2020, to January 27, 2024. For general comparison, the results are shown as light curves (Figure 4) for MRK 1040 from 2015 to 2024. The obtained data indicate that the studied object experiences irregular fluctuations in brightness in all three filters, with amplitudes of $B=0^m.337$, $V=0^m.874$, $R=0^m.734$.

The above-described spectral analysis methodology was applied to the spectral observations of the Seyfert galaxies MRK 1040 and MRK 6. Analysis of the spectra of MRK 6 obtained on February 6, 2024, showed that the model with three components of the broad Hα profile is more statistically significant compared to models with one or two components (Figure 4, Figure 6).

Table 4. The results of processing spectral data for the galaxy MRK 1040 obtained in 2023

Emission line of the spectrum of Seyfert galaxies	λ (Å)	Continuum flux (erg s^{-1} cm^{-2} Å^{-1})	Line flux (erg s^{-1} cm^{-2})	Equivalent width (Å)	Telescope
MRK 1040 (20.01.2023)					
Hα+[NII]	6562	4.062E-15	7.211E-13	177.6	AZT-20
MRK 1040 (23.01.2023)					
Hα+[NII]	6562	4.007E-15	9.080E-13	225.6	AZT-20
MRK 1040 (25.01.2023)					
H_β	4861	2.810E-13	1.164E-11	41.42	AZT-20
[OIII]	4959	3.011E-13	1.664E-12	5.525	
[OIII]	5007	2.891E-13	5.921E-12	20.48	

As a result, we obtained the following velocity dispersion values for the narrow lines (NL) FWHM (NL) = 360^{+22}_{-22} $(km \cdot s^{-1})$ the line-of-sight velocity of the broad profile component 2525^{+45}_{-49} $(km \cdot s^{-1})$ and the velocity dispersion across the width of the broad central component of the lines (BL) FWHM (BL, central) = 1073^{+28}_{-29} $(km \cdot s^{-1})$ and components shifted relative to the central in the red and blue sides FWHM (BL, blue/red) = 1239^{+50}_{-45} $(km \cdot s^{-1})$ in the Hα region.

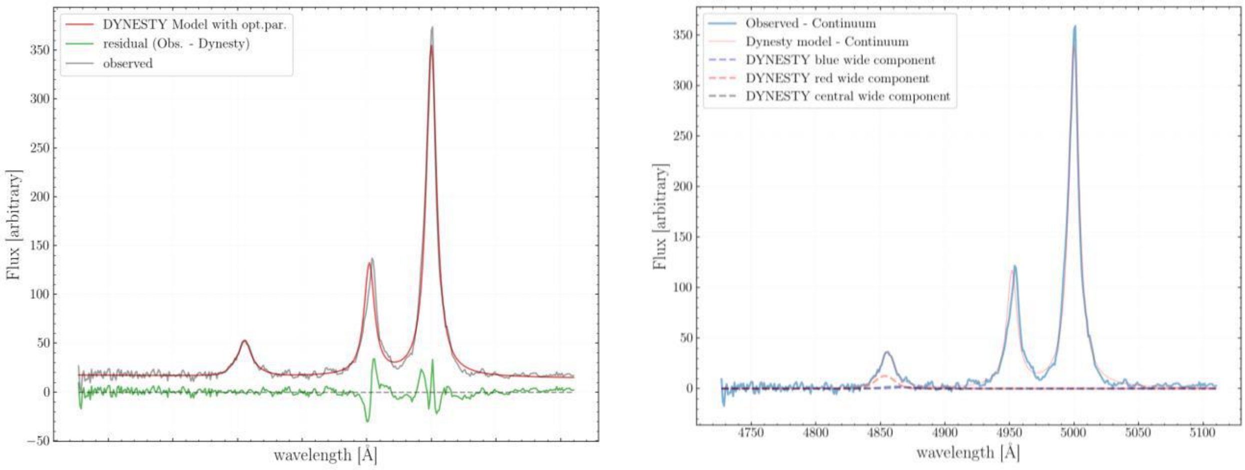

a) Hβ, 3-component model b) Hβ, 3-component model

Fig.5. The result of the model approximation of the broad H_β line spectrum of MRK 6 obtained on AZT-20 06.02.2024

Approximation of the Hβ region resulted in the velocity dispersion values for the narrow emission lines FWHM (NL) = $335^{+1.4}_{-1.0}$ $(km \cdot s^{-1})$, the line-of-sight velocity from the “blue” and “red” components of the broad profile 475^{+44}_{-62} $(km \cdot s^{-1})$. The velocity dispersion of the broad profile central component H_β FWHM (BL, central) = 1435^{+746}_{-271} $(km \cdot s^{-1})$ and the corresponding dispersion of the broad components profile H_β, shifted to the red and blue regions of the spectrum FWHM (BL, blue/red) = 1084^{+84}_{-57} $(km \cdot s^{-1})$.

The analysis of Mrk 1040 spectra obtained on January 21 and 23, 2023, showed that a model with a single component of the broad Hα profile is more statistically significant than models with more components (2 or 3) (Figure 6, Figure 7).

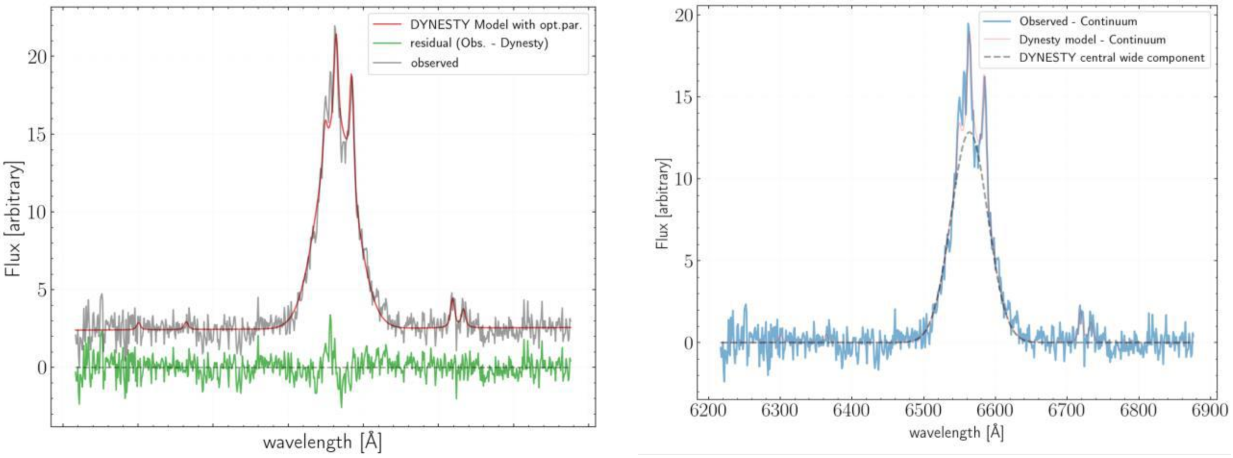

a) Hα, 1-component model b) Hα, 1-component model

Fig.6. The result of the model approximation with one component of the broad Hα line spectrum of Mrk 1040 obtained on AZT-20 23.01.2023

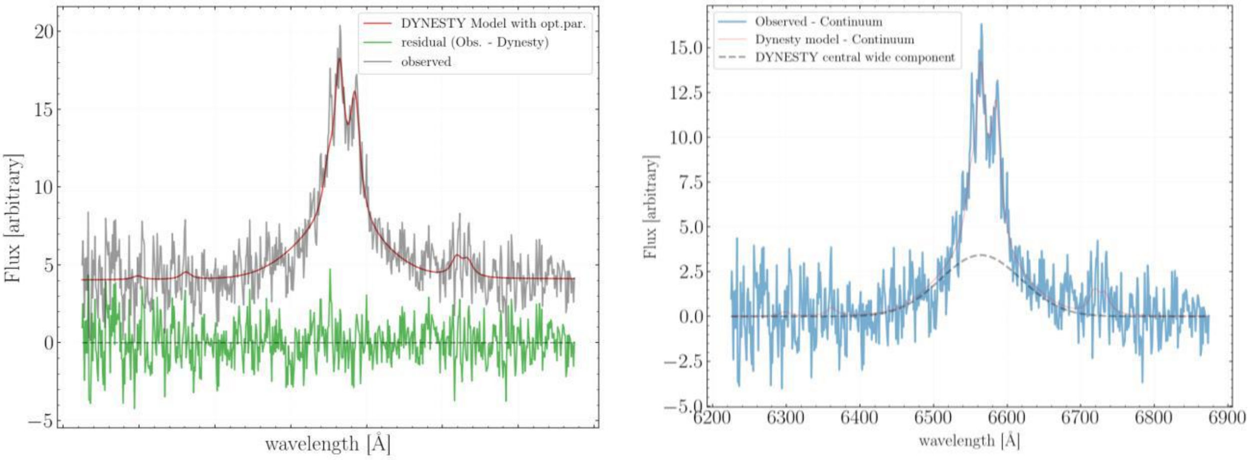

a) Hα, 1-component model b) Hα, 1-component model

Fig.7. The result of the model approximation with one component of the broad Hα line spectrum of Mrk 1040 obtained on AZT-20 20.01.2023

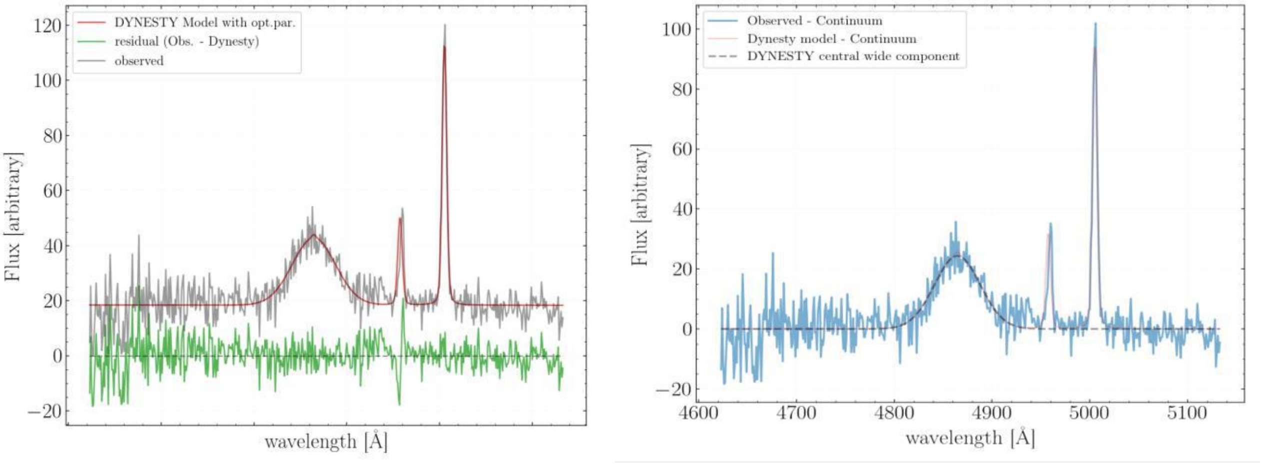

a) Hα, 1-component model b) Hα, -component model

Fig.8. The result of the model approximation with one component of the broad Hβ line spectrum of Mrk 1040 obtained on AZT-20 25.01.2023

For Hα region approximation of the spectra taken on January 23, 2023, the velocity dispersion value for the narrow emission lines FWHM (NL) = 149^{+51}_{-63} $(km \cdot s^{-1})$. The velocity dispersion of the central component of the broad profile Hα FWHM (BL, central) = 1369^{+30}_{-28} $(km \cdot s^{-1})$.

For spectral data obtained on January 20, 2023, the approximation of the Hα region resulted in velocity dispersion value for the narrow emission lines FWHM (NL) = 52^{+46}_{-29} $(km \cdot s^{-1})$. The velocity dispersion of the central component of the broad profile Hα FWHM (BL, central) = 2950^{+284}_{-267} $(km \cdot s^{-1})$ (Figure 7).

The results of approximation of the Hβ region of the spectrum of Mrk1040 obtained on January 25, 2023, indicated that the broad Hβ profile was described by a single component (Figure 8). As a result of approximation the velocity dispersion value for the narrow emission lines FWHM (NL) = 232^{+5}_{-6} $(km \cdot s^{-1})$. The velocity dispersion of the central component of the broad profile H_β FWHM (BL, central) = 1695^{+20}_{-19} $(km \cdot s^{-1})$.

4. Conclusion

The paper presents new photometric and spectral data for galaxies from the Markarian list: Mrk 6 and Mrk 1040. Different research methods used by different scientists in the field of active galaxy nuclei are described. All the results obtained by other authors point to the complexity of the physical processes occurring in the studied objects. In the course of photometric studies of the galaxy Mrk 6, it was found that the brightness of this object for the period from 2016 to 2024 is unstable. The object reached its maximum luminosity in early 2017, and then by early 2018, its luminosity decreased by about ~1m. Since then, it has slowly continued to decrease. Observations of Mrk 1040 in the BVRc photometric system have been conducted since 2015. The data obtained show that the galaxy Mrk 1040 is subject to irregular light fluctuations in all three filters. The amplitudes of these oscillations are B=0^{m}.337, V=0^{m}.874, and R=0^{m}.734. Interestingly, spectrograms of the active nucleus of the Mrk 6 galaxy obtained on February 4, 1976, on the left wing of the Hα line showed an additional component displaced from the center of the line by 45 angstroms. Surprisingly, this component was also detected in the modern spectra obtained in 2024. Its radial velocity is 2450 km/s. Determining the number of components in broad spectral lines is a difficult task requiring a precise approach and taking into account many factors. Observations of spectra of active galactic nuclei are often difficult because of the overlap of different components. To adequately model such spectra, it is necessary to use methods capable of distinguishing and approximating individual components with high accuracy. Studies show that using several Gaussians to describe broad components of spectral lines can be an effective approach. However, it is important to keep in mind that the optimal number of components and their shape should be chosen taking into account the specifics of a particular observation and taking into account the statistical validity of the model. Methods of analyzing spectral data, such as Bayesian probability analysis and the nested sampling method, allow not only to determine the optimal number of components, but also to assess the reliability of the resulting model. This is important to avoid excessive model complexity or underestimation of the physical processes underlying the observed spectra. To determine the parameters of the Hα and Hβ region models and to analyze the broad components of Hα and Hβ, we recommend using the nested sampling method using the DYNESTY package. As a result of this method, we extracted narrow components of emission lines from the total spectrum, as well as broad components, the number of which was determined from an estimate of the relative statistical probability of a particular model. We determined the velocity dispersions for the components of the emission lines, as well as for the broad components of Hα and Hβ where detected, which may indicate the outflow of matter from the central regions of galaxies.

Conflict of interest statement

The authors declare that they have no conflict of interest in relation to this research, whether financial, personal, authorship or otherwise, that could affect the research and its results presented in this paper.

CRediT author statement

Shomshekova S.A.: Processing and analysis; Denissyuk E.K.: Processing; Kondratyeva L.N.: Observations; Serebryanskiy A.V.: Modeling; Aimanova G.K.& Aktay L.: Processing.
The final manuscript was read and approved by all authors.

.

Funding

This research is funded by the Science Committee of the Ministry of Education and Science of the Republic of Kazakhstan (Grant No. AP19676713) and by the Aerospace Committee of the Ministry of Digital Development, Innovations and Aerospace Industry of the Republic of Kazakhstan (Grant No. BR20381077).

Acknowledgements

We thank the FAI observers for their efficient work.

References

1 Layek N., Nandi P., Naik S., Kumari N., Jana A., Chhotaray B. (2024) Long-term X-ray temporal and spectral study of a Seyfert galaxy Mrk 6. *Monthly Notices of the Royal Astronomical Society,* 528 (3), 5269–5285. https://doi.org/10.48550/arXiv.2401.16780

2 Smirnova A.A., Moiseev A.V., Dodonov S.N. (2018) A close look at the well-known Seyfert galaxy: extended emission filaments in Mrk 6. *Monthly Notices of the Royal Astronomical Society,* 481 (4), 4542–4547. https://doi.org/10.1093/mnras/sty2569

3 Shablovinskaya E.S., Afanasiev V. L., Popović L.Č. (2020) Measuring the AGN Sublimation Radius with a New Approach: Reverberation Mapping of Broad Line Polarization. *The Astrophysical Journal,* 892, 2. https://doi.org/10.48550/arXiv.2003.12809

4 Pu Du, Michael S. Brotherton, Kai Wang, Zheng-Peng Huang, Chen Hu, David H. Kasper, William T. Chick, My L. Nguyen, Jaya Maithil, Derek Hand, Yan-Rong Li, Luis C. Ho, Jin-Ming Bai, Wei-Hao Bian, Jian-Min Wang (2018) Monitoring AGNs with Hβ Asymmetry. I. First Results:Velocity-resolved Reverberation Mapping. *The Astrophysical Journal*,869 (2), 17. https://doi.org/10.48550/arXiv.1810.11996

5 Nakhonthong N., Chainakun P., Luangtip W., Young A.J. (2024) Tracing the evolving X-ray reverberation lags within an individual AGN light curve. *Monthly Notices of the Royal Astronomical Society*, 530, 2. 1894-1906. https://doi.org/10.48550/arXiv.2404.04493

6 James Reeves, Valentina Braito, Ehud Behar, Travis Fischer, Steve Kraemer, Andrew Lobban, Emanuele Nardini, Delphine Porquet, Jane Turner. (2017) High-resolution X-Ray Spectroscopy of the Seyfert 1 Galaxy Mrk 1040. Revealing the Failed Nuclear Wind with Chandra. *The Astrophysical Journal,* 837, 1. 23. https://doi.org/10.48550/arXiv.1702.00461

7 Osterbrock D.E., Pogge R.W. (2017) The spectra of narrow-line Seyfert 1 galaxies. *The Astrophysical Journal*, 1985, 297, 166-176. https://doi.org/10.1086/163513

8 Shomshekova S. A., Reva I.V., Kondratyeva L.N. (2017) Standardization of the photometric system of the 1-meter telescope on TSHAO. *News of the National Academy of Sciences of the Republic of Kazakhstan Physico-Mathematical Series.* 4, 314, 155 – 161. Available to: https://journals.nauka-nanrk.kz/physics-mathematics/issue/view/225/252

9 Holden L.R., Tadhunter C.N., Morganti R., Oosterloo T. (2023) Precise physical conditions for the warm gas outflows in the nearby active galaxy IC 5063. *Monthly Notices of the Royal Astronomical Society,* 520, 2. 1848-1871. https://doi.org/10.1093/mnras/stad123

10 Skilling J. Nested Sampling. (2004). Bayesian Inference and Maximum Entropy Methods in Science and Engineering: Proceeding of the *24th International Workshop on Bayesian Inference and Maximum Entropy Methods in Science and Engineering,* 735. 395-405. https://doi.org/10.1063/1.1835238

11 Speagle J.S. (2020) DYNASTY: a dynamic nested sampling package for estimating Bayesian posteriors and evidence *Monthly Notices of the Royal Astronomical Society,* 493, 3. 3132-3158. https://doi.org/10.1093/mnras/staa278

12 Koposov S., Speagle J., Barbary K., Ashton G., Bennett E., Buchner J., Scheffler C., Cook D., Talbot C., Guillochon J., Cubillos P., Ramos A., Johnson B., Lang D., Dartiailh I.M., Nitz A., McCluskey A., Archibald A. (2023). *Josh speagle/dynasty:* 2.1.3 (v2.1.3). https://doi.org/10.5281/zenodo.8408702

13 Dimitrijević M.S., Popović L.Č., Kovačević J., Dačić M., Ilić D. (2007) The flux ratio of the [OIII] λλ5007, 4959 lines in AGN: comparison with theoretical calculations. *Monthly Notices of the Royal Astronomical Society*, 374, 3. 1181-1184. https://doi.org/10.1111/j.1365-2966.2006.11238.x

14 Dojčinović I., Kovačević-Dojčinović J., Popović L. Č. (2023) The flux ratio of the [N II] λλ 6548, 6583 Å lines in a sample of Active Galactic Nuclei Type 2. *Advances in Space Research*, 71, 2. 1219-1226. https://doi.org/10.1016/j.asr.2022.04.041

15 Cid Fernandes R., Mateus A., Sodré L., Stasińska G., Gomes J. M. (2005) Semi-empirical analysis of Sloan Digital Sky Survey galaxies - I. Spectral synthesis method. *Monthly Notices of the Royal Astronomical Society,* 358, 2. 363-378. https://doi.org/10.1111/j.1365-2966.2005.08752.x

16 Freitas I. C., Riffel R. A., Storchi-Bergmann T., Elvis M., Robinson A., Crenshaw D. M., Nagar N. M., Lena D., Schmitt H. R., Kraemer S. B. (2018) Outflows in the narrow-line region of bright Seyfert galaxies - I. GMOS-IFU data. *Monthly Notices of the Royal Astronomical Society,* 476, 2. 2760-2778. https://doi.org/10.1093/mnras/sty303

17 Granato G., Zitelli V., Bonoli F., Bonoli F., Danese L., Bonoli C., Delpino F. (1993) A Study of a homogeneous sample of optically selected Active Galactic Nuclei. III. Optical Observations *Astrophysical Journal Supplement*, 89, 35. https://doi.org/10.1086/191838

18 Doroshenko V., Sergeev S. (2003) Spectral activity of the Seyfert galaxy Markarian 6 in 1970-1991. *Astronomy & Astrophysics,* 405, 3. 909-915. https://doi.org/10.1051/0004-6361:20030587

19 Doroshenko V. (2003) Photometric activity of the Seyfert galaxy Markarian 6 from UBV observations in 1970-2001. *Astronomy & Astrophysics*, 405, 3. 903-908. https://doi.org/10.1051/0004-6361:20030586

20 Doroshenko V., Sergeev S., Klimanov S., Pronik V.I., Efimov Yu.S. (2012) Broad-line region kinematics and black hole mass in Markarian 6. *Monthly Notices of the Royal Astronomical Society*, 426, 1. 416-426. https://doi.org/10.1111/j.1365-2966.2012.20843.x

21 Shomshekova S., Denissyuk E., Valiullin R., Kusakin A., Reva I., Omarov Ch. (2019) Photometric Research of Seyfert Galaxies MRK 766, MRK 6, MRK 1040, MRK 1513. *News of the National Academy of Sciences of the Republic of Kazakhstan Physico-Mathematical Series.* 3, 325. 64-70. https://doi.org/10.32014/2019.2518-1726.25

22 Shomshekova S., Izmailova I., Umirbayeva A., Omarov C. (2022) A method for digitization of archival astro-plates of the Fesenkov Astrophysical Institute. *New Astronomy*. 97, 01881. https://doi.org/10.1016/j.newast.2022.101881

23 Shomshekova S., Kondratyeva L., Omarov Ch., Izmailova I., Umirbayeva A., Moshkina S. (2023) Digital archival spectral data for Seyfert galaxies and their use in conjunction with modern FAI spectral data. *Experimental Astronomy*, 56. 557–568. https://doi.org/10.1007/s10686-023-09916-6

AUTHORS' INFORMATION

Shomshekova, Saule Akhmetbekovna — PhD, Leading Researcher, Fesenkov Astrophysical Institute, Almaty, Kazakhstan; https://orcid.org/0000-0002-9841-453X; shomshekova@fai.kz

Denissyuk, Eduard Konstantinovich — Candidate of Physical and Mathematical Sciences, Chief Researcher, Fesenkov Astrophysical Institute, Almaty, Kazakhstan; https://orcid.org/0000-0001-5020-2557; denissyuk@fai.kz

Kondratyeva, Ludmila Nikolaevna — Candidate of Physical and Mathematical Sciences, Chief Researcher, Fesenkov Astrophysical Institute, Almaty, Kazakhstan; https://orcid.org/0000-0002-6302-2851; kondratyeva@fai.kz

Serebryanskiy, Alexander Vladimirovich — PhD, Head of observational astrophysics department, Fesenkov Astrophysical Institute, Almaty, Kazakhstan; https://orcid.org/0000-0002-4313-7416; serebryanskiy@fai.kz

Aimanova, Gauhar Kopbaevna — Candidate of Physical and Mathematical Sciences, Chief Researcher, Fesenkov Astrophysical Institute, Almaty, Kazakhstan; https://orcid.org/0000-0002-3869-8913; gauhar@fai.kz

Aktay, Laura — Bachelor's, Engineer, Fesenkov Astrophysical Institute, Almaty, Kazakhstan; https://orcid.org/0009-0005-5862-4777; aktay@fai.kz

.

Appendix

Table A. B V R magnitudes for the galaxy MRK6 obtained in 2019-2024 Aperture 6”

Date of observations	JD-24400000	B	V	R
25.11.2019	18812	15,452	14,513	14,109
26.11.2019	18813	15,467	14,53	14,109
28.11.2019	18815	15,502	14,232	14,11
08.02.2020	18887	15,717	14,687	14,264
04.01.2021	19218	15,797	14,726	14,331
16.01.2021	19230	15,79	14,748	14,339
17.02.2021	19262	15,699	14,664	14,268
24.02.2022	19634	15,584	14,665	14,232
07.02.2023	19982	15,657	14,617	14,171
26.02.2023	20001	15,618	14,604	14,175
13.03.2023	20016	15,688	14,628	14,184
21.10.2023	20238	15,895	14,893	14,458
20.12.2023	20298	15,997	14,923	14,484
03.01.2024	20312	15,984	14,928	14,495
22.02.2024	20362	16,002	14,944	14,506

Table B. B V R magnitudes for the galaxy MRK1040 obtained in 2020-2024.Aperture 6,8”

Date of observations	JD	B	V	R
13.09.2020	19105	15,464	14,423	13,705
12.10.2020	19134	15,455	14,397	13,618
14.10.2020	19136	15,448	14,431	13,838
17.10.2020	19139	15,449	14,094	13,287
19.10.2020	19141	15,439	14,512	13,827
19.11.2020	19172	15,395	14,315	13,786
02.01.2021	19216	15,482	14,297	13,687
02.02.2021	19247	15,549	14,374	13,705
31.01.2022	19610	15,705	14,37	13,633
21.02.2022	19631	15,726	14,37	13,634
27.01.2023	19971	15,619	14,22	13,452
01.02.2023	19976	15,66	14,284	13,656
04.10.2023	20221	15,645	14,593	13,881
21.10.2023	20238	15,556	13,955	13,33
02.11.2023	20250	15,696	14,696	13,5
01.12.2023	20279	15,674	14,617	13,961
27.01.2024	20336	15,59	14,52	13,794

EURASIAN PHYSICAL TECHNICAL JOURNAL
2025, Volume 22, No.1 (51)
https://doi.org/10.31489/2025N1/127-133

Received: 28/10/2024 Revised: 26/02/2025 Accepted: 18/03/2025 Published online: 31/03/2025

Original Research Article

UDC 537.311.33(075)

PHOTOLUMINESCENCE SPECTRA OF DOPED N-TYPE INDIUM ANTIMONIDE CRYSTALS

Yegemberdiyeva S.Sh., Kushkimbayeva B.Zh., Kusherbayeva M.R.*, Keikimanova M.T.

M.Kh. Dulaty Taraz University, Taraz, Kazakhstan

**Corresponding authors*: kmaikul@mail.ru

Abstract. *This paper presents a detailed study of photoluminescence of doped indium antimonide crystals. We have conducted a detailed study of photoluminescence of doped n-type indium antimonide crystals in a wide range of concentrations* $1*10^{15}$ cm^{-3}-$1.5*10^{19}$ cm^{-3} *at temperature 77 K. In this paper, we have for the first time obtained spectra of photoluminescence of indium antimonide with* $n > 5*10^{17}$ cm^{-3} *and experimentally discovered that spectrum of photoluminescence of indium antimonide with* $n \geq 8.5*10^{16}$ cm^{-3} *consists of two lines, maxima of which shift towards higher energies with increasing concentration. It has been established that shortwave line of doped n-type indium antimonide crystals' radiation is caused by recombination of electrons, located at Fermi level, with holes in valence band top. It has been shown that the best agreement between the experiment and theory in heavily doped crystals is reached by taking into account fluctuations of donor concentrations, dependence of the band gap on the degree of doping, as well as effective reduction of Fermi energy with increasing concentration.*

Keywords: photoluminescence of crystals, indium antimonide, Fermi level, doping, concentration, fluctuation, hole, band gap

1. Introduction

Indium antimonide (InSb) is a semiconductor with a narrow direct bandgap, $\Delta E_0 \approx 0.17$ eV at ambient conditions. Therefore, since its discovery in early fifties of twentieth century, InSb has naturally become one of the major choice materials for infrared (IR)-detecting devices [1].

Moreover, indium antimonide has long been considered a model semiconductor and it was indium antimonide on which the main theories created for crystals A^3 B^5 and their analogues (such as Kane's formalism) was tested. Interest in indium antimonide is caused not only by the peculiarities of its zone structure (narrow bandgap width, small effective mass of electrons, high mobility values), but also by the possibility to obtain single crystals in a very large concentration range (n- 10^{12}-10^{19}cm^{-3}; p - 10^{11}-10^{20} cm^{-3}). Although indium antimonide is a well-studied semiconductor, there is nevertheless very little work on photoluminescence studies. Of great scientific and often practical interest are studies of indium antimonide crystals containing initial concentrations of impurities, i.e., heavily doped crystals. When studying various physical effects in heavily doped n-type indium antimonide crystals, numerous anomalies have been found that are related not only to the degree of doping, but also to the grade (i.e., chemical nature) of doping impurity.

In recent years, scientists have been studying antimonide india according to various characteristics: Monnens, W., Billiet, N., Binnemans, K., et al. gives the following description: Indium antimonide (InSb) is a III-V compound semiconductor with a narrow bandgap and a high electron mobility, and is used in various optoelectronic devices [2]. Electrodeposition represents a low-cost, scalable method for fabricating InSb films. In the literature, aqueous electrolytes and ionic liquids have commonly been applied. In this work, the electrodeposition of InSb films and nanowires from a dimethyl sulfoxide (DMSO)-based electrolyte was demonstrated. This electrolyte enabled electrodeposition in a broader potential range and at higher temperatures as compared to aqueous electrolytes. The electrolyte has a lower viscosity than ionic liquids, therefore exhibiting better mass transport properties for electrodeposition [2]. Muhammad Shafa, Sadaf Akbar, Lei Gao, Muhammad Fakhar-e-Alam & Zhiming M. Wang his work shows some important features of the growth of pure indium antimonide nanowires (InSb NWs) and their potential industrial applications [3]. Dilek Cakiroglu, Jean-Philippe Perez, Axel Evirgen and others from indium antimonide, photovoltaic cells were specially developed and manufactured for use in near-field thermophotovoltaic device demonstrators [4]. Therefore, indium antimonide, due to its specific properties, has long attracted the attention of researchers.

Unique properties of semiconductor quantum dots of the $A^3 B^5$ group are of particular interest due to high mobility of electrons, narrow band gap, and low effective mass of electrons. Manifestation of quantum size effects of such nanoclusters becomes possible even in the case of comparatively large sizes. Another advantage of narrow band gap and gapless semiconductors of the $A^3 B^5$ group is the possibility of synthesis on their basis of quantum dots with variable band gap and their further application in infrared (IR) and terahertz spectrum ranges. Nanoparticles, obtained by fine and ultrafine grinding of single-crystal plates and ingots of appropriate macro materials, are widely used in lasers [5, 6]. Besides this, development of technology to obtain $A^3 B^5$ compounds has shown that transition to creation of the large and very large integral circuits demands increasing diameter and improving structural perfection of single-crystals used as substrates [7, 8].

But of particular interest is the study of the photoluminescence spectra of n-type indium antimonide crystals. And the purpose of this work is to study the photoluminescence spectra of n-type indium antimonide doped crystals in the concentration range $2*10^{16}cm^{-3}$ - $4.8*10^{18}cm^{-3}$ at t=77K. Photoluminescence of indium antimonide is very weak and difficult to observe. There are few works on the study of photoluminescence of n-type indium antimonide crystals in the literature. They are mainly devoted to the study of crystals containing relatively small concentrations of electrons. In heavily doped indium antimonide crystals $n> 5*10^{17}cm^{-3}$ there appear “tails” of density of states in band gap, due to strong non-parabolicity of conduction band at $n \sim 10^{18}cm^{-3}$ the Fermi energy becomes of the order of band gap. Based on indium antimonide they produce sources of coherent radiation, photodetectors in wide spectral range. Besides this, InSb is used to make laser and tunnel diodes, infrared (IR) filters and magnetic field detectors [9].

Photoluminescence of indium antimonide was first investigated by Moss using optical excitation at room temperature in pure crystals. A relatively broad band with an emission maximum of 7-8 μm was detected. The author attributes this line to interzone recombination, since the position of the maximum of the emission spectrum approximately corresponds to the width of the forbidden zone of pure indium antimonide. Later, the emission of the p-n junction of indium antimonide was studied using electrical injection. In the study of photoluminescence of indium antimonide at 200 K, two intrinsic lines with emission maxima $h\nu_1 = 0.234eV$ and $h\nu_1 = 0.200eV$, and impurity lines $h\nu_1 = 0.216eV$ and $h\nu_1 = 0.230eV$ are observed.

2. Materials and research method

From the said above it is clear that most of the works on the study of photoluminescence of indium antimonide contain information related to pure crystals or to crystals alloyed to concentrations not exceeding $4.8*10^{17}$ cm^{-3}. Therefore, it is of high interest to carry out a detailed study of the photoluminescence of indium antimonide crystals with concentrations greater than $5*10^{17}$ cm^{-3}, especially crystals with $n > 10^{18}$ cm^{-3}. At such concentrations, several remarkable effects related to the degree of alloying and to the chemical nature of impurities were found. Strongly alloyed crystals of indium antimonide n-type display captivating value for the study of radiative processes also because of the already strong nonparabolicity of the conduction zone at $n \sim 10^{18}$ cm^{-3}, the Fermi energy becomes the order of the width of the forbidden zone (~0.22eV). It is also insightful that in strongly doped indium antimonide n-type crystals, the energy of plasma oscillations on the order of magnitude is close to the width of the forbidden zone.

Studied in detail photoluminescence spectra of n-type indium antimonide single crystals in a wide range (from $1.2*10^{15}cm^{-3}$ to $1.5*10^{19}cm^{-3}$) of carrier concentrations at liquid nitrogen temperature. In the literature there are n-type indium antimonide photoluminescence spectra only for concentrations up to n≤ $5*10^{17}cm^{-3}$. In the studied range of concentration, we have measured about 200 spectra of n-type indium antimonide photoluminescence [1]. Emission spectrum of indium antimonide with n=$5.4*10^{16}$ cm^{-3} consists of one line with maximum ħv=244 meV. The line width at half intensity is about 30 meV. The origin of this line was attributed to radiative direct transition of electrons from conduction band to valence band. Therefore, despite the widespread use of n-type indium antimonide, the luminescence spectra of doped crystals are not widely used, so this study is relevant . In this paper a new, not observed by authors [10,11] emission line appears in the long-wave part of the spectrum, in photoluminescence spectra of n-type indium antimonide, starting from n≥ $8.5*10^{16}cm^{-3}$ electrons concentration. Thus, with an increase in the concentration of donor impurities, the main emission consists of two bands, maxima of which shift towards shorter wavelengths with increasing doping degree. Figure 1 shows the photoluminescence spectra of n-type indium antimonide for some of the studied crystals of different concentrations at a temperature of 77 K.

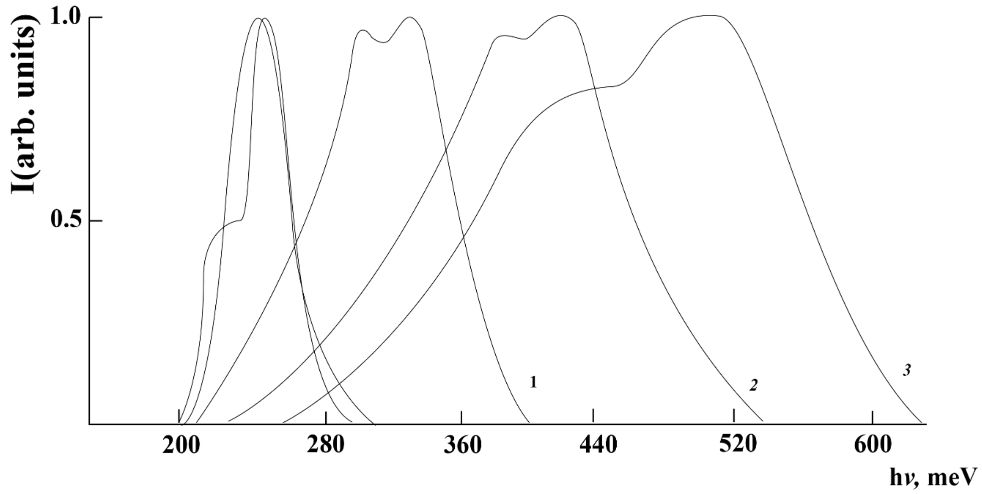

Fig.1. Photoluminescence spectra of indium antimonide at T=77 K and different concentrations,
$1 - 9.8 \cdot 10^{17}\text{cm}^{-3},\ 2 - 2.8 \cdot 10^{18}\text{cm}^{-3},\ 3 - 4.8 \cdot 10^{18}\text{cm}^{-3}$

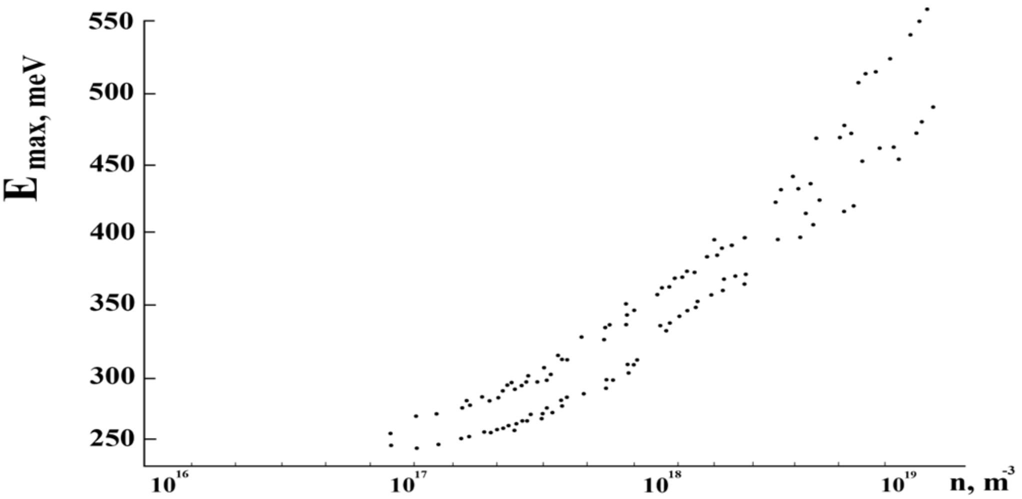

Fig. 2. Dependence of the energy position of the emission line maxima of indium antimonide crystals on the degree of doping

Figure 2 shows dependence of emission line maxima on doping level. From Figure 3 it can be seen that distance between two energy lines of emission remains approximately constant (30-40 meV) up to concentration ~$3*10^{18}cm^{-3}$, and then starts to increase, reaching ~80 meV at maximum concentrations. With

.

an increase of donor impurities concentration long-wave wing shifts towards higher spectrum energies. The integrated intensity of the emission line decreases with increasing electron concentration.

With increasing impurities concentration non-radiative recombination predominates, due to this the proportion of radiative recombination decreases, therefore the ratio of intensity of longwave and shortwave bands changes with increasing impurity concentration.

Experimental data can be explained taking into account features of the indium antimonide band structure: the spectrum of electrons in the conduction band is strongly non-parabolic, $m_e \ll m_{hh}$ (m_e- effective mass of electrons, m_{hh}- effective mass of heavy holes). If we assume that non-equilibrium holes have a lattice temperature and photoluminescence band is due to vertical transitions from conduction band to valence subbands, then the maximum of the band should be at an energy of the order of the band gap width ~E_g, which is not observed in the experiment. Another possibility may be in that effective temperature of non-equilibrium holes is significantly different from a lattice one and, as a result, there is a sufficient number of holes in the valence band with a wave vector equal to K_F (wave vector of electrons at Fermi level). In such a situation, the maximum of the emission band should be at a significantly higher photon energy than E_g (e.g. at n~10^{18}cm^{-3} Fig. 1 maximum should be at photon energy ~ $2E_g$, which roughly corresponds to experimental data for this concentration). However, for this we must assume that the effective temperature of the holes:

$$K\,T_h \sim \frac{\hbar^2 K_F{}^2}{2m_h} \sim \ E_g \frac{m_e}{m_h} \sim 25\text{мэВ}, m_e\,T_h \sim 300\text{K} \tag{1}$$

We can describe a new shortwave part of the spectrum more exactly, if we suggest that it is caused by recombination of electrons, located at Fermi level, with holes at the top of the valence band, i.e. indirect transitions take place. The impulse in such a process is transferred from photoexcited holes to a charged donor. Mean free path of heavy holes l or inverse value $2\pi/l$, which determines impulse uncertainty can be estimated using Brooks-Herring formula scattering on charged impurities:

$$l = \frac{2}{\pi}\frac{\varepsilon^2 \mathcal{H}^2}{e^4 N_Д} \ \ \Phi(U) \tag{2}$$

where $\varepsilon -$ energy of a hole, $N_Д -$ concentration of charged impurities, $U = \frac{\Delta\varepsilon}{\varepsilon}$, $\Delta\varepsilon -$ energy transferred by impurity hole $\Phi(U) \approx lnU$. Substituting $\varepsilon \approx K_0T$, we shall obtain at $N_Д = 10^{19} cm^{-3}, l = 4 * 10^{-8} cm$ and then $\Delta K = \frac{2\pi}{l} = 1.5 * 10^7 cm^{-1}$. Thus, such processes ensure the transfer of impulse during indirect transition. Taking into account the non-parabolicity of the conduction band and neglecting the contribution of light holes, the expression for the relative intensity of optical transitions I can be written as

$$I = \sqrt{x}(1+x)^{\frac{3}{2}}(1+2x)\frac{1+x}{1+3x}\left(1+exp\frac{x-\frac{\varepsilon_F}{\varepsilon_g}}{\frac{K_0T}{\varepsilon_g}}\right)^{-1} \tag{3}$$

where $x = \frac{\hbar\omega_0 - \varepsilon_g}{\varepsilon_g}$; $\varepsilon_F -$ Fermi energy, $\varepsilon_g -$ band gap width, T-temperature, factor $\frac{1+x}{1+3x} -$ determines the dependence of the matrix element on energy; $\sqrt{x}(1+x)^{\frac{3}{2}}(1+2x)$ density of states in the conduction band $\left(1+exp\frac{x-\frac{\varepsilon_F}{\varepsilon_g}}{\frac{K_0T}{\varepsilon_g}}\right)^{-1} -$ Fermi electron energy distribution function. For non-parabolic conduction band ε_F is:

$$\varepsilon_F = \frac{\varepsilon_g}{2}\left[\left(1+\frac{\hbar^2 K_F{}^2}{m_c\frac{\varepsilon_g}{2}};\right)^{1/2} - 1\right] \quad K_F{}^2 = (3\pi^2)^{2/3} n_D{}^{2/3} \tag{4}$$

Figure 3 shows the results of calculation using formula (1) for some studied crystals. It is clear that up to concentrations ~$2*10^{18}$cm^{-3} this formula describes shortwave line of emission spectrum well enough.

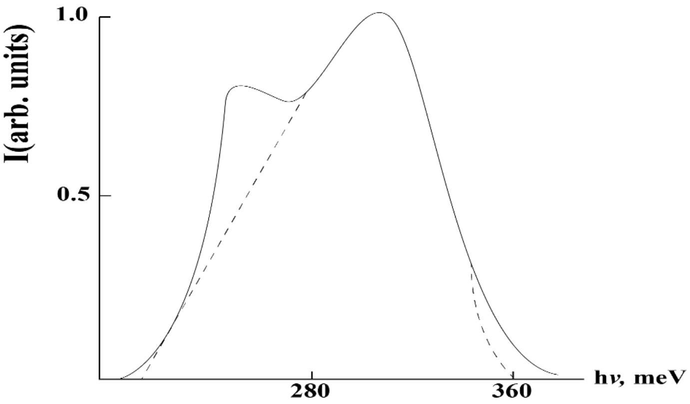

Fig. 3. Photoluminescence spectra of n-type indium antimonide 5.8*10^{17}cm^{-3} at T=77 K, where solid line - experiment, dotted line – theory

Figures show that with further increase in concentration of donor impurities in crystals (n>*10^{18}cm^{-3}) there is a lag observed between experimental maximum and theoretically calculated. This lag is growing with concentration increase, reaching ~100 meV at n=1.3*10^{19}cm^{-3}. This lag can be explained within the framework of a model, similar to the one used in paper to describe features of light absorption in heavily doped germanium.

The reason for the lag in energy of the experimentally observed short-wave peak from the theoretical prediction is that photoexcited holes are predominantly bound to fluctuations of impurities, which leads to a lag in the emission maximum from the position of the Fermi level.

Fluctuations in donor concentration lead to the formation of bound hole states. Such fluctuations will bind predominantly heavy holes. Let us estimate a value of U potential, caused by heterogeneity of donor distribution: $U = e^2 z/Lx$, L – radius of Thomas-Fermi screening, x – dielectric constant (permittivity), z – deviation of the number of donors from the average. $z = \sqrt{4/3\pi L^3 n}$. Then $= (\frac{4}{3}\pi L e^4/x^2)^{1/2}$. For a degenerate electron gas $L = (\varepsilon_F x/6\pi e^2)^{1/2}$, where ε_F is calculated with regard to non-parabolicity of the conduction band. Characteristic wave vector of holes $k_{h,e}$ - in such potential is $k_{h,e} = (2m_h, eV/h^2)^{1/2}$ where $m_{h,e}$ – effective mass of heavy (light) holes. For $n = 3 \times 10^{18} cm^{-3}$, at $E_g = 0.22\ eV$, $E_F/E_g = 1.1$, $U = 25\ meV$, $k_F = (3\pi^2 n)^{1/3} \approx 4.5 \times 10^6 cm^{-1}$, $k_h = 5.5 \times 10^6 cm^{-1}$, $k_e = 1 \times 10^6 cm^{-1}$ [12].

These estimates show that maximum may shift towards long-wave side by value of $\sim 25\ meV$ and confirm an assumption that optical transitions into the area of heavy holes are indirect. Figure 4 schematically shows the indium antimonide band structure, position of Fermi level for $n = 3 \times 10^{18} cm^{-3}$ and optical transitions.

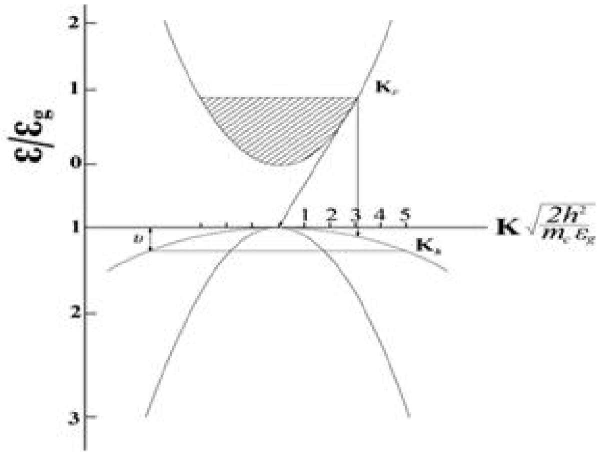

Fig.4. Zone scheme for crystal $n = 3 \times 10^{18} cm^{-3}$

.

Long-wave maximum may be caused by direct electrons transitions into the area of light holes. Presence of such transitions in indium antimonide absorption spectra was noted in the works. As it is clear from estimate, the root-mean-square fluctuation of the number of donors does not provide the necessary impulse of light holes, i.e. $k_e < k_F$. With increase in concentration of U value donors, $k_{h,e}$ increase. Experimentally this should lead to increased lag of short-wave band maximum position from theoretically calculated by (1) and its blurring which is observed experimentally .

3. Results and discussion

Taking into account changes of Fermi energy with increasing concentration shifts the theoretically calculated spectrum towards higher wavelengths, i.e. improves agreement between the experiment and theory.

From the above we can conclude that to explain shortwave radiation line in doped indium antimonide crystals it is necessary to consider all causes that lead to shifting radiation lines towards long-wave area:

a) fluctuations of donor's concentration;
b) floating of holes;
c) dependence of band gap width on doping degree;
d) effective reduction of Fermi energy in heavily doped crystals.

1. Conducted detailed study of photoluminescence spectra of doped indium antimonide crystals in ($1*10^{15}$cm^{-3} – $1.5*10^{19}$cm^{-3}) interval of electrons concentration at 77K temperature.
2. In detail obtained spectra of indium antimonide crystals' photoluminescence with n >$5*10^{17}$cm^{-3} concentrations. For the first time, experimentally discovered that the main radiation of n-type indium antimonide crystals with n > $8.5*10^{16}$ cm^{-3} concentrations consist of two lines.
3. It is shown that high-energy doped indium antimonide crystals radiation line is well explained by electrons recombination at Fermi level with holes at valence band top up to $\sim 2 * 10^{18}$ cm^{-3} concentrations.
4. It is established that to explain behaviour of shortwave indium antimonide crystals radiation line with n>$2*10^{18}$cm^{-3} it is necessary to consider fluctuations of donor's concentration, dependence of band gap width on doping degree, as well as effective reduction of Fermi energy with increasing concentration
5. It is established that the shift of long-wave edge of radiation towards higher energy with increasing concentration is explained by the influence of impurity concentration fluctuations.

4. Conclusion

As already mentioned above, the long-wave wing of radiation spectrum of doped n-type indium antimonide crystals with increasing concentration shifts towards higher energy. This effect can be explained within the framework of a model, which we used to explain the shift of short-wave radiation line towards long waves, i.e. the model of optimal fluctuation of donor's concentration. We see that long-wave wing of radiation should shift towards higher energy with increasing concentration by value U_0. It should be noted that in crystals with n>$4*10^{18}$cm^{-3} it is very difficult to precisely determine the position of long-wave edge of radiation (radiation was registered at the limit of resolution of the equipment used).

The physical causes of long-wave radiation line of doped indium antimonide crystals cannot be direct optical transitions into the light holes zone, as in this case its spectral position would not depend on impurities concentration. The dependence of impurity concentration, difference in energy positions of short-wave and long-wave maxima of the band does not allow to consider long-wave peak a background repetition of short-wave one. It is possible that long-wave line is caused by recombination of electrons, bound on the surface, as the above concentration dependences do not contradict such interpretation.

Conflict of interest statement

The authors declare that they have no conflict of interest in relation to this research, whether financial, personal, authorship or otherwise, that could affect the research and its results presented in this paper.

CRediT author statement

Yegemberdiyeva S.Sh.: Development of Facility and Measurements, Writing - Original Draft; Kushkimbayeva B.Zh.: Review & Editing; Keikimanova M.T.: Conceptualization, Data Curation; Kusherbayeva M.R.: Methodology, Investigation. The final manuscript was read and approved by all authors.

References

1 Palasyuk T., Jastrzebski C., Khachapuridze A., Litwin-Staszewska E., Suski T., Grzegory I., Porowski S. (2024) Influence of pressure on phonon properties of indium antimonide. *Physica Status Solidi (RRL) – Rapid Research Letters*, *18*(9), 54-59. https://doi.org/10.1002/pssr.202400093

2 Monnens W., Billiet N., Binnemans K., et al. (2024) Electrodeposition of indium antimonide (InSb) from dimethyl sulfoxide-based electrolytes. *Journal of Solid State Electrochemistry, 28*, 3755–3768. https://doi.org/10.1007/s10008-024-05947-x

3 Shafa M., Akbar S., Gao L., et al. (2016) Indium antimonide nanowires: Synthesis and properties. *Nanoscale Research Letters*, *11*, 164. https://doi.org/10.1186/s11671-016-1370-4

4 Cakiroglu D., Perez J.-P., Evirgen A., Lucchesi C., Pierre-Olivier C., Taliercio T., Tournié E., Vaillon R. (2019) Indium antimonide photovoltaic cells for near-field thermophotovoltaics. *Solar Energy Materials and Solar Cells*, *203*. https://doi.org/10.1016/j.solmat.2019.110190

5 Tsvetkova O.Yu., Shtykov S.N., Zhukov D.N., Smirnova T.D. (2021) Synthesis and study of some properties of colloidal quantum dots of indium antimonide. *Izvestiya of Saratov University. Chemistry. Biology. Ecology*, *21*(4), 378-381. https://doi.org/10.18500/1816-9775-2021-21-4-378-381 [in Russian]

6 Ledentsov N.N., Lott D.A. (2011) A new generation of vertical-emitting lasers as a key element of the computer communication era. *Advances in Physical Sciences, 181*(8), 884–890.

7 Kozlov R.Yu., Kormilitsina S.S., Molodtsova E.V., Zhuravlev E.O. (2021) Growing indium antimonide single crystals with a diameter of 100 mm by the modified Chochralsky method. *Izvestiya Vysshikh Uchebnykh Zavedenii. Materialy Elektronnoi Tekhniki = Materials of Electronics Engineering*, *24*(3), 190-198. https://doi.org/10.17073/1609-3577-2021-3-190-198 [in Russian]

8 Averkiev N.S., Egemberdieva S.Sh., Kalinin B.N., Konstantinov O.V., Rogachev A.A., Filipchenko A.S. (1985) Photoluminescence of highly alloyed crystals of nn-type indium-antimonide. *Pisma v Zhurnal Tekhnicheskoi Fiziki*, 1326–1330. Available to: https://www.mathnet.ru/rus/pjtf1046

9 Komkov O.S., Firsov D.D., Lvova T.V., Sedova I.V., Semenov V.A., Soloviev A.N., Ivanov S.V. (2016) Photoreflection of indium antimonide. *Physics of the Solid State, 58*(12), 2394–2400. https://doi.org/10.1134/S1063783416120106

10 Velichko A.A., Ilushin V.A. (1993) Electrophysical properties of indium antimonide films obtained by molecular beam epitaxy. *Electronic Industry*, *8*, 48-50.

11 Titkov A. N., Chaikina E.I., Komova E.M., Ermakova N.T. (1981) Low-temperature luminescence of degenerate p-type direct-bandgap semiconductors. *FTP (Semiconductors Physics and Technology*, *15*(2), 345-352. [in Russian]

12 Allen L.P., Flint P.J., Meschew G., Dallas G., Bakken D., Brown G.J., Khoshakhlagh A., Hill C. J. (2011) 100mm diameter GaSb substrates with extended IR wavelength for advanced space-based applications. *SPIE Proceedings: Infrared Technology and Applications XXXVII, 8012*, 801215. https://doi.org/10.1117/12.882937

AUTHORS' INFORMATION

Yegemberdiyeva, Sofia Shaimerdenovna – Candidate of Physical and Mathematical Sciences, Associate Professor, Department of Physics and Informatics, Taraz University named after M.H. Dulati, Taraz, Kazakhstan; https://orcid.org/0009-0005-2418-2544; s.egemberdieva@bk.ru

Kushkimbayeva, Bibara Zhailaubaevna – Candidate of Physical and Mathematical Sciences, Associate Professor, Department of Physics and Informatics, Taraz University named after M.H. Dulati, Taraz, Kazakhstan; https://orcid.org/0000-0003-0572-0800; k.bibara@mail.ru

Kusherbayeva, Maikul Rakhmanberdievna – Master (Sci.), Senior Lecturer, Department of Physics and Informatics, Taraz University named after M.H. Dulati, Taraz, Kazakhstan; https://orcid.org/0000-0002-6707-7905; k.maikul@mail.ru

Keikimanova, Meruyert Tursynkhanovna – Candidate of technical sciences, Associate Professor, Department of Physics and Informatics, Taraz University named after M.H. Dulati, Taraz, Kazakhstan; https://orcid.org/0009-0006-1566-897x; merukey1970@mail.ru

.

SUMMARIES	ТҮСІНІКТЕМЕЛЕР	АННОТАЦИИ

Козловский А.Л., Кенжина И.Е., Толенова А., Әскербеков А.

Екі фазалы керамикадағы құрамдас бөліктердің арақатынасының өзгеруінің сутектік ісіну әсерін модельдейтін жоғары дозалы протондық сәулеленуге төзімділікке ықпалын зерттеу

Мақалада сутектік ісіну процестерін модельдейтін жоғары дозалы протондық сәулеленуге ұшыраған екі фазалы литий құрамды керамиканың беріктік және жылулық параметрлерінің бұзылу процестерін бағалау нәтижелері ұсынылған. Бұл зерттеу тақырыбына деген қызығушылық, ең алдымен, литий метацирконаты мен литий ортосиликатының екі фазалы құрамындағы арақатынасының тұрақтылық пен радиациялық зақымдануға төзімділікке әсерін анықтау мүмкіндігімен, сондай-ақ десорбция процестерін модельдеу үшін маңызды болып табылатын пострадиациялық изотермиялық күйдірумен байланысты диффузиялық процестермен түсіндіріледі. Екі фазалы керамикадағы құрамдас бөліктердің арақатынасының радиацияның әсерінен жұмсару процестеріне және сынуға төзімділіктің төмендеуіне ықпалы қарастырылған зерттеулер барысында бір фазалы керамикамен салыстырғанда, екі фазаның үйлесімі бастапқы беріктік параметрлерінің артуына ғана емес, сонымен қатар фазааралық шекаралардың болуы есебінен жұмсару төзімділігінің жоғарылауына алып келетіні анықталды. Зерттелген керамиканың жылулық әсерге төзімділігіне (термиялық төзімділік сынақтары) жүргізілген сынақтар нәтижесінде екі фазалы керамикада ұзақ мерзімді температуралық өзгерістерге беріктік қасиеттерін сақтау тұрақтылығының жоғарылағаны анықталды.

Кілт сөздер: сутектік ісіну, бридерлер, екі фазалы керамика, жоғары дозалы сәулелену, литий метацирконаты, литий ортосиликаты.

Козловский А.Л., Кенжина И.Е., Толенова А., Аскербеков А.

Исследование влияния вариации соотношения компонент в двухфазных керамиках на устойчивость к высокодозному облучению протонами, моделирующим эффекты водородного распухания

В статье представлены результаты оценки процессов разрушения прочностных и тепловых параметров двухфазной литийсодержащей керамики, подвергшейся высокодозному облучению протонами, воздействие которых моделирует процессы водородного распухания. Интерес к данной теме исследования обусловлен, прежде всего, возможностью определения влияния изменения соотношения двух компонентов метацирконата лития и ортосиликата лития на поддержание стабильности и устойчивости к радиационным повреждениям, а также на диффузионные процессы, связанные с пострадиационным изотермическим отжигом образцов, характерные для моделирования процессов десорбции. В ходе проведенных исследований влияния изменения соотношения компонентов в двухфазной керамике на устойчивость к радиационно-индуцированным процессам размягчения и снижению трещиностойкости было установлено, что, в отличие от однофазной керамики, сочетание двух фаз в составе приводит не только к увеличению начальных прочностных параметров, но и к повышению устойчивости к размягчению за счет наличия межфазных границ. При испытаниях исследуемой керамики на тепловое воздействие (испытания на термостойкость) было выявлено, что в случае двухфазной керамики наблюдается повышение стабильности сохранения прочностных свойств при длительных температурных изменениях.

Ключевые слова: водородное распухание, бридеры, двухфазная керамика, высокодозное облучение, литий метацирконат, литий ортосиликат.

Солдатхан Д., Баратова А.

^{9}Be+^{12}C жүйе үшін кулон тосқауылы маңындағы энергияда B3Y-Фетал потенциалдың әсерін талдау

^{9}Be+^{12}C ядролық жүйесінің серпімді шашырау процесінің эксперименттік мәліметтері кулон тосқауылы маңындағы энергияда микроскопиялық теория тұрғысынан талданды. Екі денелік матрицаға төменгі ретті шектеулер қойылған вариациялық әдісте жасалған жаңа Botswana 3-Yukawa - Fetal потенциалы ^{9}Be+^{12}C жүйесі үшін оптикалық потенциалдың нақты бөлігі ретінде алғаш рет қолданылды. Қос фолдинг модельде нуклон тығыздығының таралу формуласына тығыздыққа тәуелді параметрлер енгізілді және олар тиімді нуклон-нуклондық өзара әрекеттесулеріне негізделген Botswana 3-Yukawa - Fetal және Michigan 3-Yukawa - Paris потенциалдарына қолданылды. Нәтижесінде модификацияланған нақты микрофолдинг потенциалдары жасалды. Жаңа микрофолдинг потенциалдары негізінде есептелген жартылай микроскопиялық талдау нәтижелері ұсынылды. Зерттеудің ерекшелігі тығыздыққа тәуелді параметрлер ядролық ортаның қанықтылық қасиеттерін сипаттайтын сығылмаушылық коэффициентіне негізделіп есептелген. Серпімді шашырау процесінің күй теңдеулері ядролық байланыс энергиясының тығыздыққа тәуелділігі арқылы анықталған (ρ_0=0.17 fm^{-3}) қанықтылық тығыздығында құрылды. Талдау нәтижелері ядролық қасиеттерді дәлірек анықтауға және ядролық ортаның қанықтылық қасиетін арттыруға мүмкіндік береді. Жаңа фолдинг потенциалдың тиімділігі микроскопиялық тұрғыдан анықталды, сондай-ақ оптикалық потенциалдың оңтайлы параметрлері табылды.

Кілт сөздері: микроскопиялық талдау, серпімді шашырау, қос фолдинг модель, B3Y-Fetal.

Солдатхан Д., Баратова А.

Анализ влияния B3Y-Фетал потенциала на энергию вблизи кулонного барьера для системы ^{9}Be+^{12}C

Экспериментальные данные процесса упругого рассеяния ядерной системы ^{9}Be+^{12}C были проанализированы с точки зрения микроскопической теории при энергии вблизи кулонного барьера. Новый потенциал Botswana 3-Yukawa - Fetal, созданный в вариационном подходе с ограничениями низшего порядка на двухчастичные матрицы, впервые был применен для системы ^{9}Be+^{12}C в качестве действительной части оптического потенциала. В модели двойного фолдинга в формулу распределения плотности нуклонов были введены параметры, зависящие от плотности, и они были применены к потенциалам Botswana 3-Yukawa - Fetal и Michigan 3-Yukawa - Paris, основанным на эффективных нуклон-нуклонных взаимодействиях. В результате были созданы модифицированные реальные микрофолдинговые потенциалы. Представлены результаты полумикроскопического анализа, рассчитанные на основе новых микрофолдинговых потенциалов. Особенность исследования заключается в том, что параметры, зависящие от плотности, рассчитаны на основе коэффициента несжимаемости, который характеризует свойства насыщения ядерной среды. Уравнения состояния процесса упругого рассеяния были сформулированы при плотности насыщения (ρ_0=0.17 fm^{-3}), определенной через зависимость энергии связи ядер от плотности. Результаты анализа позволяют более точно определить ядерные свойства и улучшить характеристики насыщения ядерной среды. Эффективность нового фолдингового потенциала была определена с микроскопической точки зрения, а также найдены оптимальные параметры оптического потенциала.

Ключевые слова: микроскопический анализ, упругое рассеяние, модель двойного фолдинга, B3Y-Fetal.

Яр-Мухамедова Г.Ш., Мұрадов А.Д., Мұқашев Қ., Умаров Ф.Ф., Иманбаева А.К., Мұсабек Г.Қ., Белисарова Ф.Б.

Полиэтилентерефталаттың полиимидті планктардың механикалық қасиеттеріне әсері

Бұл зерттеу полиэтилентерефталат толтырғышының әртүрлі концентрацияларының полиимидті үлдірлердің бір осьті созылу кезіндегі созылу беріктігіне және үзілу кезіндегі салыстырмалы ұзаруына әсерін талдауға бағытталған. Бұл толтырғыштың жүктеме кезіндегі механикалық қасиеттері мен беріктігіне қалай ықпал ететінін анықтау мақсат етіледі. Бір осьті созылу жағдайында полиимидті үлдірлердің және олардың полиэтилентерефталатпен біртекті композиттерінің механикалық қасиеттері зерттелді. Үлгілер полиимидті лак ерітінділерін полиэтилентерефталатпен механикалық араластыру арқылы дайындалды, мұнда полиэтилентерефталат арматуралық толтырғыш ретінде қызмет атқарды. Зерттеу нәтижелері барлық үлгілерде бастапқы механикалық жүктеменің салыстырмалы ұзарудың шамамен 3%-ға күрт артуына әкелетінін көрсетті. Бұл құбылыс глобулалардың айналуымен және матрица макромолекулаларының жүктеме бағыты бойынша созылған тізбектерге реттелуімен түсіндіріледі. Тұтқырлықтың аддитивті тәуелділігіне сүйене отырып, зерттеу барысында полиимид пен полиэтилентерефталат макромолекулалары арасында химиялық байланыстар түзілмейтіні және композит ішінде конформациялық өзгерістер болмайтыны анықталды.

Кілт сөздері: полиимид, полиэтилентерефталат, толтырғыш, бір осьті керілу, ИҚ-спектроскопия, вискозиметрия.

Яр-Мухамедова Г.Ш., Мурадов А.Д., Мукашев К., Умаров Ф.Ф., Иманбаева А.К., Мусабек Г.К., Белисарова Ф.Б.

Влияние полиэтилентерефталата на механические свойства полиимидных пленок

В данном исследовании анализируется влияние различных концентраций наполнителя из полиэтилентерефталата на прочность на разрыв и относительное удлинение при разрыве полиимидных пленок при одноосном растяжении с целью определения влияния наполнителя на механические характеристики и долговечность этих пленок под нагрузкой. Изучено механическое поведение полиимидных пленок и их однородных композитов с полиэтилентерефталатом при одноосном растяжении. Образцы подготовлены путем механического смешивания растворов полиимидного лака с полиэтилентерефталатом, выступающим в качестве армирующего наполнителя. Результаты показывают, что для всех типов образцов начальная механическая нагрузка вызывает резкое увеличение относительного удлинения примерно на 3%, что объясняется поворотом глобул и выстраиванием макромолекул матрицы в вытянутые цепи вдоль направления нагрузки. Аддитивная зависимость вязкости, наблюдаемая в исследовании, дополнительно подтверждает отсутствие химических связей между макромолекулами полиимида и полиэтилентерефталата, а также отсутствие конформационных изменений внутри композита.

Ключевые слова: полиимид, полиэтилентерефталат, наполнитель, одноосное растяжение, ИК-спектроскопия, вискозиметрия.

Жаңбырбай Е.Р., Аймуханов А.К., Зейниденов А.К., Гадиров Р.М., Абеуов Д.Р., Жақанова А.М.

Екі кезеңді анодтау арқылы алынған кеуекті алюминий тотығының қабыршақтары

Анодты алюминий тотығы қабыршақтары органикалық және бейорганикалық наноматериалдардың көптеген түрлерін алу үшін кеңінен қолданылады және олардан синтезделген наноматериалдардың оптикалық қасиеттерін зерттеуде практикалық маңызы бар. Бұл жұмыста мерзімді және тұрақты кеуектері бар алюминий тотығы қабыршақтарын алу үшін екі жақты және екі кезеңдік анодтау әдісі ұсынылған. Қышқыл электролиттер ерітінділеріндегі алюминийді анодты тотығу әдісі Al_2O_3 кеуекті құрылымының параметрлерін оңай өзгертуге мүмкіндік береді. Алюминий тілімін «жұмсақ» анодтау үшін электролит ретінде қымыздық қышқылы, ал оны алдын ала тазарту және жылтырату үшін этил спирті және ортофосфор қышқылы мен хром ангидридінің ерітіндісі қолданылды. Анодтау төмен температурада жүргізіліп, нәтижесінде жоғары дәрежелі кеуектері бар алюминий тотығының қабыршағын алуға болады. Кеуектердің өлшемі 60-тан 110 нм-ге дейін, ал кеуектер арасындағы қашықтық 13-27 нм аралығында байқалады. Анодталған алюминийдің кеуекті қабыршағының жұтылу және шағылу спектрлері алынып, нәтижесінде қабыршақтың жақсы жұтылу спектрдің қысқа толқынды аймағында, ал сыну көрсеткішінің максималды мәні спектрдің қысқа толқынды және ұзын толқынды аймақтарында байқалады.

Кілт сөздері: анодты алюминий тотығының қабыршақтары, алюминийді екі жақты анодтау, кеуекті мембраналар, төмен температурада анодтау, бөгет қабаты.

Жаңбырбай Е.Р., Аймуханов А.К., Зейниденов А.К., Гадиров Р.М., Абеуов Д.Р., Жақанова А.М.

Пленки пористого оксида алюминия, полученные методом двухстадийного анодирования

Пленки анодного оксида алюминия широко применяемы для получения многих видов органических и неорганических наноматериалов и имеют практическое значение при изучении оптических свойств, синтезированных из них наноматериалов. В данной работе приведен метод двухстороннего двухстадийного анодирования для получения пленок анодного оксида алюминия с периодическими и регулярно расположенными порами. Метод анодного окисления алюминия в растворах кислых электролитов позволяет достаточно легко варьировать параметры пористой структуры Al_2O_3. В качестве электролита для «мягкого» анодирования пластины алюминия была использована щавелевая кислота, а для предварительного очищения и полирования пластины алюминия были использованы этиловый спирт и раствор ортофосфорной кислоты и хромового ангидрида. Анодирование проводилось при низких температурах, в результате чего удается получить пленку оксида алюминия с высокой степенью упорядочения пор, размеры которых составили от 60 до 110 нм, а расстояние между порами составило в пределах 13–27 нм. Получены спектры поглощения и отражения пористой пленки анодированного алюминия, где наблюдается хорошее поглощение пленок анодированного алюминия в коротковолновой области спектра, а максимальное значение показателя преломления наблюдается в коротковолновой и длинноволновой областях спектра.

Ключевые слова: пленки анодного оксида алюминия, двухстороннее анодирование алюминия, пористые мембраны, анодирование при низких температурах, барьерный слой.

Турсунов М.Н., Сабиров Х., Аликулов Р.Б., Холов У.Р., Эшматов М.М.

Сусыз, құрғақ климатқа арналған жаңа салқындату жүйесі бар әртүрлі қуаттағы фототермиялық құрылғылардың тиімділігін зерттеу

Мақалада құрғақ климатқа бейімделген жаңа салқындату жүйесі бар әртүрлі қуаттағы фототермиялық батареялардың тиімділігі зерттеледі. 1 кВт қуаттылығына ие фототермиялық батарея құрылғысында алынған нәтижелер ұсынылған. Алдымен, 60 Вт және 180 Вт қуаттылығына негізделген фотоэлектрлік модульдердің тиімділігі қарастырылып, кейін 1 кВт қуаттылығына ие фототермиялық батареядан алынған нәтижелер келтірілген. Біздің республикамыздың өте құрғақ аймақтарында жаңартылатын энергия көздерін пайдаланған кезде бірнеше факторларды ескеру қажет, соның ішінде экстремалды жоғары температуралар. Мұндай жоғары температураларда (көлеңкеде 40°C және одан жоғары) фотоэлектрлік батареялардың тиімділігі төмендеп, қажетті энергия шығынға ұшырайды. Бұл шығындарды азайту үшін фототермиялық батареяны салқындату үшін тұрақты су пайдалану қажеттілігінсіз жұмыс істейтін жүйе болуы маңызды. Біз ұсынған жаңа салқындату жүйесінің әлемде аналогтары жоқ. Болашақтағы ғылыми зерттеулеріміздің мақсаты – жаңа салқындату жүйесін жетілдіру және оны автономды режимге көшіру.

Кілт сөздер: фототермиялық батарея, фотоэлектрлік батарея, жаңа салқындату жүйесі, коллектор, рефлектор.

Турсунов М.Н., Сабиров Х., Аликулов Р.Б., Холов У.Р., Эшматов М.М.

Исследование эффективности фототермических устройств различной мощности с новым типом системы охлаждения, предназначенной для сухого безводного климата без использования воды

В статье исследуются эффективности фототепловых батарей разной мощности с новой системой охлаждения, разработанной для засушливого климата. Представлены результаты, полученные на устройстве фото тепловой батареи мощностью 1 кВт. Вначале рассматривается эффективности фототепловых батарей на основе фотоэлектрических модулей мощностью 60 Вт и 180 Вт, а затем приводятся результаты, полученные на

фототепловой батарее мощностью 1 кВт. При использовании возобновляемых источников энергии в экстремально засушливых регионах нашей республики необходимо учитывать несколько факторов, включая чрезвычайно высокие температуры. При таких высоких температурах (40°С и выше в тени) снижается эффективность фотоэлектрических батарей, что приводит к потерям необходимой энергии. Для снижения этих потерь важно, чтобы для охлаждения фототепловой батареи не требовалось постоянное использование воды. Предлагаемая нами новая система охлаждения не имеет аналогов в мире. В дальнейших научных исследованиях целью является совершенствование новой системы охлаждения и перевод её на автономный режим работы.

Ключевые слова: фототепловая батарея, фотоэлектрическая батарея, новая система охлаждения, коллектор, рефлектор.

Нұрым Қ.А., Антонова А.М., Сақыпов К.Е., Воробьев А.В., Стецов Н.В.

Гелий реакторы және сутегі модулі бар бір тізбекті энергоблоктың тиімділігінің регенерация дәрежесіне тәуелділігі

Қуат блогының ең тартымды бір тізбекті сұлбасы таңдалды. Реактордың белсенді зонасының шығысындағы гелий бу генераторына түседі, онда ол электролиз қондырғысы үшін өте қызған бу шығару үшін жылудың бір бөлігін береді. Содан кейін гелий жылуды қалпына келтірумен жабық газ турбиналық циклде жұмыс істейді. Турбинасы мен компрессоры бар газбен салқындатылған реактор жоғары ПӘК-пен термодинамикалық циклді пайдалануға мүмкіндік береді. Әртүрлі регенерация дәрежесі үшін регенератордың конструктивті есептеулерінің сериясы орындалды. Жоғары және төмен қысымды жақтан регенератордың нақты кедергісіне әсерін бағалау сериясы жүргізілді. Энергияны өндірудің жылу сұлбасы регенератордың конструкторлық есептерінің сериясына сәйкес есептелінді.

Кілт сөздері: реактор, гелий, газтурбиналық қондырғы, регенератор, гидравликалық кедергі, аэродинамикалық кедергі.

Нурым К.А., Антонова А.М., Сакипов К.Е., Воробьев А.В., Стецов Н.В.

Зависимость эффективности одноконтурного энергоблока с гелиевым реактором и водородным модулем от степени регенерации

Выбрана наиболее привлекательная одноконтурная схема энергоблока. Гелий на выходе из активной зоны реактора поступает в парогенератор, где отдает часть тепла для получения высокоперегретого пара для электролизной установки. Далее гелий работает в замкнутом газотурбинном цикле с утилизацией тепла. Газоохлаждаемый реактор с турбиной и компрессором позволяет использовать термодинамический цикл с высоким КПД. Выполнен ряд проектных расчетов регенератора для различных степеней регенерации. Проведен ряд оценок влияния на реальное сопротивление регенератора со стороны высокого и низкого давления. Тепловая схема выработки энергии рассчитана в соответствии с рядом проектных расчетов регенератора.

Ключевые слова: реактор, гелий, газотурбинная установка, регенератор, гидравлическое сопротивление, аэродинамическое сопротивление.

Медетбеков Б.С., Попов Ю.А., Прозорова И.В., Сабитова Р.Р., Сысалетин А.В.

Экрандалған уран үлгісінің байытылуын анықтау үшін коаксиалды HPGe детекторын және FRAM кодын пайдалану

Уранды байыту анықтамасы қауіпсіздіктің ықтимал қауіптерін бағалау және материалдардың рұқсатсыз орнын ауыстыруды анықтау үшін қажет ядролық материалдарды бақылаудың маңызды аспектісі болып табылады. Жоғары таза германий (HPGe) детекторын пайдаланатын гамма-спектрометрия изотоптардың арақатынасын талдаудың бұзбайтын әдісін ұсынады, алайда стандартты жабдықта, көбінесе әсіресе үлгілерді экрандау кезінде дәлдік жетіспейді. Бұл зерттеудің мақсаты - экрандау жағдайында және онсыз уранның байытылуын анықтау үшін FRAM бағдарламалық жасақтамасымен үйлесімді портативті коаксиалды HPGe-детекторының мүмкіндіктерін бағалау. Осы мақсатқа жету үшін құрамында уран мөлшері аз твэльдердің үлгілерін гамма-спектрметриялық өлшеу сериясы жүргізілді. Нәтижесі бұл әдіс 10%-ға дейінгі қателік шегімен байытуды сенімді және жылдам бағалауды қамтамасыз ететінін көрсетті, әсіресе уақтылы және дәл изотоптық талдаудың мәні зор ядролық криминалистикада қолдану үшін маңызды.

Кілт сөздері: ядролық криминалистика, уранды байыту, экрандау көзі, HPGe коаксиалды детекторы бар гамма-спектрметрия, FRAM бағдарламалық жасақтама.

Медетбеков Б.С., Попов Ю.А., Сабитова Р.Р., Прозорова И.В., Сысалетин А.В.

Использование коаксиального HPGE детектора и кода FRAM для определения обогащения экранированного образца урана

Определение обогащения урана представляет собой важный аспект контроля ядерных материалов, необходимый для оценки потенциальных угроз безопасности и обнаружения несанкционированного перемещения материалов. Гамма-спектрометрия с использованием высокочистого германиевого (HPGe) детектора предлагает неразрушающий метод анализа соотношения изотопов, однако стандартному оборудованию часто не хватает точности, особенно при экранировании образцов. Цель данного исследования — оценить возможности портативного коаксиального HPGe-детектора в сочетании с программным обеспечением FRAM для определения обогащения урана в условиях экранирования и без него. Для достижения поставленной цели были проведены серии гамма-спектрометрических измерений образцов твэлов с низким содержанием урана. Результаты показали, что метод обеспечивает надежную и быструю оценку обогащения с погрешностью до 10%, что особенно важно для применения в ядерной криминалистике, где своевременный и точный изотопный анализ имеет большое значение.

Ключевые слова: ядерная криминалистика, обогащение урана, экранирующий источник, гамма-спектрометрия с коаксиальным детектором HPGe, программное обеспечение FRAM.

Ridhuan K, Mafruddin, Irawan D., Handono S.D.

Күн энергиясы мен биогаз негізінде жұмыс істейтін қос отынды дизельді қозғалтқыштардың өнімділігін арттыру және шығарындыларын азайту

Ғаламдық энергияға деген сұраныс үнемі өсуде, ал бұл сұраныс қазба отындары арқылы қамтамасыз етіліп келеді, нәтижесінде айтарлықтай экологиялық зиян келтірілуде. Биогаз сияқты балама энергия көздері қазба отындарын азайтудың тиімді шешімі болып табылады, себебі оның өздігінен тұтану температурасы жоғары (шамамен 650°C), бұл оны жоғары сығылу дәрежесіне ие қозғалтқыштарда қолдануға қолайлы етеді. Бұл зерттеудің мақсаты – қос отынды дизельді қозғалтқыштарда биогазды қолданудың өнімділік пен шығарындыларға әсерін бағалау. Эксперименттер дизельді қозғалтқышта бір отынды және қос отынды режимдерде жүргізілді, биогаздың шығын мөлшері 3, 4 және 5 л/мин аралығында өзгертілді. Зерттеу нәтижелері көрсеткендей, қос отынды режимде биогазды қолдану 3 және 4 л/мин шығын мөлшерінде бір отынды режиммен салыстырғанда жоғары айналу моменті мен тежегіш қуат береді. Сонымен қатар, бір отынды дизельді қозғалтқыштың шығарындылары CO (0,29%) және CO_2 (5,67%) ең жоғары мәндерге ие болғаны анықталды, ал қос отынды қозғалтқышта CO (0,27%) және CO_2 (5,51%) деңгейлері байқалды. Бұл нәтижелер биогазды қос отын ретінде пайдалану қозғалтқыштың өнімділігін жақсартумен қатар, зиянды шығарындыларды азайтуға көмектесетінін көрсетеді, бұл оны тұрақты энергетикалық балама ретінде қарастыруға мүмкіндік береді.

Кілт сөздері: биогаз, қос отындық, дизель, өнімділік, шығарындылар.

Ridhuan K, Mafruddin, Irawan D., Handono S.D.

Повышение производительности и снижение выбросов двухтопливных дизельных двигателей, работающих на солнечной энергии и биогазе.

Глобальные потребности в энергии продолжают расти, и они удовлетворяются за счет ископаемого топлива, что приводит к значительному ущербу для окружающей среды. Альтернативная энергия, такая как биогаз, является эффективным решением для сокращения использования ископаемого топлива, поскольку она имеет высокую температуру самовоспламенения (±650 °C), что делает ее пригодной для использования в двигателях с высокой степенью сжатия. Целью данного исследования является оценка влияния использования биогаза в двухтопливных дизельных двигателях на производительность и выбросы выхлопных газов. Эксперименты проводились на дизельных двигателях с одним и двумя видами топлива с использованием изменений расхода биогаза 3, 4 и 5 л/мин. Результаты исследования показывают, что использование биогаза в двухтопливных двигателях обеспечивает более высокие значения крутящего момента и тормозной мощности по сравнению с однотопливными при расходе 3 и 4 л/мин. Кроме того, выбросы выхлопных газов однотопливных дизельных двигателей показывают самые высокие значения для CO (0,29%) и CO_2 (5,67%), в то время как двухтопливные двигатели производят CO (0,27%) и CO_2 (5,51%). Эти результаты показывают, что биогаз как двухтопливное топливо может улучшить производительность двигателя, одновременно снижая вредные выбросы, что делает его устойчивой энергетической альтернативой.

Ключевые слова: биогаз, двухтопливный, дизель, производительность, выбросы выхлопных газов.

Солдатов А.И., Солдатов А.А., Костина М.А., Абуэллаиль А.А., Борталевич С.И.

Электр желісіндегі ақаулы контактты қосылыстарды анықтау алгоритмі

Мақалада контактты қосылыстың өтпелі кедергісін бақылау үшін термоэлектрлік әдіс ұсынылады. Электрмен жабдықтау желісіндегі нормативтік құжаттарда көрсетілген мәннен асатын кедергісі бар контактты қосылысты анықтау алгоритмі сипатталған. Алгоритм құрамында бес контактты қосылыс және үш электр қондырғысы бар сұлба негізінде қарастырылған. Алгоритм тек электр қондырғысын қосу сәтінде өлшенген термиялық ЭҚК

және өтетін ток мәндері бойынша контактты кедергіні есептеуге негізделген, бұл тек қондырғы қосылған контакттың кедергісін есептеуге мүмкіндік береді. Қосылатын немесе ажыратылатын электр қондырғысының нөмірі арқылы осы қондырғының электрмен жабдықтау тізбегін құрайтын контактты қосылыстардың нөмірлері анықталады.

Кілт сөздері: контактты жалғау, электрмен жабдықтау жүйесі, термиялық ЭҚК, алгоритм.

Солдатов А.И., Солдатов А.А., Костина М.А., Абуэллаиль А.А., Борталевич С.И.

Алгоритм обнаружения неисправных контактных соединений в электрической сети.

В статье предложен термоэлектрический метод для контроля величины переходного сопротивления контактного соединения. Описан алгоритм обнаружения контактного соединения в сети электроснабжения с сопротивлением превышающем значения указанное в нормативных документах. Алгоритм рассмотрен на примере схемы, содержащей пять контактных соединений и три электроустановки. Алгоритм основан на вычислении контактного сопротивления по измеренным значениям термоЭДС и протекающего тока только в момент включения электроустановки, что позволяет вычислять сопротивление только того контакта, через которое подключена электроустановка. По номеру включаемой или отключаемой электроустановки определяют номера контактных соединений, составляющих цепь электропитания этой установки.

Ключевые слова: контактное соединение, система электроснабжения, термоЭДС, алгоритм.

Меркулов В.В., Ульева Г.А., Ахметова Г.Е., Яковлева Д.А., Волокитина И.Е.

Жол белгілерін салу материалдарын таңдауды негіздеу және оларды алу технологиясын әзірлеу

Мақала жол белгілеріне арналған жабындарды зерттеуге арналған. Жол белгілерінің жабындары жоғары атмосфераға төзімділікке, температура ауытқуларына төзімділікке, ылғалдылық төзімділігіне және жақсы коррозияға қарсы қасиеттерге ие болғандықтан, оларды ашық болат конструкцияларын қорғау үшін де пайдалануға болады, бірақ олардың негізгі мақсаты жол белгілерін қолдану болып табылады. Жол таңбалары үшін материал түрін таңдағанда, олардың техникалық сипаттамаларын ескеру маңызды. Таңбаның тәуліктің кез келген уақытында жақсы көрінуі өте маңызды. Күндіз таңбаның көрінуіне оның өлшемдері мен жарықтығы әсер етеді. Бұл жұмыста бояумен қапталған үлгілерге жүргізілген зертханалық тәжірибелер сериясы сипатталып, олардың су және қышқылмен жанасқан кездегі қорғаныс қасиеттері анықталды. Осы бағыттағы зерттеулер жалғасуда. Қазіргі уақытта авторлар металл емес материалдар (бетон және т.б.) үшін полимерлі жабын жасау бойынша эксперименттер жүргізуде.

Кілт сөздері: жол таңбаларына арналған жабын, зертханалық тәжірибелер сериясы, төзімділік.

Меркулов В.В., Ульева Г.А., Ахметова Г.Е., Яковлева Д.А., Волокитина И.Е.

Обоснование выбора материалов для дорожной разметки с целью разработки технологии их получения

Статья посвящена исследованию покрытий для дорожных разметок. Поскольку покрытия для дорожных разметок обладают высокой атмосферостойкостью, стойкостью к перепадам температур, влагостойкостью, а также хорошими антикоррозионными свойствами, то их можно использовать для защиты открытых стальных конструкций, но основной их целью является использование для нанесения дорожных разметок. При выборе вида материалов для разметки важно учитывать их технические характеристики. Очень важно, чтобы разметка была хорошо видна в любое время суток. Днём на видимость влияют размеры и яркость разметки. В данной работе описана серия лабораторных опытов с образцами, покрытыми красками и выявлены их защитные свойства при контакте с водой и кислотой. Работа в данном направлении продолжается. Так, в настоящее время авторы проводят эксперименты по созданию полимерного покрытия для неметаллических изделий (бетоны и т.д.).

Ключевые слова: покрытие для дорожных разметок, серия лабораторных опытов, стойкость.

Қажыкенова С.Ш., Шайхова Г.С., Шалтақов С.Н.

Балқымалардың кейбір физикалық және құрылымдық қасиеттерін ультара дыбыс арқылы зерттеу

Балқытылған металға әсер етудің заманауи тиімді әдісі ультрадыбыстық өңдеу болып табылады - сұйық және кристалданатын металға динамикалық әсер ету түрі. Сұйық металдың акустикалық кавитациясын тудыратын ультрадыбыстық өңдеудің қарқындылығының белгілі бір параметрлері кезінде тазарту процесі белсенді түрде жүреді. Сонымен қатар, қуатты ультрадыбыстық модификация процесінде кристалдық торға тікелей әсер ететін металға әртүрлі композиттік элементтер мен отқа төзімді қорытпаларды енгізуге мүмкіндік береді. Серпімді толқындардың қасиеттері бойынша жүргізілген есептеулер политермдердің дыбыс жұту коэффициентінің тәртібіне осындай ерекшеліктерді анықтауға мүмкіндік береді, олар жеткілікті сенімділікпен балқыманы қыздырған кезде құрылымдық өзгерістердің жоқтығын немесе болуын көрсетеді және әртүрлі температура диапазонында бір балқымадағы құрылымдық өзгерістердің әртүрлі механизмдерін жүзеге асыру мүмкіндігін белгілейді. Серпімді толқын энергиясын жұтуы , сондай-ақ ультрадыбыстық жылдамдық бойынша жүргізілген зерттеулер балқымаларды қыздыру кезінде құрылымдық өзгерістердің жоқтығын немесе болуын көрсететін дыбыс жұту коэффициентінің политерминдерінің тәртібіндегі осындай ерекшеліктерді анықтауға мүмкіндік береді. Салыстырмалы талдаулар құрылымдық өзгерістердің біртұтас механизмі жоқ деген қорытынды жасауға мүмкіндік береді. Әр түрлі температура диапазонында бір балқымадағы құрылымдық өзгерістердің әртүрлі механизмдерін жүзеге асыру мүмкіндігі көрсетілген.

Кілт сөздері: тұтқыр металда, сұйық металдар, ультрадыбыстың таралу жылдамдығы, құрылымдық өзгерістер, балқыма.

Кажикенова С.Ш., Шаихова Г.С., Шалтаков С.Н.

Исследование некоторых физических и структурных свойств расплавов ультразвуком

Современным эффективным способом воздействия на расплавленный металл является ультразвуковая обработка — вид динамического воздействия на жидкий и кристаллизующийся металл. При определенных параметрах интенсивности ультразвуковой обработки, вызывающей акустическую кавитацию жидкого металла, активно протекает процесс рафинирования. Более того, мощный ультразвук позволяет в процессе модифицирования вводить в металл различные композиционные элементы и тугоплавкие сплавы, воздействуя непосредственно на кристаллическую решетку. Проведенные расчеты свойств упругих волн позволяют выявить такие особенности в поведении политерм коэффициента поглощения звука, которые с достаточной достоверностью свидетельствуют об отсутствии или наличии структурных изменений при нагревании расплава, и установить возможность реализации различных механизмов структурных изменений в одном и том же расплаве в различных температурных диапазонах. Проведенные исследования поглощения энергии упругих волн, а также скорости ультразвука позволяют выявить такие особенности в поведении политермов коэффициента поглощения звука, которые свидетельствуют об отсутствии или наличии структурных изменений при нагреве расплава. Сравнительный анализ позволяет сделать вывод об отсутствии единого механизма структурных изменений. Показана возможность реализации различных механизмов структурных изменений в одном и том же расплаве в разных температурных диапазонах.

Ключевые слова: вязкие металлы, жидкие металлы, скорость распространения ультразвука, структурные изменения, расплав.

Есбол Ж., Саттинова З.К., Туралина Д.Е., Мусенова Э.К.

Термопластикалық бериллий оксиді керамикасын қалыптау кезіндегі жылу алмасудың әсерін зерттеу

Ультрадыбысты қолдану арқылы түзілетін бериллий оксиді (BeO) керамикасы қарқынды агломерациямен сипатталады және ультрадыбыссыз түзілген керамикамен салыстырғанда, шөгуі және агломерация температурасы төмен болады. Ультрадыбыстық өңдеу кезінде керамиканың агломерациялануын белсендіруге ықпал ететін заттың біркелкілігіне және ұнтақтардың тығыз орналасуына байланысты. Термопластикалық шликердің реологиясының өзгеруі ультрадыбыстың белсендірілуі нәтижесінде жүзеге асты. Белсендіру кезінде пайда болатын өзгерістер дисперсиялық фаза процестерімен және масса алмасуымен байланысты. Ультрадыбыстық белсендіру құймалардың қасиеттерін біршама жақсартады. Құймалардың тығыздығы мен беріктігінің артуы, қатаю кезінде ультрадыбыстың әсерінен шөгудің тиімді азаюымен түсіндіріледі. Яғни құйманың шөгуін өтеу сұйық шликермен толтыру және қысымның әсерінен оның тығыздалуымен анықталады. Термопластикалық бериллий оксиді шликерін ультрадыбыстық құю үшін байланыстырғыш құрамы 10,0 нан 11,7 % дейінгі композицияларды қолданған жөн. Өйткені бұл байланыстырғыш құрамдары бериллий ұнтағымен араласып, беріктігі жоғары шликерге айналып, үлкен температураға шыдамды керамика түзейді.

Кілт сөздері: ультрадыбыстық белсендіру, бериллий оксиді, термопластикалық шликер, қалыптау процесі, тұтқырлыпластикалық күй.

Есбол Ж., Саттинова З.К., Туралина Д.Е., Мусенова Э.К.

Изучение влияния теплопередачи при формовании термопластичной керамики на основе оксида бериллия

Керамика из оксида бериллия (BeO), сформированная с использованием ультразвука, демонстрирует более интенсивное спекание, меньшую усадку и пониженную температуру спекания по сравнению с керамикой, полученной без применения ультразвука. Эффективность сверхбыстрого спекания зависит от сплошности керамического агломерата и правильного расположения частиц. Реологические свойства термопластичных суспензий изменились в результате ультразвуковой активации. Эти изменения связаны с дисперсно-фазовыми процессами и массопереносом. Ультразвуковая активация также несколько улучшает свойства отливок. Увеличение плотности и прочности отливок объясняется эффективным снижением усадки под воздействием ультразвука при затвердевании. То есть компенсация осадки ингот определяется заполнением жидким шликером и его уплотнением под действием давления. Для ультразвукового нагнетания термопластичной суспензии оксида бериллия рекомендуются составы с содержанием связующего от 10,0 до 11,7 %. Поскольку такие связующие составы смешиваются с бериллиевым порошком, превращаясь в высокопрочный шликер, образующий керамику, способную выдерживать большие температуры.

Ключевые слова: ультразвуковая активация, оксид бериллия, термопластичный шликер, процесс формования, вязкопластичное состояние.

Шомшекова С.А., Денисюк Е.К., Кондратьева Л.Н., Серебрянский А.В., Айманова Г.К., Актай Л.

MRK6 және MRK1040 галактикаларының оптикалық диапазондағы спектралік және фотометрлік зерттеулері

Бұл мақала ядролары белсенді галактикалардың айнымалылығын зерттеуге арналған, олар өздерінің орталық аймақтарында жүретін физикалық процестерді түсінуде маңызды рөл атқарады. Бұл зерттеу MRK 6 және MRK 1040 екі сейферт галактикаларының фотометрлік және спектрлік айнымалылығын мұрағаттық және заманауи бақылаулар негізінде талдауға бағытталған. Алғаш рет MRK 6 галактикасының фотометрлікқ бақылауларының нәтижелері өңделді, онда эмиссиялық сызықтардың профильдеріне және газ шығарындыларының бар екенін көрсетуі мүмкін қосымша спектрлік компоненттерді анықтауға ерекше назар аударылды. Зерттелген галактикалар үшін эмиссиялық сызықтардың әрбір компонентінің жылдамдық дисперсиялары анықталды. Кейбір Hα және Hβ профильдері үшін олардың жылдамдық дисперсиялары және көру сәулесі бойымен сәйкес жылдамдықтары бағаланды, бұл галактикалардың орталық аймақтарынан заттың ағып шығуының белгісі болуы мүмкін.

Кілт сөздері: галактикалардың белсенді ядролары, сейферт галактикалары, фотометрия, спектроскопия, жарқырау қисықтары, эмиссиялық сызықтар.

Шомшекова С.А., Денисюк Е.К., Кондратьева Л.Н., Серебрянский А.В., Айманова Г.К., Актай Л.

Спектральные и фотометрические исследования MRK6 и MRK1040 в оптическом диапазоне

Статья посвящена изучению изменчивости активных ядер галактик, которые играют ключевую роль в понимании физических процессов в их центральных областях. Данное исследование направлено на анализ фотометрической и спектральной изменчивости двух сейфертовских галактик, MRK 6 и MRK 1040, на основе архивных и современных наблюдений. Впервые обработаны результаты фотометрических наблюдений MRK 6, где особое внимание уделено профилям эмиссионных линий и выявлению дополнительных спектральных компонентов, которые могут свидетельствовать о газовых выбросах. Для исследуемых галактик определены дисперсии скоростей каждой из компонент эмиссионных линий. В некоторых профилях Hα и Hβ оценены их дисперсии скоростей и соответствующие скорости вдоль луча зрения, что может свидетельствовать об истечении вещества из центральных областей галактик.

Ключевые слова*:* активные ядра галактик, сейфертовские галактики, фотометрия, спектроскопия, кривые блеска, эмиссионные линии.

Егембердиева С.Ш., Кушкимбаева Б.Ж., Кушербаева М.Р., Кеикиманова М.Т.

Қоспаланған n-типті индий антимониді кристалдарының фотолюминесценция спектрлері

Бұл жұмыста қоспаланған n-типті индий антимонид кристалдарының фотолюминесценциясының жан-жақты зерттеуі ұсынылған. Қоспаланған n-типті индий антимониді кристалдарының фотолюминесценциясын жан-жақты зерттеу 77 К температурада және $1 \cdot 10^{15}$ $см^{-3}$-$1{,}5 \cdot 10^{19}$ $см^{-3}$ кең концентрация диапазонында жүргізілді. Бұл жұмыста $n > 5 \cdot 10^{17}$ $см^{-3}$ индий антимонидінің фотолюминесценция спектрлері алғаш рет алынды және $n \geq 8{,}5 \cdot 10^{16}$ $см^{-3}$ индий антимонидінің фотолюминесценция спектрі екі сызықтан тұратыны эксперименттік түрде анықталды, олардың максимумдары концентрация артқан сайын жоғары энергияға жаққа қарай ығысады. Зерттеу барысында n-типті қоспаланған индий антимонид кристалдарының қысқа толқынды сәулелену сызығының Ферми деңгейіндегі электрондардың валенттік зонаның жоғарғы бөлігіндегі тесіктермен рекомбинациясынан туындайтыны анықталды. Күшті қоспаланған кристалдардағы эксперимент пен теория арасындағы ең жақсы сәйкестікке донор концентрацияларының ауытқуын, тыйым салынған аймақ ені мен қоспалану деңгейінің арасындағы тәуелділікті, сондай-ақ концентрация өскен сайын Ферми энергиясының тиімді төмендеуін ескеру арқылы қол жеткізілді.

Кілт сөздері: кристалдардың фотолюминесценциясы, индий антимониді, Ферми деңгейі, қоспалау, концентрация, флуктуация, тесік, тыйым салынған аймақ.

Егембердиева С.Ш., Кушкимбаева Б.Ж., Кушербаева М.Р., Кеикиманова М.Т.

Спектры фотолюминесценции легированных кристаллов антимонида индия n-типа

В данной работе представлено детальное исследование фотолюминесценции легированных кристаллов антимонида индия n-типа. Проведено детальное исследование фотолюминесценции легированных кристаллов антимонида индия n-типа в широком диапазоне концентраций $1 \cdot 10^{15}$ $см^{-3}$-$1{,}5 \cdot 10^{19}$ $см^{-3}$ при температуре 77 К. В данной работе впервые получены спектры фотолюминесценции антимонида индия с $n > 5 \cdot 10^{17}$ $см^{-3}$ и экспериментально обнаружено, что спектр фотолюминесценции антимонида индия с $n \geq 8{,}5 \cdot 10^{16}$ $см^{-3}$ состоит из двух линий, максимумы которых смещаются в сторону больших энергий с ростом концентрации. Установлено, что коротковолновая линия излучения легированных кристаллов антимонида индия n-типа обусловлена

рекомбинацией электронов, находящихся на уровне Ферми, с дырками в вершине валентной зоны. Показано, что наилучшее согласие эксперимента с теорией в сильно легированных кристаллах достигается при учете флуктуаций концентраций доноров, зависимости ширины запрещенной зоны от степени легирования, а также эффективного снижения энергии Ферми с ростом концентрации.

Ключевые слова: фотолюминесценция кристаллов, антимонид индия, уровень Ферми, легирование, концентрация, флуктуация, дырка, запрещенная зона.